PhD Program in Design, Modeling and Simulation in Engineering
University of Pavia, Italy

DICAr – Department of Civil Engineering and Architecture

DEVELOPMENT OF ADVANCED EQUIVALENT-FRAME MODELS FOR THE NONLINEAR SEISMIC ANALYSIS OF MASONRY STRUCTURES

A Thesis Submitted in Partial Fulfilment of the Requirements
for the Degree of Doctor of Philosophy in

Design, Modeling and Simulation in Engineering

by

Christian Salvatori

Supervisors:
Prof. Andrea Penna – University of Pavia, Italy
Prof. Gabriele Guerrini – University of Pavia, Italy

June, 2024

ABSTRACT

The pronounced seismic vulnerability of unreinforced masonry (URM) structures and their extensive presence worldwide has prompted significant interest in developing strategies for an appropriate assessment and retrofit of the existing stock on the one hand, and for the design and detailing of new construction on the other hand. The seismic performance of existing URM buildings is generally governed by the activation of local overturning mechanisms, as they have been typically built without adequate consideration of horizontal actions. However, even though modern building codes and guidelines have stressed the importance of inhibiting local out-of-plane failure through structural interventions or new construction details, the in-plane seismic capacity of masonry walls might still be inadequate to withstand the demand. For this reason, strengthening and reinforcement solutions, consisting of materials with significant tensile strength applied to or embedded into the load-bearing masonry walls, are generally employed to cope with this deficiency.

In this thesis, the equivalent-frame modeling (EFM) for masonry structures is first discussed, highlighting its advantages, assumptions, and limitations through comparison with experimental results of shake-table tests on masonry buildings and aggregates. Subsequently, a novel three-dimensional macroelement is proposed to couple the in-plane and out-of-plane response of masonry walls subjected to lateral loads, resorting to a computationally efficient sectional integration for the axial-flexural behavior. More specifically, the three-dimensional macroelement builds upon a pre-existing two-dimensional formulation, which allows to effectively and efficiently reproduce the nonlinear static and dynamic behavior of an unreinforced masonry panel with a limited number of degrees of freedom. Furthermore, taking advantage of the proposed three-dimensional formulation, additional lumped and distributed reinforcement is incorporated into the macroelement, enabling the explicit modeling of several reinforcing and strengthening layouts. The resulting formulation is finally validated against the experimental results of a quasi-static cyclic shear-compression test on a stone-masonry piers strengthened by composite-reinforced mortar (CRM) jacketing.

ACKNOWLEDGEMENTS

(In Italian)

Desidero innanzitutto esprimere la mia gratitudine al Professor Andrea Penna, per avermi coinvolto in numerosissimi progetti durante tutto il mio percorso di studi ed avermi sempre incoraggiato a raggiungere gli obbiettivi prefissati con una prontezza e professionalità che in pochi possiedono.

Un ringraziamento particolare va al Professor Gabriele Guerrini, non per nulla definito "*Il Maestro*", per aver non solo supervisionato, ma anche dato un'enorme quantità di consigli e preziosi suggerimenti che, puntualmente, risolvevano o spiegavano tutte le problematiche e curiosità possibili ed immaginabili.

Ovviamente questo traguardo non sarebbe stato possibile senza il supporto, sia professionale che amichevole, di tutto il gruppo muratura, i cosiddetti "*Umarelli*", con il quale ho condiviso momenti preziosi, formali e informali. Il percorso di dottorato è senza alcun tipo di dubbio impegnativo, dispendioso e, talvolta, snervante, ma la presenza di un gruppo di colleghi e, soprattutto, amici come loro l'ha trasformato in uno dei periodi più iconici ed indimenticabili della mia vita.

Desidero inoltre ringraziare tutte le persone con cui ho avuto l'opportunità ed il piacere di lavorare, i tecnici del DICAr e del laboratorio Eucentre, sempre disponibili a fare quattro chiacchiere per alleviare anche le giornate più impegnative, nonché i componenti del gruppo di ricerca CompMech, con i quali ho scambiato molteplici idee e opinioni per far fronte a problemi numerici che, puntualmente, bussavano alla nostra porta.

Per ultimi, ma non per importanza, vorrei esprimere il più grande e sentito ringraziamento alla mia famiglia e ai miei amici più cari, di cui vorrei espressamente citare Fabri, Saiz e Afnob: è a loro e alla loro coinvolgente determinazione e dedizione che devo questo traguardo, per avermi supportato e, soprattutto, sopportato durante tutto il mio percorso di crescita.

TABLE OF CONTENTS

LIST OF FIGURES

LIST OF TABLES

1. INTRODUCTION

1.1 RESEARCH MOTIVATION AND OBJECTIVES

During the last decades, the research and engineering community has recognized existing unreinforced masonry (URM) buildings among the most vulnerable structures under seismic loading. In fact, ancient and historical masonry constructions were typically built without explicit design, merely following empirical and geometrical rules. Consequently, the lack of efficient connections among intersecting walls or with horizontal diaphragms, the bad arrangement of masonry leaves, the presence of flexible floors and thrusting elements not effectively restrained, have led to premature local out-of-plane collapses. For this reason, seismic-prone countries have issued detailing rules for the seismic design of new, and retrofit of existing, unreinforced masonry structures.

However, even after mitigating the out-of-plane response issues and thus inducing a global "box-type" behavior, the performance under seismic actions might still be unsatisfactory. In fact, the in-plane strength and ultimate deformation capacity of masonry structural elements may not be sufficient to resist the demand imposed on them. For this reason, strengthening and reinforcement solutions have also been developed to improve the in-plane response of existing and new elements, respectively, such as jacketing, near-surface-mounted bars, or embedded rebars in reinforced or confined masonry. To this scope, additional materials with significant tensile strength are applied to the surface or embedded into the masonry walls, overcoming one of the most significant deficiencies of this material.

Several modeling approaches for the seismic performance assessment of URM buildings have been proposed in the literature, ranging from simplified methodologies based on the limit analysis (Abruzzese *et al.,* 1992; Milani *et al.,* 2007) or story mechanisms (Tomaževič, 1987), to more refined ones involving micro-modeling techniques, where bricks, mortar, and interfaces are modeled in detail through suitable nonlinear finite (Alpha and Monetto, 1994; Anthoine and Pegon, 1996) or discrete elements (Lemos, 2007; Casolo and Peña, 2007; Caliò *et al.,* 2012). However, if the refined methodologies are well known for their high computational effort, thus resulting mainly applicable to structural subsystems only, the simplified counterparts are based on significant approximations, making their field of application somewhat limited.

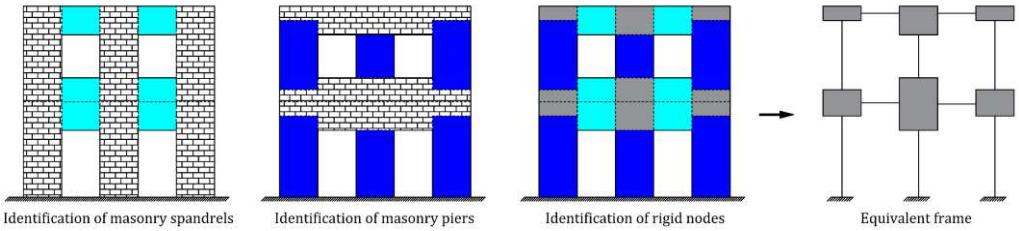

Figure 1.1: Equivalent-frame idealization.

Conversely, the equivalent-frame modeling (EFM) approach strikes a balance between result accuracy and computational effort (Magenes and Della Fontana, 1998; Lagomarsino *et al.,* 2013). In this context, each resisting wall is discretized into deformable elements, with several finite element or macroelement formulations capable of simulating the nonlinear response of piers and spandrels, and rigid nodes, which define portions of masonry generally less sensitive to deformations and damage (Figure 1.1). Piers represent the main vertical elements responsible for withstanding vertical and horizontal loadings, whereas spandrels may couple their lateral response if effectively connected and supported. Consequently, the computational time is strongly reduced, as the elements target the average behavior of the masonry panels rather than focusing on the local behavior of the material. Despite this simplification, the EFM still yields generally accurate results, making it a viable choice for ordinary building design and assessment.

Among all the formulations proposed in the literature (Magenes and Della Fontana, 1998; Roca *et al.*, 2005; Penelis, 2006; Chen *et al.*, 2008; Belmouden and Lestuzzi, 2009; Grande *et al.*, 2011; Raka *et al.*, 2015; Peruch *et al.*, 2019), the two-dimensional macroelement initially developed by Brencich and Lagomarsino (1998), further enhanced by Penna *et al.* (2014), and implemented in the software TREMURI (Lagomarsino *et al.,* 2013), appears particularly suitable and efficient for static and dynamic analyses of masonry structures. Indeed, its mechanics-based formulation and analytical description of the axial-flexural response allow capturing both shear and flexural failure mechanisms with a limited number of degrees of freedom. More specifically, the shear behavior is concentrated at the center of the macroelement with a Coulomb-like strength criterion, whereas the coupled axial-flexural response is lumped at its end-interfaces, in correspondence with the two nodes bounding the macroelement. Moreover, the analytical formulation of the end-interfaces allows to simulate two-dimensional mechanisms, such as cracking and toe-crushing of the section, without computationally demanding fiber discretization and numerical integration.

This macroelement has recently been improved by Bracchi *et al.* (2021) and Bracchi and Penna (2021) by overcoming some of its limitations, such as the inability to simultaneously capture the correct axial and flexural stiffnesses of a masonry member, and by introducing additional features, such as a more appropriate axial-flexural constitutive law for the end-

interfaces, to better account for damage accumulation and residual displacements. Moreover, Bracchi and Penna (2021) include the possibility to consider second-order geometrical effects and an automatic adaptive calibration of the Coulomb shear criterion parameters, allowing to model several strength criteria based on a linearization around the instantaneous axial load.

The equivalent-frame modeling approach has been widely investigated over the last decades (Kappos *et al.,* 2002; Marques and Lourenço, 2011, 2014; Quagliarini *et al.,* 2017; Morandini *et al.,* 2022; Penna *et al.,* 2022; Camata *et al.,* 2022; Cattari *et al.,* 2022), concluding that this simplification is reliable in reproducing the response of URM structures provided that a box-type behavior and a regular opening layout are guaranteed. Conversely, in case of irregular opening distribution, additional modeling measures and adjustments of the wall discretization might be necessary to preserve reasonable results.

Furthermore, being initially conceived for simulating the in-plane response of the walls, the main drawback of this approach is the common assumption of neglecting the out-of-plane stiffness and strength of masonry members. Indeed, it is typically assumed that the global building behavior is governed by the in-plane response of the resisting walls. In reality, in-plane and out-of-plane lateral responses are not independent from each other, and their interaction may become relevant in capturing the global building response even when local out-of-plane overturning mechanisms are substantially inhibited.

In this context, Vanin *et al.* (2020) expanded the Penna *et al.* (2014) formulation into an advanced three-dimensional macroelement, implemented in the open-source software OpenSees (McKenna, 2011). Unlike the original formulation, this macroelement consists of an assemblage of two panels bounded by three nonlinear sections, allowing for the one-way out-of-plane bending to be explicitly simulated. The macroelement also provides optional second-order geometrical effects, a consistent or lumped mass matrix, an initial- or tangent-stiffness-proportional damping model, and eventually drift capacity models for the in-plane direction. However, it lumps the shear response within a nonlinear spring at mid-height of the element and does not incorporate the adaptive Coulomb criterion developed by Bracchi and Penna (2021).

In this work, the two-dimensional formulation of the macroelement proposed by Penna *et al.* (2014), Bracchi *et al.* (2021), and Bracchi and Penna (2021), is revised, improved, and extended to the three-dimensional space for a better simulation of the nonlinear response of URM and reinforced masonry buildings. Unlike the three-dimensional macroelement proposed by Vanin *et al.* (2020), this formulation preserves the kinematics of the original version of Penna *et al.* (2014), which decouples the shear and flexural responses by means of internal axial and rotational degrees of freedom, and encompasses the adaptive linearization of the shear strength criteria implemented by Bracchi and Penna (2021).

Additionally, the versatility of the proposed formulation allows explicitly modeling the in-plane and out-of-plane contributions of strengthening and reinforcement materials.

1.2 ORGANIZATION OF THE THESIS

After this brief introduction, Chapter 2 deals with the modeling strategies available in the literature to numerically simulate masonry structures, mainly focusing on the equivalent-frame approach with nonlinear macroelements. In this context, the latter modeling strategy is thoroughly described, several macroelements are considered and classified based upon their formulations, the main laboratory tests to determine mechanical properties are described, and the procedures for the seismic performance assessment of URM buildings are explained.

Chapter 3 reports a comparison between an experimental and numerical study on the effect of different retrofit solutions for stone masonry buildings in earthquake-prone regions. The study aimed to evaluate the influence of enhanced wall-to-diaphragm connections, diaphragm stiffness, and masonry strengthening on the dynamic response of the investigated buildings. The two-dimensional macroelement currently implemented in the equivalent-frame software TREMURI is used, whereas correction coefficients are applied to the masonry mechanical properties to account for strengthening interventions, as suggested by the Italian building code.

Chapter 4 illustrates the numerical simulation of an experimental shake-table test to assess the seismic vulnerability of a typical building aggregate composed of two adjacent weakly-connected structural units. In this context, the results of nonlinear static analyses obtained from three equivalent-frame modeling strategies are compared. In all cases, the numerical simulations are performed by employing the two-dimensional macroelements currently implemented in the software TREMURI, which neglects the out-of-plane stiffness and strength of the masonry member. However, the first strategy involves an unconventional three-dimensional approach with fictitious frames and membranes, to capture the out-of-plane behavior of the walls arranged perpendicular to the shaking direction. The second option still analyzes a three-dimensional model, but all the unconventional features are removed according to common global modeling practices. Finally, given the low stiffness of the timber diaphragms, single-wall two-dimensional models are also analyzed.

Mainly focusing on its axial-flexural behavior, a thorough description of the Penna *et al.* (2014) macroelement is given in Chapter 5, where the in-plane formulation is extensively reviewed to add a nonlinear correction to better capture toe-crushing phenomena, and to implement an elasto-fragile tensile strength. Moreover, the extension to the three-dimensional space is described, to overcome the need for fictitious frames and membranes dedicated to the out-of-plane response. For this purpose, the end-interfaces are discretized in a series of analytical stripes, whose numerical integration over the thickness of the

macroelement returns the coupled in-plane and out-of-plane response. Consequently, a computationally efficient formulation is preserved. A full-fiber discretization of the end-interfaces is also provided, to allow comparisons in terms of computational efficiency and integration results, and to overcome some limitations of the analytical formulation on the choice of constitutive relationships. Finally, a novel iterative algorithm is presented to achieve a high convergence rate and numerical robustness, through a combination of initial- and tangent-stiffness Newton-Raphson methods.

In Chapter 6, the biaxial flexural contribution of lumped and distributed reinforcement is added to the end-interface formulation, allowing for rebars or surface layers to be explicitly considered instead of modifying the masonry tensile strength through enhancement coefficients. The former are modeled following the J2-plasticity theory, providing also an optional isotropic and kinematic hardening, whereas the latter are characterized by a no-compression elasto-fragile tensile response, analytically integrated over the length of the macroelement. The collaboration of the reinforcement with the masonry is enforced through kinematic compatibility relationships, similarly to the three-dimensional extension of the masonry macroelement described in Chapter 5.

In Chapter 7, the capabilities of the three-dimensional macroelement proposed in this thesis are validated through the simulation of an experimental quasi-static cyclic shear-compression test involving a stone masonry pier retrofitted with composite-reinforced mortar (CRM) on both sides. In this context, the axial-flexural contribution of the strengthening layers is explicitly reproduced through further stripes added to the end-interfaces of the macroelement, as described in Chapter 6, whereas the shear-strengthening effect of the CRM solution is modeled through an improved tensile strength of the masonry material, compatible with the findings of the complementary material characterization campaign. Moreover, cyclic and monotonic analyses investigate the effect on the response of different constitutive laws for the masonry material and the correspondence between stripe and fiber end-interface formulations.

Finally, Chapter 8 summarizes the thesis, draws the main conclusions, and presents possible future developments of this work. A comprehensive list of appendices is included at the end of the thesis, detailing the numerical implementation of the proposed macroelement. More specifically, Appendix A, Appendix B, and Appendix C report the elastic stiffness matrices of the two-dimensional macroelement, three-dimensional macroelement, and analytical surface layers, together with the computation of the relevant terms. Appendix D deals with the implementation of fiber-discretized end-interfaces, distinguishing between elastic and nonlinear contributions. Finally, Appendix E and Appendix F delve into the analytical corrections responsible for the in-plane response of the individual stripes, accompanied by the corresponding nonlinear gradients required to define the tangent stiffness matrix of the three-dimensional macroelement.

REFERENCES

Abruzzese, D., Como, M., and Lanni, G. (1992). On the Lateral Strength of Multistory Masonry Walls with Openings and Horizontal Reinforcing Connections. *In Proceedings of the 10th World Conference on Earthquake Engineering*, Balkema-Rotterdam.

Alpa, G., and Monetto, I. (1994). Microstructural Model for Dry Block Masonry Walls with In-Plane Loading. *Journal of the Mechanics and Physics of Solids*, 42(7), 1159-1175.

Anthoine, A., and Pegon, P. (1996). Numerical Analysis and Modelling of the Damage and Softening of Brick Masonry. In J. W. Bull (Ed.), *Numerical Analysis and Modelling of Composite Materials,* 152-184, Dordrecht: Springer Netherlands.

Belmouden, Y., and Lestuzzi, P. (2009). An Equivalent Frame Model for Seismic Analysis of Masonry and Reinforced Concrete Buildings. *Construction and Building Materials*, 23(1), 40-53.

Bracchi, S., Galasco, A., and Penna, A. (2021). A Novel Macroelement Model for the Nonlinear Analysis of Masonry Buildings. Part 1: Axial and Flexural Behavior. *Earthquake Engineering & Structural Dynamics*, 50(8), 2233-2252.

Bracchi, S., and Penna, A. (2021). A Novel Macroelement Model for the Nonlinear Analysis of Masonry Buildings. Part 2: Shear Behavior. *Earthquake Engineering & Structural Dynamics*, 50(8), 2212-2232.

Brencich, A., and Lagomarsino, S. (1998). A macro-elements dynamic model for masonry shear walls. *In Proceedings of the STRUMAS IV 4th Int. Symp. On Computer Methods in Structural Masonry*. E&FN Spon: London, 67–75.

Caliò, I., Marletta, M., and Pantò, B. (2012). A New Discrete Element Model for the Evaluation of the Seismic Behaviour of Unreinforced Masonry Buildings. *Engineering Structures*, 40, 327-338.

Camata G., Marano, C., Sepe, V., Spacone, E., Siano, R., Petracca, M., Roca, P., and Pelà, L. (2022). Validation of non-linear equivalent-frame models for irregular masonry walls. *Engineering Structures*, 253, 113755.

Casolo, S., and Peña, F. (2007). Rigid Element Model for In-Plane Dynamics of Masonry Walls Considering Hysteretic Behaviour and Damage. *Earthquake Engineering & Structural Dynamics*, 36(8), 1029-1048.

Cattari, S., D'Altri, A. M., Camilletti, D., and Lagomarsino, S. (2022). Equivalent frame idealization of walls with irregular openings in masonry buildings. *Engineering Structures*, 256, 114055.

Chen, S. -Y., Moon, F. L., and Yi, T. (2008). A Macroelement for the Nonlinear Analysis of In-Plane Unreinforced Masonry Piers. *Engineering Structures*, 30(8), 2242-2252.

Grande, E., Imbimbo, M., and Sacco, E. (2011). A Beam Finite Element for Nonlinear Analysis of Masonry Elements with or without Fiber-Reinforced Plastic (FRP) Reinforcements. *International Journal of Architectural Heritage*, 5(6), 693-716.

Kappos, A. J., Penelis, G. G., and Drakopoulos, C. G. (2002). Evaluation of Simplified Models for Lateral Load Analysis of Unreinforced Masonry Buildings. *Journal of Structural Engineering*, 128(7), 890-897.

Lagomarsino, S., Penna, A., Galasco, A., and Cattari, S. (2013). TREMURI Program: An Equivalent Frame Model for the Nonlinear Seismic Analysis of Masonry Buildings. *Engineering Structures*, 56, 1787-1799.

Lemos, J. V. (2007). Discrete Element Modeling of Masonry Structures. *International Journal of Architectural Heritage*, 1(2), 190-213.

Magenes, G., and Della Fontana, A. (1998). Simplified Non-Linear Seismic Analysis of Masonry Buildings. *In Proceedings of the British Masonry Society*, 8, 190-195.

Marques, R., and Lourenço, P. B. (2011). Possibilities and Comparison of Structural Component Models for the Seismic Assessment of Modern Unreinforced Masonry Buildings. *Computers & Structures*, 89(21), 2079-2091.

McKenna, F. (2011). OpenSees: A Framework for Earthquake Engineering Simulation. *Computing in Science & Engineering*, 13(4), 58-66.

Milani, G., Lourenço, P. B., and Tralli, A. (2007). 3D Homogenized Limit Analysis of Masonry Buildings Under Horizontal Loads. *Engineering Structures*, 29(11), 3134-3148.

Morandini, C., Malomo, D., and Penna, A. (2022). Equivalent Frame Discretisation for URM Façades with Irregular Opening Layouts. *Bulletin of Earthquake Engineering*, 20(5), 2589-2618.

Penelis, G. G. (2006). An Efficient Approach for Pushover Analysis of Unreinforced Masonry (URM) Structures. *Journal of Earthquake Engineering*, 10(3), 359-379.

Penna, A., Lagomarsino, S., and Galasco, A. (2014). A Nonlinear Macroelement Model for the Seismic Analysis of Masonry Buildings. *Earthquake Engineering & Structural Dynamics*, 43(2), 159-179.

Penna, A., Bracchi, S., Salvatori, C., Morandini, C., and Rota, M. (2022). Extending Analysis Capabilities of Equivalent Frame Models for Masonry Structures. *Progresses in European Earthquake Engineering and Seismology,* 473-485, Springer, Cham.

Peruch, M., Spacone, E., and Camata, G. (2019). Nonlinear Analysis of Masonry Structures using Fiber-Section Line Elements. *Earthquake Engineering & Structural Dynamics*, 48(12), 1345-1364.

Quagliarini, E., Maracchini, G., and Clementi, F. (2017). Uses and Limits of the Equivalent Frame Model on Existing Unreinforced Masonry Buildings for Assessing their Seismic Risk: A Review. *Journal of Building Engineering*, 10, 166-182.

Raka, E., Spacone, E., Sepe, V., and Camata, G. (2015). Advanced Frame Element for Seismic Analysis of Masonry Structures: Model Formulation and Validation. *Earthquake Engineering & Structural Dynamics*, 44(14), 2489-2506.

Roca, P., Molins, C., and Mari, A. R. (2005). Strength Capacity of Masonry Wall Structures by the Equivalent Frame Method. *Journal of Structural Engineering*, 131(10), 1601-1610.

Tomaževič, M. (1987). Dynamic Modelling of Masonry Buildings: Storey Mechanism Model as a Simple Alternative. *Earthquake Engineering & Structural Dynamics*, 15(6), 731-749.

Vanin, F., Penna, A., and Beyer, K. (2020). A Three-Dimensional Macroelement for Modelling the In-Plane and Out-of-Plane Response of Masonry Walls. *Earthquake Engineering & Structural Dynamics*, 49(14), 1365-1387.

2. EQUIVALENT FRAME MODELING TECHNIQUE FOR THE SEISMIC RESPONSE ANALYSIS OF MASONRY BUILDINGS

Adapted from: Zarzour, N., Salvatori, C., Santisi d'Avila, M. P., and Penna, A. Equivalent frame modeling technique for the seismic response analysis of masonry buildings. *In Masonry Structures: Building archaeology, characterization, modeling and analysis of masonry structures*. (*Manuscript in preparation*)

2.1 INTRODUCTION

Seismic design and risk assessment of unreinforced masonry (URM) buildings present significant challenges related with the simulation of the building response to horizontal loadings in an efficient and reliable way. This chapter focuses on the equivalent frame modeling (EFM) strategy, according to which load bearing masonry walls are subdivided into deformable members connected by rigid nodes, inspired by damage observations after post-earthquake surveys and experimental campaigns. This approach, developed as a strategy for the seismic analysis of both new and existing URM buildings, is recommended in several seismic codes (e.g. Eurocode 8, CEN 2004). In fact, it strikes a balance between accuracy of results and computational efficiency, mainly in the context of professional practice, in which the spatial model of extended URM buildings is demanded, as well as a clear interpretation of damage is required.

After a brief overview of modeling strategies, the mechanical characterization of masonry to calibrate the EFM is discussed, considering various aspects such as structural element definition and assemblage, connection effects, strength domains, and damage limit assumptions. Finally, the key parameters and the procedures for the seismic performance assessment of URM structures are presented.

2.2 MODELING STRATEGIES FOR THE SEISMIC PERFORMANCE ASSESSMENT OF MASONRY STRUCTURES

Simplified and advanced formulations have been proposed for an efficient and more comprehensive understanding of the behavior of URM structures. However, because of the complex and uncertain response of masonry material, the topic is not trivial and is always open to further improvements.

The dynamic response of masonry, defined as a composite material made up of units and mortar arranged with various bond patterns, is strongly affected by the mechanical behavior of the individual components, especially of mortar joints, which usually represent the weakest element. The elasto-plastic response of masonry can be modeled by employing nonlinear constitutive laws associated to each material (units, mortar and interfaces), to the units and their interfaces only, or to the structural element as a whole, according to the adopted scale of representation (Lourenço, 1996).

In this context, D'Altri *et al.* (2019) attempted to make some order by comprehensively reviewing and classifying the modeling strategies available in the literature. Accordingly, the masonry modeling approaches are distinguished into four main categories: block-based models, in which masonry is modeled following the actual texture of the material; continuum modeling, where masonry is represented as a continuum deformable body, potentially ignoring the actual texture of the material; macroelement models, in which the structure is discretized into panel-scale deformable elements; and geometry-based models, where the structure is modeled as a rigid body and the solution is achieved by resorting to limit analysis procedures.

The block-based approach covers a wide range of methodologies depending on the modeling assumptions. Even though more refined classifications can be found in the literature for block-based methods, the one proposed by Lourenço (1996) is adopted in the following, i.e., detailed (Figure 2.1a) and simplified (Figure 2.1b) micro-modeling approaches. The first one represents units and mortar joints as continuum elements, whereas discontinuous elements are employed for unit-to-mortar interfaces (Ali and Page, 1988; Arnau *et al.*, 2015; Addessi and Sacco, 2016; D'Altri *et al.*, 2018). The constitutive behavior of the elements is defined in terms of mechanical parameters calibrated through small-scale experimental tests. In this spatial discretization strategy, the mesh size is influenced by the smaller joint elements and returns a significant computational time.

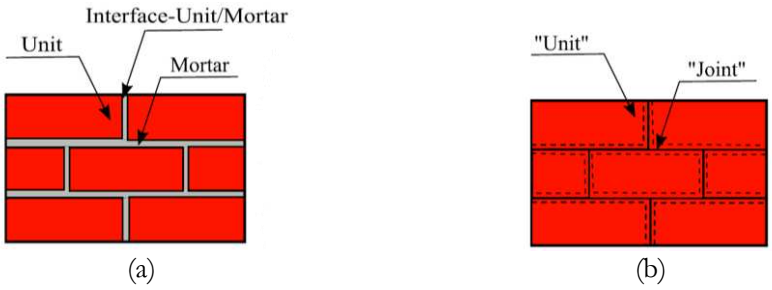

Figure 2.1: Example of (a) detailed micro-modeling, and (b) simplified micro-modeling (Prakash *et al.*, 2020).

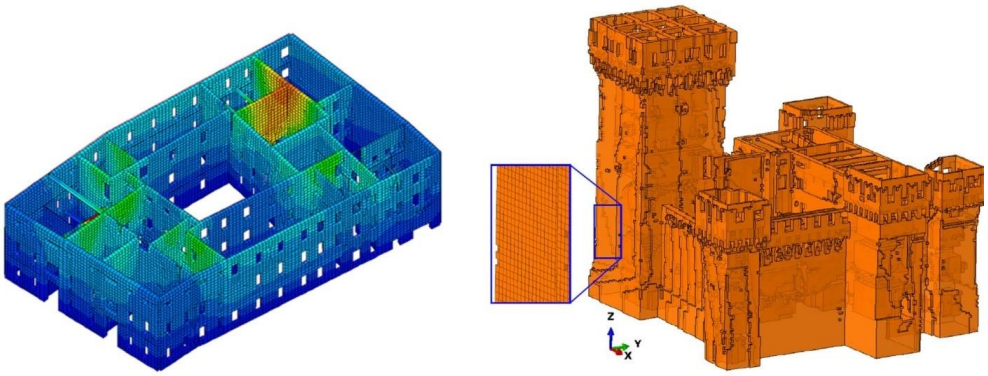

(a) (b)

Figure 2.2: Examples of (a) continuum modeling for buildings (curtesy of Bellinzoni and Morandi, PE); and (b) more complex structures (Degli Abbati *et al.*, 2019).

On the other hand, in the simplified micro-modeling, mortar joints are not directly considered. In fact, expanded elements represent the behavior of units, whereas contact laws simulate mortar layers and unit-to-mortar interfaces (Lotfi and Shing, 1994; Lourenço and Rots, 1997; Oliveira and Lourenço, 2004; Guo *et al.*, 2022). The simplified micro-modeling approach based on the discrete element method (DEM) is one of the prevailing choices and proved successfully accurate in predicting the response of masonry structures (Damiani *et al.*, 2023). Simplified micro-modeling approaches allow to reduce the computational time compared to refined micro-modeling methodologies. However, also the accuracy may be influenced, as the Poisson effect on mortar layers may not be properly captured.

Overall, the significant computational effort required by micro-modeling approaches and the need to define a large number of mechanical parameters, require expert users and generally restrict their application to structural subsystems, making them impractical for conventional building design and assessment. Conversely, in the continuum modeling (Figure 2.2), masonry is treated as a deformable body consisting of homogeneous material, without distinguishing between units and mortar layers. Consequently, the spatial discretization may not directly correspond to masonry units, therefore the possibility of defining a larger mesh size could reduce the computational efforts. Nonetheless, results might be sensitive to the adopted element dimensions. For this reason, several efforts have been made to ensure mesh objectivity, e.g., through defining a characteristic length, as a function of the element formulation and material properties, or through an adaptive mesh refinement.

A constitutive relationship is assumed for the masonry material and can be calibrated either using mechanical parameters deduced from analytical homogenization procedures (de Felice, 2001; de Felice, 2009; Zucchini and Lourenço, 2009; Marfia and Sacco, 2012;

Stefanou *et al.*, 2015; Bertolesi *et al.*, 2017) or directly from experimental tests on masonry panels (Lourenço *et al.*, 1998; Pelà *et al.*, 2013; Bruggi and Taliercio, 2015; Degli Abbati *et al.*, 2019). The definition of the mechanical properties is crucial, since the accuracy of the constitutive laws assigned to the homogenized material governs the structural response.

In the macro-modeling approach, each masonry façade is subdivided into panel-scale deformable elements (Figure 2.3), characterized by phenomenological or mechanical-based constitutive laws. A pioneering macro-modeling strategy is the POR method proposed by Tomaževič (1978), in which the behavior of each story is described independently, by an interstory shear force versus displacement curve. This method assumes that only in-plane shear forces in vertical elements could cause damage, while spandrels and nodal regions are considered rigid, resulting in strong approximation. Consequently, the displacement capacity of each story is determined by the superposition of the responses of the individual masonry piers. Moreover, the axial force variation due to overturning effects and the internal force redistribution after damage or failure of the elements are not accounted for.

The equivalent frame modeling strategy is a type of macro-modeling approach that overcomes the limitations of the POR method on the internal force prediction. The structural model is characterized by deformable macroelements, such as piers and spandrels connected by rigid nodes (Figure 2.3). In this context, masonry members are still considered homogeneous but, unlike the continuum strategy, the constitutive laws try to reproduce the average mechanical behavior of the elements rather than the local response of the material.

The macroelement response is defined either in terms of assigned strength domains, considering the coupling of generalized forces for multiaxial loading (Magenes and Della Fontana, 1998; Lagomarsino *et al.*, 2013), or relying on sectional integrations (Belmouden and Lestuzzi, 2009; Raka *et al.*, 2015). As a result, this methodology ensures a reasonable compromise between accuracy of results and computational effort, making it the most employed solution for the static and dynamic analysis of URM buildings (Figure 2.3c), mainly in the context of ordinary engineering practice.

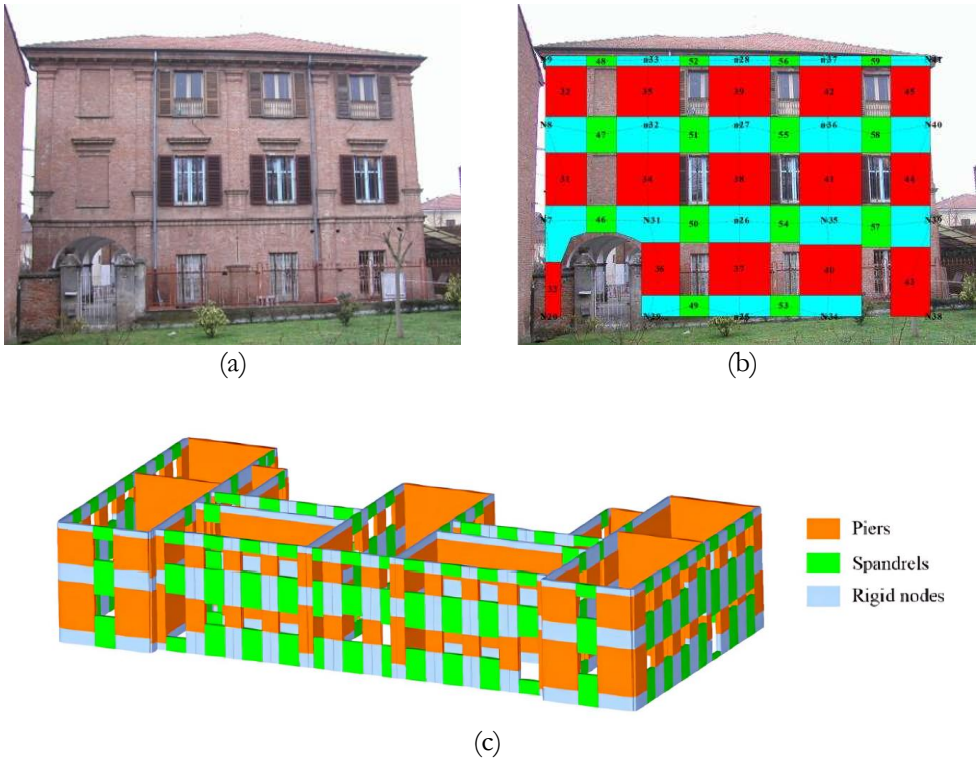

Figure 2.3: Examples of equivalent frame discretization for masonry buildings: (a) and (b) curtesy of Prof. Penna; (c) Segovia-Verjel *et al.* (2019).

Unlike the abovementioned strategies, geometry-based modeling describes the masonry building response assuming rigid elements, neglecting thus their intrinsic deformability. These approaches are mostly adopted for studying the equilibrium state in masonry arches and vaults (O'Dwyer, 1999; Block *et al.*, 2006; Marmo and Rosati, 2017) and for assessing global or local mechanisms in masonry buildings (Chiozzi *et al.*, 2018a,b).

Geometry-based modeling relies on limit analysis solutions, governed by either static or kinematic theorem. In this context, the static theorem assumes an admissible stress field that respects a given yield criterion, whereas the kinematic one rests upon the definition of an admissible kinematic mechanism. The structure geometry consists of the only input required for the analysis, beyond the definition of the loading conditions. However, the limit analysis only returns the collapse load multiplier. In particular, the static theorem provides a lower-bound limit of the collapse multiplier, whereas the kinematic theorem provides an upper-bound limit.

2.3 EQUIVALENT FRAME MODELING STRATEGY

When dealing with unreinforced masonry buildings, two types of resisting elements can be identified: piers and spandrels. Piers are the vertical load-bearing elements, identified between adjacent openings, supporting both gravity and lateral loads. On the other hand, spandrels lay horizontally and are positioned above and below the openings. They transfer vertical loads from the diaphragms to the piers, coupling and restraining also their horizontal generalized displacements under lateral loads.

The observation of damage after seismic events and experimental campaigns supports the equivalent frame modeling strategy as a viable approach for the seismic design and risk assessment of URM buildings. In some cases, the damage is principally localized in spandrels, whereas piers appear relatively undamaged (Figure 2.4a). This behavior might be associated with weak spandrels, hindering the transfer of shear load to other structural elements. Conversely, if stronger spandrels are present, the damage mostly affects masonry piers (Figure 2.4b), in particular at lower stories. Generally, the damage is diffuse, with piers and spandrels experiencing cracks (Figure 2.4c). However, even in this case, observations highlight zones between the resisting elements without significant signs of damage.

The load-bearing capacity of masonry walls is essentially related to the in-plane strength and stiffness of the involved macroelements (Figure 2.5a), neglecting any out-of-plane response (Figure 2.5b). In fact, it is assumed that the local mechanisms are prevented through adequate details such as tie rods, ring beams, solid interlocking among intersecting walls, and effective connections between vertical walls and horizontal diaphragms. These measures allow the building to experience the so-called box-like behavior (Figure 2.5c) and to obtain a global three-dimensional response during static and dynamic loading. However, a posteriori analysis is necessary to check for the activation of out-of-plane local mechanisms, resorting to hands-on simplified calculations, typically based on the kinematic analysis.

(a) (b) (c)

Figure 2.4: Buildings with in-plane damage concentrated (a) in spandrels, (b) in piers, and (c) in both structural elements (Ma *et al.*, 2022; Bilgin *et al.*, 2020).

(a) (b) (c)

Figure 2.5: (a) in-plane and (b) out-of-plane response of an unreinforced masonry panel. (c) desired box-like behavior of a masonry building (Touliatos, 1996).

Unfortunately, the EFM approach requires an a priori estimation of the effective height of piers and length of spandrels. In this context, various pier discretization criteria are proposed in the literature: some of them rely on experimental tests (Moon *et al.*, 2006; Yi *et al.*, 2006), others on post-earthquake damage observations (Augenti, 2006; Parisi and Augenti, 2013).

Bracchi *et al.* (2015) analyze the in-plane damage pattern experienced by the ground floor of an URM building after the 6.1 M_w 2012 Emilia earthquake (Figure 2.6). Although the outer piers are damaged according to a rocking-flexure failure mode (*F*), due to their higher aspect ratio (height-to-length ratio), the damage on the inner ones results influenced by the load direction. In fact, in the case of the rightwards load (Figure 2.6a), the left central pier fails according to a flexural mechanism (*F*), whereas the right central pier has a diagonal crack in shear (*S*). The opposite behavior is observed when the loading is reversed (Figure 2.6b). The vertical axial load on both piers can be assumed to be similar as they are close to the frame symmetry axis, but the aspect ratio of the same pier changes with the load direction. In particular, when the pier is restrained by the ground floor spandrel, under the window, its effective height decreases and, consequently, the aspect ratio.

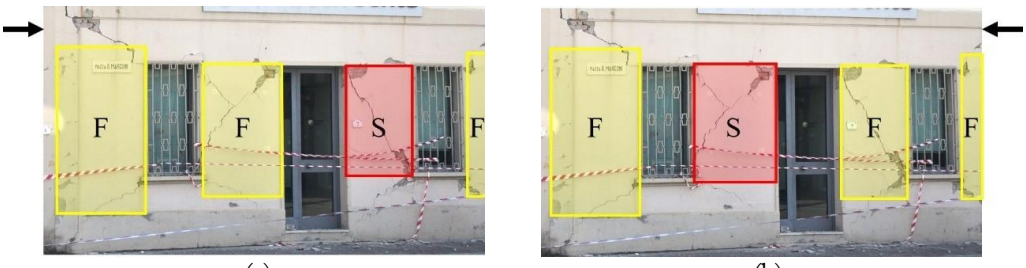

(a) (b)

Figure 2.6: Damage observation after the 6.1 M_w 2012 Emilia earthquake: definition of the equivalent pier height and associated failure mode (S: shear; F: flexure) in the case of (a) rightwards and (b) leftwards load (Bracchi *et al.,* 2015).

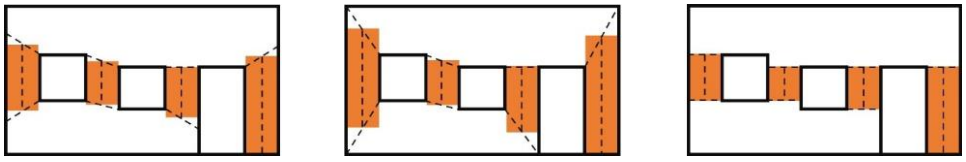

Figure 2.7: Examples of discretization criteria for masonry piers: (a) Dolce (1991), (b) Lagomarsino *et al.* (2013), and (c) Bracchi *et al.* (2015).

Therefore, according to Bracchi *et al.* (2015), the same pier can be squat or slender for each horizontal load direction, depending on the restrained conditions. Nevertheless, in the framework of the EFM application, the definition of effective dimensions for piers and spandrels is unique and independent of the loading direction. Consequently, the choice is usually delegated to engineering judgement, especially in the case of irregular façades.

Three of the most common criteria for determining the effective height of piers in masonry structures are reported in Figure 2.7. Dolce (1991) proposes an approach in which the effective pier height is calculated starting from the distance between midpoints of segments connecting adjacent element corners or element corners with the closest floor levels, with a maximum inclination of ideal crack lines of 30° (Figure 2.7a). Lagomarsino *et al.* (2013) propose a similar criterion but without any limitation on the maximum slope of the crack lines, resulting in generally higher piers (Figure 2.7b). On the other hand, according to Bracchi *et al.* (2015), the effective height of vertical elements could be taken as the minimum clear distance between adjacent openings (Figure 2.7c). As a result, this method implicates smaller piers, especially penalizing the outer ones.

Concerning the identification of spandrels, a straightforward method for regularly distributed openings considers the spandrel as the portion of masonry between two vertically aligned openings (Figure 2.8a). In case of irregularly distributed openings, Lagomarsino *et al.* (2013) suggest conventionally assuming a mean value for the length of spandrel elements based on the overlapping part between openings at two levels (Figure 2.8b). In situations where the is no overlap between adjacent openings, it is advisable to treat that portion as a rigid element. Finally, in case of absence of opening, a good practice is to model the portion as a fully deformable element.

The ability of the different discretization criteria in predicting the response of a building is comprehensively investigated in the literature. In particular, Siano *et al.* (2018) performs analyses on walls with regular opening layout by resorting to a finite element discretization, as well as Siano *et al.* (2017), Camata *et al.* (2022), Cattari *et al.* (2022) and Morandini *et al.* (2022) do for irregular opening distributions, and they compared the results obtained when adopting different discretization criteria for the equivalent-frame modeling strategy.

Figure 2.8: Examples of discretization criteria for masonry spandrels in case of (a) regular and (b) irregular opening distribution (Lagomarsino *et al.*, 2013).

Despite the EFM generally provides satisfactory results for regular geometries, as the geometrical affinity with an ideal frame configuration decreases, also the accuracy of the results decreases. In fact, as thoroughly investigated by Morandini *et al.* (2022), particular attention should be given to small openings. In this context, comparisons with a more refined modeling approach show only a marginal influence on the lateral response of the building. Conversely, applying the abovementioned criteria might lead to an unbalanced discretization, generally resulting in a stiffer and higher base shear resistance prediction.

Similarly, Camata *et al.* (2022) highlights the insufficient accuracy of some discretization criteria when a discontinuous opening patterns along the height of the façades is provided. In these cases, the absence of an opening at the ground floor only, might not justify the assumption of discretizing the ground floor pier with a single element. In fact, comparison with refined modeling approaches shows a better accuracy when split in two elements connected through rigid links.

To conclude, even though identifying piers and spandrels elements is rather trivial for regular masonry façades, it becomes challenging when dealing with irregular opening layouts. In this context, an a priori elastic finite element analysis could help to delineate the equivalent frame structure. Alternatively, in case of very complex geometries, more refined modeling approaches, such as continuum modeling or geometry-based modeling, are more convenient and lead to more consistent results.

Furthermore, spandrel elements should be considered only if adequately interlocked to the surrounding masonry and properly supported by lintel, arch, or flat arch elements, able to withstand the masonry member after cracking and ensuring the development of a diagonal strut resisting mechanism. Otherwise, the collaboration of spandrels is unreliable, and the model should consider the response of masonry piers only.

2.4 MACROELEMENTS FOR THE EQUIVALENT FRAME MODELING APPROACH

The equivalent frame modeling strategy consists of identifying a fictitious frame layout composed of macroelements. The common assumption when adopting this modeling strategy is to rely only on the in-plane behavior of the walls, thus neglecting the out-of-plane response of the elements. For this reason, the equivalent frame approach generally resorts to one or two-dimensional wall elements. However, three-dimensional formulations can also be adopted (Raka *et al.*, 2015; Vanin *et al.*, 2020). Moreover, masonry piers and spandrels are generally characterized by comparable in-plane dimensions, resulting in prevailing squat elements. Consequently, macroelement formulations account for both flexural and shear deformations of the members.

In the early stages of the equivalent frame approach, macroelements were primarily designed to emulate the behavior of a displacement-based beam-column element with concentrated plasticity. In this context, the flexural and shear nonlinear behaviors are essentially lumped at the ends of the member, where rigid offsets are also provided to simulate pier-to-spandrel intersections (Magenes and Della Fontana, 1998; Lagomarsino *et al.*, 2013).

More recently, beam-based macroelements have also implemented a force-based formulation, which allows the exact interpolation of resultant stress components along the length of the member and mitigates the shear-locking problem (Addessi *et al.*, 2015). Additionally, certain formulations adopt a diffuse plasticity (Grande *et al.*, 2011; Addessi *et al.*, 2014). In this framework, the nonlinear behavior can occur at any point along the element length. However, it is worth noticing that this leads to an increase in the computational time compared to concentrated plasticity (Figure 2.9a).

Alternatively, spring-based macroelements consist of rigid or deformable portions connected through springs or interfaces (Figure 2.9b,c). In this case, the formulation mainly focuses on representing the typical failure mechanisms of a masonry panel, such as flexural and shear modes (Brencich *et al.*, 1998; Chen *et al.*, 2008; Penna *et al.*,2014; Rinaldin *et al.*, 2016; Vanin *et al.*, 2020).

Elasto-perfectly plastic relationships, governed by assigned strength domains according to code prescriptions, are the most common observations when dealing with simplified formulations (Magenes and Della Fontana, 1998; Lagomarsino *et al.*, 2013). On the other hand, advanced and refined macroelements rely on more complex constitutive laws, potentially resorting to a sectional fiber integration to determine internal actions. While the latter approach automatically captures the coupled axial-flexural response without explicitly defining a strength domain and accurately predicts the stress profile along the section, it returns an increased computational effort (Raka *et al.*, 2015).

To address this drawback, some macroelements implement an analytical integration of the cross-section, preserving the advantages of a fiber discretization while drastically reducing the analysis demand. However, this methodology is generally applicable to simple constitutive relationships (Grande *et al.*, 2011; Penna *et al.*, 2014; Addessi *et al.*, 2014; Vanin et al., 2020).

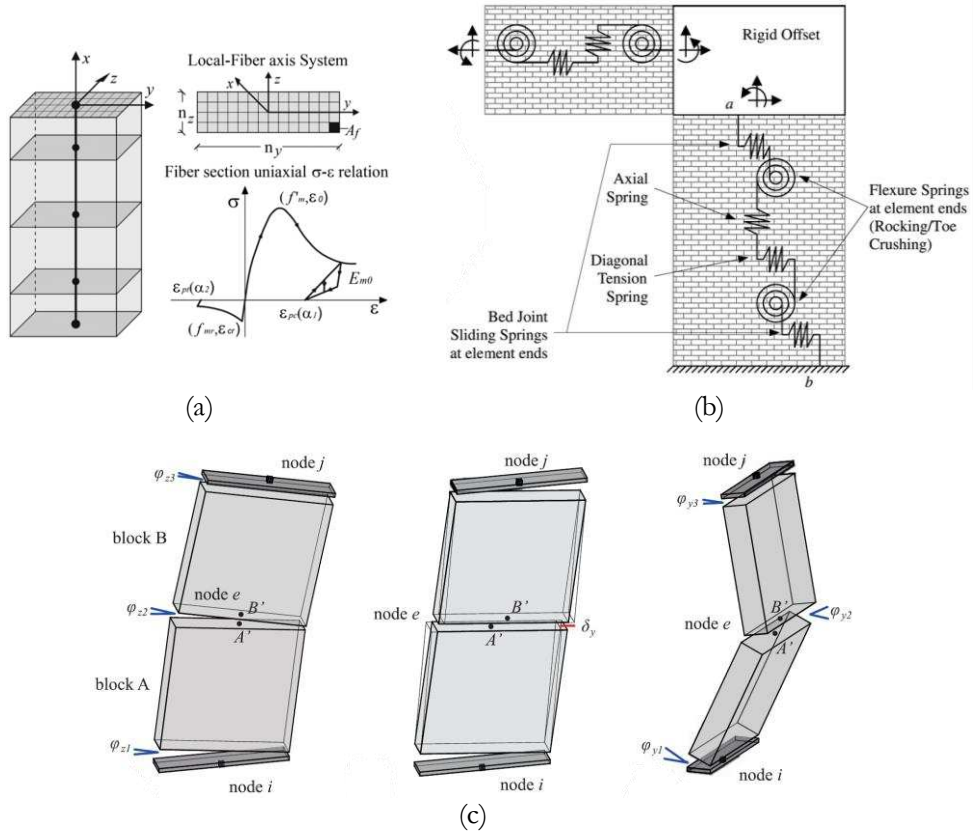

Figure 2.9: Examples of macroelements: (a) Raka *et al.*, (2015);.(b) Chen *et al.*, (2008); (c) Vanin et al, (2020).

2.5 FAILURE MECHANISMS

During post-earthquake surveys and experimental campaigns on masonry buildings, recurrent in-plane damage patterns are observed. In particular, flexural failure modes are associated with the achievement of the maximum bending moment at the extremities of piers, or with rocking motions governed by rigid-body equilibrium conditions (Figure 2.10a). Shear mechanisms on piers are generally associated with diagonal cracks (Figure 2.10b) or sliding over the bed joints (Figure 2.10c).

(a) (b) (c)

Figure 2.10: Masonry failure mechanism observations in piers: (a) flexural; (b) diagonal shear; (c) sliding shear (D'Altri *et al.*, 2019).

On the other hand, in-plane failure of masonry spandrels occurs due to flexural failure (Figure 2.11a) or diagonal shear failure (Figure 2.11b). In fact, sliding is not a mechanism that can initiate cracking in spandrels (Beyer and Mangalathu, 2013) due to the orthogonal direction of shear load with respect to the bed joints.

The occurrence of a particular failure mode in piers and spandrels depends on the aspect ratio, boundary conditions, mechanical properties of constituents, geometrical features of masonry (unit aspect ratio, masonry bond pattern), and the level of axial load (Calderini *et al.*, 2009). Parametric experimental analyses show that rocking most occurs in slender piers, whereas bed joint sliding happens in squat piers (Abrams and Shah, 1992; Anthoine *et al.*, 1995; Magenes and Calvi, 1997). Diagonal cracking becomes more prevalent as the vertical compression increases, in an intermediate slenderness range (Vasconcelos and Lourenço, 2006). More specifically, diagonal cracking propagating through blocks is dominant compared with diagonal cracking propagating through mortar joints if the vertical compression increases (Lourenço *et al.*, 2005) or for a higher mortar-to-block strength ratio (Drysdale and Hamid, 1984). Finally, crushing generally occurs when vertical compression reaches high levels, approaching the compressive strength of the material.

(a) (b)

Figure 2.11: Masonry failure mechanism observation in spandrels after the 6.3 M_w 2009 L'Aquila earthquake: (a) flexural and (b) diagonal shear (Beyer and Dazio, 2012)

According to the interpretation of post-earthquake damage observations, the failure mode is influenced by the instantaneous axial load. In fact, during a cyclic lateral loading, the axial load on piers, especially on those near the edges, may vary depending on the direction of the excitation. As depicted in Figure 2.12a, a rightward excitation increases the compression force in the right outer pier, and diagonal cracking may become the primary failure mechanism (Figure 2.12b). on the other hand, when the load is reversed, the axial force on the same pier decreases compared to static conditions, potentially leading to flexural rocking as the governing failure mechanism (Figure 2.12b).

In addition, experimental tests and damage observations after the 6.1 M_w 2009 L'Aquila earthquake show that spandrels typically exhibit a flexural failure when subjected to small axial load. On the other hand, in case of moderate axial load, they are prone to shear failure with diagonal cracks (Beyer and Dazio, 2012). It is worth noticing that the axial load of spandrels is usually of low intensity, whereas moderate values can be reached with post-tensioned systems, such as tie-roads. For this reason, crushing in masonry spandrel is generally of little concern.

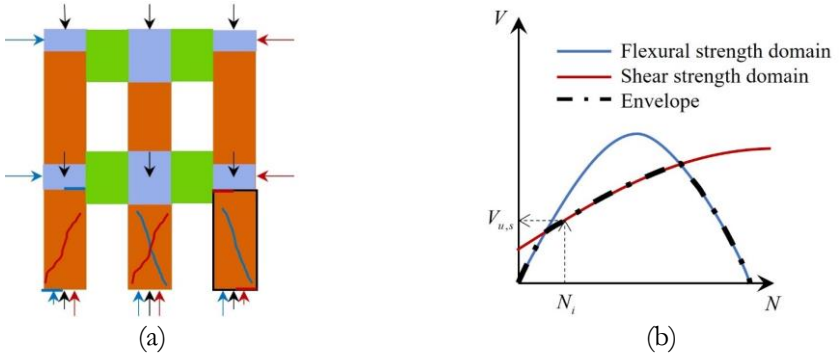

Figure 2.12: (a) masonry frame under vertical and lateral loads; (b) shear strength envelope based on the applied axial compression force.

2.6 STRENGTH CRITERIA

Within the equivalent frame modeling strategy, homogeneous macroelements govern the nonlinear response of the masonry building. In this context, each possible failure mode is usually defined in terms of strength domains, thus accounting for the coupling of the generalized internal forces. The latter are typically represented as ultimate shear force of the member versus axial load applied. In the case of flexural failure mode, the shear force is deduced from the bending moment by dividing by the effective height of the panel.

The intersection of strength domains allows the detection of the failure mode occurring first, thus the one that governs the nonlinear response of the panel. More specifically, the

ultimate lateral force is estimated as the lowest shear force obtained by intersecting the expected failure mode interaction diagrams (Figure 2.12b). After attaining the peak force, the element can further deform until reaching the collapse condition. The latter is typically defined in terms of an ultimate displacement and may vary depending on the failure mechanism experienced.

It is worth noticing that when dealing with elements involving a fiber discretization of the cross-section, the maximum bending moment associated with a particular axial load is automatically defined by integrating the contribution of each fiber. On the other hand, the ultimate shear forces related to the desired failure mechanisms are typically still retrieved through predefined failure criteria.

Magenes and Calvi (1997) and Calderini *et al.* (2009) give an overview of analytical strength criteria applied to piers, as well as Beyer and Mangalathu (2013) discuss strength criteria for spandrels. This section lists the most common criteria employed within building codes and guidelines.

2.6.1 Flexural failure modes

As regards the case of flexural failure mode, hence rocking with possible toe-crushing of the section, the ultimate bending moment M_u for masonry piers can be easily obtained by assuming the stress profile characterized by an equivalent rectangular stress-block in compression and a no-tension behavior, as reported by the following relationship (Magenes and Della Fontana, 2008):

$$M_u = \frac{N\,L}{2}\left(1 - \frac{N}{\eta\,N_u}\right) \qquad V_u = \frac{M_u^i + M_u^j}{h} \tag{2.1}$$

where N and $N_u = f_m\,L\,t$ represent the axial force acting on the considered element and its ultimate value, being f_m the compression strength of masonry, whereas L and t the length and thickness of the cross-section. Eventually, η is a coefficient that accounts for the actual stress distribution along the section. In fact, the equivalent rectangular stress-block idealization may disagree with the actual stress profile at the compressed toe. For this reason, a common and validated assumption is to set $\eta = 0.85$. The ultimate bending moment can be rewritten in terms of ultimate shear force V_u, where i and j indicate the ends of the members, while h its effective height.

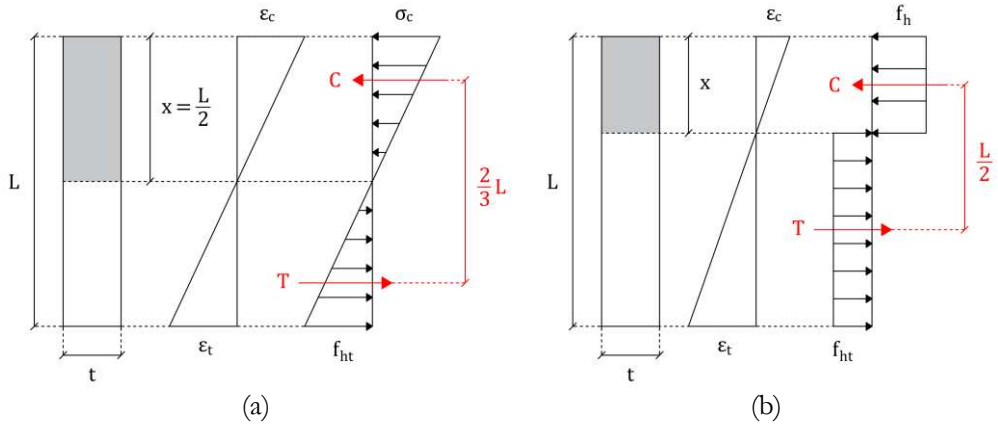

Figure 2.13: Stress profile assumption for spandrel elements accounting for tensile strength: (a) elasto-fragile and (b) ductile behavior in tension.

Unlike for piers, the ultimate bending moment of spandrel elements can be computed assuming a limited horizontal tensile strength f_{ht}, due to interlocking with the adjacent nodes (Cattari and Lagomarsino, 2008). In this context, the tensile strength could be attained by potentially splitting the units or through stair-stepped sliding on the horizontal mortar bed joints (along the overlapping length between units):

$$f_{ht} = \min\left(\frac{f_{bt}}{2}; \frac{f_{v0} + \mu\,\sigma_y}{\phi}\right) \tag{2.2}$$

where f_{bt} is the tensile strength of the units, f_{v0} represent the cohesive contribution of the mortar joints (often conservatively neglected), whereas μ and ϕ are the local friction and interlocking coefficients, being the latter function of the height and overlapping length of the units. Finally, σ_y is the mean vertical compressive stress acting at the end sections of the spandrel element, conventionally assumed as half of the compressive stress on the adjacent pier.

With this being discussed, the strength domain for the flexural failure mode reported in (2.1) can be replaced by assuming an elasto-fragile (Figure 2.13a) or ductile behavior in tension (Figure 2.13b), for the case of rupture of bricks or sliding on the horizontal mortar joints, respectively. Furthermore, unless accurately and precisely estimated, the axial load should not be considered for spandrel elements.

The previous assumptions respectively lead to the relationships reported in equations (2.3), with f_h indicating the horizontal compressive strength of masonry, while L refers to the depth of the spandrel element:

$$M_u = \begin{cases} \dfrac{L^2\, t}{6\,\eta} f_{ht} & if \quad f_{ht} = \dfrac{f_{bt}}{2} \\ \dfrac{L^2\, t}{2}\left(\dfrac{f_{ht}\, f_h}{f_{ht} + f_h}\right) & if \quad f_{ht} = \dfrac{f_{v0} + \mu\, \sigma_y}{\phi} \end{cases} \tag{2.3}$$

It is worth noticing that, in case of ductile behavior both in tension and in compression, the η factor is neglected. Therefore, the sum of the lengths undergoing plasticity in compression and in tension covers the whole section. As regards the elasto-fragile response, instead, the tensile strength of masonry is assumed to be attained first, as it is generally a fraction of the compressive counterpart.

On the other side, in spandrel coupled with horizontal elements capable of resisting tensile forces, such as tie rods or ring beams, the ultimate bending moment can be computed following equation (2.4):

$$M_u = \frac{H_p\, L}{2}\left(1 - \frac{H_p}{\eta\, f_h\, L\, t}\right) \tag{2.4}$$

where H_p is the minimum between the tensile strength of the horizontal member coupled with the spandrel, and the compressive strength of the diagonal masonry strut formed for equilibrium. The latter can be assumed equal to $0.4\, L\, t\, f_h$. However, as pointed out by Betti *et al.* (2008), the maximum axial force in spandrel is generally less than H_p, leading to a possible overestimation of the lateral strength.

Finally, in the case of the simultaneous presence of a tensile resisting member and a non-negligible tensile strength due to interlocking, the ultimate bending moment should be taken as the maximum obtained through equations (2.3) and (2.4).

2.6.2 Shear failure modes

The shear strength of masonry members is strongly influenced by the bond pattern and masonry typology. In this context, shear sliding on the bed joints is typically considered only in case of masonry piers with regular texture, following a Mohr-Coulomb criterion, as reported in equation (2.5):

$$V_{u,s} = L'\, t\, (f_{v0} + \mu\, \sigma_n) \leq V_{s,lim} \qquad V_{s,lim} = f_{v,lim}\, L'\, t \tag{2.5}$$

where f_{v0} and μ are defined according to equation (2.2), L' represents the compressed length of the cross-section, whereas $\sigma_n = N/L't$ is the average axial stress on the

compressed part. Finally, $V_{s,lim}$ accounts for the limited tensile strength of units through the $f_{v.lim}$ parameter, as described by several national and international building codes.

The compressed length of the cross-section can be retrieved from the current internal forces acting on the considered element, leading to equation (2.6), according to the mechanical and physical length limitations (Magenes and Calvi, 1997). In this context, the shear span ratio α_V is introduced. The latter is defined as the ratio between the distance from the section of maximum moment to the contraflexure point (h_0), and the length of element cross-section (L).

$$L' = \frac{3\,L\,N\,(1-2\,\alpha_V\,\mu)}{2\,N+6\,f_{v0}\,\alpha_V\,L\,t} \qquad \frac{N}{\eta\,f_m\,t} \le L' \le L \tag{2.6}$$

Another type of shear failure mechanisms is associated with diagonal cracking. In this context, when dealing with piers or spandrels made up of irregular masonry, national and international building codes generally prescribes the Turnšek and Sheppard (1980) criterion, where the masonry is idealized as a homogeneous material and the failure is attained once the diagonal tensile strength f_{td} at the middle section of the panel is exceeded, as described by equation (2.7):

$$V_{u,d} = \frac{L\,t}{b} f_{td} \sqrt{1+\frac{\sigma_0}{f_{td}}} \tag{2.7}$$

where $\sigma_0 = N/L\,t$ is the average axial force acting on the considered element, assumed zero in case of spandrel elements, whereas $b = h/L$ is a correction coefficient accounting for the shear stress distribution along the middle section of the member. The latter is limited within a range from 1 to 1.5 for very slender and squat piers, respectively.

On the other hand, in the case of piers or spandrel members characterized by regular masonry, diagonal cracking can occur by either a stair-stepped crack through the mortar joints or failure of the units. In this case, a Mohr Coulomb criterion is still used, but the local cohesive and friction coefficients, f_{v0} and μ, are corrected through the factor k, as discussed by Mann and Müller (1982), being ϕ the interlocking coefficient:

$$\tilde{f}_{v0} = k\,f_{v0} \qquad \tilde{\mu} = k\,\mu \qquad k = \frac{1}{1+\mu\,\phi} \tag{2.8}$$

The shear failure criterion accounting for stair-stepped cracking in the mortar joints and consequent sliding along the bed joints, is finally reported:

$$V_{u,d} = L\,t\left(\tilde{f}_{v0} + \frac{\tilde{\mu}\,N}{L\,t}\right) \leq V_{d,lim} \qquad V_{d,lim} = \frac{L\,t}{2.3}\,f_{bt}\sqrt{1+\frac{\sigma_0}{f_{bt}}} \tag{2.9}$$

where $V_{d,lim}$ is related to a diagonal cracking with cracks passing through the units, and is expressed according to the Mann and Müller (1982) theory. However, after a comparison with experimental tests on brick masonry, Magenes and Calvi (1997) proposed an additional correction to better account for the shear span ratio. In this context, equations (2.9) should be divided by a factor equal to $(1+\alpha_V)$.

2.7 MASONRY CONSTITUTIVE PARAMETERS

As discussed, the formulations of strength criteria and constitutive laws, governing the elastic and plastic behavior of masonry, depend on mechanical parameters. Laboratory tests are essential to characterize the mechanical properties of materials and calibrate the constitutive relationships (Figure 2.14).

Detailed and simplified micro-models are calibrated using tensile and compressive tests performed separately on the masonry constituents (Figure 2.14a), such as on units (Ganbaatar *et al.*, 2022) and mortar (Marastoni *et al.*, 2016). Additionally, tests on interfaces are carried out through tests on couplet and triplet samples (Figure 2.14b) composed of two (Churilov and Jovanoska, 2013) and three (Thaickavil and Thomas, 2018) stack-bonded units, respectively.

Macroelements are more adequately calibrated using tests on wall samples (Figure 2.14c). In this context, vertical (Budiwati, 2009) and diagonal (Milosevic *et al.*, 2013) compression tests are performed on wallettes. The tensile strength of masonry is not directly addressed, due to its low value compared to the compressive counterpart and its statistical scattering. However, diagonal compression tests allow to recover an equivalent value associated with diagonal shear failure. Similarly, material properties for continuum elements may still be calibrated by means of tests on wallettes. Nonetheless, small-scale tests may be required to fully characterize the adopted constitutive formulation.

Quasi-static shear-compression tests (Magenes *et al.*, 2008; Beyer *et al.*, 2010; Graziotti *et al.*, 2012), also named pushover tests (Figure 2.14d), are carried out on panel-scale specimens to provide an accurate representation of the masonry in-plane behavior and give information on the drift limit, dominant failure mode and ductility. Pushover tests can be performed with increasing load, cycles of loading and unloading, and reversed cycles.

Finally, the response of an entire masonry building is reproduced using dynamic shaking-table tests (Magenes *et al.*, 2010a, Miglietta *et al.*, 2021) and on-site pushover tests (Hogan

et al., 2018), which are an essential tool for understanding the structural vulnerabilities, to calibrate numerical modeling approaches, and to determine the effectiveness of strengthening solutions (Figure 2.14e).

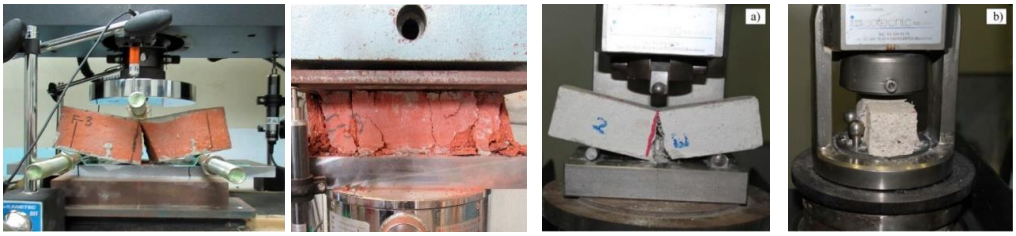

(a) Component scale: unit and mortar tests

(b) Masonry element scale: couplet and triplet samples

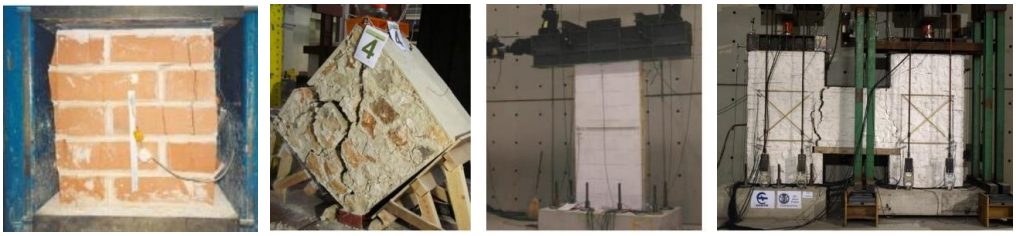

(c) Wallette scale (d) Panel scale

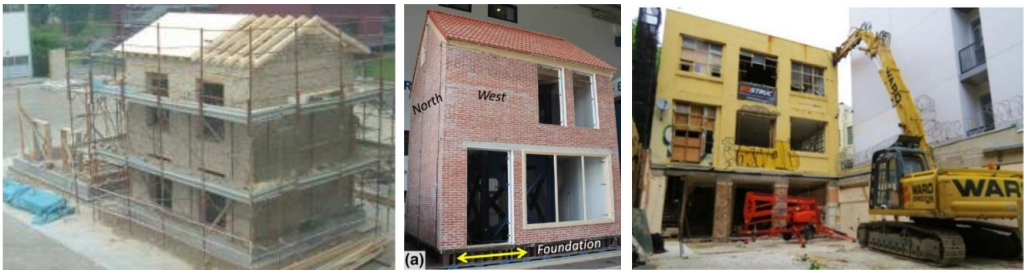

(e) Building scale: shake table

Figure 2.14: Examples of masonry tests at different scales: (a) Ganbaatar *et al.* (2022) and Marastoni *et al.* (2016); (b) Churilov and Jovanoska (2013) and Thaickavil and Thomas (2018); (c) Budiwati (2009) and Milosevic *et al.* (2013); (d) Magenes *et al.* (2008) and Graziotti *et al.* (2012); (e) Magenes et al (2010), Miglietta *et al.* (2021), and Hogan *et al.* (2008).

2.8 THREE-DIMENSIONAL EQUIVALENT FRAME MODEL

In the EFM approach, the three-dimensional response of a building is obtained by assembling vertical walls and horizontal diaphragms. The typical assumption is to consider only the wall in-plane strength and stiffness contributions, neglecting any source of out-of-plane response. Consequently, it is intrinsically assumed that all the local mechanisms are inhibited and that a box-type behavior can be achieved. However, a posteriori analyses should be conducted to check that local mechanisms are not activated and ensure the reliability of results.

URM buildings usually present timber floors, generally composed of a mono-directional or bi-directional framing completed by a single layer of floorboards, which leads to a relatively low in-plane stiffness. On the other hand, diaphragms involving an adequate and collaborating reinforced concrete topping can be assumed as rigid in-plane elements. In this context, the adequate calibration of the timber floor in-plane stiffness has a significant impact on the overall response of the building (Zarzour *et al.*, 2023; Zarzour *et al.*, 2024).

Three- or four-node orthotropic membrane finite elements with a linear-elastic plane-stress formulation are generally employed to model the diaphragm flexibility. The membrane stiffness is defined by assuming an isotropic or orthotropic constitutive law, with the latter being the most employed choice. In this context, the overall response of the element is governed by three parameters: the Young's modulus along the longitudinal E_1 and transverse E_2 direction, and the shear modulus G_{12}, which is the most relevant parameter as it controls the redistribution of the actions among non-coplanar walls.

If the masonry wall does not extend to the roof, the roof system is generally assumed as a non-structural element, and its contribution in the analysis is taken into account in terms of mass only.

2.9 NONLINEAR STATIC AND DYNAMIC ANALYSES

The EFM is widely adopted as a spatial discretization strategy to perform static analyses within ordinary engineering practice. Nevertheless, it can be applied also for the investigation of the dynamic structural response. The static analysis is preferred due to the lower computational time and easier interpretation of the results.

One of the first applications of the nonlinear static analysis, also named pushover analysis, is reported by Tomaževič (1978), inspiring the name of its POR (Push-Over Response) method. The pushover analysis consists of a numerical procedure to exploit the nonlinear behavior of a building under horizontal actions. In this context, a load distribution is incrementally applied to the structure until its collapse conditions, and the response of the

structure is expressed in terms base shear restoring force F versus horizontal displacement of a particular control node D.

The pushover analysis gives exhaustive information about the capacity of the structure at different limit states, about the global ductility, and about the local failure mechanisms. Nevertheless, it does not directly involve the seismic demand, as no seismic input amplitude is explicitly introduced. On the other hand, the nonlinear dynamic analysis allows the simulation of the structural response when subjected to a predefined ground motion, giving direct information about the structure capacity associated with the selected seismic event.

In a pushover analysis, the shape of the horizontal load distribution is maintained constant throughout the analysis, whereas the amplitude is progressively increased to attain the whole capacity of the investigated building. The pushover analysis stops when a structural collapse is reached, defined in terms of global strength decay, or in terms of drift at the element level.

The so-called pushover curve is defined as the base shear restoring force versus horizontal displacement of a particular control node, and should represent the first-loading (backbone) curve of the hysteresis loops obtained for cyclic loading. The choice of the control node is not unique, and the results are strongly influenced by its selection. An adequate control node should be representative of the global response of the building. More specifically, in the case of walls with a significant difference in stiffness, especially when dealing with flexible diaphragms, the control node should be positioned on the portion expecting the greatest displacements. As an alternative, the control node can be defined in a fictitious location obtained by considering an averaged floor displacement, possibly weighted on nodal masses (Galasco *et al.*, 2006).

Also, the shape of the horizontal force distribution is not unique, and the load distribution influences the deformed shape of the building. National and international building codes provide suggestions regarding the shape of the horizontal load distribution, depending on the building typology. The modal and uniform load distributions are the most employed. The first assumes a load distribution proportional to the building deformed shape in the elastic regime, whereas the second is associated with a constant horizontal acceleration profile with height, in agreement with the soft-story response in the plastic phase.

The modal load pattern can be defined according to the fundamental period mode shape (unimodal distribution), possibly approximated with a triangular load pattern (height-proportional distribution), or through a combination of modes that involves a cumulative effective mass higher than a fixed fraction of the total mass of the building (multimodal distribution).

According to Augenti and Parisi (2019), the pushover curves obtained using a uniform load distribution attain higher base shear forces, compared with the unimodal and triangular distributions. This is because the centroid of loading distribution is located at a lower height, inducing a reduced overturning moment. The results obtained using a multimodal distribution and a dynamic analysis are intermediate.

Pushover analyses are typically reliable when applied to regular three-dimensional buildings, whose behavior is dominated by the first modal shape, even though some attempts have been made to consider the influence of higher modes (multimodal distributions). However, the load distribution applied does not change during the analysis. To overcome this limitation, pushover analyses with adaptive load patterns have been developed (adaptive pushover analyses). In this context, the load distribution is updated at each step of the analysis, reflecting the progressive damage and consequent stiffness decay of the structure. Adaptive pushover procedures proved better results compared to the non-adaptive counterparts, especially when performed in displacement control (Pinho and Antoniou, 2005). However, even in this scenario, as the load applied is unidirectional, the responses of buildings highly prone to torsional modes are still better captured by employing nonlinear dynamic analyses.

In a nonlinear dynamic analysis, the structural response is instead obtained by solving the dynamic equilibrium equation, involving not only the restoring forces due to the structural stiffness, but also the inertial and damping contributions. A time integration procedure is necessary for the numerical step-by-step solution of the differential equation representing the dynamic equilibrium, according to explicit or implicit algorithms (Hughes, 1987; Chopra, 2001). More specifically, in the explicit time integration methods, the structural response at the current step is calculated in terms of quantities related to the previous time step. Consequently, the equations are solved directly since all the terms are already known. For this reason, explicit methods are characterized by a straightforward implementation and are computationally less demanding than the implicit counterparts. However, the reliability of results is associated with a reduced time step size to avoid numerical instability of the algorithm.

Conversely, in the implicit time integration methods, the response at current time step is estimated in terms of quantities related to the previous step (known parameters) and to the current step (unknown parameters). Consequently, an iterative process is necessary, and the solution of the dynamic equilibrium equation becomes time-consuming, even though the unconditional stability of some implicit methods allows the use of larger time steps.

Furthermore, it is worth noticing that a single ground motion input is not representative of the seismic response of a building. For this reason, a set of seismic records or synthetic

signals should be properly selected, according to a probabilistic approach, considering the local seismicity and spectral compatibility requirements.

2.10 COLLAPSE OF MASONRY BUILDINGS

The definition of the collapse limit state of a building can involve a local or global criterion. More specifically, the analysis can be stopped when a single element or a set of elements, considered significant for the stability of the building, reach a predefined drift limit. On the other hand, global criteria are expressed in terms of decay of the global lateral strength of the building during a pushover analysis.

Defining the displacement capacity according to the achievement of a predefined damage level in a single element is a conservative assumption, inspired by the behavior of reinforced concrete buildings, in which the limit condition of different elements in the weakest story is reached simultaneously due to the similar geometrical dimensions of columns. In this context, when an element collapses, the analysis can be stopped because the failure of the building is associated with the first element collapsing. Otherwise, if accepted, the element maintains only the capacity to carry vertical loads, and its lateral stiffness is set to zero for the following load steps. Consequently, a force redistribution occurs among the remaining resisting elements of the model.

On the other hand, a global damage approach based on a lateral strength decay should be valid only for rigid diaphragms. In fact, if flexible diaphragms are present, some walls may already be severely damaged.

2.11 BUILDING SAFETY VERIFICATION

The seismic design and the assessment of new and existing masonry buildings are carried out by comparing the displacement capacity of the structure with the displacement demand associated to the construction site.

As previously mentioned, the pushover analysis gives exhaustive information about the capacity. However, the seismic displacement demand is not directly accounted for. For this reason, national and international building codes provide nonlinear static procedures for its identification on the capacity curve. In particular, the seismic demand is expressed in terms of a response spectrum and, accordingly, the comparison between capacity and demand is performed by means of an equivalent single-degree-of-freedom (SDOF) system. Therefore, the pushover curve obtained for the three-dimensional multi-degrees-of-freedom model (F, D) is scaled through the modal participation factor Γ to obtain the capacity curve representative of an equivalent SDOF (f, d) system. Subsequently, the SDOF capacity curve (f, d) is idealized as an equivalent bilinear relationship.

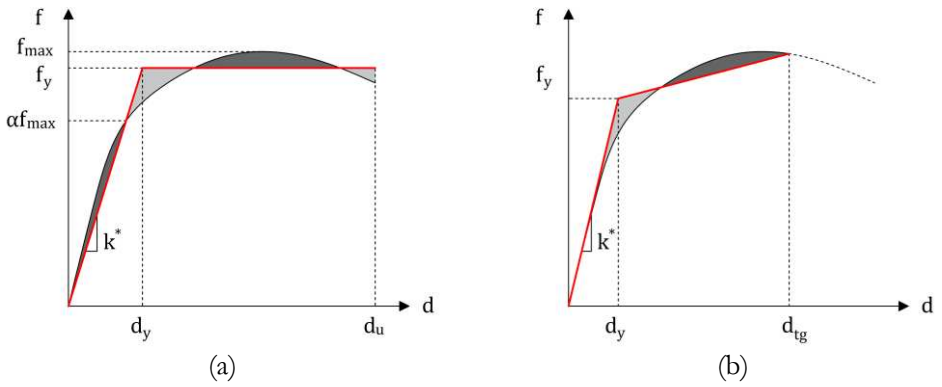

Figure 2.15: Bilinear idealization curves for (a) demand-independent and (b) demand-dependent procedures.

In case the bilinear relationship is independent of the displacement demand (Figure 2.15a), an elasto-perfectly plastic curve is typically adopted: the elastic branch is defined by transitioning to a certain fraction α of the maximum lateral strength f_{max} of the SDOF system, whereas the yielding force f_y is computed through an equivalent energy criterion, ensuring preservation of the area under the capacity curve until the ultimate displacement point d_u.

On the other hand, in scenarios where the bilinear relationship depends on the displacement demand (Figure 2.15b), the initial branch is typically computed according to the initial tangent stiffness of the equivalent SDOF system. Subsequently, the yielding force f_y is obtained by imposing the passage of the second branch to the force associated with the displacement demand d_{tg} while ensuring the equivalent energy preservation. As the displacement demand is not known in advance, an iterative procedure is required.

The Capacity Spectrum Method (Freeman *et al.*, 1998) and the N2 method (Fajfar *et al.*, 2000) are the most employed criteria for the identification of the seismic demand. The first adopt and overdamped spectrum, whereas the second assumes a reduction factor to obtain an inelastic spectrum.

In the Capacity Spectrum Method (Freeman *et al.*, 1998), the seismic demand is represented by the so-called acceleration-displacement response spectrum (ADRS). Consequently, radial lines starting from the origin are characterized by a constant value of period. On the other hand, the capacity is described by a capacity spectrum obtained from the bilinear capacity curve by dividing the SDOF forces f by the equivalent mass m^* of the system. In this context, the bilinear relationship is defined according to Figure 2.15b, in which the initial trial point for the target displacement (associated to the seismic demand) could be taken by assuming the principle of equal displacements with an elastic SDOF system (Figure 2.16a).

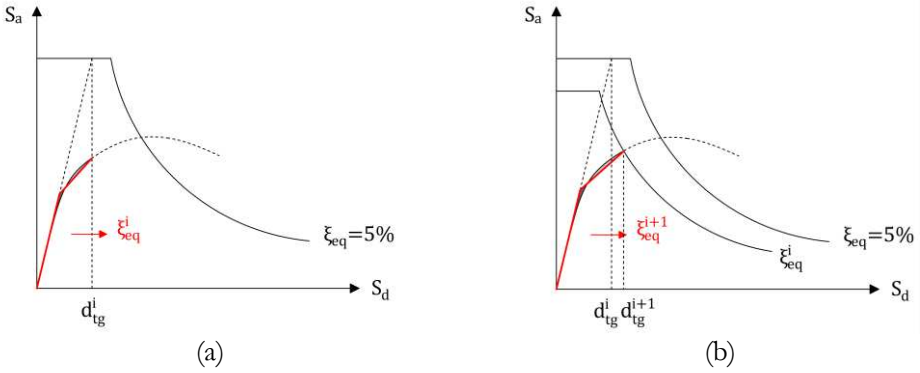

Figure 2.16: Graphical representation of the Capacity Spectrum Method (Freeman *et al.*, 1998): (a) initial target displacement, and (b) next iteration.

An equivalent damping ratio is then estimated as a function of the ductility of the bilinear relationship, and the associated overdamped ADRS is computed. Finally, the capacity and the demand spectra are superimposed, and the intersection determines the new performance point of the structure (Figure 2.16b). The iterations proceed until the displacement associated to the intersection is close enough to the previous trial.

On the other side, the N2 method (Fajfar *et al.*, 2000) does not need an iteration procedure. In this context, the method involves a demand-independent bilinear idealization (Figure 2.15a) and a ductility-based reduction factor R_μ for evaluating an inelastic spectrum. The latter is defined as the target load for an equivalent SDOF system having equivalent mass m^* in the case of unlimited elastic behavior, normalized with respect to the yield force f_y attained in the case of elasto-plastic response:

$$R_\mu = \frac{m^* \, S_e(T^*)}{f_y} \geq 1 \qquad \textbf{(2.10)}$$

The fundamental period T^* of the equivalent SDOF system is computed according to equation (2.11):

$$T^* = 2\pi \sqrt{\frac{m^*}{k^*}} = 2\pi \sqrt{\frac{m^* \, d_y}{f_y}} \qquad \textbf{(2.11)}$$

Subsequently, the comparison with the corner period T_C is performed. The latter is defined as the upper limit of the period of the constant acceleration branch in the elastic response spectrum. More specifically, for long-period ($T^* \geq T_C$) or elastic ($R_\mu = 1$) structures, the

equal-displacement rule applies ($d_{tg} = d_e$). On the other hand, the inelastic target displacement is amplified following the relationships proposed by Vidiç *et al.* (1994):

$$d_{tg} = \frac{d_e}{R_\mu}\left[\left(R_\mu - 1\right)\left(\frac{T_C}{T^*}\right) + 1\right] \qquad d_e = S_a(T^*)\left(\frac{T^*}{2\pi}\right)^2 \tag{2.12}$$

The inelastic displacement demand calculated for the equivalent SDOF system, according to the Capacity Spectrum Method or the N2 method, need to be converted into the inelastic displacement demand for the multiple-degree-of-freedom system. This is accomplished by multiplying the target displacement by the modal participation factor Γ. Finally, the seismic performance of the building is assessed by verifying that the ultimate displacement of the building exceeds the calculated displacement demand.

A comprehensive and critical review on the nonlinear static procedures to estimate the displacement demand is given by Guerrini *et al.* (2017) and Guerrini *et al.* (2021). In particular, they propose a modified version of the original N2 method to better predict the inelastic displacement demand in case of short-period structures, such as masonry buildings.

REFERENCES

Abrams, D. P. and Shah, N. (1992). Cyclic Load Testing of Unreinforced Masonry Walls. *Report No. 92-26-10*, University of Illinois, Advanced Construction Technology Center, Urbana.

Addessi, D., Mastrandrea, A., and Sacco, E. (2014). An Equilibrated Macro-Element for Nonlinear Analysis of Masonry Structures. *Engineering Structures*, 70, 82-93.

Addessi, D., Liberatore, D., and Masiani, R. (2015). Force-Based Beam Finite Element (FE) for the Pushover Analysis of Masonry Buildings. *International Journal of Architectural Heritage*, 9(3), 231-243.

Addessi, D. and Sacco, E. (2016). Nonlinear Analysis of Masonry Panels using a Kinematic Enriched Plane State Formulation. *International Journal of Solids and Structures*, 90, 194-214.

Ali, S. and Page, A. W. (1988). Finite Element Model for Masonry Subjected to Concentrated Loads. *Journal of Structural Engineering*, 114(8), 1761-1784.

Anthoine, A., Magonette, G., and Magenes, G. M. (1995). Shear-Compression Testing and Analysis of Brick Masonry Walls. *In Proceedings of the 10th European Conference on Earthquake Engineering*, (pp. 1657-1662). Vienna, Austria.

Arnau, O., Sandoval, C., and Vila, D. (2015). Determination and validation of input parameters for detailed micro-modelling of partially grouted reinforced masonry walls. *Proceedings of the 10th Pacific Conference on Earthquake Engineering*, Sydney, Australia.

Augenti, N. (2006). Seismic Behavior of Irregular Masonry Walls. *In Proceedings of the 1st European Conference on Earthquake Engineering and Seismology*. Geneva, Switzerland.

Augenti, N. and Parisi, F. (2019). Teoria e tecnica delle strutture in muratura. Analisi e progettazione (In Italian). *Hoepli*.

Belmouden, Y. and Lestuzzi, P. (2009). An Equivalent Frame Model for Seismic Analysis of Masonry and Reinforced Concrete Buildings. *Construction and Building Materials*, 23(1), 40-53.

Bertolesi, E., Milani, G., and Casolo, S. (2017). Homogenization towards a mechanistic rigid body and spring model (HRBSM) for the non-linear dynamic analysis of 3D masonry structures. *Meccanica*, 53(7), 1819-1855.

Betti, M., Galano, L., and Vignoli, A. (2008). Seismic response of masonry plane walls: A numerical study on spandrel strength. *In Proceedings of the 2008 Seismic Engineering Conference Commemorating the 1908 Messina and Reggio Calabria Earthquake*, Reggio Calabria, Italy.

Beyer, K., Abo, E. E. A., and Dazio, A. (2010). Experimental investigation of the cyclic behaviour of unreinforced masonry spandrels. *In Proceedings of the 9th U.S. National and 10th Canadian Conference on Earthquake Engineering*. Toronto, Ontario, Canada, Paper No 525.

Beyer, K. and Dazio, A. (2012). Quasi-Static Cyclic Tests on Masonry Spandrels. *Earthquake Spectra*, 28(3), 907-929.

Beyer, K. and Mangalathu, S. (2013). Review of Strength Models for Masonry Spandrels. *Bulletin of Earthquake Engineering*, 11(2), 521-541.

Bilgin, H., Bidaj, A., Shkodrani, N., and Hysenlliu, M. (2020). Performance of masonry structures during the 2019 Durres, Albania Earthquake. *Proceedings in the International Symposium on Durrës Earthquakes and Eurocodes*, Albania.

Block, P., Ciblac, T., Ochsendorf, J. (2006). Real-time limit analysis of vaulted masonry buildings. *Computers and Structures*., 84 (29-30), 1841-1852.

Bracchi, S., Rota, M., Penna, A., and Magenes, G. (2015). Consideration of Modelling Uncertainties in the Seismic Assessment of Masonry Buildings by Equivalent-Frame Approach. *Bulletin of Earthquake Engineering*, 13(11), 3423-3448.

Brencich, A., and Lagomarsino, S. (1998). A macro-elements dynamic model for masonry shear walls. *In Proceedings of the STRUMAS IV 4th Int. Symp. On Computer Methods in Structural Masonry*. E&FN Spon: London, 67–75.

Bruggi, M. and Taliercio, A. (2015). Analysis of No-Tension Structures under Monotonic Loading through an Energy-Based Method. *Computers & Structures*, 159, 14-25.

Budiwati, I. A. M. (2009). Experimental compressive strength and modulus of elasticity of masonry. Jurnal Ilmiah Teknik Sipil, 13(1), 71–81.

Calderini, C., Cattari, S., and Lagomarsino, S. (2009). In-Plane Strength of Unreinforced Masonry Piers. *Earthquake Engineering & Structural Dynamics*, 38(2), 243-267.

Camata, G., Marano, C., Sepe, V., Spacone, E., Siano, R., Petracca, M., Roca, P., and Pelà, L. (2022). Validation of non-linear equivalent-frame models for irregular masonry walls. *Engineering Structures*, 253, 113755.

Cattari, S., D'Altri, A. M., Camilletti, D., and Lagomarsino, S. (2022). Equivalent frame idealization of walls with irregular openings in masonry buildings. *Engineering Structures*, 256, 114055.

Chen, S. -Y., Moon, F. L., and Yi, T. (2008). A Macroelement for the Nonlinear Analysis of In-Plane Unreinforced Masonry Piers. *Engineering Structures*, 30(8), 2242-2252.

Chiozzi, A., Milani, G., Grillanda, N., and Tralli, A., (2018a). A fast and general upper-bound limit analysis approach for out-of-plane loaded masonry walls. *Meccanica*, 53(7), 1875–1898.

Chiozzi, A., Grillanda, N., Milani, G., and Tralli, A. (2018b). UB-ALMANAC: an adaptive limit analysis NURBS-based program for the automatic assessment of partial failure mechanisms in masonry churches. *Engineering Failure Analysis*, 85, 201-220.

Chopra, A. K. (2001). Dynamics of structures: theory and applications to earthquake engineering. *Prentice-Hall*, Upper Saddle River, New Jersey.

Churilov, S. and Jovanoska, E. D. (2013). In-plane shear behaviour of unreinforced and jacketed brick masonry walls. *Soil Dynamics and Earthquake Engineering*, 50, 85–105.

D'Altri, A. M., de Miranda, S., Castellazzi, G., Sarhosis, V. (2018). A 3D Detailed Micro-Model for the In-Plane and Out-Of-Plane Numerical Analysis of Masonry Panels. *Computers and Structures*, 206, 18–30.

D'Altri, A. M., Sarhosis, V., Milani, G., Rots, J., Cattari, S., Lagomarsino, S., Sacco, E., Tralli, A., Castellazzi, G., and De Miranda, S. (2019). Modeling Strategies for the Computational Analysis of Unreinforced Masonry Structures: Review and Classification. *Archives of Computational Methods in Engineering*, 27(3), 1-33.

Damiani, N., DeJong, M. J., Albanesi, L., Penna, A., and Morandi, P. (2023). Distinct element modeling of the in-plane response of a steel-framed retrofit solution for URM structures. *Earthquake Engineering & Structural Dynamics*, 52(10), 3030-3052.

de Felice, G. (2001). Overall elastic properties of brickwork via homogenization. *In Structural Engineering, Mechanics and Computation*, Zingoni, A. (ed.), vol. 1. Elsevier: Amsterdam, 411–418.

de Felice, G. (2009). Elasto-plastic analysis of block structures through a homogenization method. *International Journal for Numerical and Analytical Methods in Geomechanics*, 34, 221–247.

Degli Abbati, S., D'Altri, A. M., Ottonelli, D., Castellazzi, G., Catteri, S., de Miranda, S., and Lagomarsino, S. (2019). Seismic assessment of interacting structural units in complex historic masonry constructions by nonlinear static analysis., *Computers and Structures*., 213, 51-71.

Dolce, M. (1991). Schematizzazione e Modellazione degli Edifici in Muratura Soggetti ad Azioni Sismiche. *Industria delle Costruzioni*, 25(242), 44-57.

Drysdale, R. and Hamid, A. A. (1984). Tension Failure Criteria for Plain Concrete Masonry. *Journal of Structural Engineering*, 110(2), 228-244.

European Committee for Standardization (CEN). (2004). Eurocode 8: Design of Structures for Earthquake Resistance. Part 1: General Rules, Seismic Actions and Rules for Buildings; EN 1998-1:2004. *European Committee for Standardization*, Brussels, Belgium.

Fajfar, P. (2000). A nonlinear analysis method for performance-based seismic design. *Earthquake Spectra*, 16(3), 573–592.

Freeman, S. A. (1998). The capacity spectrum method as a tool for seismic design. *In Proceedings of the 11th European Conference on Earthquake Engineering*, Paris, France, 6–11.

Galasco, A., Lagomarsino, S., and Penna, A. (2006). On the use of pushover analysis for existing masonry buildings. *In Proceedings of the 1st European Conference on Earthquake Engineering and Seismology*. Geneva, Switzerland, Paper No. 1080.

Ganbaatar, A., Mori, T., Inoue, R., and Danzandorj. S. (2022). Strength Performance of the Connection between Brick and SPF Lumber, *Buildings*, 12(4), 465.

Grande, E., Imbimbo, M., and Sacco, E. (2011). A Beam Finite Element for Nonlinear Analysis of Masonry Elements With or Without Fiber-Reinforced Plastic (FRP) Reinforcements. *International Journal of Architectural Heritage*, 5(6), 693-716.

Graziotti, F., Magenes, G., and Penna, A. (2012). Experimental cyclic behaviour of stone masonry spandrels. *In Proceedings of the 15th European Conference on Earthquake Engineering*, Lisbon, paper No. 3261.

Guerrini, G., Graziotti, F., Penna, A., and Magenes, G. (2017). Improved evaluation of inelastic displacement demands for short-period masonry structures. *Earthquake Engineering & Structural Dynamics*, 46, 1411-1430.

Guerrini, G., Kallioras, S., Bracchi, S., Graziotti, F., and Penna, A. (2021). Displacement Demand for Nonlinear Static Analyses of Masonry Structures: Critical Review and Improved Formulations. *Buildings*, 11, 118.

Guo, Y. T., Bompa, D. V., and Elghazouli, A.Y. (2022). Nonlinear numerical assessments for the in-plane response of historic masonry walls. *Engineering Structures*, 268.

Hogan, L. S., Giongo, I., Walsh, K. Q., Ingham, J. M., and Dizhur, D. (2018). Full-scale Experimental Pushover Testing of an Existing URM Building. *Structures*, 15, 66–81.

Hughes, T. J. R. (1987). The finite element method, linear static and dynamic finite element analysis. *Prentice-Hall*.

Lagomarsino, S., Penna, A., Galasco, A., and Cattari, S. (2013). TREMURI Program: An Equivalent Frame Model for the Nonlinear Seismic Analysis of Masonry Buildings. *Engineering Structures*, 56, 1787-1799.

Lotfi, H. R. and Shing, P. B. (1994). Interface Model Applied to Fracture of Masonry Structures. *Journal of Structural Engineering*, 120, 63-80.

Lourenço, P. B. (1996). Computational Strategies for Masonry Structures. *Ph. D. Dissertation*, Delft University of Technology, Netherlands.

Lourenço, P. B. and Rots, J. G. (1997). Multisurface Interface Model for Analysis of Masonry Structures. *Journal of Engineering Mechanics*, 123(7), 660-668.

Lourenço, P. B., Rots. J. G., Blaauwendraad, J. (1998). Continuum model for masonry: parameter estimation and validation. *Journal of Structural Engineering*, 124(6), 642–652.

Lourenço, P. B., Oliveira, D. V., Roca, P., and Orduña, A. (2005). Dry Joint Stone Masonry Walls Subjected to In-Plane Combined Loading. *Journal of Structural Engineering*, 131(11), 1665-1673.

Ma, P., Yao, J., and Hu, Y. (2022). Numerical Analysis of Different Influencing Factors on the In-Plane Failure Mode of Unreinforced Masonry (URM) Structures. *Buildings*, 12(2), 183.

Magenes, G. and Calvi, G. M. (1997). In-plane Seismic Response of Brick Masonry Walls. *Earthquake Engineering & Structural Dynamics*, 26(11), 1091-1112.

Magenes, G. and Della Fontana, A. (1998). Simplified Non-Linear Seismic Analysis of Masonry Buildings. *Proceedings of the British Masonry Society*, 8, 190-195.

Magenes, G., Morandi, P., and Penna, A. (2008). Experimental in-plane cyclic response of masonry walls with clay units. *In Proceedings of the 14th World Conference on Earthquake Engineering*, Beijing, China.

Magenes, G., Penna, A., and Galasco, A. (2010). A Full-Scale Shaking Table Test on a Two Storey Stone Masonry Building. *In Proceedings of the 14th European Conference on Earthquake Engineering*. Ohrid, North Macedonia.

Mann, W. and Müller, H. (1982). Failure of Shear-Stressed Masonry: an Enlarged Theory, Tests and Application to Shear Walls. *In Proceedings of the British Ceramic Society*, 30, p. 223-235.

Marmo, F. and Rosati, L. (2017). Reformulation and extension of the thrust network analysis. *Computers and Structures*., 182, 104-118.

Marastoni, D., Pelà, L., Benedetti, A. and Roca, P. (2016). Combining Brazilian tests on masonry cores and double punch tests for the mechanical characterization of historical mortars. *Construction and Building Materials*, 112, 112–127.

Marfia, S. and Sacco, E. (2012). Multiscale damage contact-friction model for periodic masonry walls. *Computer Methods in Applied Mechanics and Engineering*, 205, 189–203.

Miglietta, M., Damiani, N., Guerrini, G., and Graziotti, F. (2021). Full-scale shake-table tests on two unreinforced masonry cavity-wall buildings: effect of an innovative timber retrofit. *Bulletin of Earthquake Engineering*, 19, 2561–2596.

Milosevic, J., Gago, A. S., Lopes, M., and Bento, R. (2013). Experimental assessment of shear strength parameters on rubble stone masonry specimens. *Construction and Building Materials*, 47, 1372–1380.

Moon, F. L., Yi, T., Leon, R. T., and Kahn, L. F. (2006). Recommendations for Seismic Evaluation and Retrofit of Low-Rise URM Structures. *Journal of Structural Engineering*, 132(5), 663-672.

O'Dwyer, D. (1999). Funicular Analysis of Masonry Vaults. *Computers and Structures*, 73(1), 187-197.

Oliveira, D. V. and Lourenço P. B. (2004). Implementation and validation of a constitutive model for the cyclic behaviour of interface elements. *Computers and Structures*., 82, 1451–1461.

Parisi, F. and Augenti, N. (2013). Seismic capacity of irregular unreinforced masonry walls with openings. *Earthquake Engineering & Structural Dynamics*. 42(1), 101-121.

Pinho, R., and Antoniou, S. (2005). A displacement-based adaptive pushover algorithm for assessment of vertically irregular frames. *4th European Workshop on the Seismic Behavior of Irregular and Complex Structures*. Thessaloniki, Greece.

Stefanou, I., Sab, K., and Heck, J. V. (2015). Three dimensional homogenization of masonry structures with building blocks of finite strength: a closed form strength domain. *International Journal of Solids and Structures*., 54, 258-270.

Pelà, L., Cervera, M., and Roca, P. (2013). An Orthotropic Damage model for the Analysis of Masonry Structures. *Construction and Building Materials*, 41, 957-967.

Prakash, P. R., Azenha, M., Pereira, J. M., and Lourenço, P. B. (2020). Finite element based micro modelling of masonry walls subjected to dire exposure: Framework validation and structural implications. *Engineering Structures*, 213, 110545

Raka, E., Spacone, E., Sepe, V., and Camata, G. (2015). Advanced Frame Element for Seismic Analysis of Masonry Structures: Model Formulation and Validation. *Earthquake Engineering & Structural Dynamics*, 44(14), 2489-2506.

Rinaldin, G., Amadio, C., and Macorini, L. (2016). A Macro-Model with Nonlinear Springs for Seismic Analysis of URM Buildings. *Earthquake Engineering & Structural Dynamics*, 45(14), 2261-2281.

Segovia-Verjel, M. L., Justo-Moscardó, E., Morales-Esteban, A., Requena García Cruz, M. V., Romero-Sánchez, E., de-Miguel-Rodríguez, J., and Estêvão, J. (2019). A cost-effective retrofitting technique for URM buildings based on steel encirclements in openings: a case study. *Proceedings of the 7th International Conference on Computational Methods in Structural Dynamics and Earthquake Engineering*, Crete, Greece.

Siano, R., Sepe, V., Camata, G., Spacone, E., Roca, P., and Pelà, L. (2017). Analysis of the performance in the linear field of Equivalent-Frame Models for regular and irregular masonry walls. Engineering Structures, 145, 190-2010.

Siano, R., Roca, P., Camata, G., Pelà, L., Sepe, V., Spacone, E., and Petracca, M. (2018). Numerical investigation of non-linear equivalent-frame models for regular masonry walls. Engineering Structures, 173, 512-529.

Thaickavil, N. N. and Thomas, J. (2018). Behaviour and strength assessment of masonry prisms. *Case Studies in Construction Materials*, 8, 23–38.

Tomaževič, M. (1978). The Computer Program POR. *Report*, ZRMK.

Touliatos, P. G. (1996). Seismic Behaviour of Traditionally-Built Constructions. *In: Petrini, V., Save, M. (eds) Protection of the Architectural Heritage Against Earthquakes. International Centre for Mechanical Sciences*, vol 359. Springer, Vienna.

Turnšek, V. and Sheppard, P. (1980). The Shear and Flexural Resistance of Masonry Walls. *In Proceedings of the International Research Conference on Earthquake Engineering*. Skopje, Yugoslavia.

Yi, T., Moon, F. T., Leon, R. F., and Kahn, L. (2006). Lateral Load Tests on a Two-Story Unreinforced Masonry Building. *Journal of Structural Engineering*, 132(5), 643-652.

Vanin, F., Penna, A., and Beyer, K. (2020). A Three-Dimensional Macroelement for Modelling the In-Plane and Out-of-Plane Response of Masonry Walls. *Earthquake Engineering & Structural Dynamics*, 49(14), 1365-1387.

Vasconcelos, G. and Lourenço, P. B. (2006). Assessment of the In-Plane Shear Strength of Stone Masonry Walls by Simplified Models. *In Proceedings of the Conference Structural Analysis of Historical Constructions*. New Delhi, India.

Vidiç, T., Fajfar, P., and Fischinger, M. (1994). Consistent inelastic design spectra: strength and displacement, *Earthquake Engineering & Structural Dynamics*, 23, 502–521.

Zarzour, N., Santisi d'Avila, M. P., Mercerat, E. D., Lenti, L., and Oggero, M. (2023). Behavior factor estimation for seismic design of unreinforced masonry buildings. *Case Studies in Construction Materials*, 19.

Zarzour, N., Santisi d'Avila, M. P., Lenti, L., and Oggero, M. (2024). Impact of in-plane stiffness of floors on the seismic response of geo-sourced masonry. *In Proceedings of the 18th World Conference on Earthquake Engineering*, Milan, Italy.

Zucchini, A. and Lourenço, P. B. (2009). A micro-mechanical homogenisation model for masonry: Application to shear walls. *International Journal of Solids and Structures*, 46(3-4), 871-886.

3. EXPERIMENTAL AND NUMERICAL ASSESSMENT OF SEISMIC RETROFIT SOLUTIONS FOR STONE MASONRY BUILDINGS

Guerrini, G., Salvatori, C., Senaldi, I. E., and Penna, A. (2021). Experimental and Numerical Assessment of Seismic Retrofit Solutions for Stone Masonry Buildings. *Geosciences*, 11(6). doi:10.3390/geosciences11060230

ABSTRACT

This paper presents an experimental and numerical study on different retrofit solutions for stone masonry buildings with timber diaphragms in earthquake-prone regions, aiming at enhancing wall-to-diaphragm connections, diaphragms' stiffness, and masonry properties. The experimental results of incremental dynamic shake-table tests on three full-scale two-story buildings, complemented by material and component characterization tests, are initially summarized. The first building specimen was unstrengthened. The second one was retrofitted at the floor and roof levels with improved wall-to-diaphragm connections and a moderate increase in diaphragm stiffness. Connections were also improved in the third specimen together with a significant enhancement of diaphragm stiffness. The calibration of two numerical models, versus the experimental response of the retrofitted building specimens, is then presented. The models were further modified and reanalyzed to assess the effects of masonry mechanical upgrades, which could be achieved in practice through deep joint repointing or various types of jacketing. These solutions were simulated by applying correction coefficients to the masonry mechanical properties, as suggested by the Italian building code. The effectiveness of the experimentally implemented and numerically simulated interventions are discussed in terms of strength enhancement and failure modes.

Keywords: natural stone masonry; timber diaphragm; seismic retrofit; wall-to-diaphragm connection; ring beam; diaphragm stiffening; mechanical properties enhancement; nonlinear pushover analysis; equivalent frame model; nonlinear macroelement.

3.1 INTRODUCTION

Masonry constitutes most of the building stock worldwide, especially concerning heritage construction systems. Among the different masonry types, natural stone masonry is rather common in mountain and rural areas as well as in historical centers. As a material, stone masonry is typically characterized by high heterogeneity and anisotropy combined with low

tensile and shear strength, often due to the poor mechanical properties of its constitutive materials. Moreover, historical masonry buildings have been usually conceived to only carry vertical loads, without any consideration for lateral resistance, and have been subjected to a continuous process of modification over the ages. These factors result in the high vulnerability of ordinary and monumental stone masonry buildings, as observed for example after recent major earthquakes in Italy (D'Ayala and Paganoni, 2011, Carocci, 2012, Da Porto *et al.*, 2012, Lagomarsino, 2011, Penna *et al.*, 2019, Sorrentino *et al.*, 2019).

Among other parameters affecting the seismic vulnerability of masonry structures, the degree of connection between intersecting walls and between walls and floors plays a significant role, as well as the in-plane stiffness of floor diaphragms (Tomaževič *et al.,*1991, Benedetti *et al.*, 1998, Rota *et al.*, 2011). In fact, poor connections may lead to the development of local out-of-plane overturning mechanisms of individual walls, even under low or moderate shaking intensity (Costa *et al.*, 2013a, Costa *et al.*, 2013b, Senaldi *et al.*, 2019). On the other hand, excessively flexible floor diaphragms may not allow an efficient distribution of the horizontal inertia forces among different walls, and may not be effective at preventing local mechanisms.

Consequently, enhancing the in-plane response of individual masonry walls can influence the building seismic performance only if local out-of-plane mechanisms are restrained and sufficient stiffness is provided to the diaphragms, enabling a box-type global behavior of the structure (Tolles *et al.*, 1996, Vintzileou *et al.*, 2015, Mouzakis *et al.*, 2017). At the same time, however, connection strengthening and diaphragm stiffening interventions can be implemented only if the masonry walls can resist the forces transferred locally; this often requires improving the masonry properties, to avoid some detrimental effects observed over the past three decades (Decanini *et al.*, 2004, Binda *et al.*, 2005, Valluzzi, 2006, Modena *et al.*, 2011, Sisti *et al.*, 2019). In particular, masonry disgregation and leaf delamination typical of poor bond and constituents should be preliminarily addressed by material enhancements.

In light of these considerations, three main strategies interact with each other in the retrofit of a stone masonry building (Karantoni *et al.*, 1992, Frumento *et al.*, 2006):

i. improvement of connections;
ii. stiffening of floor diaphragms;
iii. enhancement of masonry properties.

The first group encompasses interventions such as anchor rods (Modena *et al.*, 2004, Moreira *et al.*, 2014, Moreira *et al.*, 2015, Guerrini *et al.*, 2019), tie-rods (Guerrini *et al.*, 2019, Tomaževič *et al.,*1996, Celik *et al.*, 2009, Calderini *et al.*, 2014, Podestà and Scandolo, 2019), and ring beams (Tolles *et al.*, 2000, Sikka *et al.*, 2009, Borri *et al.*, 2009, Guadagnuolo and

Faella, 2020). Solutions for increasing the diaphragm in-plane shear stiffness include additional layers of timber planks or panels, or cast-in-place reinforced concrete (RC) slabs, properly connected to the existing joists (Modena *et al.*, 2004, Piazza *et al.*, 2008a, Valluzzi *et al.*, 2010, Nunes *et al.*, 2020). Several techniques can be adopted to improve masonry mechanical properties (Valluzzi *et al.*, 2002, Mazzon *et al.*, 2010) depending on the desired effect and compatibility issues; this study focuses on the structural effectiveness of deep joint repointing (Vintzileou and Toumbakari, 2001, Corradi *et al.*, 2008) and jacketing with reinforced plasters and composite materials (Prota *et al.*, 2006, Papanicolaou *et al.*, 2006, Borri *et al.*, 2011, De Felice *et al.*, 2014, Gattesco *et al.*, 2014, Gattesco and Boem 2015, Carozzi *et al.*, 2017, Del Zoppo *et al.*, 2019, Türkmen *et al.*, 2020).

A comprehensive experimental campaign on the seismic performance of double-leaf stone masonry was undertaken at the EUCENTRE Foundation and at the University of Pavia, Italy. The project was centered on the uniaxial incremental dynamic shake-table tests of three full-scale, two-story buildings, representative of various levels of strengthening interventions on the same original structure (Magenes *et al.*, 2010a, Magenes *et al.*, 2013, Senaldi *et al.*, 2013). The testing program included material characterization tests (Magenes *et al.*, 2010b) and in-plane cyclic tests of masonry piers (Magenes *et al.*, 2010c) and spandrels (Graziotti *et al.*, 2012).

More specifically, the first building specimen was initially tested in an unretrofitted configuration, and tie-rods were tensioned only after the activation of a local overturning mechanism. The second specimen was retrofitted by improving its wall-to-diaphragm connections with steel and reinforced masonry (RM) ring beams at the first floor and roof level, respectively; diaphragm stiffness was only slightly increased by adding a layer of 45-degree oriented timber planks. Connections were also enhanced in the third specimen but they were associated with a significant increase in diaphragm stiffness; in this case, a lightweight RC slab was cast on the first-floor and connected to the timber joists and masonry walls, while additional plywood panels and an RC ring beam were provided to the roof diaphragm.

After summarizing the experimental work, this paper focuses on the numerical modeling of the two strengthened building specimens, to simulate the test results and to evaluate further seismic performance enhancements due to masonry mechanical improvements. An equivalent frame approach has been adopted, as implemented in the software TREMURI (Lagomarsino *et al.*, 2013, Penna *et al.*, 2014), with nonlinear macroelements for masonry piers and spandrels, linear elastic membranes for floor and roof diaphragms, and linear elastic elements for ring beams. Material properties have been calibrated against the results of material and component characterization tests. Nonlinear pushover analyses have been carried out on the building models, to capture the backbone curves obtained from the shake-table tests.

Strengthening interventions for the enhancement of the masonry material have then been assessed numerically by repeating the pushover analyses after the application of correction coefficients to the masonry mechanical properties, as suggested by the Italian building code (MIT, 2018, MIT, 2019), since these retrofit details could not be explicitly modeled through the chosen macroelement discretization. In particular, correction coefficients compatible with deep joint repointing or various types of reinforced plasters have been considered. The effectiveness of different retrofit approaches and combinations is finally discussed.

3.2 EXPERIMENTAL PROGRAM

The three building specimens tested in the experimental campaign are similar in terms of geometry and masonry characteristics. They differ, however, for the strengthening/stiffening interventions adopted. The following sections describe the masonry structure and the floor framing common to all three building specimens. Then, they provide details of the retrofit interventions adopted at the floor and roof levels of Building 2 (Magenes *et al.*, 2013) and Building 3 (Senaldi *et al.*, 2013), while Building 1 (Magenes *et al.*, 2010a) was tested in unstrengthened original configuration.

3.2.1 Masonry structures

The reference geometry of the specimens simulates the characteristics of a common type of historical residential construction in Italy. The building was designed as a single-room structure with an external footprint of $5.8 \times 4.4\ m$. It included two stories with pitched roof, as shown in Figure 3.1 and Figure 3.2. The longitudinal walls, namely the East and West façades, were oriented in the direction of the shaking table motion, while the North and South walls were perpendicular to it. In order to induce in-plan shear distortional or torsional effects under uniaxial shake-table motion, the building was characterized by an asymmetric distribution of openings on the longitudinal walls.

The structural walls consisted of double-leaf undressed stone masonry with overall nominal thickness of $32\ cm$, with some smaller stones mixed with mortar but no loose material to fill the irregular gaps between the leaves. Connection between intersecting walls was achieved by providing through stones alternatively in the internal or external leaf of the two walls at the corners (Figure 3.3a). Through stones were also located at opening edges (Figure 3.3b,c).

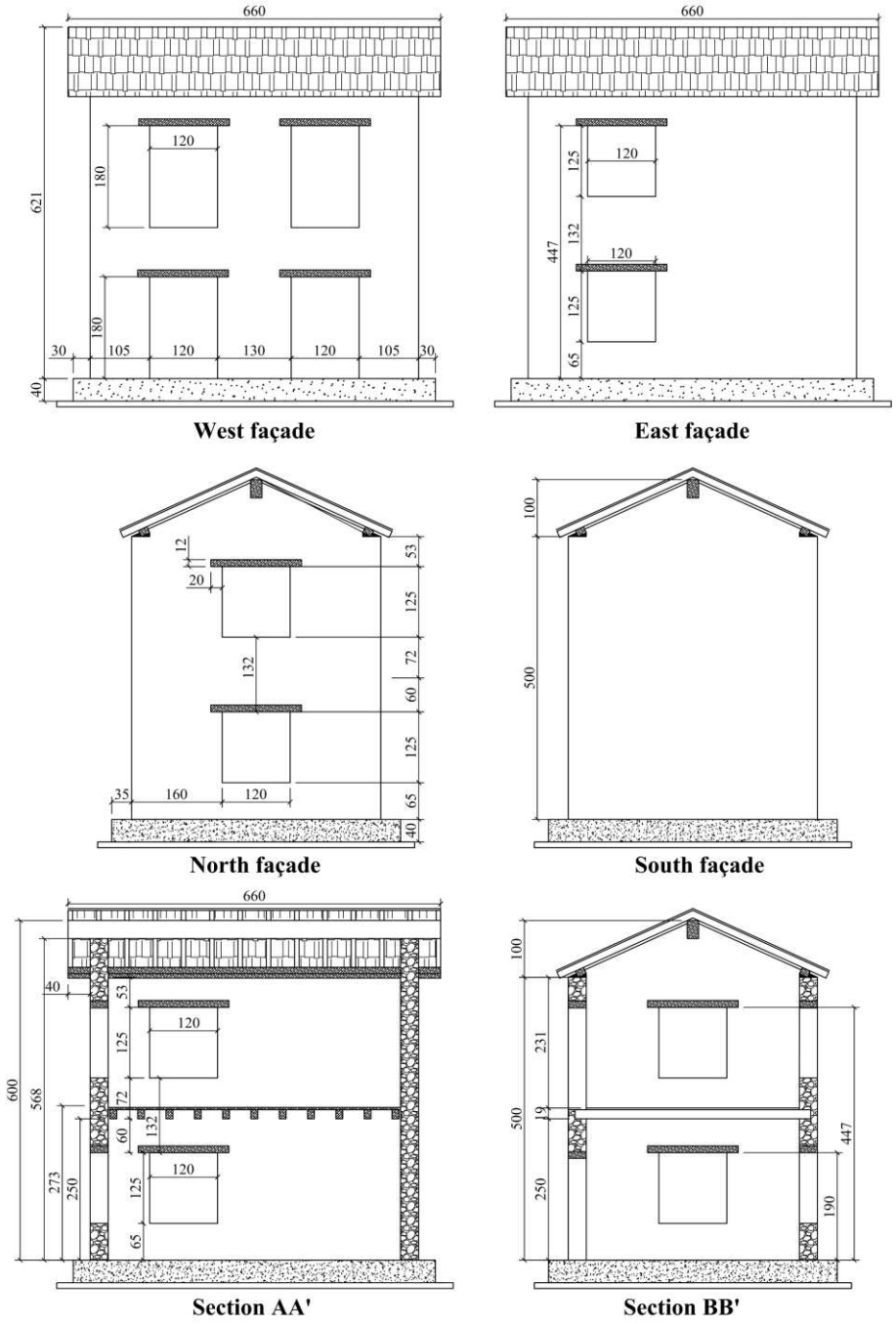

Figure 3.1: Elevation views and vertical sections of the reference building prototype (Building 1). Units of *cm*.

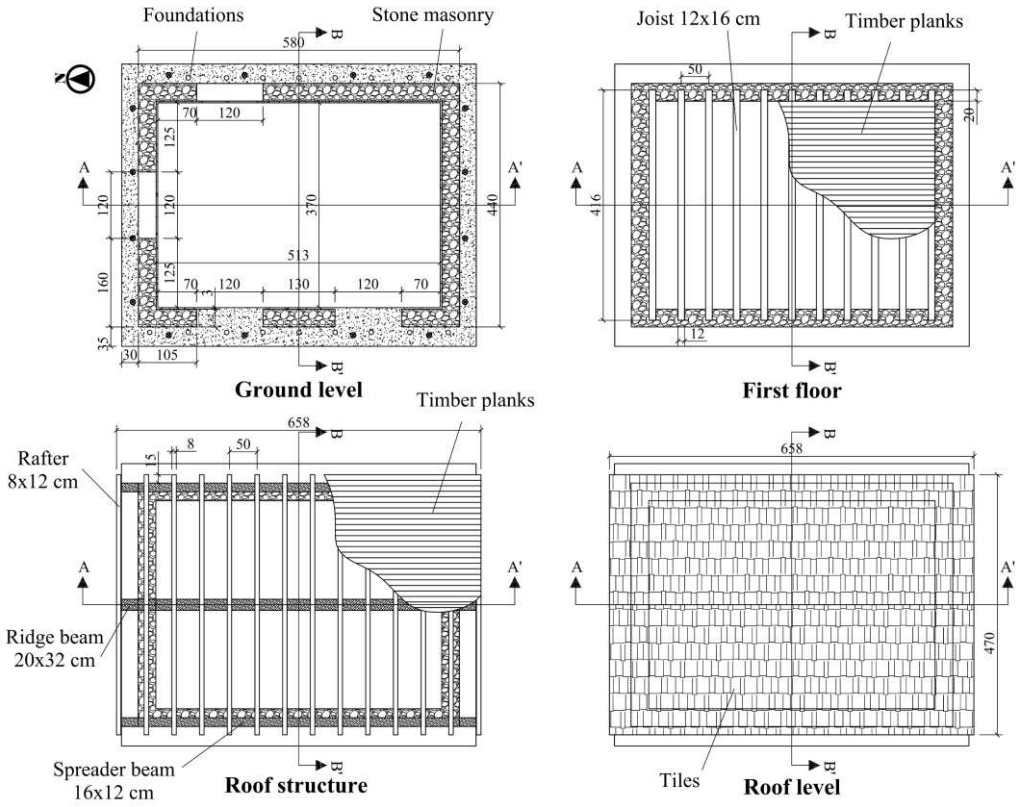

Figure 3.2: Plan views of the reference building prototype (Building 1). Units of *cm*.

(a) (b) (c)

Figure 3.3: Double-leaf stone masonry: (a) stone interlocking at corners, (b) and (c) through stones at opening edges.

3.2.2 Timber floor and roof structures

To reproduce the features of similar existing buildings, the reference timber floor framing system consisted of $12 \times 16\ cm$ joists, inserted within the internal leaf of the supporting longitudinal walls for about 15 to $20\ cm$ (Figure 3.4a,b).

The inclined roof pitches consisted of $8 \times 12\ cm$ rafters, resting on spreader beams above the longitudinal walls and extending beyond them by approximately $15\ cm$, to simulate the roof eaves (Figure 3.5a,b). The rafters were also supported by a $20 \times 32\ cm$ ridge beam. Thin perforated steel plates ensure connection between each pair of rafters matching above the ridge beam (Figure 3.5c).

Floor and roof diaphragms were completed by a single layer of 3-cm-thick timber planks, nailed to the floor joists and roof rafters (Figure 3.4c and Figure 3.5b). The roof was covered with clay tiles, nailed to the timber planks to avoid any sliding of the tiles during the dynamic tests.

Building 1 was simply constructed according to the reference details of the unstrengthened prototype, with flexible floor and roof diaphragms. Different retrofit interventions were added to the floors and roofs of Building 2 and Building 3 to increase the diaphragm stiffness, as described in the following paragraphs.

(a) (b) (c)

Figure 3.4: Timber floor: (a) and (b) floor joist supported by the internal wall leaf, (c) timber planks nailed to the floor joists.

(a) (b) (c)

Figure 3.5: Timber roof: (a) rafters resting on the spreader beam above longitudinal walls; (b) inside view of the spreader beam, rafters, and nailed timber planks; (c) rafters supported by the ridge beam and connected by perforated steel plates.

3.2.3 Retrofit of first-floor diaphragms and connections

The retrofit interventions applied on Building 2 (Magenes *et al.*, 2013) aimed mainly at enhanced connection between the masonry walls and the first-floor diaphragm, while only moderately increasing the timber floor in-plane stiffness. Common interventions from building strengthening practice were selected for these purposes.

Steel angles with dimensions of $120 \times 120 \times 10\ mm$ were used as a ring beam to allow an easy connection with the timber floor and the masonry walls, as shown in Figure 3.6a. The ring beam was connected to external rectangular steel anchor plates by pre-tensioned 14-*mm*-diameter threaded bars, unbonded through the wall thickness.

(a) (b)

Figure 3.6: Building 2, retrofit at the first-floor level: (a) structural detail of the wall-to-diaphragm connection; (b) steel-angle ring beam at a building corner and 45-degree-oriented additional timber planks. Units of *cm*.

Anti-shrinkage mortar was applied between steel angles or plates and masonry surfaces to create an even and distributed contact interface and a homogeneous confinement effect against out-of-plane wall overturning.

The floor in-plane stiffness of Building 2 was moderately increased by adding a second layer of diagonal timber planks, oriented at 45 degrees with respect to the existing floor joists and planks (Figure 3.6b). The planks were connected to the joists underneath, using at least two nails at intermediate intersections and four nails when connecting two adjacent planks to the same joist.

On the other hand, strengthening of the first floor of Building 3 (Senaldi *et al.*, 2013) was designed not only to improve its connection with the walls, but also to significantly increase the in-plane diaphragm stiffness, implementing another common approach (Piazza *et al.*, 2008b).

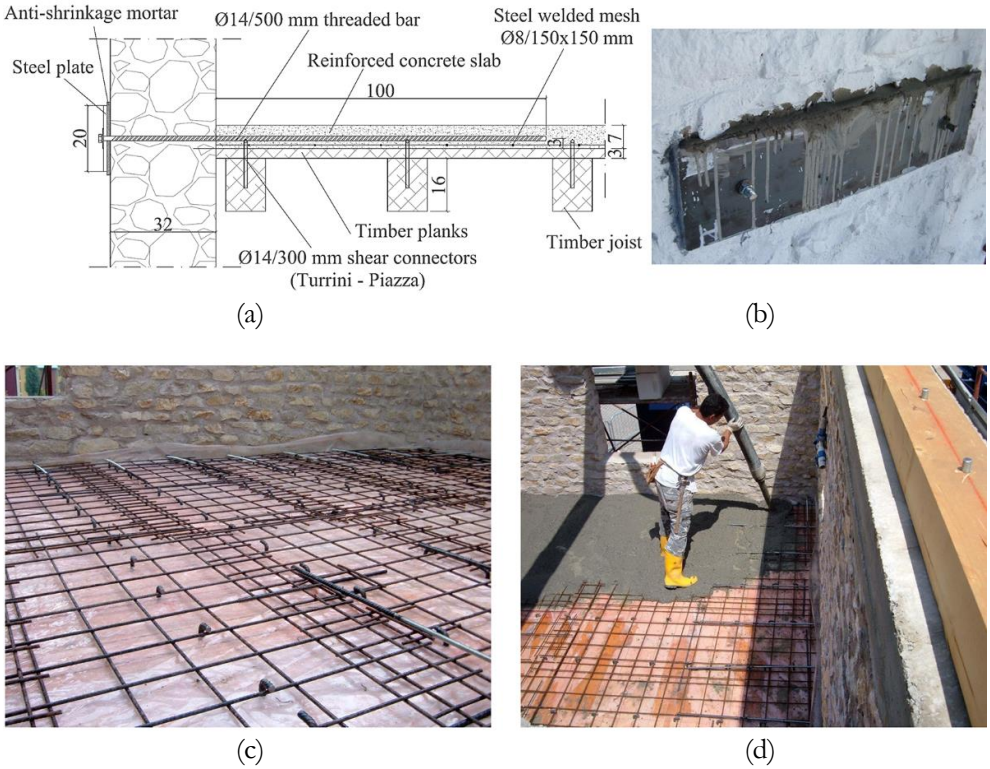

Figure 3.7: Building 3, retrofit at the first-floor level: (a) structural detail of the wall-to-diaphragm connection and of the RC slab; (b) external steel plates; (c) shear connectors, steel welded mesh and threaded bars for the wall-to-diaphragm connection; (d) lightweight RC slab casting. Units of *cm*.

A 7-cm-thick lightweight concrete slab was cast above the original floor structure (Figure 3.7a), connected to the timber floor by shear connectors consisting of 14-mm-diameter reinforcing bars bent at 90 degrees (Turrini and Piazza, 1983) (Figure 3.7c). The connectors crossed through the planks and were chemically anchored to the floor joists at a spacing of 30 cm. The slab was reinforced by a 15×15 cm steel welded mesh of 8-mm-diameter bars (Figure 3.7c,d).

Threaded bars 14 mm in size were embedded by 100 cm in the RC slab and tied against external steel plates (Figure 3.7b,c), to enhance the wall-to-diaphragm connection and prevent the activation of overturning mechanisms. Anti-shrinkage mortar was applied between steel plates and masonry walls to regularize the contact interface.

3.2.4 Retrofit of roof diaphragms and connections

The roof retrofit of Building 2 (Magenes *et al.*, 2010a) was conceived mainly to enhance the connection between walls and diaphragm, while only moderately increasing the timber pitches in-plane stiffness, as was carried out for the first-floor diaphragm.

The wall-to-roof diaphragm connection of Building 2 was enhanced with a RM ring beam, made of two solid brick veneers and an inner cement mortar core, located above the masonry walls (Figure 3.8a). The ring beam was longitudinally reinforced with three layers of 26-cm-wide, 5-mm-diameter reinforcement trusses, placed in the bed-joints and connecting the brick veneers (Figure 3.8c). Two 16-mm-diameter reinforcing bars were located in the mortar core above the longitudinal walls, while two 12-mm-diameter bars were provided above the gables (Figure 3.8d).

The perimeter timber spreader beam was doweled to the RM ring beam by pairs of chemically anchored 16-mm-diameter threaded bars, spaced at 80 cm above the longitudinal walls and at 75 cm above the gables, while the ridge beam was anchored to a steel shoe fixed to the ring beam (Figure 3.8b). To avoid the dispersion of epoxy resin into the masonry voids during injection, a steel sock was inserted in the holes accommodating the threaded bars.

The timber roof pitches were strengthened by adding a second layer of diagonal timber planks, oriented at 45 degrees with respect to the existing floor joists and planks, similarly to the intervention executed on the first-floor diaphragm.

An RC ring beam was provided above the longitudinal walls and transverse gables of Building 3 (Senaldi *et al.*, 2013) to improve connection with the roof, while the timber roof pitches were stiffened by multilayer spruce plywood panels (Figure 3.9a).

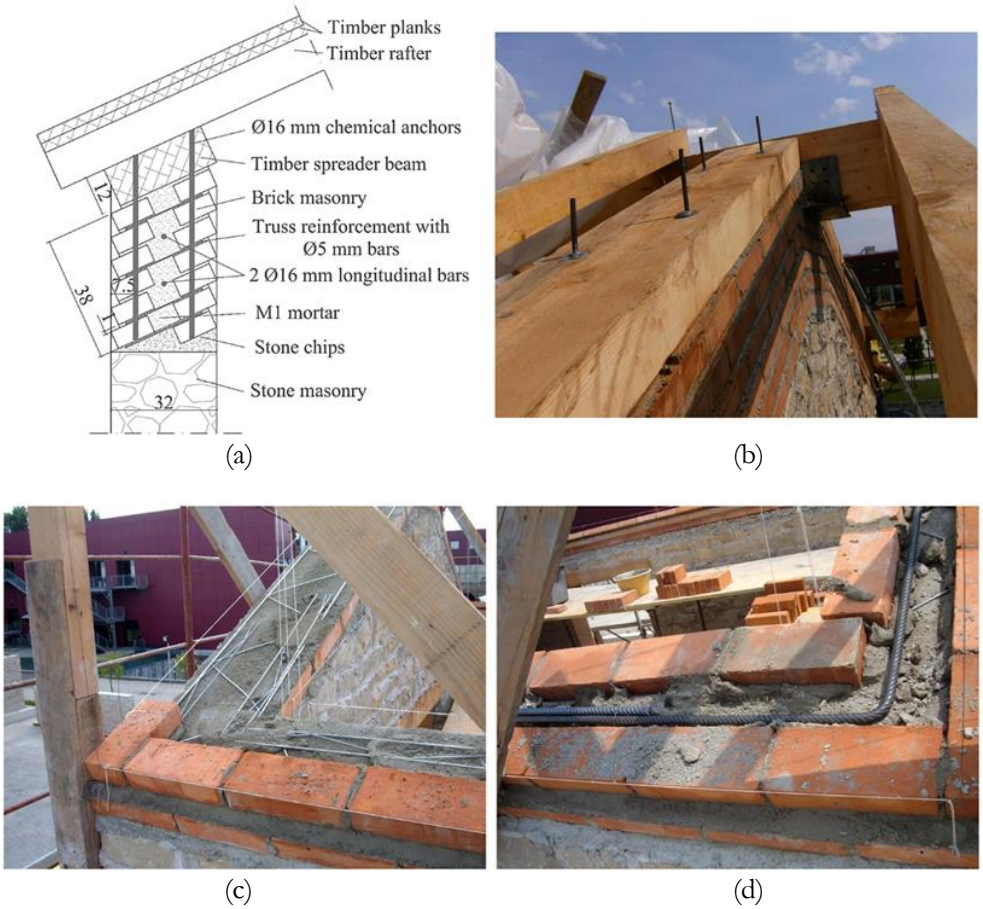

Figure 3.8: Building 2, retrofit at the roof level: (a) structural detail of the RM ring beam; (b) timber spreader and ridge beams connected to the RM ring beam above a gable; (c) horizontal truss reinforcement at corner; d) longitudinal reinforcing bars at corner. Units of *cm*.

The $32 \times 20\ cm$ RC ring beam was cast on top of all perimeter walls. The reinforcement consisted of four 16-mm-diameter longitudinal bars and 8-mm-diameter stirrups spaced at $20\ cm$ (Figure 3.9b). The rafters were supported by a $16 \times 12\ cm$ timber spreader beam, doweled to the RC ring beam every $40\ cm$ by chemically anchored 16-mm-diameter threaded bars (Figure 3.9c).

The roof diaphragm(Figure 3.9d) was stiffened by adding three layers of 2-cm-thick spruce plywood panels, glued to the planks and to each other with polyurethane adhesive and connected to the rafters by 10-mm-diameter chemically anchored steel bars every $30\ cm$. Panels of adjacent layers were staggered to avoid aligned joints. To improve the mechanical behavior of the roof, $80 \times 5\ mm$ continuous steel plates were placed all along the perimeter of each pitch.

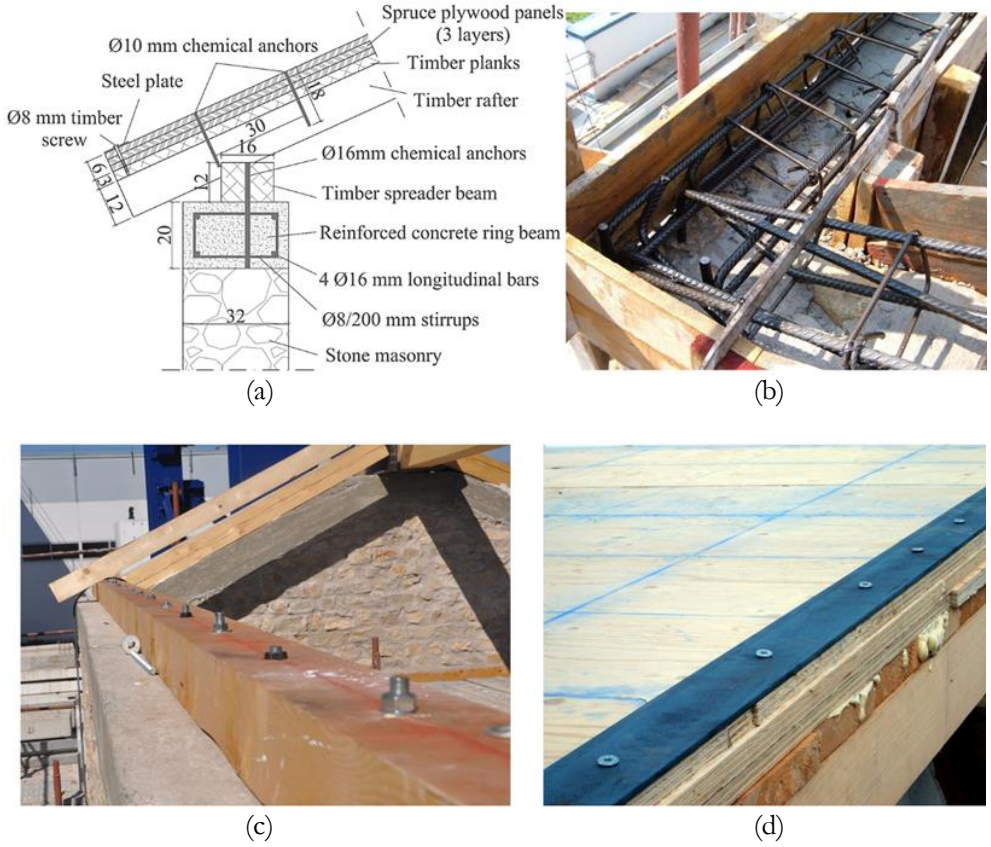

Figure 3.9: Building 3, retrofit at the roof level: (a) structural detail of the RC ring beam; (b) ring beam reinforcement at corner; (c) timber spreader beam connected to the RC ring beam above a longitudinal wall; (d) spruce plywood layers and continuous steel plate along the perimeter. Units of *cm*.

3.2.5 Material properties and masses

The mechanical properties of the masonry constituting the three building specimens were determined from vertical compression and diagonal compression tests (Magenes *et al.*, 2010b). Table 3.1 summarizes the mean values and the dispersions of Young's and shear moduli, E and G, as well as of compressive and tensile strengths, f_m and f_t.

Table 3.1: Masonry mechanical properties after characterization tests.

	E [MPa]	G [MPa]	f_m [MPa]	f_t [MPa]
Mean	2550	840	3.28	0.137
St. Dev.	345	125	0.26	0.031
C.o.V	13.5%	14.8%	8.0%	21.8%

C25/30 concrete (normal weight for the ring beam, lightweight for the slab) and B450 steel reinforcement were used for the strengthening interventions applied to Building 3, whereas the tests performed on the cement mortar used for the RM ring beam of Building 2 provided a mean compressive of approximately $15\ MPa$. Young's and shear moduli of $10\ GPa$ and $630\ MPa$, respectively, were assumed for all timber components, corresponding to class C22 timber (CEI, 2016a, CEI, 2016b).

A list of the nominal density of the construction materials is given in Table 3.2. Additional masses of $2\ kN/m^2$ were distributed on the first floor of each building specimen, to simulate the pavement load plus 30% of residential live load. The tiles installed on the roof provided a total weight of $12.7\ kN$.

Table 3.2: Construction material densities.

Material	$\rho\ [kg/m^3]$
Double-leaf stone masonry	2250
Normal weight RC	2500
Lightweight	1500
Steel	7850
Timber	600

3.2.6 Testing protocol and results

The three building specimens were subjected to a similar sequence of unidirectional dynamic tests, with increasing ground motion intensity obtained by scaling the amplitude of the selected signal to predefined nominal peak ground acceleration (PGA) levels (Magenes *et al.*, 2010a, Magenes *et al.*, 2013, Senaldi *et al.*, 2013). The Ulcinj-Hotel Albatros station East–West record of the 15 April 1979 Montenegro event was used for all dynamic tests, to allow for the comparison of the damage progression and of the effect of the selected retrofit techniques.

For all three buildings, the first test was carried out with nominal PGA of $0.05g$; then, amplitude scaling factors were increased up to reaching a near collapse conditions. Table 3.3 outlines the testing sequence for the three specimens, with the recorded PGA for each test run. Discrepancies between the PGA actually recorded for the different specimens occurred because of difficulties in the control procedure of the shaking table.

Table 3.3: Shake-table testing protocols.

Test	Building 1 PGA [g]	Building 2 PGA [g]	Building 3 PGA [g]
1	0.07	0.06	0.12
2	0.14	0.14	0.27
3	0.31	0.26	0.55
4	0.50	0.36	0.92
5	0.63	0.56	1.28
6	0.70*	0.71	1.04
7	-	0.88	1.49
8	-	1.16	0.66**

* Test performed on Building 1 after post-tensioning of tie-rods.
** Simulation of an aftershock on the damaged Building 3.

Building 1 was subjected to the last test at PGA of $0.70g$ only after tightening preinstalled tie-rods to contrast out-of-plane local mechanisms already activated; because of this variation in the structural configuration, this test run is not given further consideration. Additionally, the last test of Building 3, representing a lower-intensity aftershock with PGA of $0.66g$, is not taken into account in the following discussion.

Figure 3.10 shows the backbone curves in terms of total base shear versus average top displacement (at the roof base), by taking the points corresponding to maximum positive and negative base shear with the associated displacement from each test run; only the last point of each curve is taken at the maximum positive or negative displacement with the corresponding base shear. Figure 3.11 represents instead the incremental dynamic test (IDT) curves in terms of maximum absolute recorded PGA versus maximum absolute average top displacement from each test run.

The reference Building 1 was characterized by smaller lateral strength and displacement capacity compared to retrofitted Building 2 and Building 3, and reached near-collapse conditions at a PGA of $0.63g$ due to out-of-plane overturning of the upper portions of the transverse façades. Instead, Building 2 and Building 3 exhibited a global response up to higher PGA intensities of $1.16g$ and $1.49g$, respectively, thanks to the effectiveness of the enhanced wall-to-diaphragm connections. Their ultimate conditions were associated with in-plane failure mechanisms rather than out-of-plane local overturning.

The IDT curves of Figure 3.11 show that the same displacement demand was reached for higher PGA as the connections were enhanced with minor floor stiffness variation (Building 2 compared to Building 1) and as the diaphragms were significantly stiffened (Building 3 compared to Building 2). In particular, despite similar lateral strength, Building

3 underwent smaller displacement demand under higher PGA compared to Building 2, thanks to better engagement of all longitudinal and transverse piers by the nearly rigid diaphragms.

None of the specimens suffered from masonry disgregation, leaf delamination, or wall separation at corners, even though the masonry was characterized by relatively low strength. This performance was achieved thanks to a combination of mortar binding quality, sharp-cornered stones, and absence of loose filling, representative of good existing or improved stone masonry.

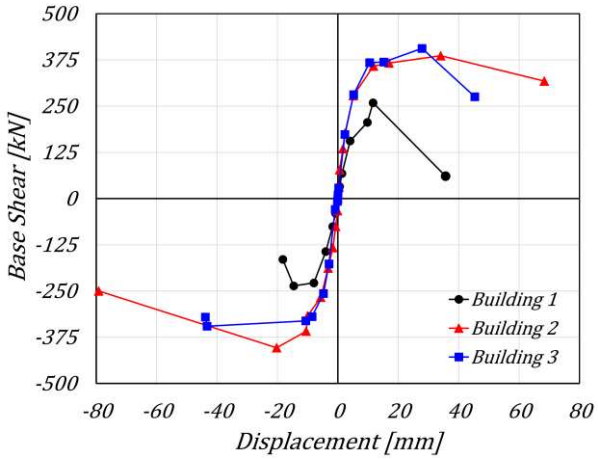

Figure 3.10: Shake table test results: backbone curves.

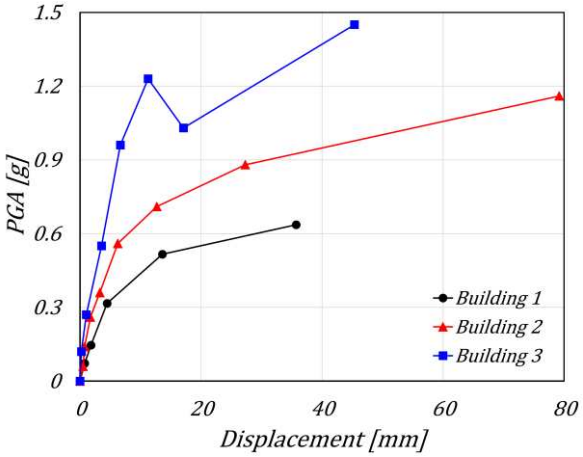

Figure 3.11: Shake table test results: incremental dynamic test (IDT) curves.

3.3 NUMERICAL SIMULATIONS

3.3.1 Modeling strategy

Several approaches can be followed to model masonry structures, ranging from the most complex micro-modelling techniques to simplified methods based on limit analysis, equivalent truss models, or story mechanisms (Penna *et al.*, 2014). In this study, the intermediate strategy of three-dimensional equivalent-frame modeling was adopted, as it is one of the most widely used in professional practice to reproduce the global response of masonry buildings. This choice is particularly appropriate to simulate the response of structures with fairly regular wall layouts when local mechanisms are prevented. The TREMURI program (Lagomarsino *et al.*, 2013) was chosen for this purpose.

The software simulates the behavior of an entire building by assembling vertical walls and horizontal diaphragms, referring to their in-plane strength and stiffness contributions. Walls are discretized into two-node macroelements (Penna *et al.*, 2014), corresponding to pier (vertical) and spandrel (horizontal) members, and rigid nodal regions at their intersections. These macroelements allow one to reproduce the two main in-plane failure mechanisms of a masonry panel (flexure and shear), keeping a reasonable compromise between the accuracy of the results and computational effort.

Various strategies are proposed in the literature and codes to discretize masonry walls into macroelements (Bracchi *et al.*, 2015). In this work, the pier height was taken as equal to the one of the adjacent openings, to capture better the damage mechanisms observed during the shake-table tests and to account for the presence of timber lintels anchored into the masonry walls, which effectively prevented the diffusion of cracks in the nodal regions (Penna *et al.*, 2015).

The structural behavior of a building is strongly affected by the in-plane stiffness of floor and roof diaphragms. For this reason, TREMURI includes linear three- or four-node orthotropic membrane finite elements, with two in-plane displacement degrees of freedom at each node. Moreover, the equivalent-frame model of a wall allows one to introduce other structural elements, such as steel, RC, and RM ring beams, with both linear and nonlinear beam element formulation.

The out-of-plane flexural responses of diaphragms and walls are not accounted for because they are considered negligible in the context of the global building response, which is governed by their in-plane behavior. As a consequence, local disgregation, delamination, and out-of-plane overturning mechanisms cannot be captured by this modeling technique: in fact, the underlying assumption of global building modeling is that local mechanisms are inhibited. For this reason, only Building 2 and Building 3 models were analyzed, since the

failure of Building 1 was governed by local overturning of the transverse façades (Magenes *et al.*, 2010a).

As shown in Figure 3.12, the four walls of the models representing the two buildings were very similar to each other. Differences were limited to cross-sections and materials assigned to diaphragms and ring-beams. All masses actually present in the experimental building specimens were considered in the models. In particular, the stone masonry mass was automatically obtained by assigning its density to nodal regions and macroelements: a reduced value of $2200\ kg/m^3$ was used to account for the penetration of lighter timber lintels and joists in the walls. Floor, roof, retrofit components, and additional masses were instead assigned as lumped nodal values.

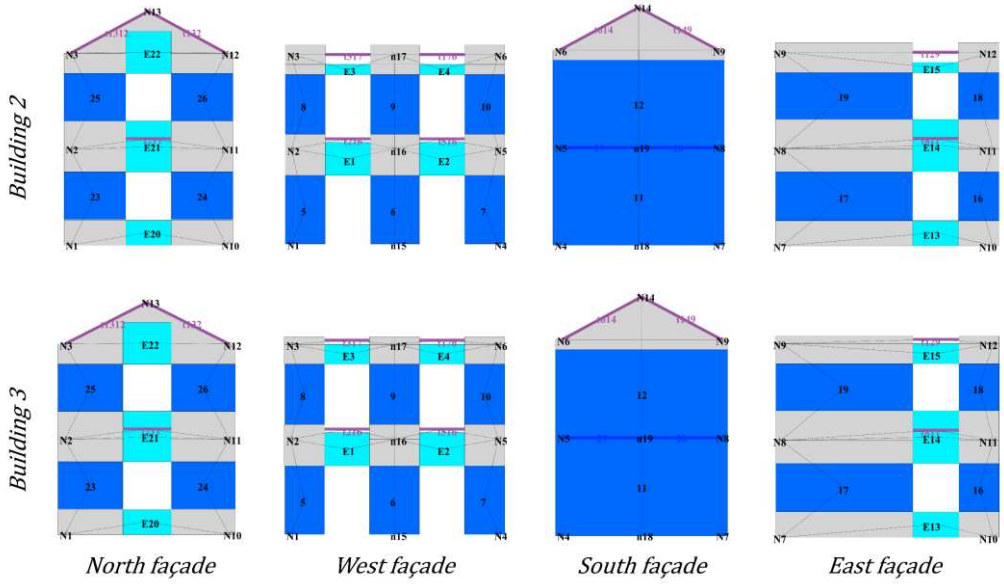

Figure 3.12: Geometrical discretization of walls in Building 2 and Building 3 models.

3.3.2 Calibration of masonry material properties

The masonry mechanical properties adopted in the numerical models were derived from a comprehensive characterization campaign carried out on material samples and components built together with the three building specimens at the EUCENTRE Foundation and University of Pavia laboratories (Magenes *et al.*, 2010b, Magenes *et al.*, 2010c, Graziotti *et al.*, 2012).

In particular, the normal compressive strength was directly taken as the mean value from vertical compression tests on wallettes (Magenes *et al.*, 2010b). Instead, the Young's modulus E and the shear modulus G assigned to the macroelements were different from

the values obtained from the characterization tests. In fact, the two specimens were built elsewhere and then transported on the shake-table, resulting in some preliminary cracking (Magenes *et al.*, 2013, Senaldi *et al.*, 2013). For this reason, stiffness parameters of masonry macroelements were reduced to 80% of the characterization values. All spandrels and some piers were particularly damaged in Building 3: only 40% of the elastic moduli were assigned to the corresponding macroelements.

The tensile strength associated with diagonal shear cracking was derived from quasi-static cyclic shear-compression tests on four piers (Magenes *et al.*, 2010c) rather than from diagonal compression tests to account for geometric and axial load effects. The specimen dimensions were chosen to be representative of slender and squat piers of the building prototype. The two specimens of each geometry were tested under distinct levels of axial compression.

At the end of each test, the maximum positive and negative values of shear strength V_R^+ and V_R^- were recorded. By inverting Turnšek and Sheppard's strength criterion (Turnšek and Sheppard, 1980), the corresponding tensile strengths f_t^+ and f_t^- were obtained from equation (3.1):

$$V_R = L\,t\,\frac{f_t}{b}\sqrt{1+\frac{\sigma_0}{f_t}} \tag{3.1}$$

where L, h, and t are pier length, height, and thickness, respectively, $b = h/L$ is a coefficient accounting for shear stress distribution in the center of the panel, and σ_0 is the axial compressive stress. A summary of the tensile strength calculation is reported in Table 3.4. It can be noted that almost all the tensile strength values determined from cyclic shear-compression tests fall around the mean value from diagonal compression tests ($0.137\ MPa$) plus or minus one standard deviation ($0.031\ MPa$).

Table 3.4: Determination of the tensile strength from cyclic shear-compression tests on piers.

Pier	L $[mm]$	h $[mm]$	t $[mm]$	σ_0 $[MPa]$	b $[-]$	V_R^+ $[kN]$	V_R^- $[kN]$	f_t^+ $[MPa]$	f_t^- $[MPa]$
Slender 1	1250	2500	320	0.5	1.5	86	94	0.16	0.18
Slender 2	1250	2500	320	0.2	1.5	45	48	0.10	0.11
Squat 1	2500	2500	320	0.5	1	234	225	0.13	0.13
Squat 2	2500	2500	320	0.2	1	135	154	0.10	0.12

As the shear failure criterion of the macroelement implemented in TREMURI is based on a Coulomb model, equivalent cohesion c_{eq} and friction coefficient μ_{eq} can be calculated by linearizing the Turnšek and Sheppard's criterion (Turnšek and Sheppard, 1980) around the static axial load $N_0 = Lt\sigma_0$ due to gravity loads only (Penna *et al.*, 2015), according to equation (3.2):

$$\begin{cases} \mu_{eq} = \dfrac{dV_R}{dN}\Big|_{N_0} = \dfrac{1}{2b}\sqrt{\dfrac{f_t}{f_t + N_0/Lt}} \\ c_{eq} = \dfrac{f_t}{b}\sqrt{1 + \dfrac{N_0}{Lt f_t}} - \mu_{eq}\dfrac{N_0}{Lt} \end{cases} \tag{3.2}$$

The equivalent parameters were assigned, distinguishing between slender piers, squat piers, and spandrels. For slender piers, the upper-bound tensile strength of $0.18\ MPa$ from Table 3.4, the static axial load acting on the first-story West-wall central pier ($68\ kN$ for Building 2, while $78\ kN$ for Building 3), and element dimensions of $1.30 \times 1.80 \times 0.32\ m$ were considered. Instead, for squat piers, the lower-bound tensile strength of $0.10\ MPa$, the axial load on the first-story East-wall squat pier ($149\ kN$ for Building 2, while $173\ kN$ for Building 3), and dimensions of $3.55 \times 1.25 \times 0.32\ m$ were used. The same equivalent cohesion and friction coefficient of the slender piers were also applied to the spandrels.

Parameters Gc_t and β complete the definition of the nonlinear shear response of the macroelement (Penna *et al.*, 2014). In particular, Gc_t controls the shear deformation corresponding to the peak strength, while β governs the softening branch following the peak. All mechanical properties assigned to the macroelements of the two models are summarized in Table 3.5.

Table 3.5: Masonry macroelement properties.

Model	Element	E $[MPa]$	G $[MPa]$	f_m $[MPa]$	μ_{eq} $[-]$	c_{eq} $[MPa]$	β $[MPa]$	Gc_t $[-]$
Building 2	Slender p.	2030	560	3.28	0.261	0.137	0.4	10
	Squat p.	2030	560	3.28	0.328	0.109	0.4	10
	Spandrels	2030	560	3.28	0.261	0.137	0.0	10
Building 3	Slender p.	2030*	560*	3.28	0.253	0.138	0.4	10
	Squat p.	2030*	560*	3.28	0.315	0.111	0.4	10
	Spandrels	1015	280	3.28	0.253	0.138	0.0	10

* Value halved for piers with extensive preexisting damage.

3.3.3 Calibration of membrane and beam element stiffness

The in-plane stiffness of floor and roof diaphragms can be simulated in TREMURI through orthotropic membrane elements with linear elastic formulation. The mechanical properties of the aforementioned elements are defined through a principal direction, with Young's modulus E_1, an orthogonal direction, with Young's modulus E_2, the Poisson coefficient ν, and the shear modulus G_{12}. The most critical parameter is the last one, which influences the diaphragm shear stiffness and its ability to redistribute lateral forces among masonry walls, both in linear and nonlinear phases.

In this work, the mechanical properties for floor and roof diaphragms were evaluated with equation (3.3):

$$\begin{cases} E_1 = \dfrac{E_{tj}\,A_j/s_j + E_{ta}t_a \sin^2\varphi_a + E_{tp}t_p + E_c t_c}{t_m} \\ E_2 = \dfrac{E_{te}t_e + E_{ta}t_a \cos^2\varphi_a + E_{tp}t_p + E_c t_c}{t_m} \\ G_{12} = \dfrac{C_d G_{12,e}t_e + G_c t_c}{t_m} \end{cases} \tag{3.3}$$

where the equivalent shear modulus of the originally existing timber diaphragm, $G_{12,e}$, includes the three in-series contributions (Brignola *et al.*, 2008) due to flexural and shear deformation of each plank and rigid rotation of the plank due to nail slip, according to equation (3.4):

$$G_{12,e} = \frac{\chi}{A_e}\left(\frac{s_j^2}{12\,E_{te}\,I_e} + \frac{\chi}{G_{te}\,A_e} + \frac{s_j}{k_{ser}\,s_n^2}\right)^{-1} \tag{3.4}$$

The symbols that appear in equations (3.3) and (3.4) have the following meanings:

i. E_1 is oriented parallel to the timber joists, orthogonal to the shaking direction;
ii. E_2 is oriented parallel to the original timber planks and to the shaking direction;
iii. t_m is the thickness assigned to the model membrane;
iv. E_{tj} is the Young's modulus of timber for the joists;
v. A_j and s_j are the cross-section area and the spacing of the timber joists;
vi. E_{te} and G_{te} are the Young's and shear moduli of timber for the existing planks;
vii. t_e, A_e, and I_e are the thickness, cross-section area, and moment of inertia of each existing timber planks;
viii. E_{ta} is the Young's modulus of timber for the additional planks;

ix. t_a and φ_a are the thickness of the additional timber planks or panels and their orientation with respect to the existing planks;
x. E_{tp} is the Young's modulus of timber for the additional panels;
xi. t_p is the thickness of the additional timber panels;
xii. E_c and G_c are the Young's and shear moduli of concrete;
xiii. t_c is the thickness of the additional reinforced concrete slab;
xiv. k_{ser} is the nailed connection stiffness according to Eurocode 5 (CEI, 2004a);
xv. s_n is the nail spacing at a plank–joist intersection;
xvi. $\chi = 1.2$ is the shear factor for a rectangular cross-section;
xvii. C_d is a correction coefficient accounting for additional timber layers.

Correction coefficients C_d were applied to the equivalent shear modulus derive from equation (3.4), to account for retrofit interventions increasing the diaphragm stiffness through further planks or plywood layers (Mirra *et al.*, 2020). $C_d = 5$ was chosen for the floor and roof diaphragms in Building 2, where an additional plank layer was provided with $45°$ orientation with respect to the original one. Coefficient $C_d = 20$ was instead used to simulate Building 3 roof improvement with three additional layers of plywood panels.

The lightweight RC slab cast on the floor of Building 3 was explicitly modeled by considering its collaboration with the timber floor underneath, as expressed by equation (3.3). The Young's modulus of concrete was calculated according to Eurocode 2 (CEI, 2004b) and the Italian building code (MIT, 2018, MIT, 2019) based on the concrete strength class and density. The concrete shear modulus was approximated as $G_c = E_c/2.6$, according to a Poisson's ratio of $\nu = 0.3$.

The values of the main parameters assigned to the floor and roof diaphragms are reported in Table 3.6. It is noteworthy that combining the literature formulations with the material properties adopted for the specimens resulted in good agreement with the experimental results without further calibration of the diaphragm models.

Table 3.6: Floor and roof diaphragm properties.

Model	Diaphragm	t_m $[m]$	E_1 $[MPa]$	E_2 $[MPa]$	ν $[-]$	G_{12} $[MPa]$
Building 2	Floor	0.05	11 186	9000	0	12
	Roof	0.05	11 186	9000	0	12
Building 3	Floor	0.10	13 928	13 088	0	3881
	Roof	0.10	8220	9300	0	71

The quality of the wall-to-diaphragm connections was improved by steel, RM, or RC ring beams. These components were modeled using linear elastic beam elements with axial stiffness corresponding to the actual material and cross-section area. The clay RM elastic moduli were calibrated in a previous numerical study of the same test campaign (Penna *et al.*, 2015).

The out-of-plane flexural stiffness of the lightweight RC slab of Building 3 was also simulated through linear beam elements, with the moment of inertia corresponding to the actual slab thickness and half the floor width perpendicular to the element; the cross-section area of these elements was set to zero, as the slab axial stiffness was already assigned to the linear elastic membrane.

Table 3.7 lists the main properties assigned to the linear elastic beam elements.

Table 3.7: Linear elastic beam elements properties.

Model	Element	E $[MPa]$	G $[MPa]$	A $[cm^2]$	I $[cm^4]$
Building 2	Steel ring beam	206 000	78 400	23.2	313
	RM ring beam	5600	1400	16	310 000
Building 3	E-W RC slab	14 411	5543	0	5370
	N-S RC slab	14 411	5543	0	7370
	RC ring beam	31 000	13 000	640	21 333

3.3.4 Comparison between numerical and experimental results

Nonlinear static (pushover) analyses were performed on three-dimensional models of the two retrofitted buildings described in the previous sections, in order to reproduce the experimental backbone force-displacement curves. Pushover analyses were carried out considering two different horizontal load patterns. The first one, named "Modal", consisted of a first-mode-type force distribution, with forces proportional to the product of nodal masses times the nodal height above the base. In contrast, the second load pattern, termed "Uniform", consisted of a force distribution proportional only to the nodal masses. Due to the vertical regularity and the diaphragm stiffness of both buildings, other load patterns were not deemed relevant (Marino *et al.*, 2019).

Figure 3.13 and Figure 3.14 compare experimental backbone curves with numerical pushover curves. In particular, since most of the damage occurred at the first story in both buildings, the uniform distribution (proportional to nodal masses) resulted in curves closer to the experimental backbones for stiffness and strength. Consequently, the modal distribution will not be given further consideration.

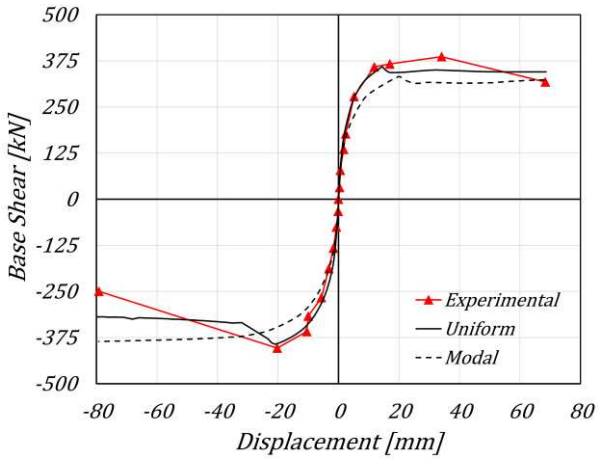

Figure 3.13: Comparison between backbone and pushover curves: Building 2.

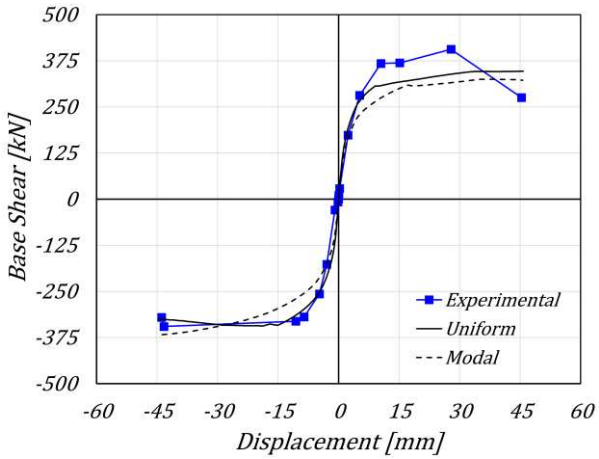

Figure 3.14: Comparison between backbone and pushover curves: Building 3.

Given the asymmetric experimental response of Building 3, a slightly larger discrepancy between numerical and experimental curves can be observed than for Building 2.

As depicted in Figure 3.15 and Figure 3.16, both numerical models were able to correctly capture the damage patterns observed on masonry piers and spandrels at the end of the shake-table tests. Lines perpendicular to the macroelement axis close to its ends indicate the extent of flexural cracks. A cross through a macroelement means that its shear strength was reached. Colors ranging from yellow to brown correspond to increasing levels of shear damage from moderate to post-peak phase, while a green color indicates axial tension instead. Both the flexural-rocking mechanism, that characterized the West façade, and the shear mechanism, observed on the East one, were properly simulated. Moreover, the

numerical models correctly reproduced the shear cracking of the transverse South wall engaged by global torsion of the whole structure.

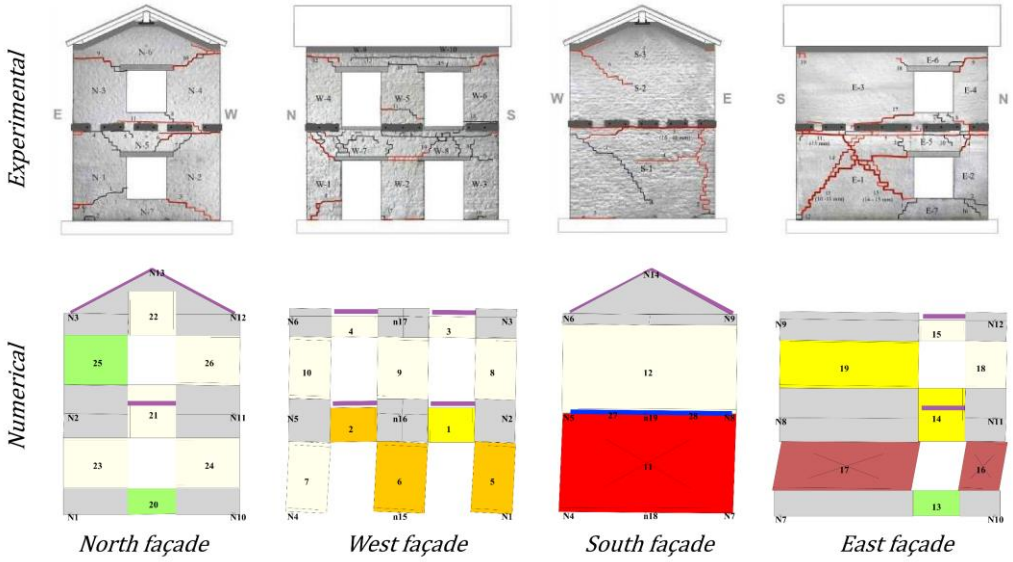

Figure 3.15: Comparison between experimental and numerical damage patterns for Building 2 (with magnified lateral displacements).

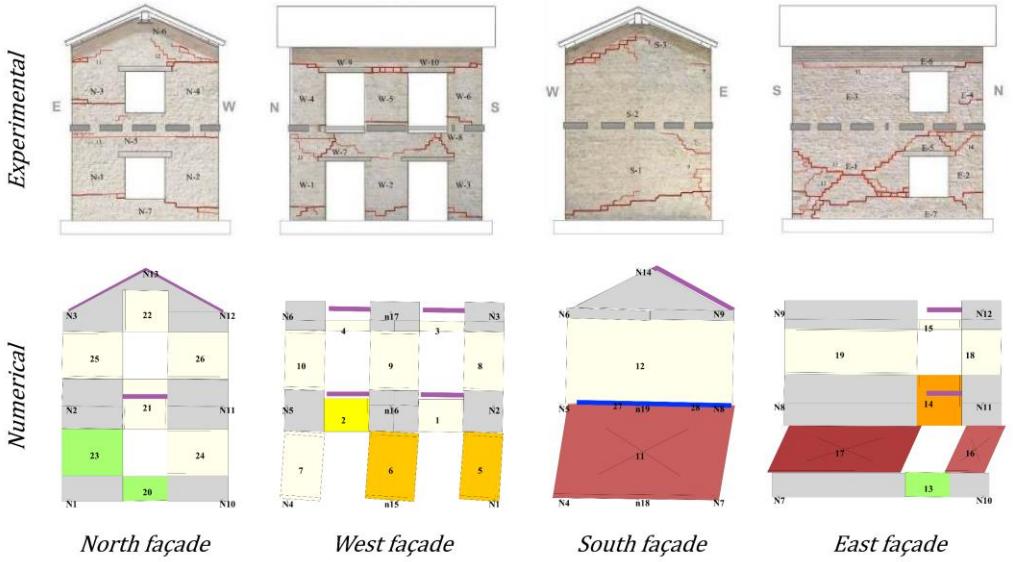

Figure 3.16: Comparison between experimental and numerical damage patterns for Building 3 (with magnified lateral displacements).

3.3.5 Parametric study on masonry mechanical improvements

Various techniques can be used in the professional practice to increase the masonry mechanical characteristics: their choice should be guided by consideration of compatibility with the existing substrate. Deep joint repointing and jacketing are two solutions often adopted for this purpose. The parametric study discussed herein focuses on some macroscopic effects of masonry improvement on the overall seismic response of masonry buildings, without addressing specific construction details of any intervention.

Deep joint repointing consists in replacing low-quality mortar with better performing materials, reaching a depth of a few centimeters from the wall surface. Sometimes, steel reinforcement is embedded in the new mortar. Jacketing instead covers a variety of interventions with the application of composite materials to one or both surfaces of masonry walls. Fiber-reinforced polymers (FRP), fabric-reinforced cementitious matrices (FRCM), composite-reinforced mortars (CRM), and steel-reinforced grouts (SRG) are among the most common jacketing materials.

The effects of these techniques on the masonry strength and stiffness are highly dependent on the constituents, bond pattern, and thickness of the original walls. Moreover, the equivalent-frame modeling strategy adopted for this study, relying on macroelement discretization of the masonry walls, cannot explicitly encompass construction details of the material strengthening. In light of these considerations, the simplified approach proposed by the Italian building code (MIT, 2018, MIT, 2019) was followed, which estimates the mechanical enhancements through simple correction coefficients starting from unstrengthened material properties. This method was deemed appropriate to compare the overall impact of increasing levels of masonry mechanical improvements.

Consequently, a parametric study has been conducted with correction coefficients C_c of 1.5 and 2.0, similar to the values proposed by the Italian building code for deep joint repointing and jacketing. Higher values of 3.0 and 4.0 have also been considered, to better cover the experimental range available in the literature for jacketing alternatives (Corradi *et al.*, 2008, Borri *et al.*, 2011, Gattesco *et al.*, 2014, Gattesco *et al.*, 2015, Del Zoppo *et al.*, 2019, Türkmen *et al.*, 2020). These coefficients were applied to the masonry Young's and shear moduli, as well as compressive and tensile strengths. Due to the Coulomb-type shear strength criterion adopted for the macroelements, equivalent cohesion c_{eq} and friction coefficient μ_{eq} were recalculated based on the increased tensile strength using equation (3.2).

Jacketing techniques rely on layers of composite materials with non-negligible tensile strength. These interventions can be detailed to provide tensile continuity with the foundation and across the floors, thus enhancing the pier axial tensile response. For this

reason, the parametric study was repeated including the axial tensile strength for masonry macroelements, neglected so far. The mean tensile strength of $0.137\,MPa$ from experimental material characterization (Magenes *et al.*, 2010b) was assigned to the unstrengthened models. The same correction coefficients used for the other properties were also applied to the axial tensile strength in the retrofitted models. Figure 3.17 and Figure 3.18 show the pushover curves obtained with the uniform load distribution for Building 2 and Building 3, applying correction coefficients C_c between 1.5 and 4.0 and ignoring any axial tensile strength.

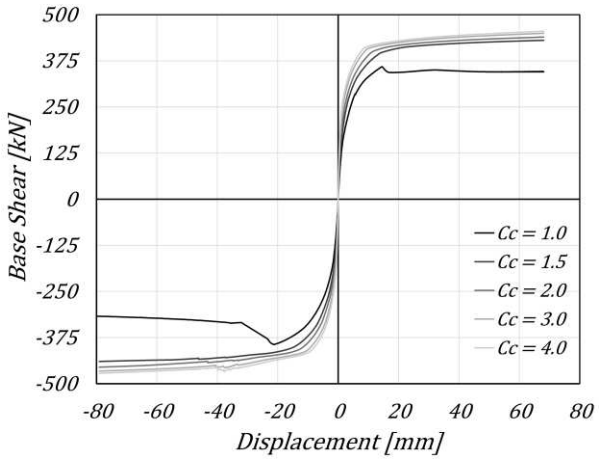

Figure 3.17: Comparison between pushover curves obtained with various correction coefficients neglecting any masonry tensile strength: Building 2.

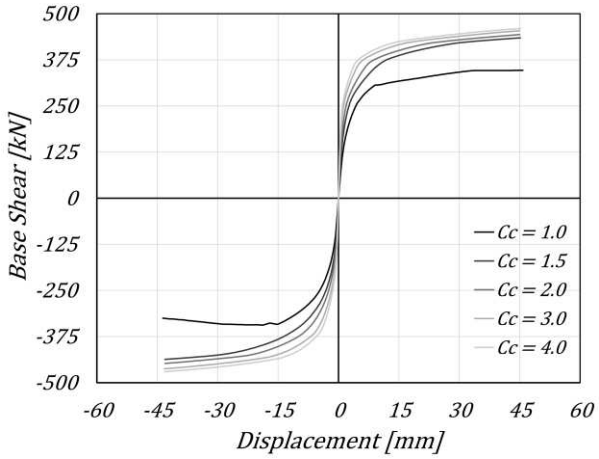

Figure 3.18: Comparison between pushover curves obtained with various correction coefficients neglecting any masonry tensile strength: Building 3.

Considering also an improved, non-zero axial tensile strength (Figure 3.19 and Figure 3.20) had minor effects on the stiffness of both numerical models and on the strength of Building 3; however, it conferred more pronounced hardening to the response of Building 2. All analyses were stopped at a top displacement equal to the maximum demand from the dynamic tests.

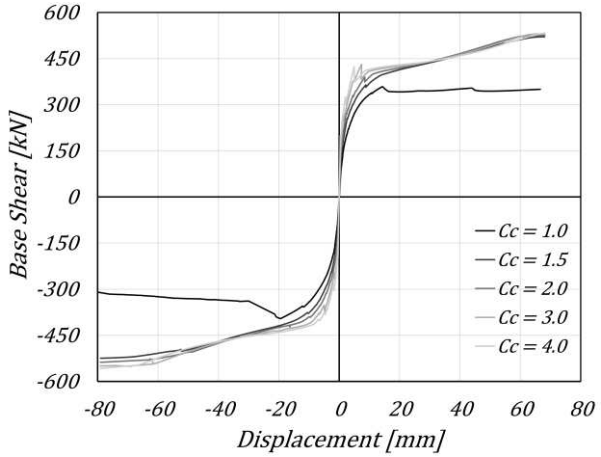

Figure 3.19: Comparison between pushover curves obtained with various correction coefficients including masonry tensile strength: Building 2.

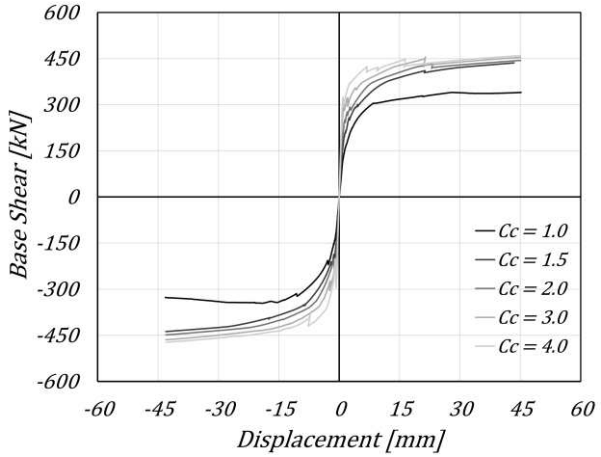

Figure 3.20: Comparison between pushover curves obtained with various correction coefficients including masonry tensile strength: Building 3.

It can be emphasized that applying correction coefficients beyond 1.5 resulted in a sort of saturation of the global lateral strength for both buildings. This can be understood by looking at Figure 3.21 and Figure 3.22, which depict the damage patterns when the maximum experimental displacement is achieved with the analyses. Increasing the correction coefficient resulted in lower shear damage to the macroelements. Shear failure on the East façade of the unstrengthened models transitioned into a global flexural mechanism on both longitudinal walls, with strength limited by rigid-body equilibrium and only barely sensitive to the material properties. The simultaneous enhancement of both axial and diagonal shear strength did not affect the failure mechanisms: in fact, a flexural behavior continued to govern the numerical responses with improved masonry properties.

The change of failure mechanism from shear to flexure and the increase in lateral strength, especially if associated with hardening behavior, constitute a combined positive effect for the general performance of masonry buildings. In fact, higher lateral strength usually results in smaller inelastic amplification of the seismic displacement demand (Guerrini *et al.*, 2017, Guerrini *et al.*, 2021); however, care should be taken when choosing jacketing materials which add excessively to the lateral stiffness, as they may result in the opposite effect. Moreover, larger displacement capacity is typically associated with flexural than with shear failures, as recognized by building codes which provide deformation, drift or chord-rotation limitations for various failure modes of piers and spandrels (MIT, 2018, MIT, 2019).

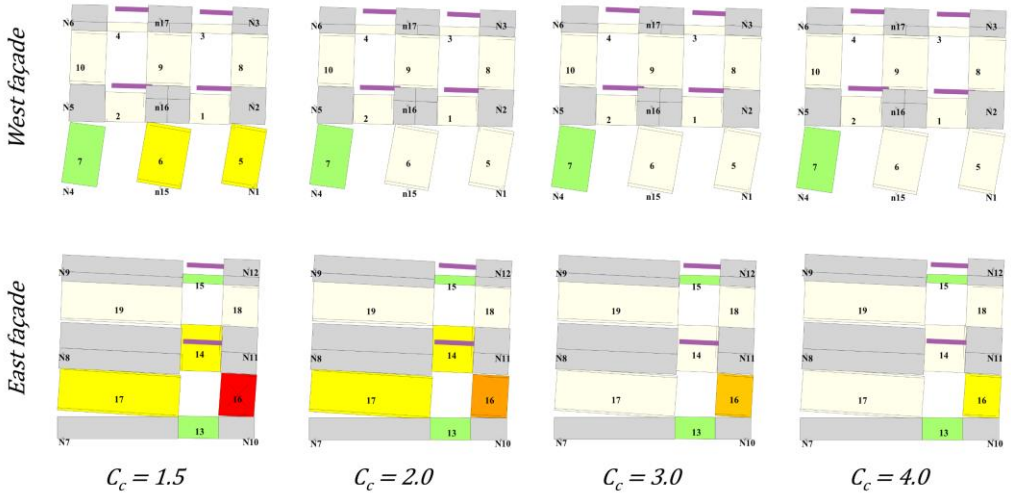

Figure 3.21: Comparison between damage patterns obtained with various correction coefficients for Building 2 neglecting any masonry tensile strength (with magnified lateral displacements).

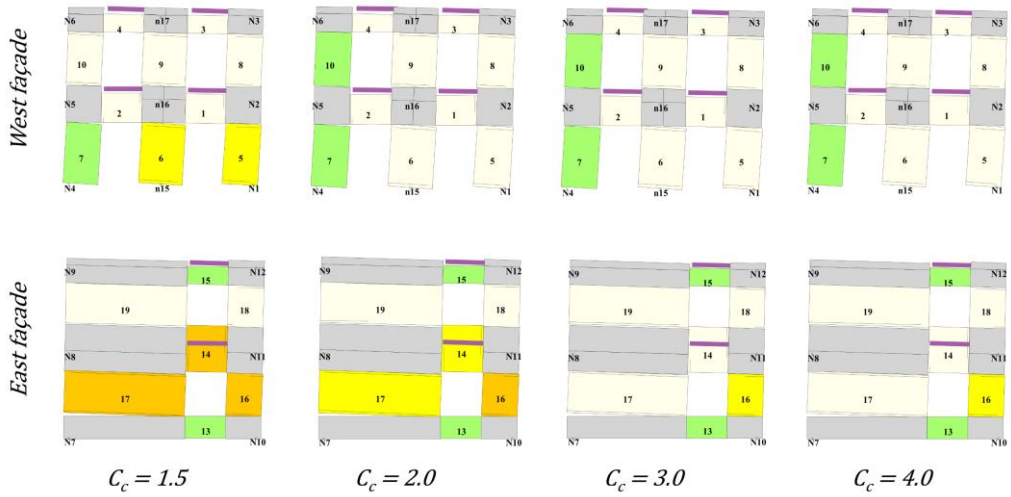

Figure 3.22: Comparison between damage patterns obtained with various correction coefficients for Building 3 neglecting any masonry tensile strength (with magnified lateral displacements).

3.4 SUMMARY AND CONCLUSIONS

This paper discussed the effectiveness of different seismic retrofit strategies for stone masonry buildings with flexible timber diaphragms, combining experimental and numerical findings.

Unidirectional incremental dynamic shake-table tests were performed on three full-scale two-story buildings, to prove the effectiveness of enhancing wall-to-diaphragm connections and increasing floor and roof diaphragm stiffness. A local out-of-plane overturning mechanism developed in the unstrengthened Building 1, but was inhibited by the selected interventions in Building 2 and Building 3. Moreover, the same lateral displacement demands were achieved under higher-intensity ground motion as connections were improved (Building 2 compared to Building 1) and diaphragms significantly stiffened (Building 3 compared to Building 2).

None of the specimens suffered from masonry disgregation, leaf delamination, or wall separation at corners, thanks to a combination of mortar binding quality, sharp-cornered stones, and the absence of loose filling, corresponding to good natural stone masonry. Generally, preliminary interventions may be required to address poor existing bond and constituents. Otherwise, connection improvement and diaphragm stiffening would result ineffective if the masonry walls could not resist the forces transferred locally.

Nonlinear pushover analyses were carried out on numerical three-dimensional models based on an equivalent frame approach. The software TREMURI was used for this scope. Nonlinear macroelements represented the in-plane behavior of masonry piers and spandrels, while linear elastic elements that of diaphragms and ring beams. This modeling strategy cannot capture out-of-plane local mechanisms and is appropriate for structures governed by a global response. Consequently, only Building 2 and Building 3 were analyzed; Building 1 was excluded because it exhibited out-of-plane overturning of walls.

Material properties were calibrated versus the experimental results from material and component characterization tests, which were conducted on samples and components constructed together with the building units. A good match was achieved between the numerical pushover curves and the experimental backbone curves, as well as between the simulated and observed damage patterns on the masonry elements.

The two numerical models were subsequently modified to simulate masonry mechanical upgrades, which could be achieved in practice through deep joint repointing or various types of jacketing among other techniques. Construction details of the masonry enhancement could not be explicitly modeled with the chosen equivalent-frame strategy, relying on macroelement discretization. Consequently, these solutions were simulated through correction coefficients applied to the masonry elastic moduli, compressive, tensile and shear strength, as suggested by the Italian building code.

It was shown that, as the shear tensile strength of piers increases, the overall lateral strength tends to saturate. In fact, failure of the two buildings transitioned from shear to flexural mechanisms, with the flexural strength limited by rigid-body equilibrium and nearly independent of material properties. However, flexural mechanisms are generally associated with larger displacement capacity than shear failures, while higher lateral strength results in smaller inelastic amplification of the displacement demand, if the elastic period does not increase excessively. Combining these two effects together is expected to have a net positive impact on the seismic performance of masonry buildings in general.

Special details can be implemented with jacketing techniques to provide tensile continuity with the foundation and across the floors. This condition was modeled by accounting for the axial tensile strength of the piers, and by applying to it the same correction coefficient used for the other material properties. The simultaneous enhancement of shear and axial tensile strength resulted in appreciable differences only on Building 2, characterized by more deformable diaphragms: its pushover curves exhibited more pronounced hardening compared to the case of zero-axial tensile strength. This additional strength would result in further reduction in the inelastic displacement amplification.

The experimental and numerical results of this study confirmed that the biggest benefit was achieved by improving wall-to-diaphragm connections, because this allowed one to prevent the local out-of-plane overturning of a wall, and by stiffening timber diaphragms. Masonry mechanical enhancement induced additional positive effects, but to a lesser extent. These outcomes constitute the basis for future developments related to the selection and design of appropriate seismic retrofit measures for stone masonry buildings. Among other aspects, the optimal quantification of the required connection strength and diaphragm stiffness will be of particular interest.

Author Contributions: Conceptualization, G.G. and A.P.; methodology, G.G. and C.S.; software, A. P.; validation, G.G. and I.S.; formal analysis, C.S.; investigation, G.G. and C.S.; resources, A.P.; data curation, G.G.; writing original draft preparation, G.G., C.S. and I.S.; writing review and editing, A.P.; visualization, I.S. and C.S.; supervision, A.P.; project administration, A.P.; funding acquisition, A.P. All authors have read and agreed to the published version of the manuscript.

Funding: The experimental program, forming the basis for this research, was funded by the Italian Department of Civil Protection through the 2005-2008 EUCENTRE Executive Project, the 2005-2008 ReLUIS Project Line 1, and the 2010-2013 ReLUIS Project Task AT1-1.1. The numerical study was conducted within the 2019-2021 ReLUIS Project W10 "Code contributions for existing masonry constructions", funded by the Italian Department of Civil Protection.

Data Availability Statement: Data can be made available upon request to the corresponding author.

Acknowledgments: The authors would like to gratefully acknowledge the valuable contributions of G. Magenes, A. Galasco, F. Graziotti, M. Rota, and M. Da Paré to the experimental program and preliminary numerical simulations.

Conflicts of Interest: The authors declare no conflict of interest. The funders had no role in the design of the study; in the collection, analyses, or interpretation of data; in the writing of the manuscript, or in the decision to publish the results.

REFERENCES

Benedetti, D., Carydis, P., and Pezzoli, P. (1998). Shaking Table Tests on 24 Simple Masonry Buildings. *Earthquake Engineering & Structural Dynamics*, 27(1), 67-70.

Binda, L., Cardani, G., and Saisi, A. (2005). A Classification of Structures and Masonries for the Adequate Choice of Repair. *In Proceedings of the International RILEM Workshop on Repair Mortars for Historic Masonry*, Delft, The Netherlands, 26-28.

Borri, A., Castori, G., and Grazini, A. (2009). Retrofitting of Masonry Building with Reinforced Masonry Ring-Beam. *Construction and Building Materials*, 23, 1892-1901.

Borri, A., Castori, G., and Corradi, M. (2011). Shear Behavior of Masonry Panels Strengthened by High Strength Steel Cords. *Construction and Building Materials*, 25, 494-503.

Bracchi, S., Rota, M., Penna, A., and Magenes, G. (2015). Consideration of modelling uncertainties in the seismic assessment of masonry buildings by equivalent-frame approach. *Bulletin of Earthquake Engineering,* 13(11), 3423–3448.

Brignola, A., Podestà, S., and Pampanin, S. (2008). *In-plane stiffness of wooden floor. In Proceedings of the 2008 New Zealand Society for Earthquake Engineering Conference*, Wairakei, New Zealand.

Calderini, C., Lagomarsino, S., Rossi, M., de Canio, G., Mongelli, M.L., and Roselli, I. (2014). Shaking Table Tests of an Arch-Pillars System and Design of Strengthening by the use of Tie-Rods. *Bulletin of Earthquake Engineering*, 13, 279-297.

Carocci, C. F. (2012). Small Centres Damaged by 2009 L'Aquila Earthquake: On Site Analyses of Historical Masonry Aggregates. *Bulletin of Earthquake Engineering*, 10(1), 45-71.

Carozzi, F. G., Bellini, A., D'Antino, T., de Felice, G., Focacci, F., Hojdys, Ł., Laghi, L., Lanoye, E., Micelli, F., Panizza, M., *et al.* (2017). Experimental Investigation of Tensile and Bond Properties of Carbon-FRCM Composites for Strengthening Masonry Elements. *Composites Part B: Engineering*, 128, 100-119.

Celik, O., Sesigur, H., and Cili, F. (2009). Importance of Wood and Iron Tension Members on Seismic Performance of Historic Masonry Buildings: Three Case Studies from Turkey. *In Proceedings of the ATC and SEI Conference on Improving the Seismic Performance of Existing Buildings and Other Structures*, San Francisco, CA, USA.

Corradi, M., Tedeschi, C., Binda, L., and Borri, A. (2008). Experimental Evaluation of Shear and Compression Strength of Masonry Wall before and after Reinforcement: Deep Repointing. *Construction and Building Materials*, 22, 463-472.

Costa, A. A., Arêde, A., Costa, A., Penna, A., and Costa, A. (2013a). Out-of-plane Behaviour of a Full Scale Stone Masonry Façade. Part 1: Specimen and Ground Motion Selection. *Earthquake Engineering & Structural Dynamics*, 42(14), 2081-2095.

Costa, A. A., Arêde, A., Costa, A., Penna, A., and Costa, A. (2013b). Out-of-plane Behaviour of a Full Scale Stone Masonry Façade. Part 2: Shaking Table Tests. *Earthquake Engineering & Structural Dynamics*, 42(14), 2097-2111.

D'Ayala, D. F., and Paganoni, S. (2011). Assessment and Analysis of Damage in L'Aquila Historic City Centre after 6th April 2009. *Bulletin of Earthquake Engineering*, 9(1), 81-104.

da Porto, F., Silva, B., Costa, C., and Modena, C. (2012). Macro-Scale Analysis of Damage to Churches after Earthquake in Abruzzo (Italy) on April 6, 2009. *Journal of Earthquake Engineering*, 16(6), 739-758.

Decanini, L., de Sortis, C.A., Goretti, A., Langenbach, R., Mollaioli, F., and Rasulo, A. (2004). Performance of Masonry Buildings during the 2002 Molise, Italy, Earthquake. *Earthquake Spectra*, 20 (Suppl. 1), 191-220.

De Felice, G., de Santis, S., Garmendia, L., Ghiassi, B., Larrinaga, P., Lourenco, P., Oliveira, D.V., Paolacci, F., and Papanicolaou, C.G. (2014). Mortar-Based Systems for Externally Bonded Strengthening of Masonry. *Materials and Structures*, 47, 2021-2037.

Del Zoppo, M., di Ludovico, M., and Prota, A. (2019). Analysis of FRCM and CRM Parameters for the In-Plane Shear Strengthening of Different URM Types. *Composites Part B: Engineering*, 171, 20-33.

European Committee for Standardization (2004a). Eurocode 5: Design of Timber Structures - Part 1-1: General - Common Rules and Rules for Buildings, EN 1995-1-1:2004; *European Committee for Standardization*: Brussels, Belgium.

European Committee for Standardization (2004b). Eurocode 2: Design of Concrete Structures - Part 1-1: General Rules and Rules for Buildings, EN 1992-1-1:2004; *European Committee for Standardization*: Brussels, Belgium.

European Committee for Standardization (2016a). Structural Timber - Strength classes, EN338:2016; *European Committee for Standardization*: Brussels, Belgium.

European Committee for Standardization (2016b). Timber structures - Strength graded structural timber with rectangular cross section - Part 1: General requirements, EN 14081-1:2016; *European Committee for Standardization*: Brussels, Belgium.

Frumento, S., Giovinazzi, S., Lagomarsino, S., and Podestà, S. (2006). Seismic Retrofitting of Unreinforced Masonry Buildings in Italy. *In Proceedings of the New Zealand Society for Earthquake Engineering Conference*, Napier, New Zealand.

Gattesco, N., Boem, I., and Dudine, A. (2014). Diagonal Compression Tests on Masonry Walls Strengthened with a GFRP Mesh Reinforced Mortar Coating. *Bulletin of Earthquake Engineering*, 13, 1703-1726.

Gattesco, N. and Boem, I. (2015). Experimental and Analytical Study to Evaluate the Effectiveness of an In-Plane Reinforcement for Masonry Walls using GFRP Meshes. *Construction and Building Materials*, 88, 94-104.

Guadagnuolo, M. and Faella, G. (2020). Simplified Design of Masonry Ring-Beams Reinforced by Flax Fibers for Existing Buildings Retrofitting. *Buildings*, 10(1), 12.

Graziotti, F., Magenes, G., and Penna, A. (2012). Experimental Cyclic Behaviour of Stone Masonry Spandrels. *In Proceedings of the 15th World Conference on Earthquake Engineering*, Lisbon, Portugal.

Guerrini, G., Graziotti, F., Penna, A., and Magenes, G. (2017). Improved evaluation of inelastic displacement demands for short - period masonry structures. *Earthquake Engineering and Structural Dynamics*, 46(9), 1411−1430.

Guerrini, G., Senaldi, I., Graziotti, F., Magenes, G., Beyer, K., and Penna, A. (2019). Shake-Table Test of a Strengthened Stone Masonry Building Aggregate with Flexible Diaphragms. *International Journal of Architectural Heritage*, 13, 1078-1097.

Guerrini, G., Kallioras, S., Bracchi, S., Graziotti, F., and Penna, A. (2021). Displacement demand for nonlinear static analyses of masonry structures: Critical review and improved formulations. *Buildings*, 11(3), 118.

Karantoni, F.V., and Fardis, M. (1992). Effectiveness of Seismic Strengthening Techniques for Masonry Buildings. *Journal of Structural Engineering*, 118, 1884-1902.

Lagomarsino, S. (2011). Damage Assessment of Churches after L'Aquila Earthquake (2009). *Bulletin of Earthquake Engineering*, 10(1), 79-92.

Lagomarsino, S., Penna, A., Galasco, A., and Cattari, S. (2013). TREMURI program: An equivalent frame model for the non-linear seismic analysis of masonry buildings. *Engineering Structures*, 56, 1787–1799.

Magenes, G., Penna, A., and Galasco, A. (2010a). A full-scale shaking table test on a two storey stone masonry building. *In Proceedings of the 14th European Conference on Earthquake Engineering*, Ohrid, Rep. of Macedonia.

Magenes, G., Penna, A., Galasco, A., and Rota, M. (2010b). Experimental characterization of stone masonry mechanical properties. *In Proceedings of the 8th International Masonry Conference*, Dresden, Germany.

Magenes, G., Galasco, A., Penna, A., and Da Paré, M. (2010c) "In-plane cyclic shear tests of undressed double leaf stone masonry panels. *In Proceedings of the 8th International Masonry Conference*, Dresden, Germany.

Magenes, G., Penna, A., Senaldi, I., Rota, M., and Galasco, A. (2014). Shaking table test of a strengthened full scale stone masonry building with flexible diaphragms. *International Journal of Architectural Heritage*, 8(3), 349–375.

Marino, S., Cattari, S., and Lagomarsino, S. (2019). Are the nonlinear static procedures feasible for the seismic assessment of irregular existing masonry buildings?. *Engineering Structures,* 200, 109700.

Mazzon, N., Chavez, C.M., Valluzzi, M.R., Casarin, F., and Modena, C. (2010). Shaking Table Tests on Multi-Leaf Stone Masonry Structures: Analysis of Stiffness Decay. *Advanced Materials Research*, 133–134, 647-652.

Ministry of Infrastructures and Transport (2018). Norme Tecniche per le Costruzioni, DM 17/01/2018; *Ministry of Infrastructures and Transport*: Rome, Italy (in Italian).

Ministry of Infrastructures and Transport (2019). Istruzioni per l'Applicazione dell'Aggiornamento delle "Norme Tecniche per le Costruzioni", Circ. 7 of 21/01/2019; *Ministry of Infrastructures and Transport*: Rome, Italy (in Italian).

Mirra, M., Ravenshorst, G., and van de Kuilen, J.W. (2020). Experimental and analytical evaluation of the in-plane behaviour of as-built and strengthened traditional wooden floors. *Engineering Structures,* 211, 110432.

Modena, C., Valluzzi, M.R., Garbin, E., and da Porto, F. (2004). A Strengthening Technique for Timber Floors using Traditional Materials. *In Proceedings of the 4th Structural Analysis of Historical Constructions Conference*, Padova, Italy.

Modena, C., Valluzzi, M.R., da Porto, F., and Casarin, F. (2011). Structural Aspects of The Conservation of Historic Masonry Constructions in Seismic Areas: Remedial Measures and Emergency Actions. *International Journal of Architectural Heritage*, 5, 539-558.

Moreira, S.M.T., Ramos, L.F., Oliveira, D.V., and Lourenco, P. (2014). Experimental Behavior of Masonry Wall-to-Timber Elements Connections Strengthened with Injection Anchors. *Engineering Structures*, 81, 98-109.

Moreira, S., Ramos, L.F., Oliveira, D.V., and Lourenco, P. (2016). Design Parameters for Seismically Retrofitted Masonry-to-Timber Connections: Injection Anchors. *International Journal of Architectural Heritage*, 10, 217-234.

Mouzakis, C., Adami, C. E., Karapitta, L., and Vintzileou, E. (2017). Seismic behaviour of timber-laced stone masonry buildings before and after interventions: Shaking table tests on a two-storey masonry model. *Bulletin of Earthquake Engineering*, 16, 803-829.

Nunes, M., Bento, R., and Lopes, M. (2020). In-plane stiffening and strengthening of timber floors for the improvement of seismic behaviour of URM buildings. *International Journal of Masonry Research and Innovation*, 5, 85.

Papanicolaou, C.G., Triantafillou, T.C., Karlos, K., and Papathanasiou, M. (2006). Textile-Reinforced Mortar (TRM) versus FRP as Strengthening Material of URM Walls: In-plane Cyclic Loading. *Materials and Structures*, 40, 1081-1097.

Penna, A., Lagomarsino, S., and Galasco, A. (2014). A nonlinear macro-element model for the seismic analysis of masonry buildings. *Earthquake Engineering and Structural Dynamics,* 43(2), 159–179.

Penna, A., Senaldi, I.E., Galasco, A., and Magenes, G. (2015). Numerical simulation of shaking table tests on full-scale stone masonry buildings. *International Journal of Architectural Heritage,* 10(2–3), 146–163.

Penna, A., Calderini, C., Sorrentino, L., Carocci, C. F., Cescatti, E., Sisti, R., Borri, A., Modena, C., and Prota, A (2019). Damage to Churches in the 2016 Central Italy Earthquakes. *Bulletin of Earthquake Engineering*, 17(10), 5763-5790.

Piazza, M., Baldessari, C., and Tomasi, R. (2008a). The Role of In-Plane Floor Stiffness in the Seismic Behaviour of Traditional Buildings. *In Proceedings of the 14th World Conference on Earthquake Engineering*, Beijing, China.

Piazza, M., Baldessari, C., Tomasi, R., and Acler, E. (2008b). Behaviour of refurbished timber floors characterized by different in-plane stiffness. *In Structural Analysis of Historic Construction: Preserving Safety and Significance*, D'Ayala, D., Fodde, E., Eds.; Taylor & Francis, London, UK; Vol 2, pp. 843–850.

Podestà, S., and Scandolo, L. (2019). Earthquakes and Tie-Rods: Assessment, Design, and Ductility Issues. *International Journal of Architectural Heritage*, 13, 329-339.

Prota, A., Marcari, G., Fabbrocino, G., Manfredi, G., and Aldea, C. (2006). Experimental In-Plane Behavior of Tuff Masonry Strengthened with Cementitious Matrix–Grid Composites. *Journal of Composites for Construction*, 10, 223-233.

Rota, M., Penna, A., Strobbia, C., and Magenes, G. (2011). Typological Seismic Risk Maps for Italy. *Earthquake Spectra*, 27(3), 907-926.

Senaldi, I., Magenes, G., Penna, A., Galasco, A., and Rota M. (2013). The effect of stiffened floor and roof diaphragms on the experimental seismic response of a full-scale unreinforced stone masonry building. *Journal of Earthquake Engineering*, 18(3), 407–443.

Senaldi, I. E., Guerrini, G., Comini, P., Graziotti, F., Penna, A., Beyer, K., and Magenes, G. (2020). Experimental Seismic Performance of a Half-Scale Stone Masonry Building Aggregate. *Bulletin of Earthquake Engineering*, 18(2), 609-643.

Sikka, S. and Chaudhry, C. (2009). Research on the Upgrade of Traditional Seismic Retrofits for Ancient Buddhist Temples in the Region of Spiti and Kinnaur in the Western Himalayas. *In Proceedings of the Getty Seismic Adobe Project 2006 Colloquium*, Los Angeles, CA, USA.

Sisti, R., Di Ludovico, M., Borri, A., and Prota, A. (2019). Damage Assessment and the Effectiveness of Prevention: The Response of Ordinary Unreinforced Masonry Buildings in Norcia during the Central Italy 2016–2017 Seismic Sequence. *Bulletin of Earthquake Engineering*, 17, 5609-5629.

Sorrentino, L., Catteri, S., da Porto, F., Magenes, G., and Penna, A. (2019). Seismic Behaviour of Ordinary Masonry Buildings during the 2016 Central Italy Earthquakes. *Bulletin of Earthquake Engineering*, 17(10), 5583-5607.

Tolles, E. L., Webster, F. A., Crosby, A., and Kimbro, E. E. (1996). Survey of Damage to Historic Adobe Buildings after the January 1994 Northridge Earthquake. *GCI Scientific Program Report*, Getty Conservation Institute, Los Angeles, CA, USA.

Tolles, E.L., Kimbro, E.E., Webster, F.A., and Ginell, W.S. (2000). Seismic Stabilization of Historic Adobe Structures. *Final Report of the Getty Seismic Adobe Project*, The Getty Conservation Institute: Los Angeles, CA, USA.

Tomaževič, M., Lutman, M., Weiss, P., and Velechovsky, T. (1991). The influence of Rigidity of Floors on the Seismic Behaviour of Old Stone-Masonry Buildings. *European Earthquake Engineering*, 3, 28–41.

Tomaževič, M., Lutman M., and Weiss, P. (1996). Seismic Upgrading of Old Brick-Masonry Urban Houses: Tying of Walls with Steel Ties. *Earthquake Spectra*, 12, 599-622.

Türkmen, Ö.S., de Vries, B.T., Wijte, S.N.M., and Vermeltfoort, A.T. (2020). In-Plane Behaviour of Clay Brick Masonry Wallettes Retrofitted with Single-Sided Fabric-Reinforced Cementitious Matrix and Deep Mounted Carbon Fibre Strips. *Bulletin of Earthquake Engineering*, 18, 725-765.

Turnšek, V. and Sheppard, P. (1980). The shear and flexural strength of masonry walls. *In Proceedings of the International Research Conference on Earthquake Engineering*, Skopje, Yugoslavia.

Turrini, G. and Piazza, M. (1983). Una tecnica di recupero statico dei solai in legno. *Recuperare 5*, 224–227 (in Italian).

Valluzzi, M.R., Binda, L., and Modena, C. (2002). Experimental and analytical studies for the choice of repair techniques ap-plied to historic buildings. *Materials and Structures,* 35(5), 285-292.

Valluzzi, M.R. (2006). On the Vulnerability of Historical Masonry Structures: Analysis and Mitigation. Mater. *Materials and Structures*, 40, 723-743.

Valluzzi, M.R., Garbin, E., Dalla Benetta, M., and Modena, C. (2010). In-plane Strengthening of Timber Floors for the Seismic Improvement of Masonry Buildings. *In Proceedings of the 11th World Conference on Timber Engineering*, Riva del Garda, Italy.

Vintzileou, E.N. and Toumbakari, E.E. (2001). The Effect of Deep Rejointing on the Compressive Strength of Brick Masonry. In *Historical Constructions*, Lourenço, P.B., Roca, P., Eds., University of Minho: Guimarães, Portugal, 995-1002.

Vintzileou, E., Mouzakis, C., Adami, C. E., and Karapitta, L. (2015). Seismic Behavior of Three-Leaf Stone Masonry Buildings before and after Interventions: Shaking Table Tests on a Two-Storey Masonry Model. *Bulletin of Earthquake Engineering*, 13, 3107-3133.

4. GLOBAL MODELING STRATEGIES FOR MASONRY BUILDINGS WITH TIMBER DIAPHRAGMS UNDER SEISMIC ACTIONS

Salvatori, C., Guerrini, G., Senaldi, I. E., and Penna, A. (2023). Global Modeling Strategies for Masonry Buildings with Timber Diaphragms under Seismic Loadings. *Procedia Structural Integrity, XIX ANIDIS Conference, Seismic Engineering in Italy*, Turin, Italy, 44, 520-527. doi:10.1016/j.prostr.2023.01.068

ABSTRACT

This paper discusses the effects of different modeling strategies on the simulated global response of masonry buildings with timber diaphragms under earthquake excitation. The benchmark for this study was provided by a unidirectional dynamic shake-table test on a three-story, half-scale natural stone masonry building aggregate, incorporating the main architectural and structural features of the historical center of Basel (Switzerland). The global response of the specimen was simulated through nonlinear static analyses using an equivalent frame approach, with nonlinear macroelements for masonry members and linear orthotropic membranes for diaphragms. Three modeling strategies were followed. First, an unconventional modeling strategy was adopted, to implement explicitly the out-of-plane stiffness of walls orthogonal to the shaking direction through a particular combination of equivalent frames and membranes. The second option consisted of a 3D model with walls in both directions and finite-stiffness diaphragms, however neglecting the out-of-plane overturning response of walls. In the third case, given their low stiffness compared to masonry walls, the timber diaphragms were considered infinitely flexible and single-wall 2D models were analyzed in the shaking direction. Numerical capacity curves were compared to experimental backbone curves, showing satisfactory accuracy even when diaphragm and out-of-plane wall stiffness were neglected.

Keywords: equivalent-frame model; flexible timber diaphragm; nonlinear macroelement; nonlinear static analysis; out-of-plane response; seismic performance; natural stone masonry.

4.1 INTRODUCTION

Equivalent-frame modeling approaches are widely accepted for the global analysis of masonry buildings. Unlike more refined methods, this modeling technique allows a

reasonable compromise between accuracy of results and computational effort. However, a common assumption whenever adopting this modeling technique is not to account for the out-of-plane response of masonry walls, with the underlying assumption that it is effectively inhibited by construction details or retrofit interventions. However, this assumption may be questioned in case of flexible and/or poorly connected diaphragms.

For this reason, three modeling strategies were considered and compared to the experimental results of a unidirectional, incremental dynamic shake-table test on a three-story, half-scale natural stone masonry building aggregate (Guerrini *et al.*, 2019; Senaldi *et al.*, 2020). The first option involved a complete three-dimensional model of the experimental prototype, with an unconventional strategy to explicitly account for the out-of-plane stiffness and strength of the walls orthogonal to the shaking direction (Kallioras *et al.*, 2019). The second one, following the common practice, ignored this out-of-plane behavior. Finally, the third solution aimed at simulating an infinitely flexible diaphragm condition, resulting in single-wall 2D models of the façades parallel to the shaking direction.

Experimental and numerical outcomes were compared in terms of backbone and pushover curves, respectively, to quantify the influence of the out-of-plane behavior on the global response and to further validate the single-wall modeling approach in case of flexible diaphragms, suggested by national and international building codes (ASCE 2017; MIT 2018).

4.2 BENCHMARK EXPERIMENTAL CAMPAIGN

The adopted modeling strategies were evaluated with reference to a half-scale masonry building specimen tested on the shake table at the EUCENTRE Laboratories in Pavia, Italy, within a comprehensive research project aiming at the seismic vulnerability assessment of the historical center of Basel, CH, (Guerrini *et al.*, 2019; Senaldi *et al.*, 2020). The specimen consisted of an aggregate of two adjacent three-story, weakly connected structural units, characterized by different roof heights and sharing a transverse party wall (Figure 4.1).

The dimension of the EUCENTRE shake-table imposed constructing the prototype at half scale ($\lambda = 0.5$). To obtain physically sound results, the similitude relationship discussed by Senaldi *et al.* (2020) was adopted, where material densities and accelerations were not to be affected. For this purpose, the same $\lambda = 0.5$ factor was applied to lengths and stresses, whereas a $\lambda^{1/2} = 0.707$ coefficient had to be used to scale time and period parameters.

4.2.1 Geometry and details

The specimen consisted of five walls: the East and West ones oriented along the shaking direction, and the North, Centre, and South ones arranged transversely. All the façades

presented several openings, except for the South and Central ones, which were completely solid. The entire prototype was 5.79-m-large and 5.58-m-wide, with the roof ridges at about $6.65\ m$ and $7.60\ m$ above the foundation level for the North and South units, respectively (Figure 4.1).

Construction details of the historical center of Basel were reproduced. Walls consisted of double-leaf undressed stone masonry and river pebbles, with a thickness starting from $35\ cm$ at the first story and decreasing to $25\ cm$ at the third one. Through stones provided a better connection between the masonry leaves only at opening edges and corners. Flexible timber diaphragms were adopted for floors and roofs.

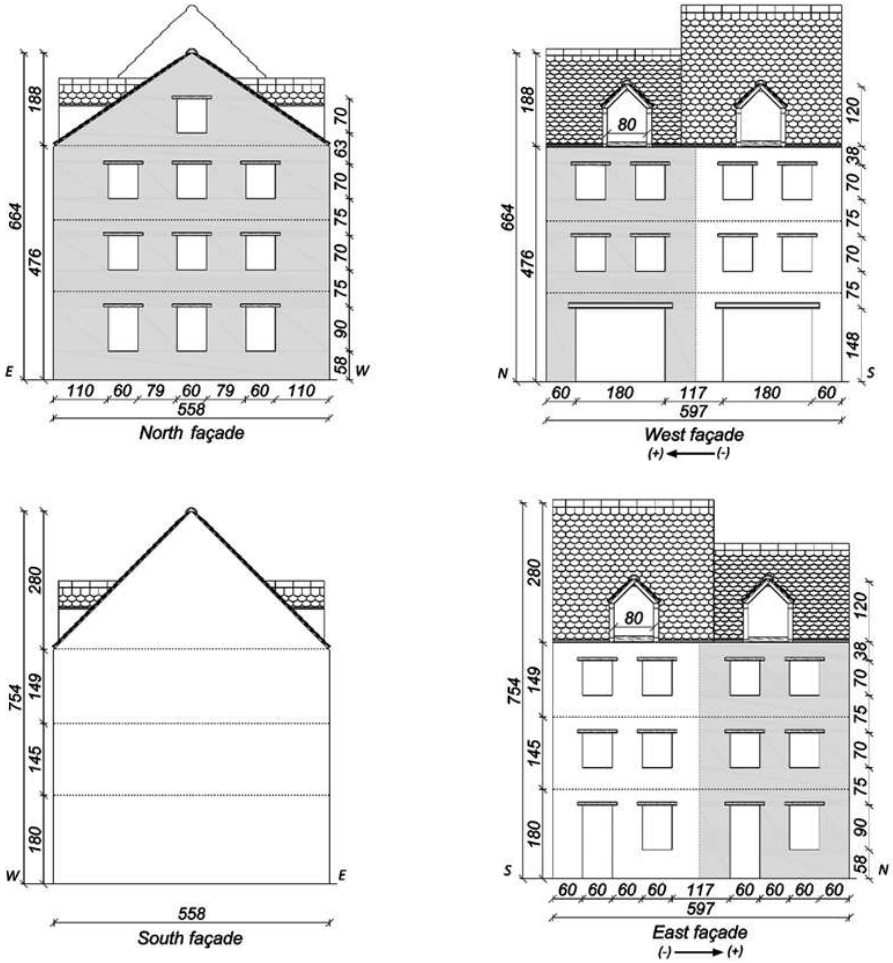

Figure 4.1: Dimensions of the half-scale masonry building aggregate specimen.

Three-dimensional timber frames, consisting of trusses and diagonal braces, constituted the roof structure, whereas $10 \times 16\,cm$ timber joists with a single $2\text{-}cm$-thick layer of planks formed the flooring systems. The joists of the first two floors were arranged in the shaking direction (North-South), while the roof trusses were oriented orthogonally (East-West). The truss tie beams acted as joists for the third floor, spanning perpendicular to the shaking direction.

Most building aggregates originated from a linear growth along the street. Consequently, the connection between adjacent units might be weak and vulnerable to local damage due to their mutual interaction. To reproduce a similar situation, the North (shortest) unit of the specimen was built first, whereas the South (tallest) unit was realized with some delay, providing a through-stone every third masonry course.

4.2.2 Material properties and masses

Complementary characterization tests on materials and components constituting the prototype were conducted at the University of Pavia (Guerrini *et al.*, 2017). Vertical and diagonal compression tests allowed evaluating the mean Young's modulus ($3460\,MPa$), shear modulus ($1520\,MPa$ from vertical and $1900\,MPa$ from diagonal compression), Poisson's ratio (0.14), compressive strength ($1.30\,MPa$) and tensile strength ($0.17\,MPa$). Moreover, cyclic shear-compression tests were performed on masonry piers (Senaldi et al, 2018).

The double-leaf stone masonry had an average density of $1980\,kg/m^3$. In addition to the self-weight of walls and diaphragms, mortar bags were evenly distributed over each floor level to emulate superimposed dead and live loads without influencing their stiffness.

4.2.3 Testing protocol

The shake-table input consisted of a series of ground motion records to simulate increasing levels of intensity, up to ultimate conditions of the specimen. Three different natural accelerograms were chosen. The first two were low-intensity records from recent seismic events in Basel and Linthal, CH, respectively, and were applied with their actual acceleration amplitude. The third signal came from the Ulcinj station during the 1979, $M_w\,6.9$ Montenegro earthquake, with PGA of $0.224\,g$, and was selected due to its spectral displacement compatibility with the 475-years-return-period design spectrum for Basel; it was applied scaling its acceleration amplitude from 25% to 175% in increments of 25%. The time step of all records was compressed by a factor $\lambda^{1/2} = 0.707$ to satisfy the chosen similitude relationship.

4.3 NUMERICAL SIMULATIONS

The response of the specimen was simulated through nonlinear static (pushover) analyses with the equivalent frame modeling approach implemented in the software TREMURI (Lagomarsino *et al.*, 2013). Advanced and conventional 3D models, as well as single-wall 2D models, were analyzed to assess the influence of explicitly modeling the walls excited out-of-plane and the diaphragm stiffness.

4.3.1 In-plane masonry macroelement

The overall behavior of a building can be obtained by assembling vertical walls and horizontal diaphragms, considering only their in-plane strength and stiffness contributions (Figure 4.2a). Within the equivalent frame modeling framework, each wall is discretized into macroelements capable of simulating the response of piers and spandrels, and rigid nodes, which define portions of masonry less sensitive to deformations and damage (Figure 4.2b and Figure 4.2c).

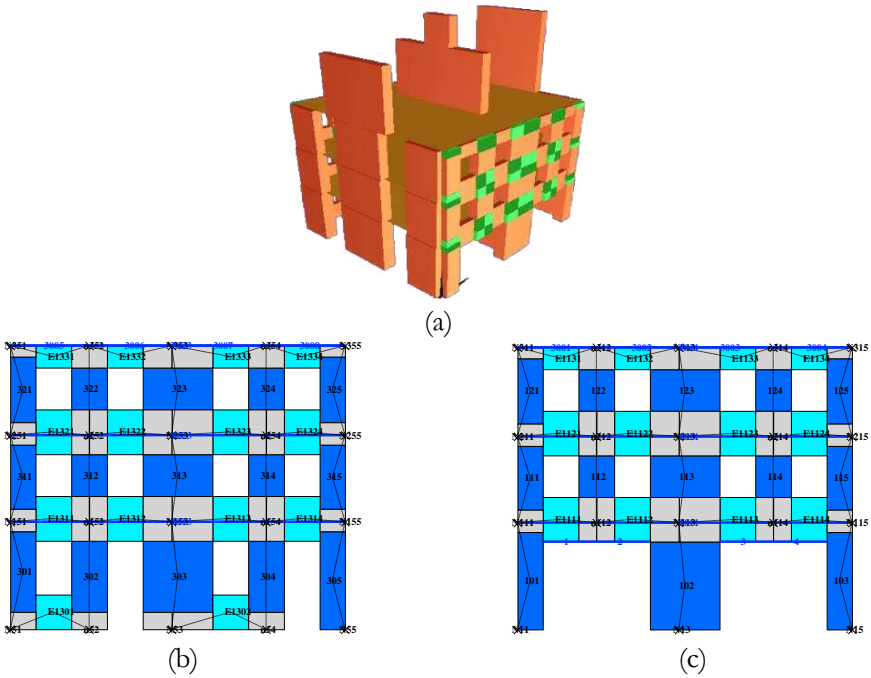

Figure 4.2: Numerical model: (a) overall 3D model; (b) East façade equivalent frame; (c) West façade equivalent frame.

In this work, the two-dimensional macroelement proposed by Penna *et al.* (2014) and the improved version described by Bracchi *et al.* (2021) and Bracchi and Penna (2021) were adopted to model spandrel and pier elements, respectively. In fact, the capability of these macroelements to capture the main failure mechanisms of a masonry panel, together with their analytically integrated formulation, make them particularly suitable for performing static and dynamic analyses.

Macroelement mechanical properties were calibrated against the nonlinear response of piers subjected to in-plane quasi-static cyclic shear-compression tests (Senaldi *et al.*, 2018), and are summarized in Table 4.1. This required increasing the compressive (f_c) and tensile (f_t) strengths by factors of 2.75 and 1.1 respectively, and dividing the Young's modulus (E) by a factor of 1.5. The shear modulus was taken as $G = 0.3E$. Because the macroelement by Penna *et al.* (2014) concentrates flexural deformations at the member ends, multiplying the Young's modulus by 3.0 was necessary in order to capture the correct stiffness. Moreover, the macroelement by Penna *et al.* (2014) requires dividing the shear modulus by the shear factor $\chi = 1.2$, as it considers the full cross-section also in shear.

The Turnšek and Sheppard's (1980) criterion was adopted for the shear strength. Since the shear formulation of the Penna *et al.* (2014) macroelement is based on a Coulomb-like criterion, equivalent cohesion (c_{eq}) and friction coefficient (μ_{eq}) had to be provided by linearizing the desired criterion at the static axial compression. On the other hand, the improved version proposed by Bracchi and Penna (2021) is able to calibrate such parameters automatically; therefore, the tensile strength of masonry (f_t) was directly assigned. Finally, parameters Gc_t and β, which govern the nonlinear shear response at and beyond the peak strength, complete the description of the macroelements.

Table 4.1: Parameters for the masonry macroelements.

Element	f_c $[MPa]$	f_t $[MPa]$	E $[MPa]$	G $[MPa]$	ρ $[kg/m^3]$	c_{eq} $[MPa]$	μ_{eq} $[-]$	Gc_t $[-]$	β $[-]$
Piers	3.58	0.187	2310	690	1950	-	-	10	0.5
Spandrels	3.58	-	6930	575	1950	0.17	0.15	10	0.0

4.3.2 Floor and roof diaphragms

Timber floor diaphragms were simulated through four-node linear-elastic orthotropic membranes. These finite elements are thoroughly characterized by defining the Young's modulus in the principal (E_1) and orthogonal (E_2) direction, the Poisson's coefficient (ν), and the shear modulus (G_{12}), which mainly influences the capability of redistributing lateral forces among masonry walls.

The diaphragms of the specimen consisted of a single layer of planks nailed to the floor joists or to the tie-beams of the roof trusses. The membranes were assigned the thickness of the planks and the equivalent stiffness properties from equation (4.1). The shear modulus was calculated according to Brignola *et al.* (2009), considering the three in-series contributions of flexural and shear deformation of planks, and the rigid rotation of planks due to nail slip:

$$\begin{cases} E_1 = \dfrac{E_t\, A_j}{t_p\, i_j} + E_t \\ E_2 = E_t \\ G_{12} = \dfrac{\chi}{A_p}\left(\dfrac{L_p}{k_{ser}\, s_n^2} + \dfrac{\chi}{G_t\, A_p} + \dfrac{L_p^2}{12\, E_t\, I_p}\right)^{-1} \end{cases} \tag{4.1}$$

where A_j and i_j are the cross-section area and the spacing of the floor joists or roof tie-beams; t_p, A_p, I_p, and L_p are the thickness, cross-section area, moment of inertia, and length of a plank; $\chi = 1.2$ is the shear factor; $E_t = 10\ GPa$ and $G_t = 0.75\ GPa$ are the assumed Young's and shear modulus of timber; and $s_n = 9\ cm$ is the nail spacing. $k_{ser} = 678.7\ kN/m$ has been calculated according to Eurocode 5 (CEN, 2004) for 3-mm-diameter nails without pre-drilling, assuming a timber density of $415\ kg/m^3$. Table 4.2 summarizes the membrane properties.

The stiffness of each roof pitch was simulated by a pair of diagonal linear truss elements of cross-section area:

$$A_t = \frac{k_{db,H}\, L_t}{4\, E_t \cos^2(\alpha_t)} \tag{4.2}$$

where L_t ($4.43\ m$ and $5.00\ m$) and α_t (49.4° and 51.2°) are the length of a truss element and its angle with respect to the shaking direction; $E_t = 10\ MPa$ its Young's modulus; and $k_{db,H}$ ($3331\ kN/m$ and $2441\ kN/m$) the lateral stiffness of the actual roof structures (Salvatori, 2020), calibrated against the experimental response through nonlinear dynamic analyses. This resulted in areas of $8.35\ cm^2$ and $7.71\ cm^2$ for the North and South units, respectively.

Table 4.2: Parameters for the masonry macroelements.

Diaphragm	A_j $[cm^2]$	i_j $[cm]$	t_p $[cm]$	L_p $[cm]$	A_p $[cm^2]$	I_p $[cm^4]$	E_1 $[MPa]$	E_2 $[MPa]$	G_{12} $[MPa]$
1st and 2nd floor	160	53	2	53	240	288	25063	10000	25.48
3rd floor - North	200	48	2	48	240	288	10000	30921	28.32
3rd floor - South	200	43	2	43	240	288	10000	33166	31.35

4.3.3 Advanced 3D model

During the incremental shake-table test, the specimen exhibited the activation of an out-of-plane overturning mechanism of the façades orthogonal to the shaking direction. However, a common assumption with equivalent-frame modeling is not to account for this mode of response, assuming implicitly that it is inhibited by original or retrofit details. To better reproduce the complete experimental behavior, an unconventional strategy was employed.

The transverse walls were subdivided in: (i) edge macroelements working in their planes, connected with the longitudinal façades at the intersections, to capture the so-called flange effect; and (ii) inner macroelements oriented perpendicular to the transverse walls, belonging to a fictitious wall $P6$ along the shaking direction, to model the vertical out-of-plane behavior (Figure 4.3a and Figure 4.3b). Horizontal truss elements completed the equivalent frame of fictitious wall $P6$. The longitudinal stiffness of the floor diaphragms was equally distributed between the 4-node membranes and these truss elements. Additional vertical and horizontal beam elements were assigned to the transverse walls, to make-up for the in-plane stiffness of the masonry portions attributed to the out-of-plane piers (Salvatori, 2020).

The horizontal flexural stiffness of the walls excited out of plane was represented by three-node linear-elastic orthotropic membranes at each level (Figure 4.3c). Their shear modulus (G_{eq}) was calculated by equating the elastic shear stiffness of the membrane to the flexural stiffness of the wall portion resisting horizontal bending:

$$G_{eq} = \beta \left(\frac{E \, \chi \, \bar{h} \, t^3}{6 \, s \, b \, L^2} \right) \tag{4.3}$$

where $E = 2310 \, MPa$ is the elastic modulus assigned to the masonry; t and $\bar{h}$ are the thickness and the height of the wall portion involved in the mechanism; $\chi = 1.2$ is the shear

factor; L is half the length of the transverse wall; b is the distance between consecutive out-of-plane walls; and $s = 2\ cm$ is the membrane thickness. Coefficient β depends on the boundary conditions, ranging from 3 (simply-supported) to 12 (double-fixed); values of 9, 12, and 6 were assigned to the membranes for the North (A), Center (B, C), and South (D) walls, respectively, from calibration through nonlinear dynamic analyses (Salvatori, 2020). The main properties of these membranes are summarized in Table 4.3.

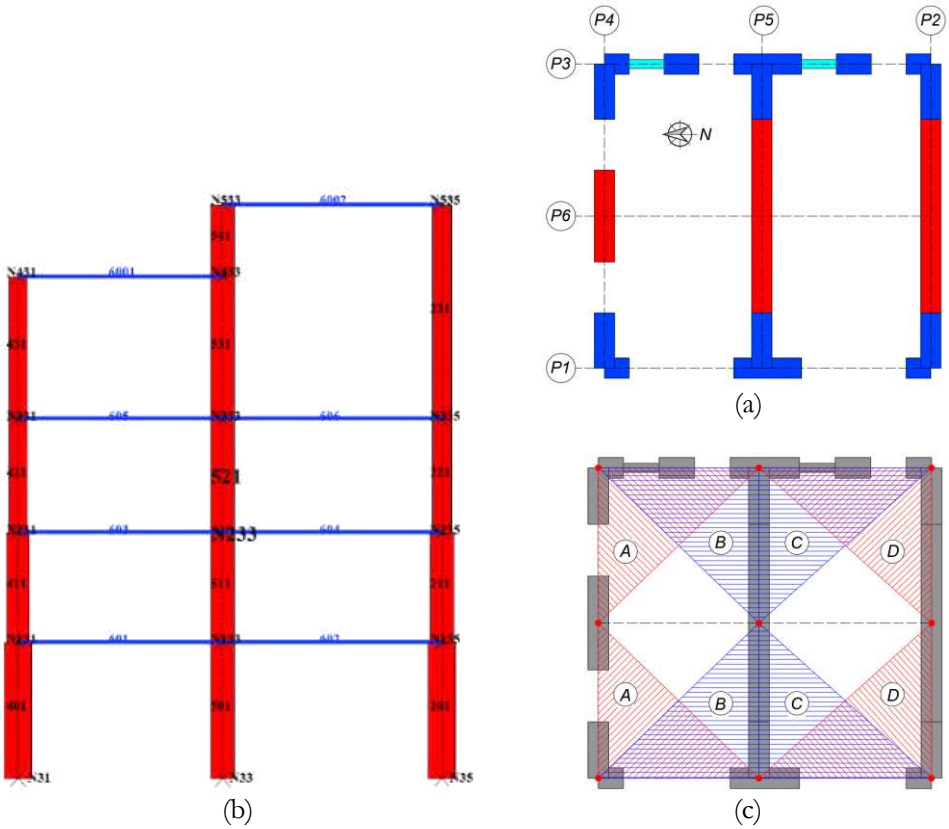

Figure 4.3: Out-of-plane modeling: (a) plan view with piers of fictitious wall P6 in red; (b) fictitious frame for wall P6; (c) triangular membranes.

Table 4.3: Parameters for the out-of-plane three-node orthotropic membranes.

Label	b $[cm]$	L $[cm]$	1st floor			2nd floor			3rd floor		
			$\bar{h}$ $[cm]$	t $[cm]$	G_{eq} $[MPa]$	$\bar{h}$ $[cm]$	t $[cm]$	G_{eq} $[MPa]$	$\bar{h}$ $[cm]$	t $[cm]$	G_{eq} $[MPa]$
A	271	262	75	15	28	75	15	28	37	15	14
B	271	262	163	30	328	148	30	298	75	30	151
C	291	262	163	30	306	148	30	277	75	30	141
D	291	262	163	30	306	148	25	161	75	25	82

4.3.4 Conventional 3D model

The second strategy consisted of following the common modeling practice, that is, neglecting the out-of-plane response of masonry walls. In this context, all elements of the unconventional approach explained above, such as the fictitious frame of wall $P6$, the additional vertical beam elements, and the three-node membranes were omitted. The transverse walls were explicitly discretized in piers, spandrels, and nodes, following the actual opening layout.

4.3.5 Single-wall 2D models

Starting from the conventional 3D model, the two façades (East and West) parallel to the shaking direction were extracted to perform 2D single-wall nonlinear static analyses. Macroelements were added at the intersection with each transverse wall, to capture the flange effect. The length of these flanges was equal to half the length of the South and Central walls. For the North façade, only the vertical strip bounded by the first opening alignment was included.

Horizontal truss elements were modeled with half the longitudinal stiffness of the floor diaphragms. Moreover, additional masses were introduced to consider the out-of-plane contributions of the North wall central strip and of the three gables, not explicitly modeled. The contribution of the North wall and gable had to be considered in terms of dynamic mass only, because their weight was independently transferred to the ground; for this reason, the vertical forces generated by their masses were canceled out by applying upwards static forces.

4.4 COMPARISON BETWEEN NUMERICAL AND EXPERIMENTAL RESULTS

Nonlinear pushover analyses were performed on all 3D and single-wall 2D models, considering two different horizontal force distributions. The first, named "uniform", consisted of a force distribution proportional to the nodal masses, whereas the second one, termed "modal", represented a first-mode-type force distribution, with forces proportional

to the product of the nodal masses times their height above the base. In the following figures, results from the 3D model with the out-of-plane unconventional approach are labeled "OOP". Drift limits of 3% and 1% were assigned to both piers and spandrels for flexural and shear failure, respectively, according to the experimental behavior of masonry piers subjected to complementary in-plane cyclic shear-compression tests (Senaldi *et al.*, 2018).

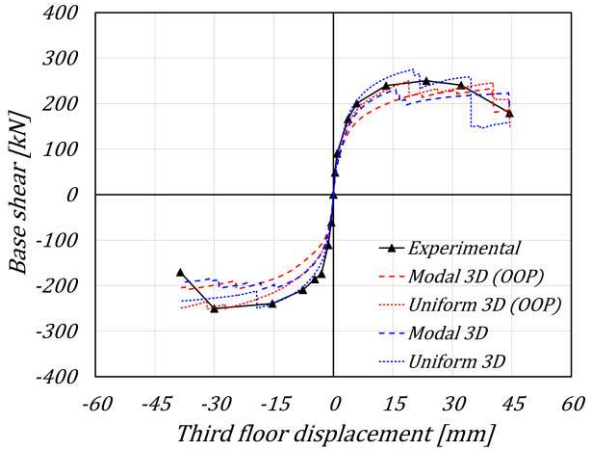

Figure 4.4: Comparison between numerical and experimental results: entire building.

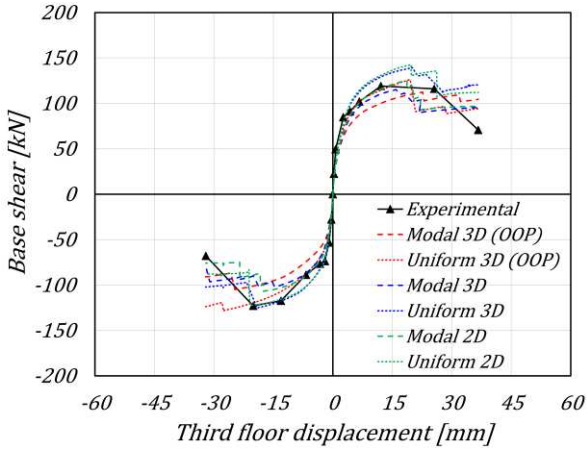

Figure 4.5: Comparison between numerical and experimental results: East façade.

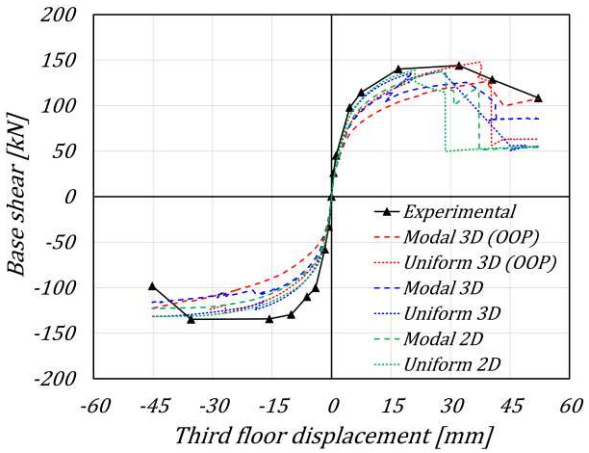

Figure 4.6: Comparison between numerical and experimental results: West façade.

Numerical and experimental results were compared in terms of capacity and backbone curves, respectively. The latter were derived as the envelope of the hysteretic responses of each dynamic test, taking the point of maximum base shear with the associated average third-floor displacement. The overall experimental base shear was determined by summing the inertia contributions at each accelerometer location, as the product between the recorded acceleration and its tributary mass. For 2D analysis discussion the average displacement was calculated for each individual façade; the base shear was evaluated from the masses of that façade, plus half the out-of-plane contributions of the transverse walls.

Figure 4.4 compares the global response from both 3D models to the experimental one. For this building, the modal force distribution underestimated the initial stiffness and, in the negative verse, also the lateral strength. Instead, the uniform one provided better results and successfully caught the degrading behavior due to the failure mechanisms. With this force distribution, explicitly modeling the out-of-plane response led to a particularly good prediction in the positive direction, with a little stiffness underestimation in the negative one. On the other hand, the conventional 3D model resulted in a minor strength overestimation in the positive verse, while yielding more accurate results in the negative one.

Figure 4.5 and Figure 4.6 show the comparison between numerical and experimental responses for the individual East and West walls. For each façade, the total base shear of its piers was plotted against its third-floor mean displacement; in the unconventional 3D model, the out-of-plane force contributions were distributed evenly among the two longitudinal walls. Again, the uniform force distribution resulted in better accuracy than the modal one. For both walls, the capacity curves from 2D models were very close to the corresponding ones extracted from the conventional 3D model.

Focusing on the uniform distribution results, both 3D models provided good agreement with the experimental backbone curve for the East wall. Moreover, despite the two large openings in the first story introduced a source of irregularity, the numerical models proved reasonably accurate also in predicting the West façade response; in this case, the 3D model with out-of-plane features underestimated the stiffness slightly more than the conventional 3D or single-wall 2D models.

4.5 CONCLUSIONS

This paper discussed the numerical simulation of the experimental response of a masonry building aggregate with timber floors and roofs subjected to a unidirectional incremental dynamic shake-table test. Two structural units constituted the specimen, which incorporated structural and architectural features of the historical center of Basel, CH. The test was simulated by nonlinear static (pushover) analyses, adopting the equivalent-frame approach implemented in the software TREMURI, with nonlinear macroelements for masonry members and linear orthotropic membranes or truss elements for floor or roof diaphragms, respectively.

Three modeling strategies were followed. An unconventional strategy was implemented in the first 3D model, partially calibrated through nonlinear dynamic analyses; this intended to capture both the in-plane and out-of-plane behavior of walls and to fully describe the experimental response, with the activation of local overturning mechanisms of façades orthogonal to the shaking direction. The second 3D model followed the common practice of neglecting the out-of-plane response of masonry walls. Given the low shear stiffness of floor and roof diaphragms, the third strategy involved single-wall 2D models of the façades arranged along the shaking direction.

Pushover capacity curves were compared to the experimental backbone curves. Both advanced and conventional 3D models simulated well the experimental response adopting a uniform lateral force distribution. In fact, although the conventional model slightly overestimated the strength in one loading verse, it better matched the stiffness in the other one, with some differences when looking at the full building or at each longitudinal wall results. Also analyzing single-wall 2D models with the assumption of infinitely flexible diaphragms provided reasonable results, aligned with those extracted from the conventional 3D model.

This work demonstrated the validity of two common modeling assumptions for the global seismic analysis of masonry buildings. Neglecting the out-of-plane wall response did not affect the accuracy of the results, provided local collapse was no reached. Single-wall 2D analysis was justified by the low stiffness of timber diaphragms. Future investigations will extend this study to nonlinear dynamic analyses and more articulated aggregate layouts.

Acknowledgements

This work stems from the project "Seismic assessment of natural stone masonry buildings in Basel – A research and training project", jointly carried by the École Polytechnique Fédérale de Lausanne and the University of Pavia, which was supported by the Swiss Federal Office for the Environment and the Construction Department of the Canton Basel-Stadt. The modeling activity was funded by DPC-ReLUIS (2022-2024) Work Package 10 "Modelli di capacità locali e globali per la definizione degli stati limite, definiti in funzione del metodo di analisi".

REFERENCES

American Society of Civil Engineers (ASCE). (2017). Seismic Evaluation and Retrofit of Existing Buildings; ASCE 41-17. *American Society of Civil Engineers*, Reston, VA, USA.

Bracchi, S., Galasco, A., and Penna, A. (2021). A Novel Macroelement Model for the Nonlinear Analysis of Masonry Buildings. Part 1: Axial and Flexural Behavior. *Earthquake Engineering & Structural Dynamics*, 50(8), 2233-2252.

Bracchi, S. and Penna, A. (2021). A Novel Macroelement Model for the Nonlinear Analysis of Masonry Buildings. Part 2: Shear Behavior. *Earthquake Engineering & Structural Dynamics*, 50(8), 2212-2232.

Brignola, A., Pampanin, S., and Podestà, S. (2009). Evaluation and control of the in-plane stiffness of timber floors for the performance-based retrofit of URM buildings. *Bulletin of the New Zealand Society for Earthquake Engineering*, 42(3), 204-221.

European Committee for Standardization (CEN). (2004). Eurocode 5: Design of timber structures - Part 1: General - Common rules and rules for buildings; EN 1995-1-1:2004. *European Committee for Standardization*, Brussels, Belgium.

Guerrini, G., Senaldi, I., Scherini, S., Morganti, S., Magenes, G., Beyer, K., and Penna, A. (2017). Material characterization for the shaking-table test of the scaled prototype of a stone masonry building aggregate. *In Proceedings of the 17th ANIDIS Conference*, Pistoia, Italy.

Guerrini, G., Senaldi, I., Graziotti, F., Magenes, G., Beyer, K., and Penna, A. (2019). Shake-Table Test of a Strengthened Stone Masonry Building Aggregate with Flexible Diaphragms. *International Journal of Architectural Heritage*.

Kallioras, S., Graziotti, F., and Penna, A. (2019). Numerical assessment of the dynamic response of a URM terraced house exposed to induced seismicity. *Bulletin of Earthquake Engineering*, 17(3), 1521-1552.

Lagomarsino, S., Penna, A., Galasco, A., and Cattari, S. (2013). TREMURI program: an equivalent frame model for the nonlinear seismic analysis of masonry buildings. *Engineering Structures*, 56, 1787-1799.

Ministry of Infrastructures and Transport (MIT). (2018). Norme Tecniche per le Costruzioni; DM 17/01/2018. *Ministry of Infrastructures and Transport*: Rome, Italy (in Italian).

Penna, A., Lagomarsino, S., and Galasco A. (2014). A nonlinear macroelement model for the seismic analysis of masonry buildings. *Earthquake Engineering & Structural Dynamics*, 43(2), 159-179.

Salvatori, C. (2020). Simulazione Numerica della Risposta Sismica di Aggregati Edilizi in Muratura di Pietra. *Master Thesis*, University of Pavia, Pavia, Italy (in Italian).

Senaldi, I., Guerrini, G., Scherini, S., Morganti, S., Magenes, G., Beyer, K., and Penna, A. (2018). Natural stone masonry characterization for the shaking-table test of a scaled building specimen. *In Proceedings of the 10th International Masonry Conference*, Milan, Italy.

Senaldi, I., Guerrini, G., Comini, P., Graziotti, F., Penna, A., Beyer, K., and Magenes, G. (2020). Experimental seismic performance of a half-scale stone masonry building aggregate. *Bulletin of Earthquake Engineering*, 18(2), 609-643.

Turnšek, V. and Sheppard, P. (1980). The Shear and Flexural Resistance of Masonry Walls. Proceedings of the International Research Conference on Earthquake Engineering. Skopje, Yugoslavia.

5. A NOVEL MACROELEMENT FOR THE SEISMIC ANALYSIS OF MASONRY STRUCTURES

5.1 INTRODUCTION

This section describes a novel macroelement for the seismic analysis of masonry structures. Firstly, an overview of the two-dimensional macroelement of Penna *et al.* (2014) is given, as it lays the basis for the development of the proposed three-dimensional formulation. A limited description of the shear behavior is reported, as no significant improvements or changes are made with respect to the original version. Conversely, the coupled axial-flexural response is comprehensively reviewed and discussed, highlighting its advantages, simplifications, and limitations. Consequently, enhancements of the original axial-flexural formulation are proposed: the first regards an additional nonlinear correction to improve the accuracy of the analytical integration of the end-interfaces in capturing toe-crushing phenomena. Then, an elasto-fragile tensile strength is analytically integrated over the length of the macroelement to replace the original no-tension constitutive law.

The following part of the chapter involves the extension of the improved two-dimensional macroelement to the three-dimensional space. In fact, the common assumption when adopting the equivalent-frame modeling strategy is to consider only the in-plane stiffness and strength of the macroelements. However, the out-of-plane behavior might be relevant and, consequently, significantly influence the in-plane response, even when local mechanisms are inhibited. For this purpose, an out-of-plane discretization of the end-interfaces of the macroelement is implemented to incorporate the biaxial bending while preserving the computational efficiency of the formulation. The procedure to compute the three-dimensional rotation matrix associated with the novel macroelement is also given.

To conclude, the system of equations that governs the nonlinear response of the three-dimensional macroelement is solved through an adaptive iterative algorithm. In fact, the full Newton-Rapson method is first discussed. Subsequently, an adaptive version to achieve a high convergence rate while preserving numerical robustness is proposed.

All the improvements to the original two-dimensional formulation are followed by the corresponding numerical validations, assuming a fiber discretization of the end-interfaces of the macroelement as a reference configuration due to its numerical versatility and straightforward implementation.

5.2 MACROELEMENT OF PENNA *ET AL.* (2014)

The two-node macroelement originally proposed by Brencich and Lagomarsino (1998), further enhanced by Penna *et al.*, (2014), and currently implemented in the software TREMURI (Lagomarsino *et al.*, 2013), is composed of three parts: two zero-height end-interfaces (i and j), assumed infinitely rigid with respect to shear actions, where the coupled axial-flexural behavior is concentrated, and a central body (e) where only shear deformations are allowed. The two-dimensional kinematic is thoroughly described by eight degrees of freedom: each node is equipped with three DOFs, that is, the vertical (w) and horizontal (v) displacements, and the in-plane rotation (φ), whereas the remaining ones, that is, an additional vertical displacement (w_e) and in-plane rotation (φ_e), belong to the central body (Figure 5.1).

The peculiar arrangement of the degrees of freedom makes the shear and flexural failure mechanisms kinematically uncoupled, while preserving compatibility relationships to ensure equilibrium at the element level. Moreover, the internal DOFs are necessary to purify the end-interface generalized displacements from rigid body motions.

Finally, the completely mechanically based formulation, and the capability of representing the cyclic shear and flexural behavior of a masonry panel with a limited computational effort and number of degrees of freedom, make the macroelement of Penna *et al.* (2014) suitable for performing nonlinear static and dynamic analyses of masonry structures in an effective and efficient manner.

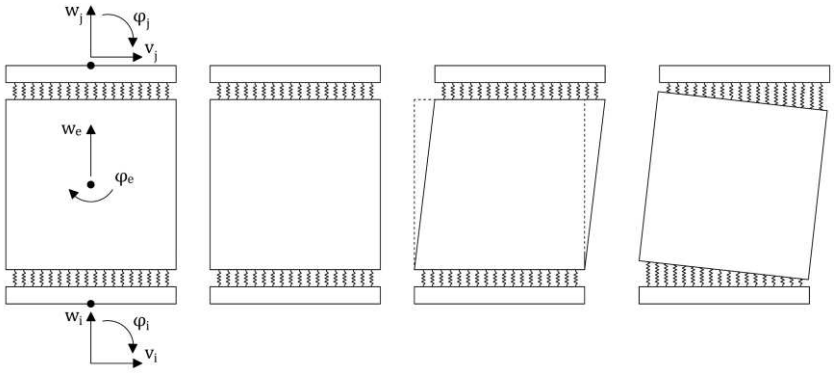

Figure 5.1: Kinematic of the macroelement of Penna *et al.* (2014).

5.2.1 Shear formulation

The Penna *et al.* (2014) macroelement is endowed with a nonlinear shear stress-strain cyclic relationship derived from the Gambarotta and Lagomarsino (1997a,b) continuum model for masonry. In fact, the macroscopic integration of the aforementioned model, representing a detailed mechanical-based behavior of mortar joints, allows to adequately describe the shear response in the inelastic regime.

The macroelement shear behavior is expressed in terms of a Coulomb criterion, therefore it depends on an elastic contribution limited by the frictional static strength V_f, and on an additional plastic response governed by the material cohesion V_c. The first contribution is written in terms of static axial load N and equivalent friction coefficient μ, provided that a positive value is obtained, whereas the second is a function of the sliding displacement s through the nonlinear stiffness parameter $k(\alpha)$, as reported in equation (5.1), with α representing a state variable accounting for shear damage accumulation (Gambarotta and Lagomarsino, 1997a,b). A more comprehensive description of the formulation is reported by Penna *et al.* (2014).

$$V = V_f + V_c \qquad V_f = \mu N > 0 \qquad V_c = k(\alpha)s \tag{5.1}$$

Overall, the macroelement shear force-displacement constitutive law is described through two parameters, whose influence is depicted in Figure 5.2: the nonlinear shear parameter Gc_t governs the position of the peak, controlling the amplitude of the inelastic displacement component (Figure 5.2a), whereas β is responsible for the slope of the post-peak softening branch (Figure 5.2b).

Finally, the nonlinear shear force V of the macroelement is obtained by correcting the elastic term by means of the inelastic counterpart s, resulting in equation (5.2) after assuming no distributed loads along the height (h) of the member and indicating with G and A the shear modulus and the cross-section area, adequately reduced through the shear factor χ.

$$V = V_j = -V_i = \frac{GA}{\chi h}(u - s) = \frac{GA}{\chi h}\left(u_j - u_i - \varphi_e h - s\right) \tag{5.2}$$

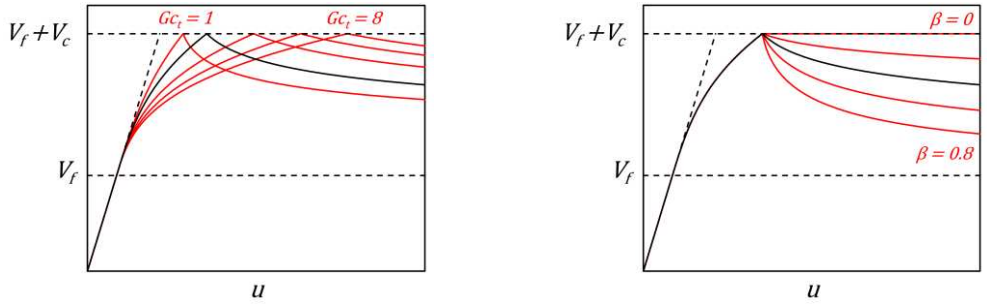

Figure 5.2: Monotonic shear response of the macroelement of Penna *et al.* (2014): influence of (a) Gc_t (for $\beta = 0.4$) and (b) β (for $Gc_t = 2$) parameters.

5.2.2 Axial-flexural formulation

A noteworthy and computationally efficient feature of the Penna *et al.* (2014) macroelement is the analytical description of the nonlinear axial-flexural response, which allows to account for cracking effects during rocking motions explicitly, as well as toe-crushing phenomena due to the limited compressive strength of masonry.

In fact, stresses and displacements resulting from the nonlinear behavior of the macroelement end-interfaces are analytically obtained by applying inelastic corrections to the linear contributions; consequently, no post-integration is required:

$$\boldsymbol{F^{int}(u)} = \boldsymbol{Ku} + \boldsymbol{F^{*}(u)} + \boldsymbol{F^{**}(u)} \tag{5.3}$$

where $\boldsymbol{K}$ represents the elastic stiffness matrix, $\boldsymbol{u}$ and $\boldsymbol{F^{int}(u)}$ the generalized displacement and internal force vectors, whereas $\boldsymbol{F^{*}(u)}$ and $\boldsymbol{F^{**}(u)}$ the analytical nonlinear correction vectors accounting for cracking and toe-crushing phenomena. Additional details about the elastic stiffness matrix and its derivation are reported in Appendix A.

As specified by Penna *et al.* (2014), the two end-interfaces of the macroelement are studied separately. The coupled axial-flexural model is described by the internal axial force N and bending moment M, as well as by their corresponding kinematic quantities, such as the vertical displacement w and in-plane rotation φ, purified from rigid motions:

$$\begin{cases} N = k\ t\ L\ w \\ M = \left(\dfrac{k\ t\ L^3}{12}\right)\varphi \end{cases} \tag{5.4}$$

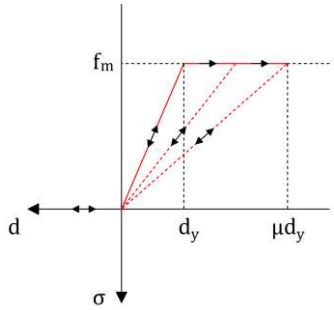

Figure 5.3: Constitutive law assigned to the end-interfaces (Penna *et al.*, 2014).

where $k = 2E/h$ is the equivalent axial stiffness of the end-interfaces, being E the Young's module of masonry, whereas h, t, and L represent the height, thickness, and length of the macroelement. The relative vertical displacement w and in-plane rotation φ are obtained as $w = w_i - w_e$ and $\varphi = \varphi_i - \varphi_e$, and as $w = w_j - w_e$ and $\varphi = \varphi_j - \varphi_e$ for the i^{th} and j^{th} interface, respectively.

The system reported in equation (5.4) holds as long as a linear-elastic behavior is ensured. Conversely, when cracking or toe-crushing occur, the internal axial force and bending moment are no longer uncoupled, and nonlinear corrections need to be applied. In this context, the interfaces of the Penna *et al.* (2014) macroelement implement a no-tension nonlinear degrading model, as depicted in (Figure 5.3).

Figure 5.4 shows in grey the effective stress profile on a section undergoing a cracking phenomenon and highlights in red the portion of stresses to be removed through a nonlinear correction. Two possible situations are depicted: in the first case, the cracking phenomenon involves a portion of the section (Figure 5.4a), whereas in the second it extends to the whole length (Figure 5.4b).

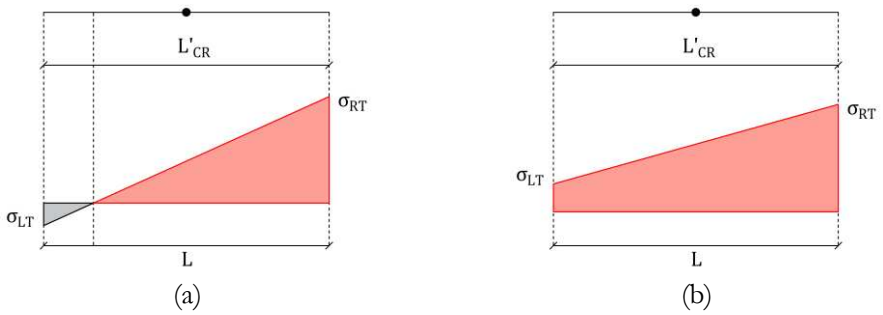

Figure 5.4: Representation of the stress profile under cracking conditions: effective stress distribution (in grey) and inelastic correction (in red).

The cracking condition can be expressed in terms of kinematic variables, by assuming small displacements and rotations. In this context, focusing on the lower i^{th} interface, the cracking length is obtained according to equation (5.5):

$$L'_{CR,i} = \frac{w}{|\varphi|} + \frac{L}{2} \tag{5.5}$$

Consequently, the corresponding inelastic corrections are hereafter reported:

$$\begin{cases} N_i^* = \dfrac{k\,t}{8\,|\varphi|}(2w + L|\varphi|)^2 H\left(L'_{CR,i}\right) \\ M_i^* = -\dfrac{k\,t}{24\varphi|\varphi|}(w - L|\varphi|)(2w + L|\varphi|)^2 H\left(L'_{CR,i}\right) \end{cases} \tag{5.6}$$

where $H\left(L'_{CR,i}\right)$ indicates the Heaviside function, assuming a zero value when no cracks develop on the considered section (i.e., equation (5.5) is not positive), equal to a unit value otherwise. It is worth noticing that relationships (5.6) apply to the first case (Figure 5.4a). Conversely, when the cracking phenomenon involves the whole length, the entire elastic contribution needs to be removed, as the section cannot withstand any tensile load. With a similar procedure, the equations governing the response of the j^{th} interface can be obtained, and all the concerning details are reported in Appendix E.

Despite the high compressive strength characterizing masonry panels, especially compared to the static axial load applied, experimental tests on masonry piers highlighted toe-crushing phenomena when subjected to in-plane rocking mechanisms, which limit the ultimate bending moment and lead to a cyclic stiffness degradation. In this context, the end-interfaces of the macroelement proposed by Penna *et al.* (2014) rely on an elasto-perfectly plastic degrading model in compression (Figure 5.3).

Unlike cracking conditions, describing the toe-crushing behavior through a single correction is no longer convenient. Instead, each edge needs to be analyzed independently, summing the individual contributions to obtain the entire cross-section correction. In this context, to account for the limited compressive strength of masonry, two damage variables at the current step (μ', ξ'), as well as their maximum recorded value throughout the load history (μ, ξ), are computed.

Overall, four nonlinear variables are therefore required for both the left and right edges of each end-interface (5.7). More specifically, μ represents the displacement ductility and, once a unit value is reached, the stiffness is degraded to the secant value at maximum displacement, whereas ξ indicates the dimensionless length involved in the crushing phenomenon:

$$\mu' = \frac{w \pm \varphi \frac{L}{2}}{d_y} \qquad \xi' = \pm \frac{(\mu' - 1)\, d_y}{\varphi\, L} \tag{5.7}$$

with L and t the length and the thickness of the macroelement, whereas $d_y = f_m/k$ the yielding displacement, being f_m and k the compressive strength and the equivalent elastic stiffness of the end-interfaces, respectively. The sign of the equations depends on the considered edge, as reported in detail in Appendix F.

Figure 5.5 depicts a list of possible situations that can be experienced depending upon the mutual behavior of the described damage variables. In particular, in Figure 5.5a both the ductility demand and the dimensionless crushing length are being exceeded on the right edge, whereas in Figure 5.5b none of them needs to be updated, as no additional nonlinearity is reached. Conversely, in Figure 5.5c and Figure 5.5d only the dimensionless crushing length and the ductility demand are being respectively exceeded.

Referring to the i^{th} interface, the inelastic corrections accounting for the limited compressive strength of masonry and associated toe-crushing mechanisms are hereafter reported:

$$\begin{cases} N_i^{**} = k\, t \left(\dfrac{\mu_i - 1}{2\, \mu_i}\right) \xi_i\, L\, (w \pm \varphi L)\, H(\xi_i\, L) \\ M_i^{**} = \pm\, k\, t \left(\dfrac{\mu_i - 1}{2\, \mu_i}\right) \xi_i\, L\, (w \pm \varphi L) \left(\dfrac{L}{2} - \dfrac{\xi_i\, L}{3}\right) H(\xi_i\, L) \end{cases} \tag{5.8}$$

where the Heaviside function $H(\cdot)$ is now controlled by a positive value of the crushing length $\xi\, L$, and the sign of the contributions is automatically determined by choosing a section edge. An analogous procedure can be followed for the j^{th} interface, and the details are reported in Appendix F.

Despite the computational efficiency of the analytical integration is evident, some drawbacks must be highlighted. In fact, even though the corrections due to cracking conditions are exact, the ones accounting for toe-crushing phenomena rely on some approximations, particularly visible in an unloading phase, where the stress profile along the section is not linear as assumed by the corrections (Figure 5.5b). Moreover, as represented in Figure 5.5c and Figure 5.5d, the linearization does not allow to follow the actual discontinuities of the stress profile. However, as Penna *et al.* (2014) reported, a linear approximation does not induce significant differences in the nodal corrections, providing thus reliable results.

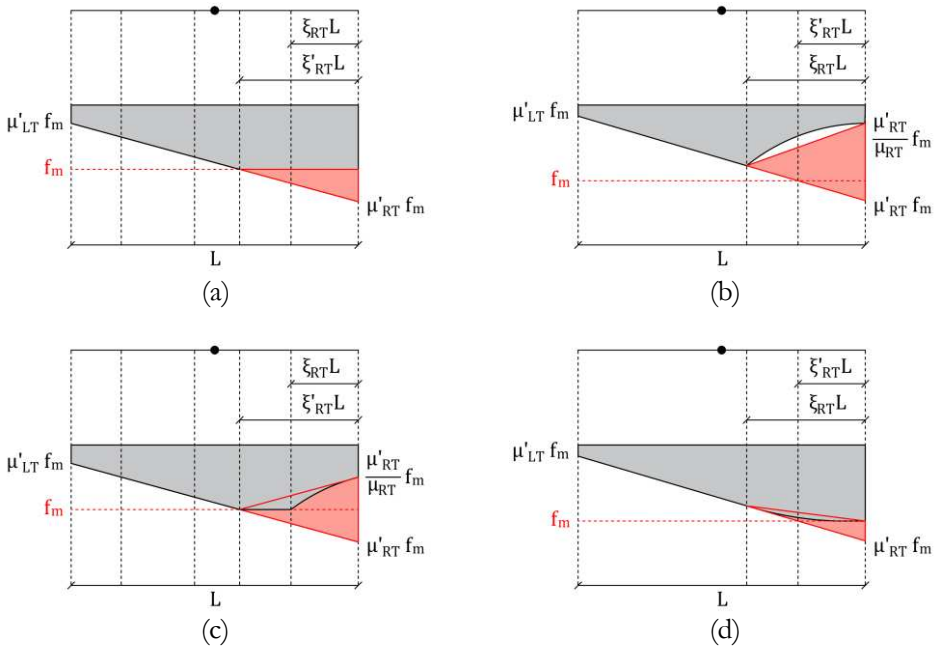

Figure 5.5: Representation of the stress profile under crushing conditions: effective stress distribution (in grey) and inelastic correction (in red).

5.3 IMPROVEMENT OF THE TWO-DIMENSIONAL MACROELEMENT

5.3.1 Additional nonlinear correction for toe-crushing conditions

As previously stated, a noteworthy point of the described macroelement is the formulation of the end-interfaces, which provides analytical inelastic corrections to obtain the nonlinear behavior from the linear-elastic response. With the Penna *et al.* (2014) constitutive law, a sole nonlinear equation suffices to describe both the loading and unloading phases within toe-crushing phenomena. However, even though some approximations are essential, a particular condition must be addressed separately to avoid physically unsound results.

In this context, when cracking develops on a section previously damaged by toe-crushing, causing an overlap between the lengths involved into cracking and toe-crushing mechanisms of opposite corners (Figure 5.6a), applying the existing correction might lead to a severe underestimation of internal actions. With this being underlined, additional equations are derived to address this issue. More specifically, if this is the case, the length undergoing crushing ξL of equations (5.8) is replaced with the compressed length $L_C = L - L'_{CR}$, leading to the nonlinear corrections reported in equations (5.9), where the sign of the contributions depends on the interface edge considered. Similar relationships can be derived for the j^{th} interface, and the concerning details are reported in Appendix F.

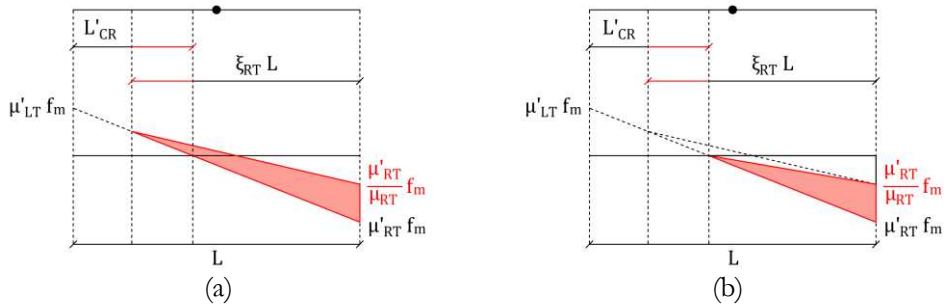

Figure 5.6: (a) Penna *et al.* (2014) and (b) improved nonlinear correction effects in the case of overlap between lengths involved into cracking and toe-crushing mechanisms of opposite corners.

$$\begin{cases} N_i^{**} = k\ t\ L\left(\dfrac{\mu_i - 1}{2\ \mu_i}\right)(w \pm \varphi L)\left(L - L'_{CR,i}\right) H\left(\mu_i, L'_{CR,i}\right) \\ M_i^{**} = \pm\ k\ t\ L^2\left(\dfrac{\mu_i - 1}{2\ \mu_i}\right)(w \pm \varphi L)\left(L - L'_{CR,i}\right)\left[\dfrac{L}{2} - \dfrac{1}{3}\left(L - L_{CR,i}\right)\right] H\left(\mu_i, L'_{CR,i}\right) \end{cases} \quad (5.9)$$

Figure 5.6a and Figure 5.6b highlight in red the portion of stress intended to be removed through nonlinear corrections without and with the improvement, respectively. It can be noticed that the existing corrections significantly overestimate the excess contribution due to the nonlinear response of the member.

5.3.1.1 *Numerical validation*

Numerical comparisons on a section with a length-to-thickness ratio $L/t = 5$, a compressive strength of $f_m = 3.6\ MPa$, and a Young's modulus of $E = 2310\ MPa$, are carried out in order to validate the additional correction proposed, and the results are depicted in Figure 5.7 and Figure 5.8 for the axial force and bending moment, respectively. In particular, a decreasing axial displacement history is assigned by maintaining an imposed in-plane rotation constant. The comparison is performed by assuming the results obtained through a fiber discretization of the end-interfaces as a reference condition, due to its straightforward implementation and numerical versatility. In fact, as a uniaxial stress-strain relationship is assigned to each fiber, the numerical integration of their individual contributions can easily capture the actual stress profile along the section.

Despite the no-tension response of the Penna *et al.* (2014) constitutive law limits the inaccuracy of the formulation, a non-negligible deviation arises with respect to the reference fiber solution. On the other hand, the improved correction proved satisfactory results, tending to follow closely the fiber formulation trend.

As already mentioned, in the case of unloading, the analytical formulation is characterized by a linearization of the stress profile along the section, which would be highly nonlinear

otherwise, as depicted in Figure 5.9. The consequence of such an approximation is noticeable at the beginning of the displacement history imposed, where a difference in terms of axial force (Figure 5.7) and bending moment (Figure 5.8) with respect to the fiber formulation is more evident. On the contrary, as the analysis proceeds, the two responses tend to get closer, leading to comparable results.

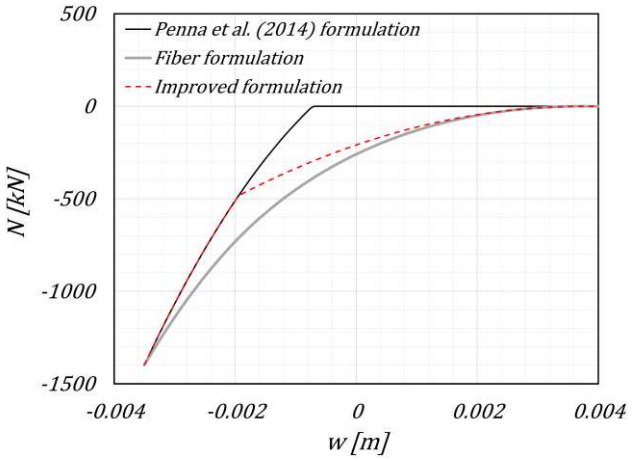

Figure 5.7: Validation of the additional nonlinear correction: axial force.

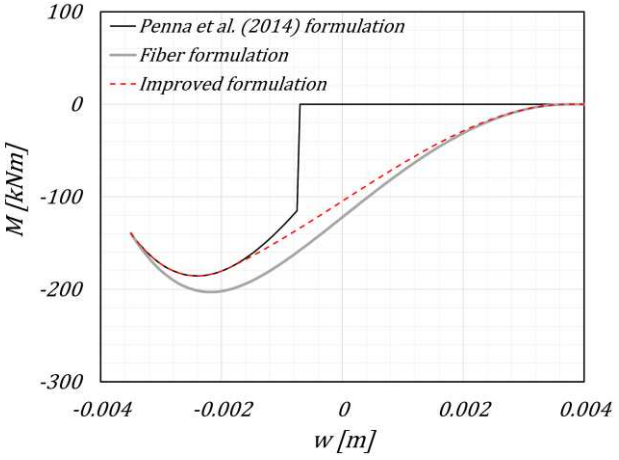

Figure 5.8: Validation of the additional nonlinear correction: bending moment.

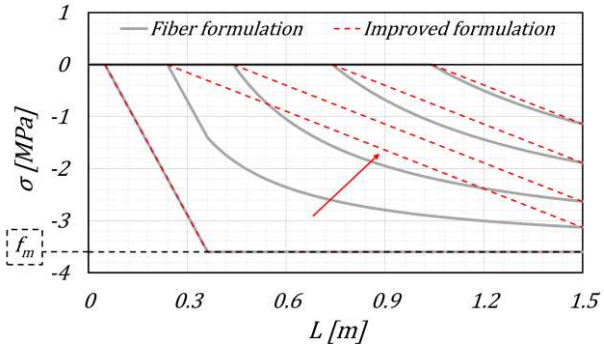

Figure 5.9: Stress profile comparison between fiber and improved analytical formulations.

5.3.2 Introduction of an elasto-fragile tensile strength

The common assumption when modeling masonry structures is to neglect the tensile strength of the material. In fact, its low value compared to the compressive counterpart and its statistical scattering corroborates this simplification. However, a tensile strength might improve the accuracy of results and help the analysis to converge when dealing with elements with low axial loads, such as spandrels. Furthermore, it can be suitable for representing the influence of masonry strengthening interventions, which strongly rely on the tensile response of the material employed to improve the seismic performance of the original structural element, as reported in the following chapters of this document.

In this context, an elasto-fragile tensile response is analytically integrated over the length of the macroelement, enhancing the original constitutive law and leading to the relationship reported in (Figure 5.10b). As a result, the cracking length at the current load step previously calculated (L'_{CR}) needs to be reviewed, and its maximum recorded value throughout the load history (L_{CR}) needs to be stored as an additional damage variable. As a matter of fact, once the tensile strength is reached along a portion of the section, only that portion is no longer able to carry any tensile stress.

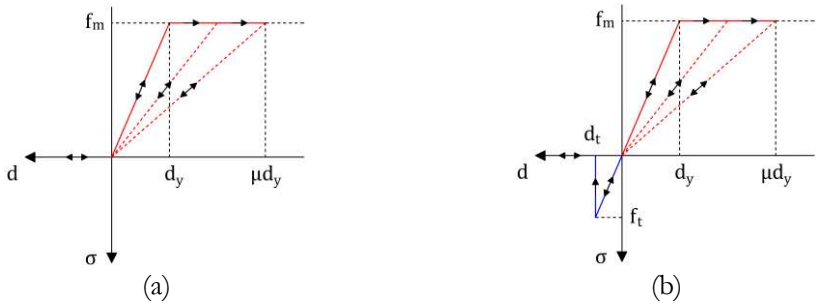

Figure 5.10: Interface stress-displacement constitutive law: (a) without (Penna *et al.*, 2014) and (b) with tensile strength.

It is noteworthy that, unlike the original no-tension formulation, the length in tension L_T might differ from the current cracking length L'_{CR}, depending on the elastic tensile displacement threshold d_t assumed. Furthermore, identifying a unique correction accounting for the behavior of both edges is no longer convenient. In fact, individual corrections need to be provided to each edge, as discussed for the toe-crushing phenomena, leading to the quantities indicated as $L'_{CR,LT}$, $L_{CR,LT}$ and $L'_{CR,RT}$, $L_{CR,RT}$ for the left and right edges, respectively.

The new definition of the current cracking length L'_{CR}, followed by the length in tension L_T and in compression L_C, are reported in equation (5.10) referring to the i^{th} interface (where the sign of the contributions depends on the edge considered), and clarified in Figure 5.11. A deeper description is given in Appendix E.

$$L'_{CR,i} = \pm\frac{w}{\varphi} + \frac{L}{2} \pm \frac{d_t}{\varphi} \qquad L_{T,i} = \frac{w}{|\varphi|} + \frac{L}{2} \qquad L_{C,i} = L - L_{T,i} \tag{5.10}$$

For each load step, the current and the maximum recorded values of the cracking length at each section edge are compared, resulting in the six possible conditions reported in Figure 5.11, where the stress portion intended to be removed through an inelastic correction is highlighted in red. The total cracking length (L_{CR}) of the end-interface is then computed by summing the single-edge values.

Figure 5.11a represents a condition in which the current cracking length on the left edge ($L'_{CR,LT}$) exceeds the maximum stored value ($L_{CR,LT}$), however without affecting the whole length of the end-interface. In this case, the section can only rely on the portion where the elastic tensile threshold has not been exceeded. On the other hand, Figure 5.11b, Figure 5.11c, and Figure 5.11d, replicate situations where the damage variable $L_{CR,LT}$ has not to be updated because a new tensile nonlinearity has not been reached (i.e., $L'_{CR,LT} < L_{CR,LT}$). In this context, the stresses involved into the already cracked portions need to be corrected to be consistent with the expected stress profile.

Unlike the previous cases, which are defined for each section edge, Figure 5.11e and Figure 5.11f describe situations where the cracking condition affects the whole length of the end-interface (i.e., the sum of the cracking lengths of the two edges is greater than the total length of the end-interface). For this reason, separating the contribution of the two edges is no longer needed, and the formulation degenerates to the original no-tension behavior proposed by Penna *et al.* (2014).

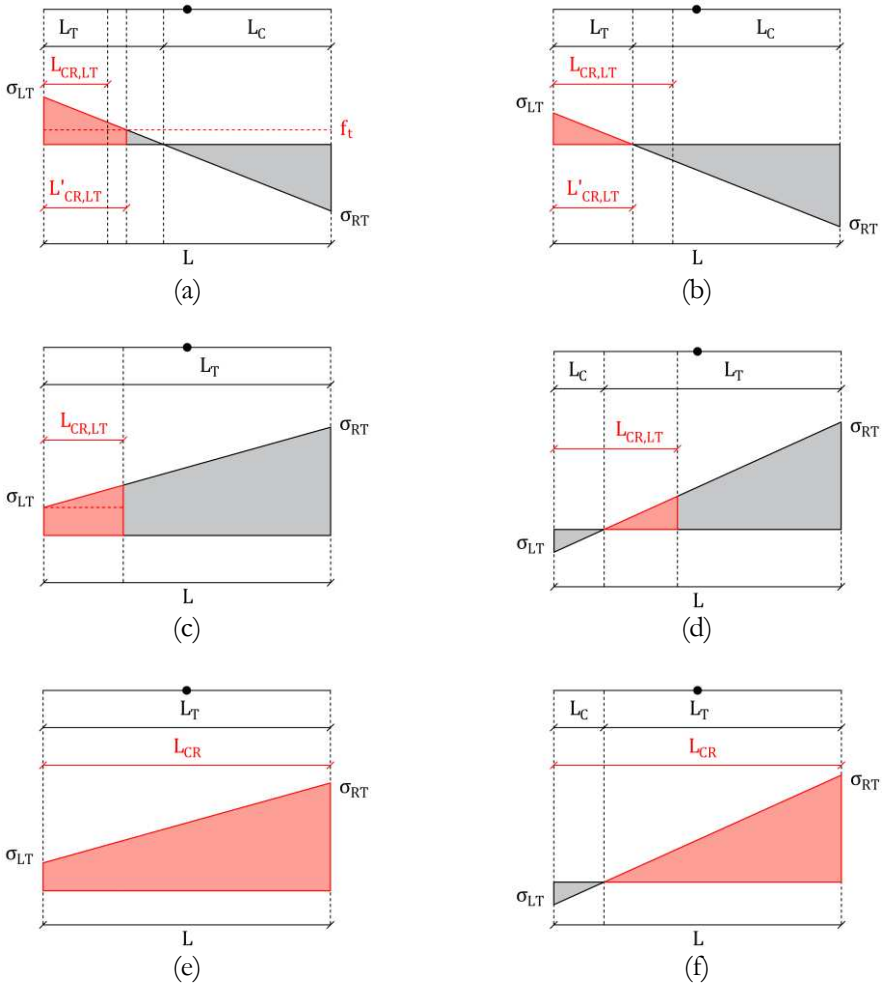

Figure 5.11: Analytical conditions addressed for a brittle tensile strength: effective stress profiles and removed portions colored in grey and red, respectively.

5.3.2.1 *Numerical validation*

Cyclic in-plane tests are performed by adopting analytical and fiber end-interface formulations on a section with a length-to-thickness ratio $L/t = 5$, a Young's modulus of $E = 2310\,MPa$, a tensile strength equal to $0.5\,MPa$, and a constant axial load ratio $\sigma = 0.16\,f_m$, being f_m the compressive strength of masonry, assumed $3.6\,MPa$. The results are reported in Figure 5.12 and Figure 5.13.

As expected, a non-zero tensile strength delays the yielding point and provides an additional source of energy dissipation. Moreover, due to the brittle nature of the constitutive law,

stiffness and strength are degraded as the section accumulates tensile damage, aligning with the no-tension response.

A fiber formulation is assumed as a reference due to its straightforward implementation and versatility. However, since the brittle tensile strength introduces significant discontinuities in the stress profile along the length of the end-interfaces, a dense discretization is necessary to reproduce the analytical response. In fact, the analytical formulation is not based on any approximation, regardless of the condition addressed, leading always to the numerically exact solution.

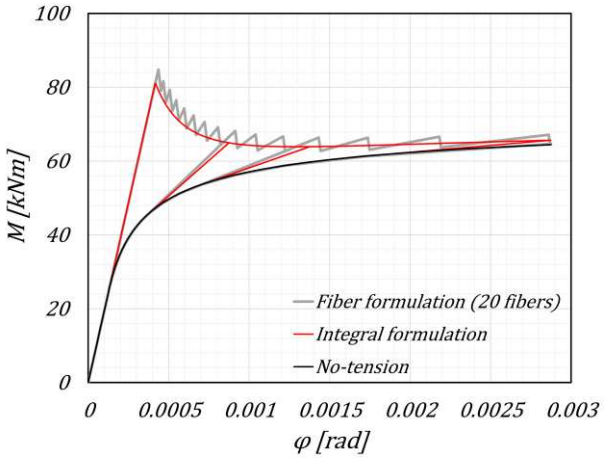

Figure 5.12: Sectional response fidelity with respect to the number of fibers employed: 20 fibers.

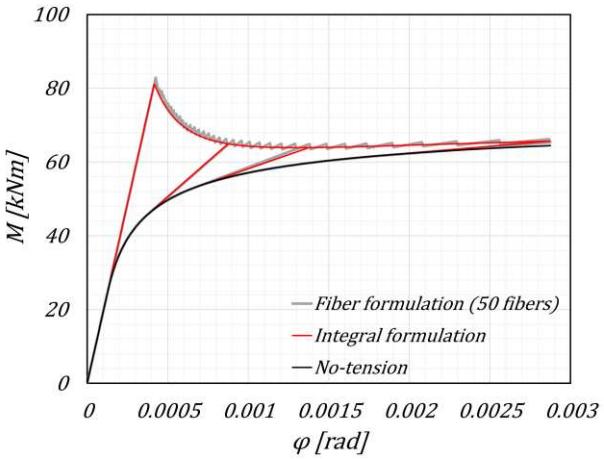

Figure 5.13: Sectional response fidelity with respect to the number of fibers employed: 50 fibers.

It is worth noticing that the additional nonlinear correction previously derived for the toe-crushing condition (§5.3.1) still applies, as it is governed by the length in tension, which is a common parameter between the original no-tension and improved formulations.

5.4 THREE-DIMENSIONAL MACROELEMENT

5.4.1 Coupled in-plane and out-of-plane formulation

The equivalent-frame approach with nonlinear macroelements is widely used for the seismic performance assessment of masonry structures. Although initially conceived for simulating two-dimensional walls, in the last decades it has been extended to three-dimensional buildings, by maintaining only the macroelement in-plane stiffness or by introducing an elastic out-of-plane one.

The main scope of this section is the formulation of a new macroelement capable of simultaneously capturing the nonlinear in-plane and out-of-plane response of a masonry panel, mainly focusing on the biaxial behavior of the end-interfaces. As a matter of fact, the new macroelement consists of an extension of the previously described Penna *et al.* (2014) formulation, and it is characterized by fifteen degrees of freedom (Figure 5.14a): six located at each end-node, involving the axial displacement (w), the shear ones along the in-plane and out-of-plane directions (v_2 and v_3), and the three rotations about the corresponding axes (φ_1, φ_2, and φ_3); whereas, the three remaining DOFs, that is, the internal axial displacement (w_e), and the internal out-of-plane ($\varphi_{2,e}$) and in-plane ($\varphi_{3,e}$) rotations, belong to the central body.

As already highlighted, a noteworthy point of the Penna *et al.* (2014) macroelement is its analytically integrated axial-flexural formulation. However, even though the same could be done in the three-dimensional space for a no-tension constitutive law (Vanin *et al.*, 2020), it would be extremely complex to analytically account for a finite tensile strength or toe-crushing phenomena under biaxial bending conditions.

To overcome this limitation, as described in Vanin *et al.* (2020), the end-interfaces are divided into n stripes, each endowed with the analytical behavior proposed in the previous chapters and considered constant along its thickness. As a result, a stripe formulation is employed: the analytical integration is responsible for the in-plane behavior of each stripe, whereas the coupled nonlinear sectional in-plane and out-of-plane response can be approximately computed by integrating the inelastic corrections of each stripe over the thickness of the macroelement (Figure 5.14c):

$$N^* = \sum_n N_n^* \qquad M_2^* = \sum_n M_{2,n}^* = \sum_n \left(N_n^* \, e_{3,n}\right) \qquad M_3^* = \sum_n M_{3,n}^* \tag{5.11}$$

$$N^{**} = \sum_n N_n^{**} \qquad M_2^{**} = \sum_n M_{2,n}^{**} = \sum_n \left(N_n^{**}\, e_{3,n}\right) \qquad M_3^{**} = \sum_n M_{3,n}^{**} \tag{5.12}$$

with $e_{3,n}$ representing the centroid out-of-plane coordinate of the n^{th} stripe, which can be expressed as:

$$e_{3,n} = \frac{t}{n}\left(n_3 - \frac{1}{2}\right) - \frac{t}{2} \tag{5.13}$$

where t is the macroelement total thickness, n the number of stripes defined, and n_3 is the stripe counter.

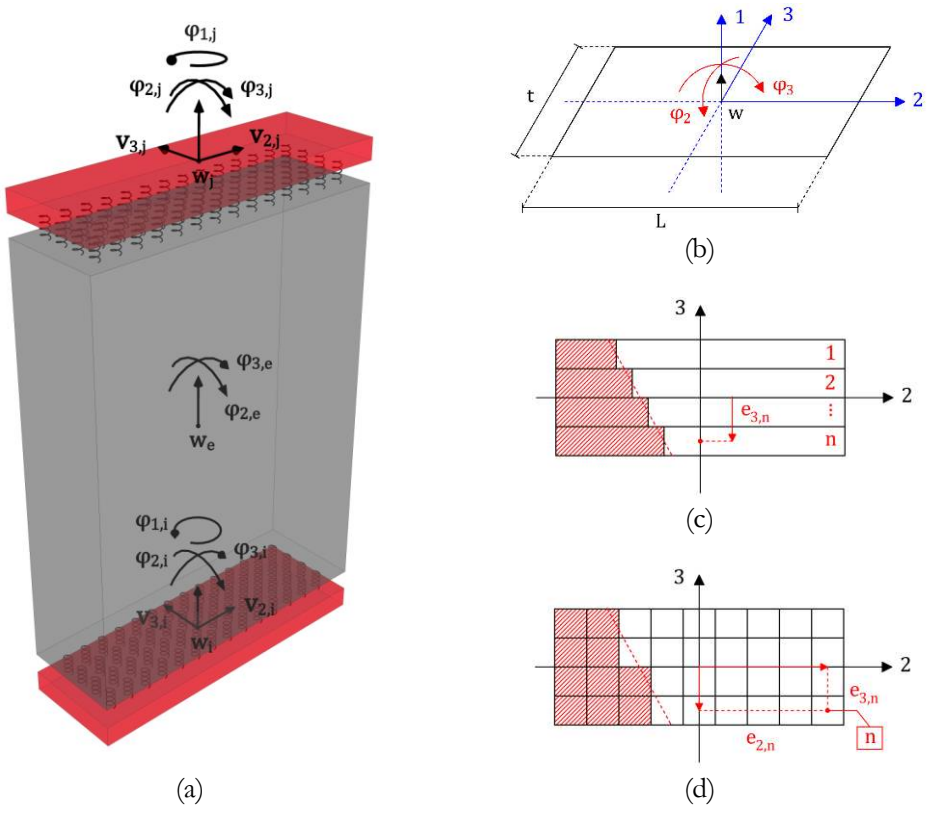

Figure 5.14: Three-dimensional macroelement: (a) node and central-body degrees of freedom, (b) end-interface degrees of freedom, (c) stripe discretization, and (d) fiber discretization of the cross-section.

Kinematic compatibility equations enforce collaboration of the individual stripes, assuming a linear profile for the deformations (5.14). Consequently, the inelastic corrections presented in the previous chapters still apply, provided that the contribution of the n^{th} stripe is obtained by accounting for the out-of-plane rotation into the corresponding vertical displacement:

$$\begin{cases} w_n = w + \varphi_2 \, e_{3,n} \\ \varphi_{3,n} = \varphi_3 \end{cases} \tag{5.14}$$

being $w = w_e - w_i$, $\varphi_2 = \varphi_{2,e} - \varphi_{2,i}$ and $\varphi_3 = \varphi_{3,e} - \varphi_{3,i}$ for the i^{th} interface, whereas $w = w_j - w_e$, $\varphi_2 = \varphi_{2,j} - \varphi_{2,e}$ and $\varphi_3 = \varphi_{3,j} - \varphi_{3,e}$ for j^{th} one.

Despite all the potentialities of the stripe formulation, in case of particularly demanding load history, a three-dimensional fiber discretization might be more suitable, leading to more accurate results. Indeed, the main assumption of the latter is that, as the number of fibers increases, the solution tends to converge to the numerically exact one. For this reason, the proposed macroelement also implements a full-fiber discretization of the end-interfaces, allowing using more refined and appropriate uniaxial stress-strain relationships (Figure 5.14d), even though slightly increasing the computational time. The fiber implementation is not directly discussed in the main text of this thesis, as it is mainly used for validating the fidelity of the analytical integration. However, all the concerning details are reported in Appendix D.

The shear and torsional behaviors are concentrated in the central body of the macroelement. However, they are not directly addressed in this thesis. Similarly to the original macroelement of Penna *et al.* (2014), the shear response is governed by the Gambarotta and Lagomarsino (1997a,b) continuum model for masonry, considered completely uncoupled along the two main horizontal directions, whereas the torsional behavior relies on a linear elastic response. It is worth emphasizing that the improvements carried out over the years on the macroelement of Penna *et al.* (2014) are also incorporated in the three-dimensional formulation, such as the correction on the elastic stiffness (Bracchi *et al.,* 2021), as well as the automatic and adaptive calibration of the shear parameters (Bracchi and Penna, 2021). However, they are not discussed in this thesis.

5.4.1.1 *Numerical validation*

The biaxial flexural formulation of the end-interfaces is validated through numerical tests performed on a section with a length-to-thickness ratio $L/t = 5$ and Young's modulus $E = 2310\ MPa$, by assigning a constant axial load (25% of the compressive strength of the material, assumed equal to $3.6\ MPa$), and by imposing a cyclic biaxial rotation.

Moreover, no tensile strength is considered, and the section is discretized with a total of 20 out-of-plane stripes and 100×20 in-plane and out-of-plane fibers, respectively.

The results in terms of bending moments (Figure 5.15) and vertical displacements (Figure 5.16) are reported by increasing the horizontal angle α between the imposed rotation vector and the out-of-plane axis. In particular, values of $\alpha = 0°$ and $\alpha = 90°$ represent a pure in-plane and out-of-plane loading, respectively.

It is worth noticing that the resulting values of bending moments M_β and rotations φ_α are obtained following equation (5.15), with β indicating the angle between the resulting bending moment and the out-of-plane axis.

$$M_\beta = \sqrt{M_2^2 + M_3^2} \qquad \varphi_\alpha = \sqrt{\varphi_2^2 + \varphi_3^2} \tag{5.15}$$

According to the results, an out-of-plane load significantly reduces the stiffness and strength of the masonry panel (Figure 5.15), as well as the uplift related to rocking motions (Figure 5.16). However, despite the fairly good fidelity characterizing the stripe section in the case of toe-crushing phenomena, the approximations involved in the analytical formulation result in a light underestimation of the energy dissipation during cyclic loadings. On the other hand, as the angle α approaches the pure out-of-plane condition, the in-plane approximations are of less impact on the response. Consequently, this discrepancy tends to vanish.

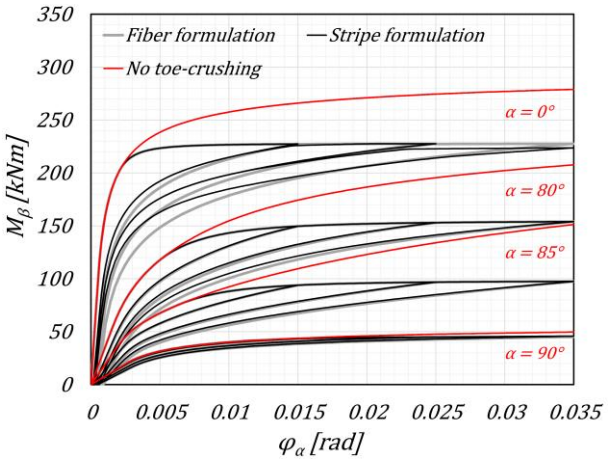

Figure 5.15: Influence of the out-of-plane behavior on the in-plane response: bending moment.

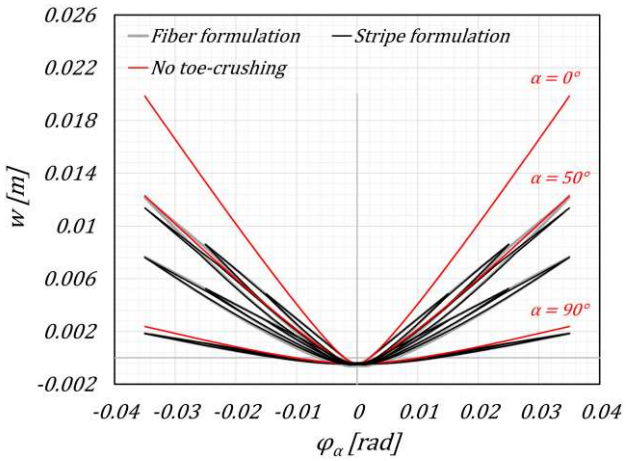

Figure 5.16: Influence of the out-of-plane behavior on the in-plane response: uplift of the section.

Figure 5.17 shows the interaction curves of the in-plane and out-of-plane bending moment as a function of the horizontal angle α. The figure confirms the reduction of the ultimate in-plane bending moment in the case of toe-crushing conditions and when a simultaneous out-of-plane load is applied.

It is worth noticing the slight discrepancy in the ultimate bending moment when a pure out-of-plane load history is applied (i.e., $\alpha = 90°$). As a matter of fact, the stripe and fiber formulation show a different envelope because of the different methodologies employed. In particular, in the first case, the three-dimensional elastic stiffness matrix is pre-defined, and then the inelastic corrections are applied to recover the nonlinear behavior. On the contrary, in the fiber formulation, the three-dimensional nonlinear stiffness matrix is directly obtained through the numerical integration of the single-fiber contributions. As a result, the stripe and fiber formulations slightly overestimates and underestimates the response, respectively. However, by increasing the number of stripes and fibers, the two solutions tend to match rapidly.

Eventually, the interaction diagram is also derived through the software VCA SLU (Gelfi, 2006), which consists of a user-friendly tool for computing the ultimate bending moment of a reinforced concrete (RC) cross-section. In fact, the assumptions of no tensile strength and elastic-perfectly plastic behavior in compression commonly assumed for the RC elements also apply to the masonry material.

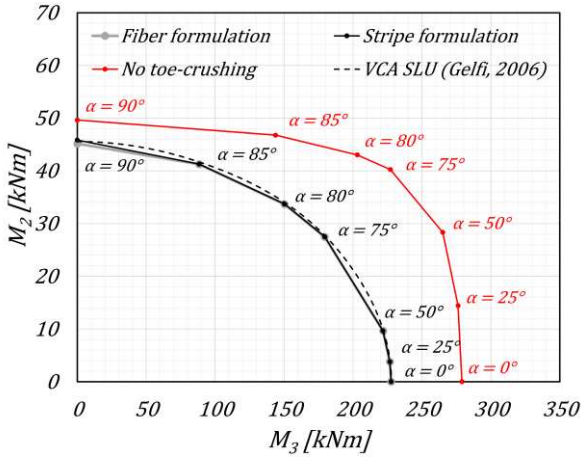

Figure 5.17: Interaction in-plane and out-of-plane curves.

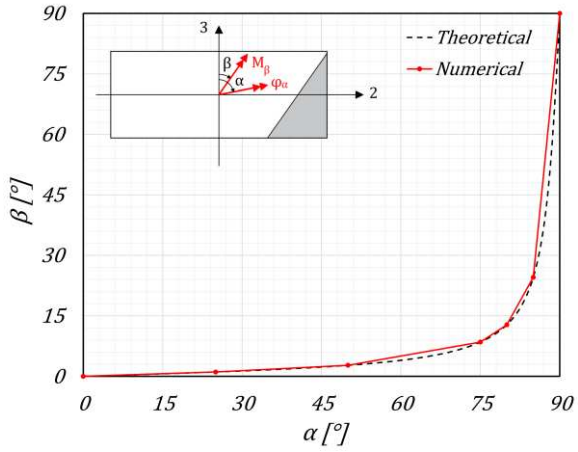

Figure 5.18: Elastic relation between the rotation (α) and the resulting bending moment (β) angles.

Another interesting result lies in the variation of the elastic resulting bending moment angle β with respect to the imposed rotation angle α. As widely investigated by Dolatshahi *et al.* (2014), and according to Figure 5.18, with the adopted dimensions the imposed angle α should be almost perpendicular to the longitudinal axis (greater than 75%) to activate the out-of-plane contribution. The theoretical angle β is calculated as follows:

$$\beta = \operatorname{atan}\left[\left(\frac{I_2}{I_3}\right)\tan\alpha\right] = \operatorname{atan}\left[\left(\frac{t}{L}\right)^2\tan\alpha\right] \quad \textbf{(5.16)}$$

with I_3 and I_2 the in-plane and out-of-plane moments of inertia of the end-interface, respectively.

5.4.2 Three-dimensional transformation matrix

In a space frame, two-node members can be oriented in any direction; as a result, the local $1-2-3$ axes may not coincide with the global $x-y-z$ reference system, thus requiring the adoption of a transformation matrix. Moreover, unlike the planar case, different transformation orders can be used, and the results might be affected. For this reason, assuming and respecting a predefined convention is essential for obtaining consistent outcomes.

Given the global coordinates of a two-node member, its orientation with respect to the global axes can be expressed in terms of director cosines:

$$C_x = \frac{x_2 - x_1}{L} \qquad C_y = \frac{y_2 - y_1}{L} \qquad C_z = \frac{z_2 - z_1}{L} \tag{5.17}$$

being $L = \sqrt{(x_2 - x_1)^2 + (y_2 - y_1)^2 + (z_2 - z_1)^2}$ the length of the element. In particular, $C_x = 0$, $C_y = 0$, and $C_z = 0$ represent a member belonging to the global $y-z$, $x-z$, and $x-y$ plane, respectively; whereas the simultaneous $C_x = 0$ and $C_y = 0$, $C_x = 0$ and $C_z = 0$, or $C_y = 0$ and $C_z = 0$, indicate an element parallel to the global z-, y-, and x-axis, respectively.

Focusing on a member oriented along its own local longitudinal axis (i.e., 1-axis), two possible local reference systems can be identified. In particular, the so-called 2-right and 2-up default orientations are adopted for vertical and non-vertical elements, respectively, providing the weak 2-axis oriented along the global x-axis in the first case, and along the global z-axis in the latter (Figure 5.19). Consequently, the 3-axis is defined following the right-hand rule. Eventually, moments and rotations are considered positive when following the right-thumb rule.

Choosing two different local reference systems depending upon the member orientation is crucial for the transformation matrix to be always well-defined and, consequently, for the global stiffness matrix to be invertible. In fact, as comprehensively discussed in the following, adopting only one local reference system would cause instability of the algorithm, as it would provide singular matrices.

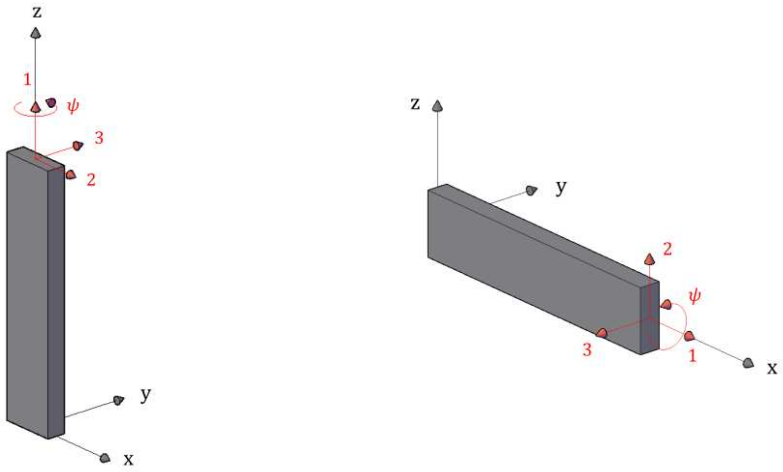

(a) (b)

Figure 5.19: Local reference system for (a) vertical and (b) non-vertical three-dimensional members.

The adopted local reference system is thoroughly defined after identifying all its local axes. In this context, the longitudinal 1-axis is simply determined through the director cosines reported in equation (5.17), and is represented through the unit vector $\boldsymbol{e_1}$:

$$\boldsymbol{e_1} = \{C_x \quad C_y \quad C_z\}^T \tag{5.18}$$

The 2-axis is instead computed by applying the Gram-Schmidt process, which consists of a sequence of operations allowing to transform a set of linearly independent vectors into a set of orthogonal vectors spanning the same space spanned by the original set.

The first step of the algorithm involves the identification of the local $1-2$ plane. In this context, the latter is obtained by offsetting the element nodes i and j (arranged along the local 1-axis by definition) towards the positive global z- and x- direction for non-vertical and vertical members, respectively. Subsequently, a vector $\boldsymbol{v_{ik}}$ connecting the i-node to a general point k belonging to the $1-2$ plane is defined. From the computational point of view, the latter point is usually taken in correspondence with the half-length of the member offset by a unit value.

The local 2-axis, defined by the unit vector $\boldsymbol{e_2}$, is obtained through the Gram-Schmidt equation reported in the following and illustrated in Figure 5.20:

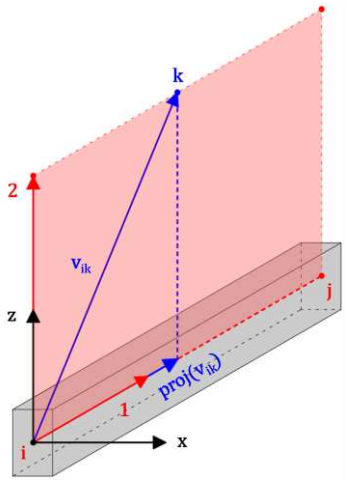

Figure 5.20: Gram-Schmidt process for computing an orthogonal vector basis.

$$\boldsymbol{e_2} = \frac{\boldsymbol{v_{ik}} - \text{proj}(\boldsymbol{v_{ik}})}{\|\boldsymbol{v_{ik}} - \text{proj}(\boldsymbol{v_{ik}})\|} = \frac{\boldsymbol{v_{ik}} - (\boldsymbol{v_k} \cdot \boldsymbol{e_1})\, \boldsymbol{e_1}}{\|\boldsymbol{v_{ik}} - (\boldsymbol{v_k} \cdot \boldsymbol{e_1})\, \boldsymbol{e_1}\|} \tag{5.19}$$

where $\text{proj}(\boldsymbol{v_k})$ represents the projection of the $\boldsymbol{v_{ik}}$ vector onto the local 1-axis, identified by $\boldsymbol{e_1}$, " $\cdot$ " the inner product, whereas $\| \cdot \|$ indicates the Euclidean norm of the vector.

Eventually, the local 3 -axis is automatically defined following the right-hand rule convention:

$$\boldsymbol{e_3} = \boldsymbol{e_1} \times \boldsymbol{e_2} \tag{5.20}$$

where " $\times$ " represent the cross product, consisting of a binary operation for obtaining a perpendicular vector with respect to the plane defined by two other given vectors.

The rotation matrix $\boldsymbol{R}$, which defines the relationship between the adopted local and global reference systems, is reported in equation (5.21), and builds upon the proper arrangement of the local unit vectors previously defined:

$$\boldsymbol{R} = \begin{bmatrix} e_{1x} & e_{1y} & e_{1z} \\ e_{2x} & e_{2y} & e_{2z} \\ e_{3x} & e_{3y} & e_{3z} \end{bmatrix} \qquad \boldsymbol{e_1} = \begin{Bmatrix} e_{1x} \\ e_{1y} \\ e_{1z} \end{Bmatrix} \qquad \boldsymbol{e_2} = \begin{Bmatrix} e_{2x} \\ e_{2y} \\ e_{2z} \end{Bmatrix} \qquad \boldsymbol{e_3} = \begin{Bmatrix} e_{3x} \\ e_{3y} \\ e_{3z} \end{Bmatrix} \tag{5.21}$$

As previously described, each member has its own local orientation, encoding the adopted local reference system. However, the default rotation about the local longitudinal 1-axis can be overwritten by assigning the so-called roll angle ψ.

Regardless of the member orientation, the rotation about the longitudinal axis is performed at last, and the resulting rotation matrix $\widetilde{\boldsymbol{R}}$ is given by:

$$\widetilde{\boldsymbol{R}} = \boldsymbol{R_x}\,\boldsymbol{R} \qquad \boldsymbol{R_x} = \begin{bmatrix} 1 & 0 & 0 \\ 0 & \cos\psi & \sin\psi \\ 0 & -\sin\psi & \cos\psi \end{bmatrix} \tag{5.22}$$

The global transformation matrix $\boldsymbol{T}$ is hence obtained by appropriately assembling the adopted $\widetilde{\boldsymbol{R}}$ matrix to transform the translation and rotation degrees of freedom of both the member nodes:

$$\boldsymbol{T} = \begin{bmatrix} \widetilde{\boldsymbol{R}} & \boldsymbol{0_{3x3}} & \boldsymbol{0_{3x3}} & \boldsymbol{0_{3x3}} & \boldsymbol{0_{3x3}} \\ \boldsymbol{0_{3x3}} & \widetilde{\boldsymbol{R}} & \boldsymbol{0_{3x3}} & \boldsymbol{0_{3x3}} & \boldsymbol{0_{3x3}} \\ \boldsymbol{0_{3x3}} & \boldsymbol{0_{3x3}} & \widetilde{\boldsymbol{R}} & \boldsymbol{0_{3x3}} & \boldsymbol{0_{3x3}} \\ \boldsymbol{0_{3x3}} & \boldsymbol{0_{3x3}} & \boldsymbol{0_{3x3}} & \widetilde{\boldsymbol{R}} & \boldsymbol{0_{3x3}} \\ \boldsymbol{0_{3x3}} & \boldsymbol{0_{3x3}} & \boldsymbol{0_{3x3}} & \boldsymbol{0_{3x3}} & \boldsymbol{I_{3x3}} \end{bmatrix}_{\boldsymbol{15x15}} \tag{5.23}$$

It is worth noticing that the internal degrees of freedom of the members are not to be transformed, as they play a predominant role in ensuring local equilibrium and kinematic admissible displacements of the external DOFs. As a matter of fact, $\boldsymbol{I_{3x3}}$ represents the identity matrix.

Finally, the transition from the local to the global reference system and vice versa is reported in equation (5.24), where $\boldsymbol{K}$ and $\boldsymbol{u}$ represent the local elastic stiffness matrix and displacement vector, whereas $\boldsymbol{K_G}$ and $\boldsymbol{u_G}$ the global counterparts.

$$\begin{cases} \boldsymbol{K_G} = \boldsymbol{T}^T\boldsymbol{K}\boldsymbol{T} \\ \boldsymbol{u_G} = \boldsymbol{T}^T\boldsymbol{u} \end{cases} \qquad \begin{cases} \boldsymbol{K} = \boldsymbol{T}\boldsymbol{K_G}\boldsymbol{T}^T \\ \boldsymbol{u} = \boldsymbol{T}\boldsymbol{u_G} \end{cases} \tag{5.24}$$

5.5 NONLINEAR SOLVING ALGORITHMS

The nonlinear system of equations that governs the response of the proposed three-dimensional macroelement, whose matrix form is reported in equation (5.3), was presented and thoroughly discussed in the previous parts of this document.

This section aims at solving the aforementioned system of equations through an iterative algorithm. More specifically, the initial-stiffness Newton-Raphson method currently implemented in the software TREMURI (Lagomarsino *et al.,* 2013) is replaced with its full version. In this context, the next trial iteration is performed by benefitting from the tangent stiffness matrix, rather than relying on the elastic stiffness matrix only. Consequently, the convergence rate of the algorithm is strongly increased.

5.5.1 Implementation of the full Newton-Raphson method

Due to its simplicity and second-order convergence rate, the full Newton-Raphson method is one of the most used iterative algorithms for solving numerical root-finding problems. As a matter of fact, it relies on the concept of linear approximation and utilizes the first derivative of the function to refine the estimation of the solution after each iteration. In this context, the residual form of the nonlinear system is reported:

$$\boldsymbol{R}(\boldsymbol{u}_{i+1}) = \boldsymbol{F}^{ext} - \boldsymbol{F}^{int}(\boldsymbol{u}_{i+1}) \tag{5.25}$$

where $\boldsymbol{F}^{ext}$ and $\boldsymbol{F}^{int}(\boldsymbol{u}_{i+1})$ represent the external and internal generalized force vectors, whereas the subscripts i and $i+1$ are used to differentiate current and next iteration quantities, respectively.

By expanding equation (5.25) in a Taylor series and by truncating the expansion at the first order, the following linearized version of the problem is obtained:

$$\boldsymbol{R}(\boldsymbol{u}_{i+1}) = \boldsymbol{R}(\boldsymbol{u}_i) + \boldsymbol{\nabla R}(\boldsymbol{u}_i)(\boldsymbol{u}_{i+1} - \boldsymbol{u}_i) = \boldsymbol{0} \tag{5.26}$$

Remodeling the aforementioned equation leads to:

$$\boldsymbol{R}(\boldsymbol{u}_i) = -\boldsymbol{\nabla R}(\boldsymbol{u}_i)(\boldsymbol{u}_{i+1} - \boldsymbol{u}_i) \tag{5.27}$$

and finally to:

$$\boldsymbol{u}_{i+1} = \boldsymbol{u}_i - [\boldsymbol{\nabla R}(\boldsymbol{u}_i)]^{-1}\boldsymbol{R}(\boldsymbol{u}_i) = \boldsymbol{u}_i + [\boldsymbol{K_T}(\boldsymbol{u}_i)]^{-1}\boldsymbol{R}(\boldsymbol{u}_i) \tag{5.28}$$

where $\boldsymbol{K_T(u_i) = -\nabla R(u_i)}$ represents the tangent stiffness matrix, as reported in equation (5.29), being $\boldsymbol{K}$ the elastic stiffness matrix, whereas $\boldsymbol{\nabla F^*(u_i)}$ and $\boldsymbol{\nabla F^{**}(u_i)}$ are the gradients of the nonlinear corrections accounting for cracking and toe-crushing phenomena, respectively. Furthermore, in the case of $\boldsymbol{K_T(u_i) = K}$, the initial-elastic Newton-Raphson algorithm is recovered.

$$\boldsymbol{K_T(u_i) = K + \nabla F^*(u_i) + \nabla F^{**}(u_i)} \tag{5.29}$$

The terms composing the nonlinear gradients are obtained by deriving the corresponding analytical inelastic corrections with respect to the degrees of freedom of the macroelement. Additional details are reported in Appendix E and Appendix F for tensile and compressive nonlinearities, respectively.

5.5.1.1 *Numerical validation*

The correct implementation of the iterative algorithm is validated by subjecting a three-dimensional macroelement to a simultaneous cyclic in-plane and out-of-plane shear force at the top. Cantilever boundary conditions are chosen, whereas a sectional length-to-thickness ratio $L/t = 5$ and a height $h = 2\ m$ are assigned to the geometrical properties. Additionally, a Young's modulus of $E = 2310\ MPa$, and a compressive and tensile strength equal to $f_m = 3.6\ MPa$ and $f_t = 0\ MPa$, respectively, are assumed for the mechanical properties.

The load history is chosen to address biaxial cracking and toe-crushing conditions. Furthermore, the results obtained through a fiber formulation are assumed as a reference, as the corresponding tangent stiffness matrix can be easily computed referring to the uniaxial response of each fiber. Additional details are reported in Appendix D.

Figure 5.21 compares the number of iterations per step between the initial-elastic Newton-Raphson method (labeled "mNR") and the full Newton-Raphson method (labeled "NR"), showing a massive reduction in the latter with a consequent saving in computational time.

Similarly, Figure 5.22 highlights the residual trends due to the investigated algorithms at peak force (whose number of iterations is also identified by the red circle in Figure 5.21), confirming a second-order convergence rate for the full Newton-Raphson method. Moreover, fiber and stripe formulations proved equivalent results.

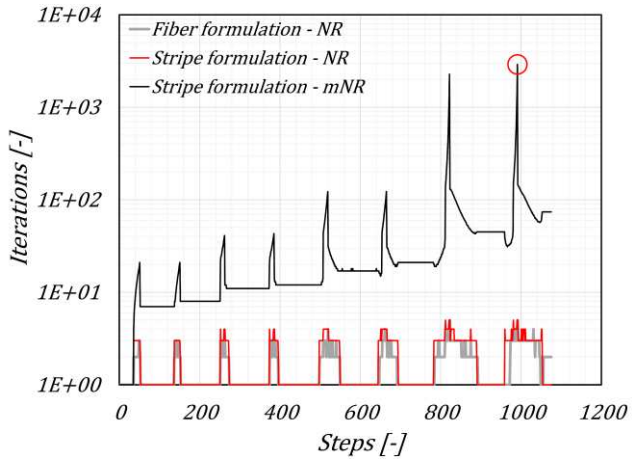

Figure 5.21: Comparison between initial-elastic (mNR) and full Newton-Raphson (NR) in terms of number of iterations per step.

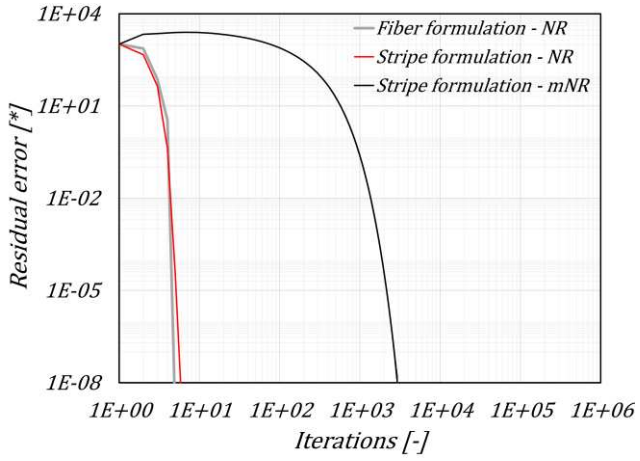

Figure 5.22: Comparison between initial-elastic (mNR) and full Newton-Raphson (NR) methods in terms of convergence rate at peak force.

5.5.2 Implementation of an adaptive Newton-Raphson method

Despite the noticeable advantages of the full Newton-Raphson method, it might lack numerical robustness. In fact, when dealing with constitutive laws characterized by significant discontinuities (e.g., brittle materials with moderate to high strength) or when the tangent stiffness matrix is close to being singular, the full Newton-Raphson method might fail to converge, and a more robust algorithm might be more suitable.

For this reason, an adaptive iterative algorithm capable of achieving both a high convergence rate and numerical robustness is proposed. In particular, the new method relies on a modified matrix $\boldsymbol{K}^*$ for inverting the system of equations and calculating the next iteration:

$$\boldsymbol{\nabla R}(\boldsymbol{u_i}) = -\boldsymbol{K}^* = -[\beta \boldsymbol{K_T}(\boldsymbol{u_i}) + (1-\beta)\boldsymbol{K}] = -\left[\boldsymbol{K} + \beta\left(\boldsymbol{\nabla F}^*(\boldsymbol{u_i}) + \boldsymbol{\nabla F}^{**}(\boldsymbol{u_i})\right)\right] \quad \textbf{(5.30)}$$

The solving stiffness matrix $\boldsymbol{K}^*$ is thus obtained as a linear combination between the tangent $\boldsymbol{K_T}(\boldsymbol{u_i})$ and the elastic $\boldsymbol{K}$ stiffness matrices through a scalar coefficient β. In this context, β is set equal to a unit value at the beginning of each load step, which results in the full Newton-Raphson method. Thereafter, if convergence problems are experienced, this coefficient is progressively decreased until reaching a zero value, which consists of relying only on the elastic stiffness matrix and thus on the initial-elastic Newton-Raphson method.

The goodness of the convergence is assessed by checking the residual vector trend. In particular, as long as residual values keep decreasing, there is no need to adjust the method. On the other hand, when convergence issues arise (i.e., fluctuating or diverging residual trends), the β parameter is decreased, the problematic-load-step information reset, and the new attempt with a more tolerant stiffness matrix performed.

It is worth noticing that there is no need to perform the maximum number of iterations before changing the value of β, since the residual vector trend is monitored as the iterating algorithm proceeds. Additionally, the switch through the methods is performed only during a problematic load step, restoring then $\beta = 1$ at the end.

5.5.2.1 *Numerical validation*

To highlight the effectiveness of the adaptive algorithm, a moderate tensile strength of $f_t = 0.23\,MPa$ is assigned to the previously described macroelement. The member is subjected to an in-plane cyclic shear load-history, and the response after exceeding its elastic tensile threshold is reported in Figure 5.23 and Figure 5.24.

It can be seen that the full Newton-Raphson (labelled "NR") often could not find any reasonable solution (points not reported in Figure 5.23 and marked with a cross symbol in Figure 5.24) since the exceeding of the tensile strength leads to a significant discontinuity in the tangent stiffness matrix in the neighborhood of two consecutive load steps, causing instability of the algorithm. On the other hand, the adaptive Newton-Raphson (labeled "aNR") always achieve the convergence, keeping the number of iterations reasonable, especially compared to the initial-elastic Newton-Raphson (labeled "mNR").

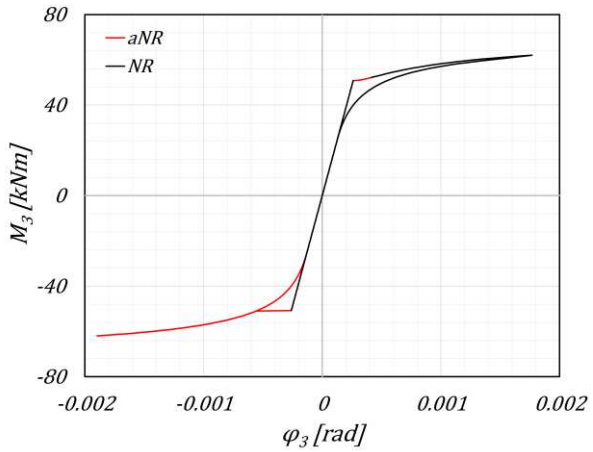

Figure 5.23: Cyclic response comparison between full (NR) and adaptive Newton-Raphson (aNR).

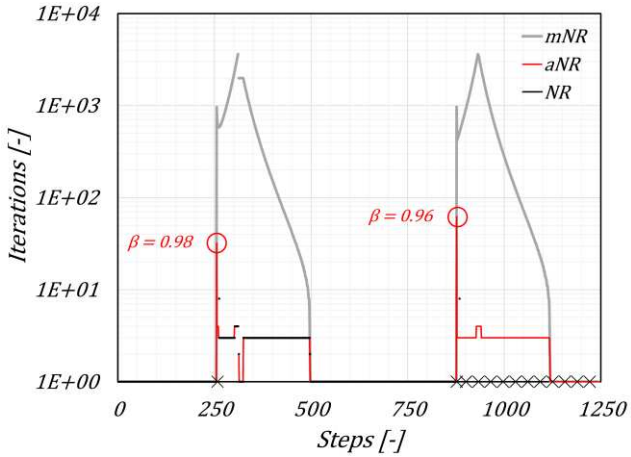

Figure 5.24: Comparison among Newton-Raphson variants in terms of number of iterations per step.

5.6 CONCLUSIONS

In this section, the macroelement of Penna *et al.* (2014) has been comprehensively reviewed to highlight limitations and possible improvements aimed at enhancing its capabilities in capturing the seismic response of a masonry panel. The axial-flexural formulation of the end-interfaces has been mainly addressed, even though some insights have also been given into the shear response of the central body. The end-interfaces resort to an analytical integration to recover the nonlinear behavior starting from the linear elastic response. In this scenario, analytical nonlinear corrections need to be provided, as each nonlinear correction is associated with a particular nonlinear stress profile over the cross-section.

Given the high level of nonlinearity that characterizes the resulting stress profile even for simple constitutive laws, some approximations reported in the original version of the macroelement were unavoidable. However, an additional nonlinear correction has been introduced to enrich the capabilities of capturing toe-crushing phenomena. In this context, the proposed nonlinear corrections proved increased fidelity in the results. Indeed, they effectively reproduced the stress profile obtained with a fiber-discretized cross-section, assumed as a reference.

The original no-tension constitutive law has then been replaced with an elasto-fragile relationship, analytically integrated over the length of the macroelement cross-section. All the possible stress profile conditions have been explained and visually reported, ensuring a straightforward computation of the associated nonlinear corrections. Comparisons with a fiber-discretized cross-section proved not only in-line results, but also higher fidelity in the stress profile. Indeed, the analytical integration of an elasto-fragile constitutive law proved numerical exact results, unlike for the fiber formulation, which needs a dense discretization to replicate the actual stress profile.

Building upon the improved two-dimensional macroelement, the formulation has been extended to the three-dimensional space. More specifically, the out-of-plane and torsional degrees of freedom have been added to the formulation, and a stripe discretization has been introduced along the out-of-plane direction of the macroelement end-interfaces. In this context, the in-plane nonlinear response of each stripe is computed by adopting the analytical integration presented for the two-dimensional macroelement. In contrast, the biaxial sectional response is obtained by integrating the nonlinear corrections of the individual stripes over the thickness of the end-interfaces. Adopting the stripe formulation yielded equivalent results to a fiber-discretized cross-section and a third-party software, but with significant improved computational efficiency due to discretization in the out-of-plane direction only.

Numerical iterative methods to solve the system of equations governing the nonlinear response of the three-dimensional macroelement have then been discussed. In particular, an adaptive Newton-Raphson algorithm has been formulated to combine the numerical robustness of the initial-elastic Newton-Raphson with the quadratic convergence rate of the full Newton-Raphson. Numerical comparisons shown a massive reduction in the number of iterations when the initial-elastic Newton-Raphson method is replaced with its full version. Additionally, the adaptive algorithm proved a promising behavior by consistently achieving convergence in a reasonable number of iterations, offering significant computational advantages.

REFERENCES

Bracchi, S., Galasco, A., and Penna, A. (2021). A Novel Macroelement Model for the Nonlinear Analysis of Masonry Buildings. Part 1: Axial and Flexural Behavior. *Earthquake Engineering & Structural Dynamics*, 50(8), 2233-2252.

Bracchi, S., and Penna, A. (2021). A Novel Macroelement Model for the Nonlinear Analysis of Masonry Buildings. Part 2: Shear Behavior. *Earthquake Engineering & Structural Dynamics*, 50(8), 2212-2232.

Brencich, A., and Lagomarsino, S. (1998). A macro-elements dynamic model for masonry shear walls. *In Proceedings of the STRUMAS IV 4th Int. Symp. On Computer Methods in Structural Masonry*. E&FN Spon: London, 67–75.

Gambarotta, L. and Lagomarsino, S. (1997a). Damage Models for the Seismic Response of Brick Masonry Shear Walls. Part I: The Mortar Joint Model and its Applications. *Earthquake Engineering & Structural Dynamics*, 26(4), 423-439.

Gambarotta, L. and Lagomarsino, S. (1997b). Damage Models for the Seismic Response of Brick Masonry Shear Walls. Part II: The Continuum Model and its Applications. *Earthquake Engineering & Structural Dynamics*, 26(4), 441-462.

Gelfi, P. (2006). Verifica Cemento Armato Stato Limite Ultimo (VCA SLU). *Programmi Gratuiti per l'Ingegneria Civile*, Brescia, Italy (in itaian).

Lagomarsino, S., Penna, A., Galasco, A., and Cattari, S. (2013). TREMURI Program: An Equivalent Frame Model for the Nonlinear Seismic Analysis of Masonry Buildings. *Engineering Structures*, 56, 1787-1799.

Penna, A., Lagomarsino, S., and Galasco, A. (2014). A Nonlinear Macroelement Model for the Seismic Analysis of Masonry Buildings. *Earthquake Engineering & Structural Dynamics*, 43(2), 159-179.

Vanin, F., Penna, A., and Beyer, K. (2020). A Three-Dimensional Macroelement for Modelling the In-Plane and Out-of-Plane Response of Masonry Walls. *Earthquake Engineering & Structural Dynamics*, 49(14), 1365-1387.

6. IMPLEMENTATION OF STRENGTHENING OR REINFORCEMENT

6.1 INTRODUCTION

Most historical centers worldwide are constituted by unreinforced masonry (URM) buildings, often made of natural stones with irregular textures. These constructions are characterized by a high vulnerability when subjected to seismic events, since some intrinsic properties of masonry, such as strong heterogeneity and poor tensile strength, play a predominant role. Furthermore, they have usually been conceived basing on simple proportioning criteria, without an adequate design to withstand vertical or horizontal loads.

Despite the greatest source of vulnerability of this type of constructions is attributable to local mechanisms not adequately restrained, insufficient performance might be exhibited even providing details to ensure a global three-dimensional collaboration between vertical walls and horizontal diaphragms. Consequently, several retrofitting and design techniques are available in the literature and building codes, and are being employed by practitioners to improve the seismic performance of masonry constructions.

This section discusses two improvements on the three-dimensional interface previously described: the first is related to a design approach involving reinforced masonry, where vertical steel rebars are coupled with masonry (Figure 6.1a), whereas the second regards post-applied strengthening surface layers (Figure 6.1b).

It is worth pointing out that the formulations reported in this chapter can be adapted to simulate a broader range of strengthening or reinforcement layouts. However, the treatment is oriented to specific elements or materials for better clarity.

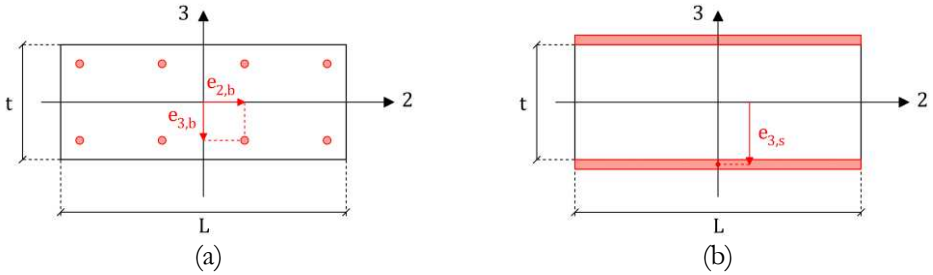

Figure 6.1: (a) Steel rebars and (b) surface layers arrangement on a macroelement interface.

6.2 STEEL REBARS

Steel rebars are implemented following the J2-plasticity theory, which also provide an optional isotropic and kinematic hardening, causing the yielding surface to expand or shift, respectively. Figure 6.2 and Figure 6.3 report the influence of the two types of hardening within the cyclic uniaxial response of a steel rebar with a Young's modulus $E_s = 200\ GPa$ and a yielding stress $\sigma_y = 450\ MPa$.

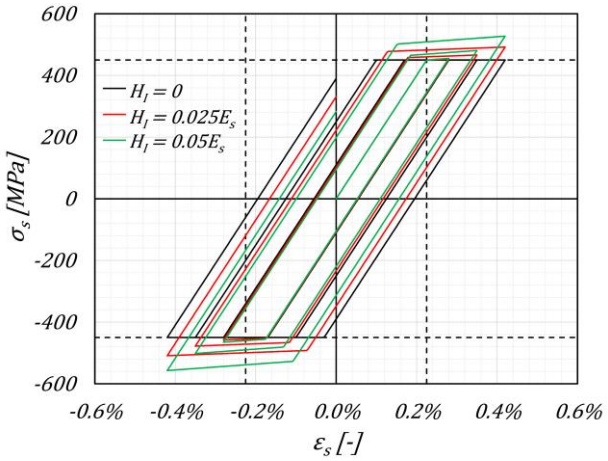

Figure 6.2: Influence of the isotropic hardening parameter H_I on a cyclic response of a steel rebar.

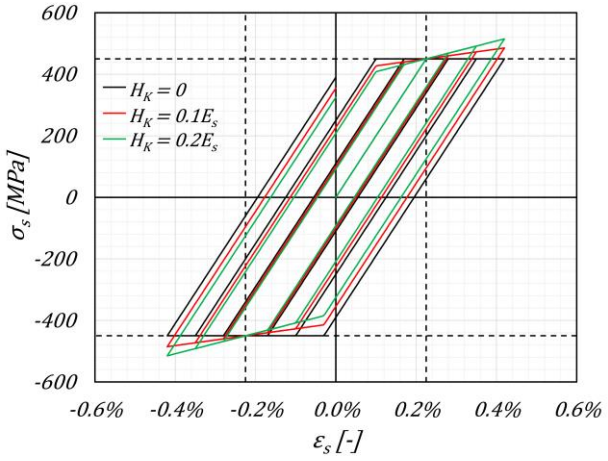

Figure 6.3: Influence of the kinematic hardening parameter H_K on a cyclic response of a steel rebar.

6.2.1 J2-plasticity theory

A brief resume of the J2-plasticity formulation is hereafter described, where equation (6.1) highlights its crucial point, that is, the additive decomposition of the elastic (ε_s^e) and plastic (ε_s^p) components of the total strain (ε_s):

$$\sigma_s = E_s \varepsilon_s^e = E_s\left(\varepsilon_s - \varepsilon_s^p\right) \qquad \varepsilon_s = \varepsilon_s^e + \varepsilon_s^p \tag{6.1}$$

being σ_s the uniaxial stress into the rebar, and E_s its Young's modulus.

When hardening occurs, the value of the yield stress may change. For this reason, plasticity models use a yield function F for mathematically identifying when yielding happens (6.2), together with internal damage variables (α and $\bar{\varepsilon}^p$ for kinematic and isotropic hardening, respectively) to describe its evolution:

$$F = |\Sigma| - \sigma_y(\bar{\varepsilon}^p) \qquad \Sigma = \sigma_s - \alpha \tag{6.2}$$

with σ_y indicating the uniaxial yielding stress. Equations (6.3) describe how the damage variables are defined; in particular, the kinematic variable α is assumed proportional to the plastic deformation, whereas the isotropic hardening is considered linear:

$$\dot{\alpha} = H_K\, \dot{\varepsilon}_s^p \qquad \dot{\varepsilon}_s^p = \gamma\, \mathrm{sgn}(\Sigma) \qquad \sigma_y(\bar{\varepsilon}^p) = \sigma_{y,0} + H_I\, \bar{\varepsilon}^p \qquad \dot{\bar{\varepsilon}}_s^p = \left|\dot{\varepsilon}_s^p\right| \tag{6.3}$$

where H_K and H_I represent the corresponding kinematic and isotropic parameters, respectively.

Since a positive value of the yield function F is not allowed, calculating the amount of plastic flow, and how the hardening level evolves such that $F = 0$, is needed. This is accomplished by solving for a consistency parameter γ. However, the whole process of elastic or elasto-plastic loading and unloading requires a meticulous mathematical description, which has led researchers to use the Kuhn-Tucker conditions (6.4):

$$\gamma \geq 0 \qquad F \leq 0 \qquad \gamma F = 0 \qquad \gamma \dot{F} = 0 \tag{6.4}$$

In order to numerically solve the governing set of equations, the transition from the continuous to the discrete form is needed, and it is reported in equations (6.5), being λ the corresponding consistency parameter in the discrete framework, and indicating with the subscript n the quantities related to the previous load step.

$$\alpha = H_K \, \varepsilon_s^p \qquad \varepsilon_s^p = \varepsilon_{s,n}^p + \lambda \, \mathrm{sgn}(\Sigma) \qquad \bar{\varepsilon}^p = \varepsilon_{s,n}^p + \lambda \tag{6.5}$$

At the beginning of each load step, it is not known a priori whether the new level of stress causes yielding or not. For this reason, a predictor-corrector algorithm is employed. In particular, each new load step is assumed linear elastic (i.e., $\lambda = 0$), the trial stress (differentiated by the superscript TR) is substituted into the yield condition (6.2), and the method for the nonlinear corrector is followed if the stress is not admissible (i.e., $F > 0$). In the latter case, the λ parameter is expressed as:

$$\lambda = \frac{|\Sigma^{TR}| - \sigma_y^{TR}}{E_s + H_I + H_K} \tag{6.6}$$

In the framework of an iterative algorithm, calculating the consistent tangent stiffness operator is necessary. In this context, the derivative of the algorithmic stress with respect to the total strain variable is reported in equation (6.7), being η the tangent hardening parameter.

$$C_T = \frac{\partial \sigma_s}{\partial \varepsilon_s} = \left(\frac{H_I + H_K}{E_s + H_I + H_K} \right) E_s = \eta \, E_s \tag{6.7}$$

6.2.2 Rebars implementation

Rebars are defined as lumped elements along the end-interfaces of the three-dimensional macroelement, and are available in both fiber and stripe formulations. Moreover, only the coupled axial-flexural behavior is influenced, without affecting the shear response.

Kinematic compatibility equations grant proper collaboration between the lumped elements and the end-interfaces, assuming a linear profile for the deformations. In this context, the axial displacement d_p of the b^{th} lumped element is expressed in terms of the end-interface degrees of freedom and of its in-plane ($e_{2,b}$) and out-of-plane ($e_{3,b}$) eccentricities with respect to the centroid of the section (Figure 6.1a):

$$d_b = w + \varphi_2 \, e_{3,b} - \varphi_3 \, e_{2,b} \tag{6.8}$$

Given the axial displacement of the individual element, the corresponding stress and strains are computed, and the predictor-corrector algorithm applied. The strain can be easily recovered from the axial displacement by dividing by half of the height of the macroelement. This equivalence is indeed necessary to preserve the correct axial stiffness

of the element (Penna *et al.*, 2014; Bracchi *et al.*, 2021), as the formulation concentrates the axial-flexural response at the end-interfaces of the macroelement.

The three-dimensional contribution of the lumped elements to the end-interfaces is then derived from equation (6.9) and (6.10), where $\boldsymbol{K_i^{rb}}$, $\boldsymbol{K_j^{rb}}$, $\boldsymbol{F_j^{rb}}$ and $\boldsymbol{F_j^{rb}}$ represent the local elastic axial-flexural stiffness matrix and the corresponding nonlinear vector related to the i^{th} and j^{th} end-interfaces, respectively:

$$\boldsymbol{K_i^{rb}} = \boldsymbol{K_j^{rb}} = \sum_b \begin{bmatrix} k_b\, A_b & k_b\, A_b\, e_{3,b} & -k_b\, A_b\, e_{2,b} \\ k_b\, A_b\, e_{3,b} & k_b\, A_b\, e_{3,b}^2 & -k_b\, A_b\, e_{2,b}\, e_{3,b} \\ -k_b\, A_b\, e_{2,b} & -k_b\, A_b\, e_{2,b}\, e_{3,b} & k_b\, A_b\, e_{2,b}^2 \end{bmatrix} \tag{6.9}$$

$$\boldsymbol{F_i^{rb}} = \sum_b \begin{Bmatrix} k_b\, A_b\, d_{p,b} \\ k_b\, A_b\, d_{p,b}\, e_{3,b} \\ -k_b\, A_b\, d_{p,b}\, e_{2,b} \end{Bmatrix} \qquad \boldsymbol{F_j^{rb}} = \sum_b \begin{Bmatrix} -k_b\, A_b\, d_{p,b} \\ k_b\, A_b\, d_{p,b}\, e_{3,b} \\ -k_b\, A_b\, d_{p,b}\, e_{2,b} \end{Bmatrix} \tag{6.10}$$

with $k_b = 2E_s/h$ and A_b indicating the equivalent axial stiffness and the area of the b^{th} rebar, $e_{2,b}$ and $e_{3,b}$ its local coordinates with respect to the centroid of the section (Figure 6.1a), whereas $d_{p,b}$ denotes the plastic displacement corresponding to the plastic strain reached. The consistent interface-level tangent stiffness matrix is simply obtained by multiplying the local elastic stiffness matrix by the tangent hardening parameter η, as described in equation (6.7). No contribution is given by the nonlinear vectors.

After assembling the interface-level contributions and corresponding nonlinear vectors, the macroelement-level matrices are obtained by properly arranging the individual terms, as described in Appendix D.

6.2.3 Numerical validation

In-plane (Figure 6.4) and out-of-plane (Figure 6.5) cyclic rotations are applied to a section with a length-to-thickness ratio $L/t = 5$, a Young's modulus of $E = 2310\ MPa$, a compressive strength $f_m = 3.60\ MPa$, a constant axial load $\sigma = 0.30 f_m$, and a no-tension behavior. The responses with and without lumped reinforcement are compared. In particular, the latter is characterized by four $8\text{-}mm$-diameter steel rebars with Young's modulus $E_s = 200\ GPa$, yielding stress $\sigma_y = 450\ MPa$, and no hardening, arranged at the corners of the section.

The results prove an increase in the lateral strength, whereas the initial stiffness remains almost unaffected, as expected. Furthermore, as previously discussed, the in-plane approximations on the masonry response that characterize the stripe formulation play a role only during the unloading phase of the load history. Consequently, the amount of

energy dissipation, as well as residual displacements, are slightly influenced (Figure 6.4). However, it is worth noticing that since in Figure 6.5 a pure out-of-plane loading is applied, no influence by the approximations of the analytical in-plane integration is experienced. For this reason, the stripe and the fiber section give the same results.

Additionally, the in-plane and out-of-plane ultimate bending moments are computed using the software VCA SLU (Gelfi, 2006), showing a satisfactory agreement with the presented results.

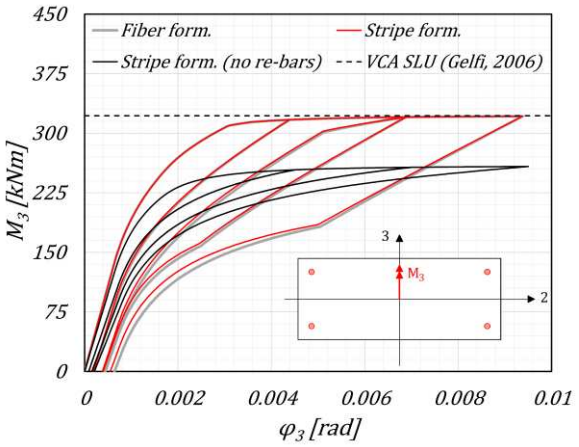

Figure 6.4: In-plane response of an interface with and without lumped reinforcement.

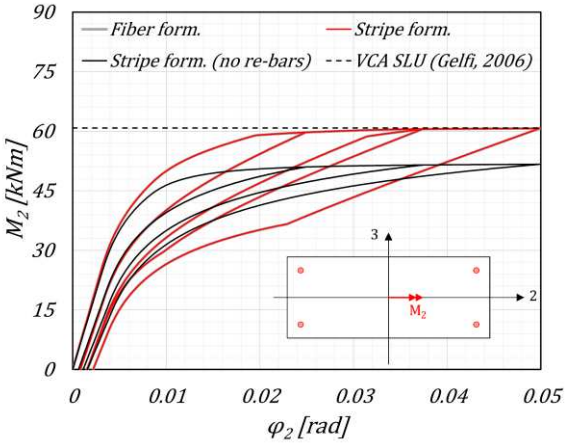

Figure 6.5: Out-of-plane response of an interface with and without lumped reinforcement.

6.3 SURFACE LAYERS

Surface layers are implemented following both an analytical and a fiber formulation, regardless of the macroelement cross-section discretization. In particular, in the first case, the stripe discretization previously described is employed. In fact, the assembling algorithm proposed proved particularly suitable for adding analytical stripes with different material properties or behaviors. Consequently, an analytical no-compression brittle-tensile relationship is adopted (Figure 6.6a). However, the constitutive law developed in the previous chapters can also be used (Figure 6.6b).

Double-sided, as well as single-sided, applications are available. In the latter case, the static moment along the 2-axis should also be computed to account for the asymmetry of the behavior. In fact, the original location of the interface degrees of freedom is no longer barycentric. Additional information on the complete elastic stiffness matrix of the surface layers can be found in Appendix C.

It is worth noticing that the shear-strengthening contribution of the additional surface layers is currently not accounted for, if not in terms of elastic response, but it will be added to the formulation in the future.

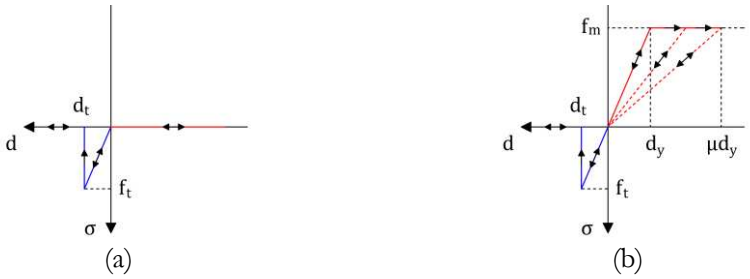

Figure 6.6: Surface layers constitutive laws implemented.

6.3.1 Numerical validation

Numerical in-plane and out-of-plane cyclic tests are performed on a section with a length-to-thickness ratio $L/t = 5$, a Young's modulus of $E = 2310\ MPa$, a compressive strength $f_m = 3.24\ MPa$, and a constant axial load $\sigma = 0.25 f_m$. A double-sided strengthening configuration is adopted, assuming a 0.06 - mm -thick mesh with Young's modulus $E_f = 200\ GPa$ and tensile strength $f_f = 1600\ MPa$, compatible with a FRCM jacketing intervention. In this context, a no-compression constitutive law is employed. On the contrary, a no-tension response is assigned to the masonry material.

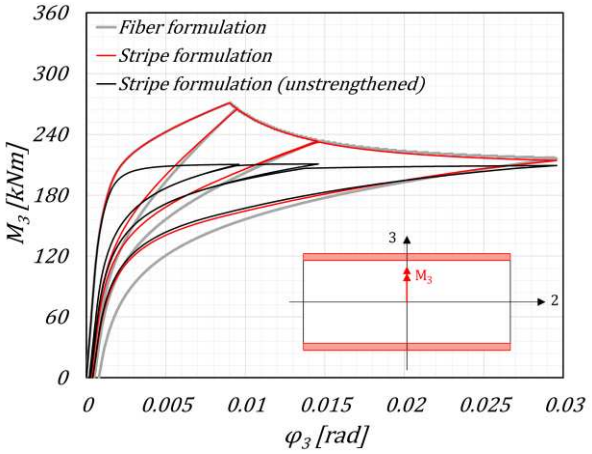

Figure 6.7: In-plane response of an interface with and without FRCM strengthening.

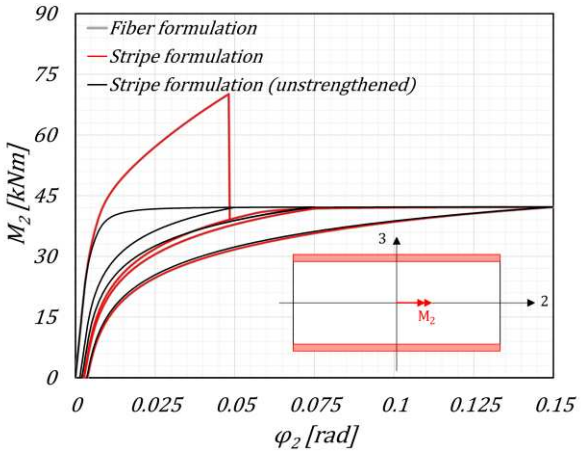

Figure 6.8: Out-of-plane response of an interface with and without FRCM strengthening.

The in-plane response shows a stiffness and strength decay as the tensile damage accumulates, in line with the brittle nature of the constitutive law (Figure 6.7). In fact, as the tensile strength is progressively exceeded, the results tend to match the unstrengthened configuration curve.

Differently, since the absence of a continuous strengthening along the out-of-plane axis, after reaching the tensile strength of the most external layer, a significant discontinuity arises, leading to a sudden drop in strength and stiffness (Figure 6.8). Moreover, as already highlighted, no influence by the approximations of the analytical in-plane integration is experienced, since a pure out-of-plane loading is applied.

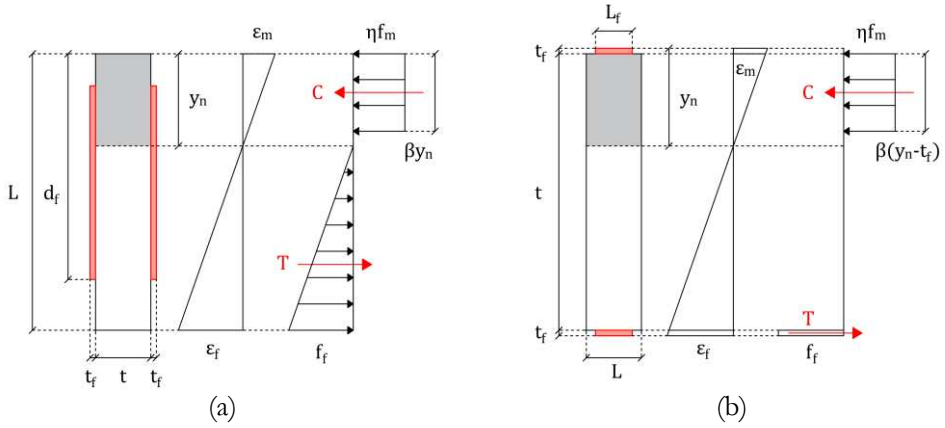

Figure 6.9: Assumptions on the stress profile for an (a) in-plane and an (b) out-of-plane response.

The Italian guidelines (CNR, 2018) provide design provisions to evaluate the ultimate bending moment (M_u) of a masonry panel strengthened with FRCM jacketing applications. More specifically, they provide different analytical formulations basing upon the constitutive law assumed for the masonry material. In this context, the common equivalent rectangular stress-block can be replaced with a more refines relationships accounting for an initial elastic branch. Conversely, a no-compression elasto-fragile behavior in tension is assumed for the FRCM mesh, thus ignoring the any mortar contribution.

In the following, the formulae consistent with the stress-block hypothesis are reported, the ultimate in-plane and out-of-plane bending moments are computed, and the results are compared with the previous numerical outcomes. Figure 6.9 reports the assumptions on the stress profile for an in-plane (Figure 6.9a) and an out-of-plane (Figure 6.9b) loading.

The CNR (2018) provide different relationships depending upon which material attains its ultimate deformation first. The neutral axis should be computed following both the formulations. Then, an a posteriori check on the admissible deformations needs to be performed to ensure the correct assumption.

i. In case the ultimate deformation of masonry in compression ε_{mu} is attained before reaching the ultimate deformation of the FRCM mesh in tension ε_{fu}, the neutral axis y_n and the corresponding ultimate in-plane bending moment M_u are computed according to equations (6.11) and (6.12):

$$y_n^{IP} = \frac{N - E_f\, t_{2f}\, d_f\, \varepsilon_{mu} + \sqrt{N^2 + 2\, E_f\, t_{2f}\, d_f\, \varepsilon_{mu}\left(\eta\, \beta\, t\, f_m\, d_f - N\right)}}{2\, \eta\, \beta\, f_m\, t - E_f\, t_{2f}\, \varepsilon_{mu}} \tag{6.11}$$

$$M_u^{IP} = \frac{\eta\,\beta\,f_m\,y_n}{2}\,(L - \beta\,y_n) + \frac{(d_f - y_n)^2}{12\,y_n}\varepsilon_{mu}\,E_f\,t_{2f}\,(4d_f - 3L + 2y_n) \quad \textbf{(6.12)}$$

Similarly, equations (6.13) and (6.14) refer to an out-of-plane loading:

$$y_n^{OOP} = t_f + \frac{N - E_f\,t_f\,L_f\,\varepsilon_{mu} + \sqrt{(t_f\,L_f\,E_f\,\varepsilon_{mu} - N)^2 + 4\,\eta\,\beta\,f_m\,L\,t_f\,L_f\,E_f\,\varepsilon_{mu}\,(2t_f + t)}}{2\,\eta\,\beta\,f_m\,L} \quad \textbf{(6.13)}$$

$$M_u^{OOP} = \frac{\eta\,\beta\,f_m\,L}{2}\,(y_n - t_f)\left[(1+\beta)t_f + t - \beta\,y_n\right] + t_f\,L_f\,E_f\,\varepsilon_{mu}\left[\frac{2t_f + t - y_n}{2(y_n - t_f)}\right](t_f + t) \quad \textbf{(6.14)}$$

where d_f is the distance between the compressed edge of the masonry section and the fiber of the FRCM mesh furthest from it, L_f is the length of the layers, N is the axial load applied, whereas η and β are the rectangular stress-block factors for masonry in compression. Eventually, $t_{2f} = 2t_f$, with t_f the thickness of the individual layer, as double-sided application.

ii. In case the ultimate deformation of the FRCM mesh in tension ε_{fu} is attained before reaching the ultimate deformation of masonry in compression ε_{mu}, the neutral axis y_n and the ultimate bending moment M_u are computed following equations (6.15) and (6.16) for an in-plane loading condition:

$$y_n^{IP} = \frac{2\,N + d_f\,E_f\,t_{2f}\,\varepsilon_{fu}}{2\,\eta\,\beta\,f_m\,t + E_f\,t_{2f}\,\varepsilon_{fu}} \quad \textbf{(6.15)}$$

$$M_u^{IP} = \frac{\eta\,\beta\,f_m\,y_n}{2}\,(L - \beta\,y_n) + \frac{(d_f - y_n)}{12}\varepsilon_{fu}\,E_f\,t_{2f}\,(4d_f - 3L + 2y_n) \quad \textbf{(6.16)}$$

and following equations (6.17) and (6.18) for an out-of-plane loading:

$$y_n^{OOP} = t_f + \frac{N + t_f\,L_f\,\varepsilon_{fu}\,E_f}{\eta\,\beta\,f_m\,L} \quad \textbf{(6.17)}$$

$$M_u^{OOP} = \frac{\eta\,\beta\,f_m\,L}{2}\,(y_n - t_f)\left[(1+\beta)t_f + t - \beta\,y_n\right] + \frac{t_f\,L_f\,E_f\,\varepsilon_{mu}}{2}(t_f + t) \quad \textbf{(6.18)}$$

Since the constitutive laws implemented in the proposed macroelement rely on a perfectly plastic response in compression without any ductility limitation for the masonry material,

the maximum values of the in-plane and out-of-plane bending moment reported in Figure 6.7 and Figure 6.8 should be compared with the result provided through equation (6.16) and (6.18). However, an a posteriori check is performed to individuate the bending moment associated with the attainment of the ultimate admissible deformation of the masonry material, assumed $\varepsilon_{mu} = 0.35\%$, and the results are compared to equations (6.12) and (6.14).

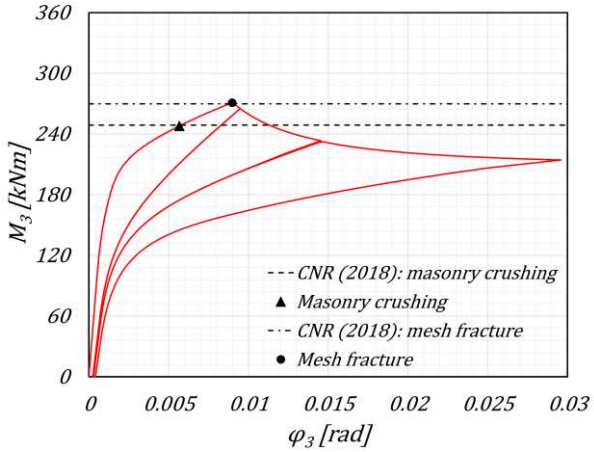

Figure 6.10: In-plane response: comparison between stripe formulation and CNR (2018) limit state predictions.

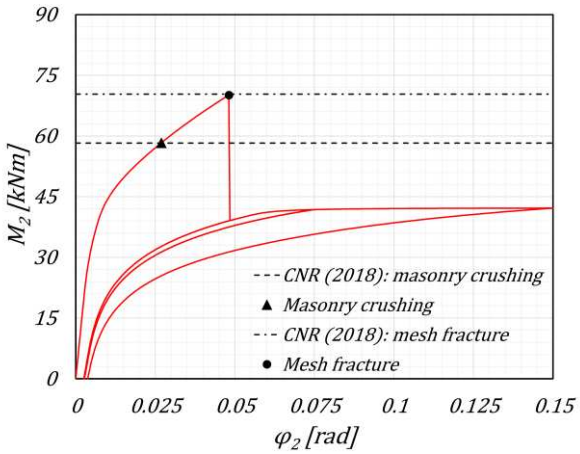

Figure 6.11: Out-of-plane response: comparison between stripe formulation and CNR (2018) limit state predictions.

In this context, Figure 6.10 and Figure 6.11 depict the results obtained by adopting the stripe formulation, and highlight the limit states associated with the crushing of the masonry and the fracture of the strengthening mesh. The comparison with the CNR (2018) predictions is also reported. In particular, a value $\beta = 0.8$ is assumed for the depth of the stress-block idealization, whereas the η coefficient is chosen equal to a unit value to be consistent with the compressive strength assigned to the numerical model. Eventually, $d_f = L_f = L$, as the FRCM strengthening is applied on the entire length of the section.

The numerical outcomes satisfactory match with the CNR (2018) predictions. In fact, the stress profiles assumed by the Italian guidelines closely reflect the constitutive laws assigned to the numerical model.

6.4 BUILDING-PHASE SEQUENCE

As well-known and already discussed, there are several reasons why a masonry building may need to be retrofitted, being the improvement of the seismic performance the most common. However, when assessing a retrofitted construction, accounting for the building phase sequence might be a discriminant in predicting the lateral response and consequent damage pattern. As a matter of fact, some retrofitting systems need to be applied to the already-statically loaded structure (e.g., jacketing or near-surface-mounted bars applications). For this reason, surface layers are endowed with an additional variable acting as a triggering point.

The selective activation is hence accomplished by calculating the strengthening contribution using a corrected global displacement vector. The latter is obtained by subtracting the global displacement vector resulting from the step prior to the surface layer activation $\boldsymbol{u_{bf}}$, from the current global displacement vector $\boldsymbol{u}$. Eventually, the governing nonlinear system of equations can be summarized as reported in equation (6.19):

$$\boldsymbol{F^{int}(u) = F_m^{int}(u) + F_{rb}^{int}(u) + F_{sl}^{int}(u, u_{bf})} \tag{6.19}$$

being $\boldsymbol{F_m^{int}(u)}$, $\boldsymbol{F_{rb}^{int}(u)}$, and $\boldsymbol{F_{sl}^{int}(u, u_{bf})}$ the internal force vectors related to masonry, rebars, and surface layers contributions, respectively reported in equation (6.20), where $\boldsymbol{K_{rb}}$ and $\boldsymbol{F_{rb}(u)}$ indicate the elastic stiffness matrix and the corresponding nonlinear plastic vector related to the rebars, whereas $\boldsymbol{K_{sl}}$, $\boldsymbol{F_{sl}^{*}(u, u_{bf})}$, and $\boldsymbol{F_{sl}^{**}(u, u_{bf})}$ represent the elastic stiffness matrix and the nonlinear correction vectors accounting for the analytical tensile and compressive behaviors of the surface layers. A similar procedure could be applied to lumped elements, but it is not discussed in this thesis.

$$\begin{cases} \boldsymbol{F}_{\boldsymbol{m}}^{\boldsymbol{int}}(\boldsymbol{u}) = \boldsymbol{K}\boldsymbol{u} + \boldsymbol{F}^{*}(\boldsymbol{u}) + \boldsymbol{F}^{**}(\boldsymbol{u}) \\ \boldsymbol{F}_{\boldsymbol{rb}}^{\boldsymbol{int}}(\boldsymbol{u}) = \boldsymbol{K}_{\boldsymbol{rb}} \cdot \boldsymbol{u} + \boldsymbol{F}_{\boldsymbol{rb}}(\boldsymbol{u}) \\ \boldsymbol{F}_{\boldsymbol{sl}}^{\boldsymbol{int}}(\boldsymbol{u}, \boldsymbol{u}_{\boldsymbol{bf}}) = \boldsymbol{K}_{\boldsymbol{sl}} \cdot (\boldsymbol{u} - \boldsymbol{u}_{\boldsymbol{bf}}) + \boldsymbol{F}_{\boldsymbol{sl}}^{*}(\boldsymbol{u}, \boldsymbol{u}_{\boldsymbol{bf}}) + \boldsymbol{F}_{\boldsymbol{sl}}^{**}(\boldsymbol{u}, \boldsymbol{u}_{\boldsymbol{bf}}) \end{cases} \quad (6.20)$$

6.5 CONCLUSIONS

Building upon the three-dimensional end-interface formulation established in Chapter 5, this section presented further enhancements to include lumped and distributed reinforcements. The out-of-plane discretization effectively facilitated the introduction of additional stripes with different material properties, thereby explicitly simulating surface strengthening applications. Lumped elements have also been included to enhance versatility and potentially address reinforced masonry design approaches. A detailed description of the uniaxial J2-plasticity theory has been provided at the beginning, as it served as the foundation for the constitutive law governing these elements. On the other hand, an on-purpose elasto-fragile no-compression constitutive law, analytically integrated over the length of the additional stripes, has been formulated. In fact, strengthening applications usually resort to material with significant tensile strength to overcome the corresponding significant deficiency of unreinforced masonry.

Numerical comparison with third-party software and analytical formulae proposed by the Italian guidelines promoted the features developed in this section as a feasible approach to simulate strengthened and reinforced masonry elements. Furthermore, numerical results have shown no tangible difference when adopting a fiber discretization of the additional layers, highlighting the attractiveness of the computationally efficient stripe discretization.

Finally, insights have been given into staged construction modeling. This technique enables the definition of a sequence of construction or application phases, which is crucial to effectively simulate the stress flow into the elements. Indeed, strengthening layers are typically applied to existing structures, thus to already-statically loaded or even damaged structures, and this has been numerically accomplished by introducing a triggering variable and by computing the strengthening contribution through a corrected displacement vector.

REFERENCES

Bracchi, S., Galasco, A., and Penna, A. (2021). A Novel Macroelement Model for the Nonlinear Analysis of Masonry Buildings. Part 1: Axial and Flexural Behavior. *Earthquake Engineering & Structural Dynamics*, 50(8), 2233-2252.

CNR (2018). CNR DT 215/2018. Istruzioni per la progettazione, l'esecuzione ed il controllo di interventi di consolidamento statico mediante l'utilizzo di compositi fibrorinforzati a matrice inorganica, *Consiglio Nazionale delle Ricerche*, Rome, Italy (in Italian).

Gelfi, P. (2006). Verifica Cemento Armato Stato Limite Ultimo (VCA SLU). *Programmi Gratuiti per l'Ingegneria Civile*, Brescia, Italy (in itaian).

Penna, A., Lagomarsino, S., and Galasco, A. (2014). A Nonlinear Macroelement Model for the Seismic Analysis of Masonry Buildings. *Earthquake Engineering & Structural Dynamics*, 43(2), 159-179.

7. A MACROELEMENT FORMULATION FOR MODELING STRENGTHENED AND REINFORCED MASONRY ELEMENTS

(Accepted) Salvatori, C., Guerrini, G., Galasco, A., and Penna, A. (2024). A Macroelement Formulation for Modeling Strengthened and Reinforced Masonry Elements. *In Proceedings of the 18th International Brick and Block Masonry Conference (IB2MaC)*, Birmingham, UK.

ABSTRACT

The poor performance often exhibited by historical masonry buildings in seismic events has prompted the development of strengthening interventions to improve the response of existing structures on one hand, and the adoption of reinforced and confined masonry systems for new buildings on the other hand. Several retrofit solutions consist of adding materials with significant tensile strength to the masonry walls, for example by jacketing with fabric- or composite-reinforced mortars, by inserting near-surface-mounted bars, or by connecting steel or timber exoskeletons. Similarly, reinforced and confined masonry elements incorporate steel or composite bars directly within the masonry or into reinforced concrete ties cast against it.

This paper discusses a new three-dimensional macroelement, developed to explicitly model the effects of tensile reinforcement on both in-plane and out-of-plane axial-flexural responses; this will enhance the accuracy of nonlinear global seis-mic analyses compared to modeling the in-plane response only and to adopting empirical correction coefficients for masonry mechanical properties. The formulation encompasses surface layers and lumped fibers, which enables representing various strengthening and reinforcing layouts. Adopting an axial-flexural behavior integrated over stripes can reduce the computational effort compared to a complete cross-section fiber discretization. The nonlinear shear response of the retrofit material can be also incorporated in the macroelement but is not discussed in this paper.

Keywords: nonlinear macroelement, strengthening interventions, quasi-static cyclic shear-compression tests, stone masonry, CRM jacketing.

7.1 INTRODUCTION

Unreinforced masonry (URM) buildings are one of the prevailing construction typologies populating historical centers worldwide. However, the well-known seismic vulnerability that characterizes these structures has prompted the development of effective, efficient, and sustainable strengthening solutions to enhance their seismic performance in terms of lateral strength and displacement capacity.

Several in-plane and out-of-plane retrofit systems were investigated over the last few decades. A pioneering strengthening intervention involved jacketing with the so-called reinforced plaster, in which welded-wire steel meshes were embedded in concrete layers directly applied to one or both sides of the masonry wall. However, drawbacks related to steel corrosion and concrete chemical compatibility with historical materials encouraged the exploration of alternative solutions.

Technological advancements resulted in jacketing with Fiber-Reinforced Polymer (FRP) stripes or sheets. The reduced thicknesses of these materials allowed also to overcome the significant increase in weight and stiffness associated with reinforced plaster. However, their direct application to the masonry substrate is now discouraged, as the epoxy matrix might compromise the preservation and durability of historical structures (Papanicolaou *et al.*, 2008; Valluzzi *et al.*, 2014).

More recent developments involve jacketing with Composite-Reinforced Mortars (CRM) or Fabric-Reinforced Cementitious Matrices (FRCM), in which an FRP mesh or a flexible fabric is embedded in appropriate inorganic matrices to ensure chemical compatibility with the existing masonry substrate (Prota *et al.*, (2006); Gattesco *et al.*, 2015; Del Zoppo *et al.*, (2019); Guerrini *et al.*, 2021a). Another retrofit solution, initially developed for strengthening reinforced concrete elements and then extended to URM walls, consists of Near-Surface-Mounted (NSM) reinforcement (Kashani *et al.*, 2023), where FRP bars are embedded in grooves or slots cut into the masonry surface.

Despite these advancements, national and international building codes lack standardized prescriptions for modeling and evaluating the effectiveness of most of these strengthening intervention on existing masonry structures, merely providing empirical correction coefficients for the masonry mechanical properties. For this reason, this paper discusses a novel three-dimensional macroelement formulation developed to explicitly capture the in-plane and out-of-plane axial-flexural influence of a strengthening intervention, and the response of newly built reinforced or confined masonry.

The formulation consists of an improved version of the macroelement proposed by Brencich *et al.* (1998), Penna *et al.* (2014), and Bracchi *et al.* (2021), laying the basis for an

effective and efficient modeling of a strengthened masonry panel. In fact, the original in-plane axial-flexural formulation is first extended to the three-dimensional space, and then further enhanced to incorporate additional reinforcement. Furthermore, the formulation provides both a stripe and a fiber discretization of the cross-section: the first approach favors computational efficiency, as each stripe is analytically integrated along its length, while the second one allows the adoption of more refined constitutive laws.

Eventually, the capabilities of the proposed formulation are proved through the simulation of an experimental quasi-static cyclic shear-compression test involving a stone masonry pier retrofitted with a CRM system (Guerrini *et al.*, 2023). The shear strengthening effect of CRM is still modeled through an improved masonry tensile strength, as the specimen did not experience this type of failure; however, its contribution will be explicitly incorporated within the shear formulation in the future.

7.2 THREE-DIMENSIONAL MACROELEMENT FORMULATION

Among other numerical formulations (Magenes and Della Fontana, 1998; Raka *et al.*, 2015; Pantò *et al.*, 2017; Pantò *et al.*, 2018), the macroelement proposed by Penna *et al.* (2014) has been widely adopted and validated in the equivalent-frame modeling of URM structures over the years. In fact, its efficient formulation allows to reproduce the main in-plane failure mechanisms of a masonry panel with a limited number of degrees of freedom. Consequently, it significantly reduces the computational effort, making it suitable for nonlinear static and dynamic analyses of URM buildings.

The macroelement by Penna *et al.* (2014) comprises three parts (Figure 7.1a): a central body, susceptible to shear deformations only, and two end-interfaces, where the coupled axial-flexural response is concentrated (Figure 7.1b,c,d). In particular, the nonlinear axial-flexural behavior is retrieved through an analytical integration, allowing to capture two-dimensional phenomena without needing to numerically integrate a fiber section. Additionally, shear deformations are not allowed in the interfaces, making shear and flexural failure mechanisms kinematically uncoupled. The original macroelement formulation is limited to the in-plane response, suppressing the torsional degree of freedom φ_1 and the out-of-plane degrees of freedom φ_2 and v_3.

This macroelement has been widely investigated over the past, overcoming some of its limitations and enhancing its capabilities (Bracchi *et al.*, 2021; Bracchi and Penna, 2021). However, the formulation has always been restricted to the in-plane response of homogeneous material elements. For this reason, a novel three-dimensional version of the Penna *et al.* (2014) macroelement was developed, adding the torsional and out-of-plane degrees of freedom (Figure 7.1a,b).

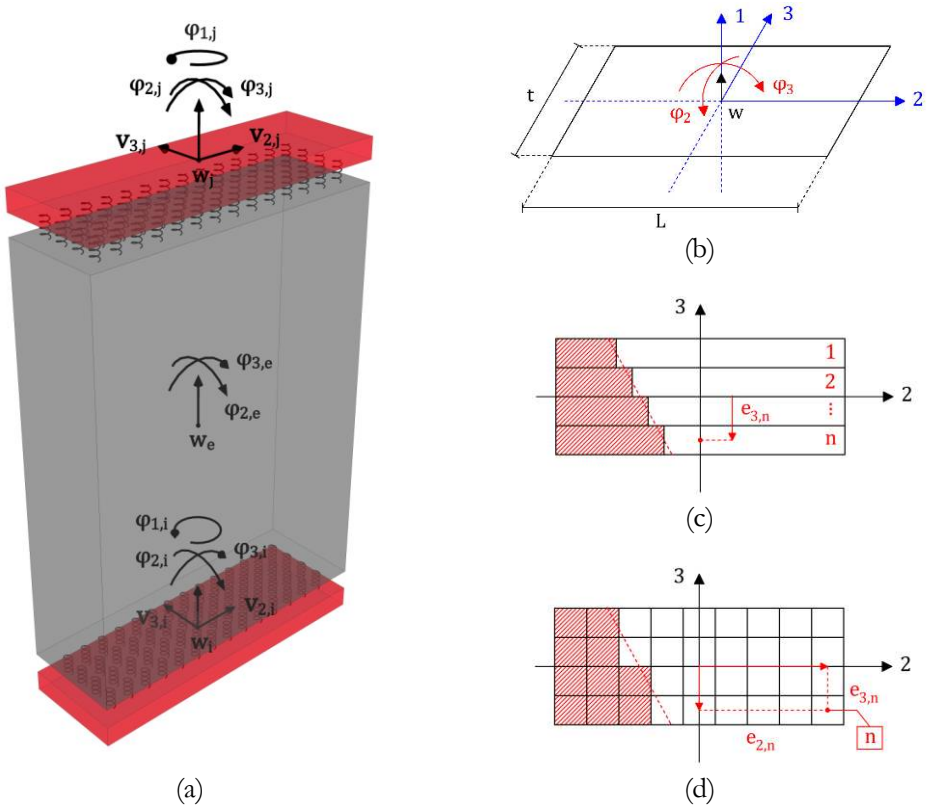

Figure 7.1: Three-dimensional macroelement: (a) node and central-body degrees of freedom, (b) end-interface degrees of freedom, (c) stripe discretization, and (d) fiber discretization of the cross-section.

To account for the biaxial flexural response, the end-interfaces of the macroelement are discretized in a series of homogeneous stripes (Figure 7.1c), starting from the work carried out by Vanin *et al.* (2020). Furthermore, assigning different mechanical properties to each individual stripes allows for the explicit incorporation of different material layers through the thickness of the macroelement.

The analytically integrated formulation is still adopted for the in-plane response of each stripe (Penna *et al.*, 2014). Instead, the combined sectional in-plane and out-of-plane behavior is computed by numerically integrating all stripe contributions over the thickness of the macroelement, accounting for their out-of-plane eccentricity e_3 with respect to the centroid of the cross-section. As a result, a computationally efficient formulation is preserved, as cross-section discretization and numerical integration involve the out-of-plane direction only.

Kinematic compatibility equations enforce collaboration of the individual stripes, assuming a linear profile for the deformations. In this context, the vertical displacement w_n and the in-plane rotation $\varphi_{3,n}$ of the n^{th} stripe are defined according to equation (7.1):

$$w_n = w + \varphi_2 \, e_{3,n} \qquad \varphi_{3,n} = \varphi_3 \tag{7.1}$$

where the interface degrees of freedom w, φ_2, and φ_3 are reported in Figure 7.1b, representing the relative generalized displacements between the node and the central body.

Despite the potentialities of the stripe formulation, the analytical integration restricts the use to simple constitutive laws to represent the axial-flexural response of a masonry member, such as the one proposed by Penna *et al.* (2014). A no-tension response captures the low cracking resistance of the cross-section, whereas an elastic-perfectly plastic behavior in compression addresses crushing phenomena. The progressive stiffness decay of the material due to cyclic loadings is simulated through a recentering unloading branch (Figure 7.2a), which might not adequately capture the residual displacements, underestimating damage accumulation and hysteretic energy dissipation.

To overcome this limitation, the interfaces of the macroelement also implement a full-fiber discretization (Figure 7.1d), granting more flexibility. Moreover, Bracchi *et al.* (2021) proposed an unloading branch parallel to the initial-elastic one (Figure 7.2b), which is currently available only with the fiber formulation but will be incorporated in the stripe formulation in the future.

Similarly to the original Penna *et al.* (2014), the shear and torsional response of the macroelement are embedded in the central body. In this context, the first is governed by the constitutive law obtained from the macroscopic integration of the Gambarotta and Lagomarsino (1997a,b) continuum model for masonry, considered completely uncoupled along the two main horizontal directions, whereas the second relies on a linear elastic response.

Figure 7.2: Constitutive laws for masonry at the end interfaces of the macroelement: (a) Penna *et al.* (2014) and (b) Bracchi *et al.* (2021).

7.3 IMPLEMENTATION OF STRENGTHENING OR REINFORCEMENT

The stripe formulation allows a straightforward implementation of additional layers with different mechanical properties and constitutive relationships, suitable to explicitly model surface strengthening interventions, such as jacketing (Figure 7.3a). Additionally, it can be easily coupled with lumped fibers, representing NSM applications or embedded rebars, also enabling the explicit simulation of reinforced and confined masonry (Figure 7.3b).

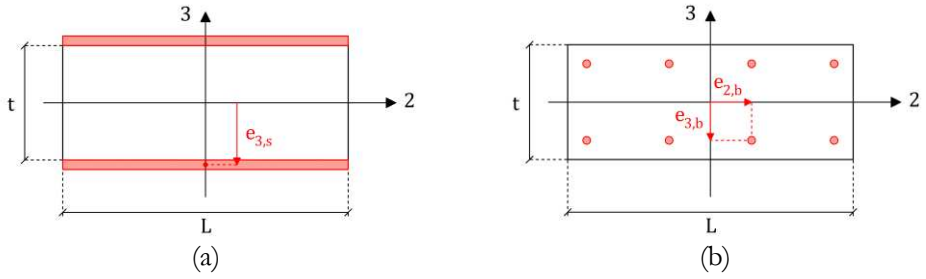

Figure 7.3: Additional strengthening/reinforcement at the end interfaces: (a) surface layers and (b) lumped elements.

7.3.1 Surface layers

As previously discussed, jacketing applications consist of additional layers with significant tensile strength (and sometimes stiffness) applied to one side or to both sides of the masonry surface. Similarly, the numerical axial-flexural contribution is accounted for by defining additional stripes at the macroelement interfaces, whose vertical displacements and in-plane rotations are obtained following compatibility equations (7.1). The shear contribution of the additional layers is currently not included, but will be added in the future to the central-body response.

Surface layers are available with both an analytically integrated and a discretized fiber formulation, regardless of the masonry cross-section discretization (Figure 7.3a). In the first case, a no-compression elasto-fragile tensile constitutive law is analytically integrated over the length of the additional stripes (Figure 7.4a). Moreover, their compressive response can also be incorporated with the original elastic-perfectly plastic recentering model (Penna *et al.*, 2014), leading to the relationship reported in Figure 7.4b.

Figure 7.4: Elasto-fragile tensile constitutive laws for strengthening/reinforcement at the end interfaces: (a) no-compression and (b) elastic-perfectly plastic recentering in compression.

On the other side, as for the cross-section of the masonry, a full-fiber discretization of the additional layers grants more flexibility in choosing the stress-strain relationship. The same constitutive laws reported in Figure 7.4 can be adopted for a direct comparison between fiber and stripe formulations.

7.3.2 Lumped reinforcement

Flexural strengthening with NSM bars or reinforcement with steel rebars embedded into the masonry can be simulated through additional lumped elements with a uniaxial stress-strain relationship.

Kinematic compatibility equations grant proper collaboration of the lumped reinforcement with the interfaces, imposing their axial displacement d_b as a function of the interface degrees of freedom and of the reinforcement in-plane (e_2) and out-of-plane (e_3) eccentricities with respect to the centroid of the section (equation (7.2), Figure 7.1b and Figure 7.3b):

$$d_b = w + \varphi_2 \, e_{3,b} - \varphi_3 \, e_{2,b} \tag{7.2}$$

For steel rebars an elastic-plastic behavior is implemented. In this context, the constitutive law is formulated following the J2-plasticity theory, which provides an optional isotropic and kinematic hardening, causing the yielding domain to expand (Figure 7.5a) or shift (Figure 7.5b), respectively.

For brittle composite reinforcing or NSM bars, the constitutive law shown in Figure 7.4a may be more suitable, neglecting their contribution in compression.

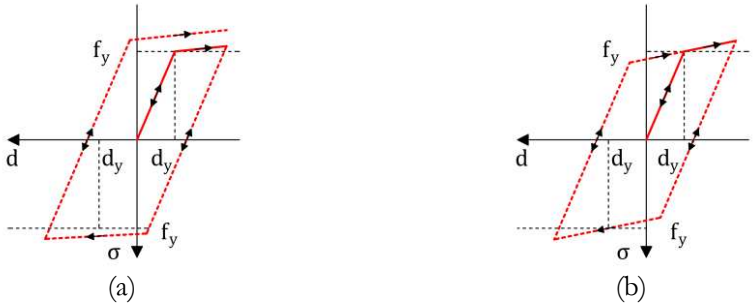

Figure 7.5: Elasto-plastic constitutive laws for strengthening/reinforcement at the end interfaces: (a) isotropic and (b) kinematic hardening.

7.4 VALIDATION AGAINST EXPERIMENTAL RESULTS

The macroelement proposed in this paper is used to simulate a strengthened masonry pier subjected to a quasi-static cyclic shear-compression test, which experienced a rocking failure mechanism. The experimental program was conducted at the Department of Civil Engineering and Architecture of the University of Pavia and at the EUCENTRE Foundation facilities in Pavia, Italy (Guerrini *et al.*, 2023).

7.4.1 Specimen and testing protocol

The specimen consisted in a masonry pier bounded by two windows (Figure 7.6). As a result, portions of spandrels above and below the openings were also included in the specimen. Timber lintels supported the upper spandrels and were fastened to the top reinforced concrete (RC) spreader beam. On the other hand, the bottom spandrels were clamped to the RC foundation. The pier had cross-section of $1.2 \times 0.3\ m$ and a clear height of $1.5\ m$, whereas spandrels had cross-section of $0.5 \times 0.3\ m$ and extended $0.85\ m$ on each side of the pier.

The pier was strengthened on both sides with CRM consisting of GFRP meshes within a $M15$-class hydraulic lime mortar. Vertical GFRP bars (weft) were spaced at $120\ mm$ and horizontal bars (warp) at $80\ mm$, for a total mesh weight of $400\ g/m^2$. The nominal thickness of $30\ mm$ could not remain constant throughout the wall, to obtain a flat finish over the stone masonry irregular surface. The CRM layers were mechanically connected to the wall by a total of 18 helicoidal steel bars passing through both masonry leaves, 8 of which were located within the pier.

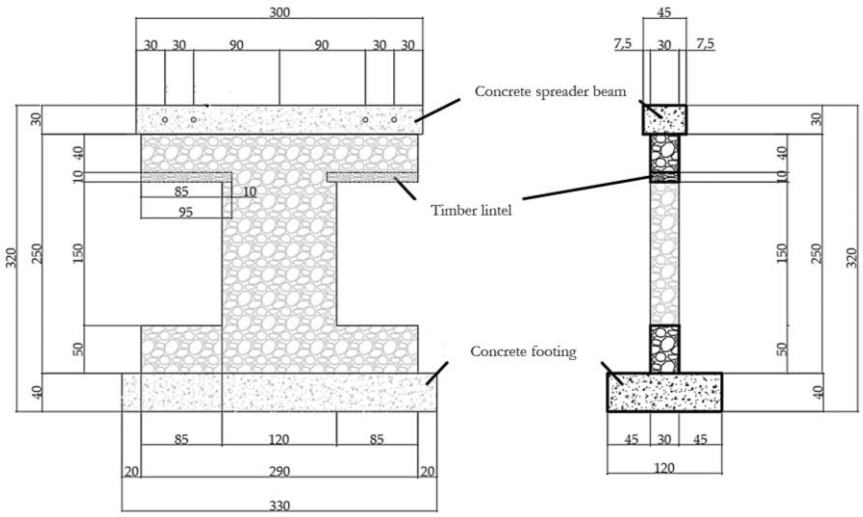

Figure 7.6: Front and lateral view of the experimental specimen. Units of *cm*.

The masonry mechanical properties were characterized through an extensive experimental campaign involving vertical and diagonal compression tests on masonry wallettes (Guerrini *et al.*, 2021b). Consequently, compressive and tensile strengths of $1.52\ MPa$ and $0.14\ MPa$ were obtained, whereas values of $3.45\ GPa$ and $1.32\ GPa$ were derived for the Young's and shear moduli. Finally, an average mass per unit volume of $1880\ kg/m^3$ was assumed.

The mechanical properties of the GFRP meshes were provided by the manufacturer, resulting in a Young's modulus of $61\ GPa$ and in a tensile strength of $74\ kN/m$ and $86\ kN/m$ in the weft (vertical) and warp (horizontal) direction, respectively. The $M15$-class mortar was characterized by compressive and tensile strengths of $18.4\ MPa$ and $4.2\ MPa$, respectively (Guerrini *et al.*, 2021b).

The specimen was subjected to a horizontal quasi-static shear history with increasing target displacements through a horizontal actuator, while two actuators above the specimen maintained the axial load constant and prevented the in-plane rotation of the spreader beam, resulting in double-fix boundary conditions for the pier. In this context, an axial force equal to 25% of the unconfined compressive strength was set at the base of the pier, whereas three cycles were imposed at each target displacement to investigate stiffness and strength degradation.

7.4.2 Numerical model and assumptions

Only the pier is modeled with its actual dimensions, in double-fix boundary conditions. The longitudinal bars of the GFRP mesh are modeled explicitly in the axial-flexural interface, while the shear strength enhancement is implicitly considered by increasing the

masonry tensile strength. The CRM mortar contribution is neglected, assuming that the effect of the retrofit is governed by the GFRP mesh. The properties assigned to the material models reflect the values obtained after the characterization campaign or those provided by the manufacturer, with some modifications.

For instance, the masonry compressive strength is first amplified by 1.33, to simulate the confining effect of the CRM steel connectors and obtain the experimental lateral strength through analytical formulations (CNR, 2018), adapted from FRCM to CRM strengthening. Then, it is multiplied by 0.85, consistently with the stress-block approach of the same formulation: in fact, an elastic-perfectly plastic relationship cannot reproduce the post-peak degradation of the actual stress-strain behavior. Therefore, the masonry compressive strength in the model is 1.7 MPa.

Taking advantage of the fiber discretization, a no-tension elastic- perfectly plastic behavior in compression with parallel-elastic unloading (Figure 7.2b), currently unavailable within the stripe formulation, is assigned to the masonry material to properly account for energy dissipation and residual displacements during cyclic loadings. On the other hand, the surface layers implement a no-compression elasto-fragile response (Figure 7.4a).

Instead, the masonry tensile strength to be used with the Turnšek-Sheppard (1980) shear criterion is magnified by 2.75, conforming to the results of diagonal compression tests on retrofitted wallettes (Guerrini *et al.*, 2021b). Parameters $Gc_t = 2$ and $\beta = 0.4$ are assigned to the Gambarotta-Lagomarsino (1997a,b) shear model.

7.4.3 Numerical results and comparison

The axial load level and horizontal displacement history are applied to the numerical model to reproduce the testing protocol, in both amplitude and number of cycles. The displacement applied at the pier top, net of any setup sliding or rotation, was recorded during the test and is taken as input for the numerical analyses. Consequently, the numerical-to-experimental comparison can be directly performed in terms of hysteretic response.

Results are presented in terms of drift ratio, namely the ratio between the lateral displacement evaluated at the top of the pier and its clear height, and base shear coefficient (BSC), computed as the shear restoring force divided by the axial load applied. Figure 7.7 depicts the numerical response, showing a good agreement with the experimental behavior not only in terms of lateral stiffness and strength (average error of about 5.25%), but also looking at strength decay, energy dissipation, and failure mode with crushing of the masonry followed by GFRP mesh fracture around 1.12% drift ratio.

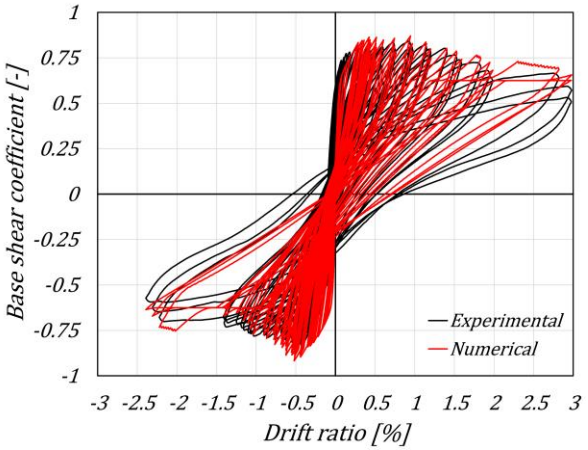

Figure 7.7: Numerical hysteretic response considering three cycles per target displacement increment. Masonry material with parallel unloading in compression (Figure 7.2b).

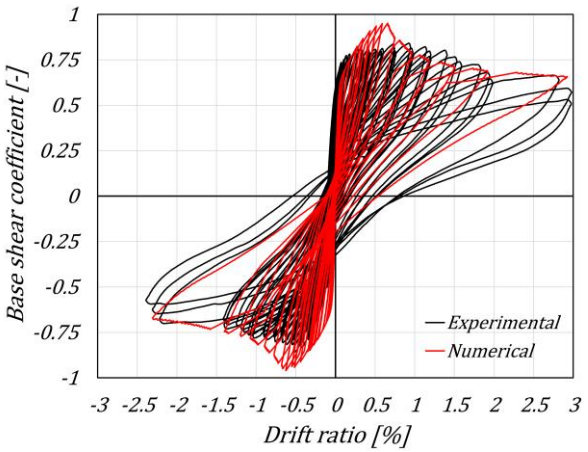

Figure 7.8: Numerical hysteretic response considering one cycle per target displacement increment. Masonry material with parallel unloading in compression (Figure 7.2b).

Figure 7.8 reports the outcomes of the same numerical model when subjected to a single cycle, rather than three cycles, per lateral displacement increment. Reducing the number of cycles results in less compressive damage accumulated by the model, as expected. Consequently, a higher lateral strength is predicted (average error of about 12.57%), associated with tensile failure of the strengthening layers under a smaller drift ratio of 0.65%, before experiencing strength degradation. However, the residual strength at maximum displacement shows a good agreement with the experimental results.

A similar response is obtained using a constitutive law unable to properly account for damage accumulation (Figure 7.9). In this case, a no-tension, elastic-perfectly plastic model in compression with recentering unloading is assigned to the masonry material (Figure 7.2a), leading again to an overestimation of the lateral strength of the specimen and allowing the GFRP mesh to reach its full capacity, before undergoing a strength decay and approaching the experimental residual strength. It is worth noticing that no appreciable influence is observed with the number of cycles per displacement increment, as damage is only minimally accumulated on the compressed masonry.

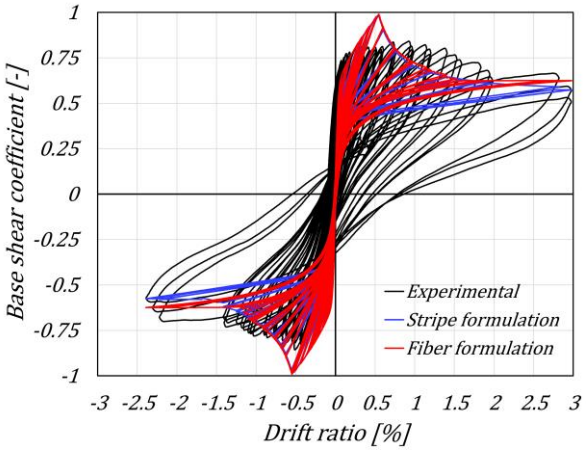

Figure 7.9: Numerical hysteretic responses considering three cycles per target displacement increment and different sectional formulations. Masonry material with recentering unloading in compression (Figure 7.2a).

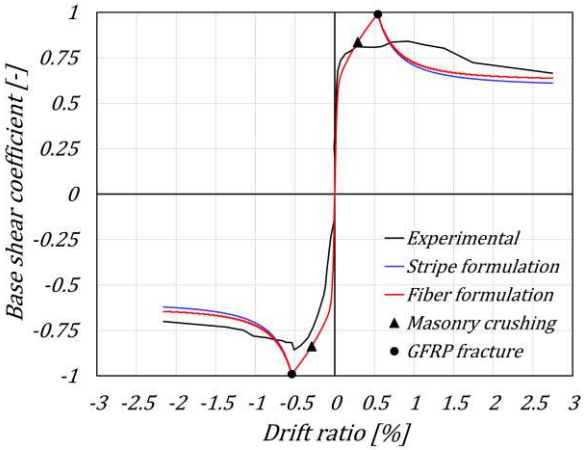

Figure 7.10: Monotonic response with different sectional formulations. Masonry material with recentering unloading in compression (Figure 7.2a).

The strength overestimation can also be found in the case of a monotonic analysis (Figure 7.10). In this figure, the points corresponding to the ultimate GFRP strain on the extreme tensile fiber, and to 0.35% compressive strain on the most compressed fiber (usually taken as the ultimate strain for masonry) are shown, confirming that the actual lateral strength was governed by masonry crushing. However, the elasto-plastic stress-strain relationship for masonry is unlimited. Consequently, it cannot capture this behavior and results in failure of the GFRP mesh.

Figure 7.9 also compares the cyclic responses with stripe and fiber formulations for the end-interfaces. In the first case, the masonry portion of the cross-section is not discretized, as no out-of-plane behavior needs to be captured. Further stripes are instead added to account for the CRM application. On the other hand, the fiber formulation provides a full-fiber discretization of the whole end-interface, involving both masonry and additional layers. Figure 7.9 shows a satisfactory agreement between the two numerical formulations. Small discrepancies arise only in the masonry contribution when the load is reversed. In fact, as widely investigated by Penna *et al.* (2014), the analytical integration is based on an approximated linearization of the stress profile on the axial-flexural interface, while the fiber discretization reproduces the actual stress profile.

7.5 CONCLUSIONS

This paper discusses a novel three-dimensional macroelement formulation developed to explicitly account for the in-plane and out-of-plane responses of masonry walls and for the influence of strengthening or reinforcing materials.

The formulation builds upon a well-established macroelement for the in-plane simulation of masonry elements, and is advanced to include the out-of-plane flexural contribution through a stripe discretization of the end-interfaces. In this context, the in-plane response of the individual stripes is modeled by analytically integrating the stress distribution to retrieve their nonlinear axial-flexural behavior. Subsequently, the combined sectional in-plane and out-of-plane response is computed by numerically integrating the single stripe contributions over the thickness of the cross-section.

The proposed formulation significantly reduces the computational effort of the analysis compared to a complete fiber discretization of the end-interfaces, as the discretization is required along the out-of-plane direction only. However, analytical integration is limited to simple constitutive laws (with minimal approximations). For this reason, the novel macroelement also provides a fiber option, enabling the implementation of more refined stress-strain relationships.

The three-dimensional formulation is well suited for the explicit modeling of flexural strengthening and reinforcement solutions. In fact, additional surface layers or lumped bars can be easily incorporated into the end-interfaces. Kinematic relationships expressed in terms of the macroelement degrees of freedom are enforced on the additional elements to grant proper collaboration with the masonry stripes or fibers end-interfaces.

The proposed macroelement is validated against the experimental results from a quasi-static cyclic shear-compression test on a masonry pier strengthened with CRM. The numerical response shows a good agreement with the experimental hysteresis cycles when the masonry material is given an elasto-plastic constitutive law in compression with unloading parallel to the elastic branch (currently available only with the fiber discretization), provided the pier is subjected to three cycles per lateral displacement increment as in the experiment.

Moreover, the model correctly overestimates the lateral strength when subjected to a single cycle per increment, because less damage is accumulated on the compressed masonry. A similar strength overestimation is experienced when a constitutive relationship with recentering unloading is assigned to the masonry material, closely reflecting the response after a monotonic analysis, because in these cases damage cannot be adequately accumulated in compression.

It can be noted that stripe and fiber discretizations of the axial-flexural interfaces lead to very similar cyclic responses, promoting the stripe formulation as a computationally efficient and effective strategy to numerically model strengthened and reinforced masonry elements. For this reason, an analytically integrated formulation will be added in the future, based on the parallel-unloading elasto-plastic masonry model in compression. Additionally, a more explicit approach to incorporate shear strengthening or reinforcement will be added to the shear formulation of the macroelement.

Acknowledgements

This experimental campaign was made possible thanks to the financial and material support by Laterlite S.p.A. The data processing was partially funded by DPC-ReLUIS (2022-2024) Work Package 10 "Modelli di capacità locali e globali per la definizione degli stati limite, definiti in funzione del metodo di analisi". The authors would like to acknowledge the help provided by the staff of the EUCENTRE Foundation and of the Department of Civil Engineering and Architecture of the University of Pavia.

REFERENCES

Bracchi, S., Galasco, A., and Penna, A. (2021). A Novel Macroelement Model for the Nonlinear Analysis of Masonry Buildings. Part 1: Axial and Flexural Behavior. *Earthquake Engineering & Structural Dynamics*, 50(8), 2233-2252.

Bracchi, S. and Penna, A. (2021). A Novel Macroelement Model for the Nonlinear Analysis of Masonry Buildings. Part 2: Shear Behavior. *Earthquake Engineering & Structural Dynamics*, 50(8), 2212-2232.

Brencich, A., Lagomarsino, S. (1998). A macro-elements dynamic model for masonry shear walls. In Proceedings of the STRUMAS IV - 4th Int. Symp. On Computer Methods in Structural Masonry. E&FN Spon: London; 67–75.

CNR (2018). CNR DT 215/2018. Istruzioni per la progettazione, l'esecuzione ed il controllo di interventi di consolidamento statico mediante l'utilizzo di compositi fibrorinforzati a matrice inorganica, *Consiglio Nazionale delle Ricerche*, Rome, Italy (in Italian).

Del Zoppo, M., Di Ludovico, M., and Prota, A., (2019). Analysis of FRCM and CRM parameters for the in-plane shear strengthening of different URM types. *Composites Part B*, 171, 20-33.

Gambarotta, L. and Lagomarsino, S. (1997a). Damage Models for the Seismic Response of Brick Masonry Shear Walls. Part I: The Mortar Joint Model and its Applications. *Earthquake Engineering & Structural Dynamics*, 26(4), 423-439.

Gambarotta, L. and Lagomarsino, S. (1997b). Damage Models for the Seismic Response of Brick Masonry Shear Walls. Part II: The Continuum Model and its Applications. *Earthquake Engineering & Structural Dynamics*, 26(4), 441-462.

Gattesco, N., Boem, I., and Dudine, A. (2015). Diagonal compression tests on masonry walls strengthened with a GFRP mesh reinforced mortar coating. *Bulletin of Earthquake Engineering*, 13(6), 1703-1726.

Guerrini, G., Bruggi, A., Senaldi, I., Quaini, M., and Penna, A. (2021a). Experimental qualification of PBO-FRCM composites for retrofitting masonry structures. *In Proceedings of the 7th International Conference on Mechanics of Masonry Structures Strengthened with Composite Materials*, Bologna, Italy.

Guerrini, G., Bruggi, A., Urso, S., Quaini, M., and Penna, A. (2021b). Diagonal compression tests on stone masonry wallettes jacketed with different techniques. *In Proceedings of the 7th*

International Conference on Mechanics of Masonry Structures Strengthened with Composite Materials, Bologna, Italy.

Guerrini, G., Bruggi, A., Urso, S., Quaini, M., and Penna, A. (2023). Cyclic shear-compression tests on two stone masonry piers strengthened with CRM and FRCM. *Procedia Structural Integrity, XIX ANIDIS Conference on Seismic Engineering in Italy*, 44, 2214-2221.

Kashani, H.K., Shakiba, M., Bazli, M. *et al.* (2023). The structural response of masonry walls strengthened using prestressed near surface mounted GFRP bars under cyclic loading. *Materials and Structures*, 56, 112.

Magenes, G., and Della Fontana, A. (1998). Simplified Non-Linear Seismic Analysis of Masonry Buildings. *In Proceedings of the British Masonry Society,* 8, 190-195.

Pantò, B., Cannizzaro, F., Caliò, I., and Lourenço, P. B. (2017). Numerical and Experimental Validation of a 3D Macro-Model for the In-Plane and Out-Of-Plane Behavior of Unreinforced Masonry Walls. *International Journal of Architectural Heritage*, 11(7), 946–964.

Pantò, B., Caliò, I, and Lourenço, P. B. (2018). A 3D discrete macro-element for modelling the out-of-plane behaviour of infilled frame structures. *Engineering Structures*, 175, 371-385.

Papanicolaou, C.G., Triantafillou, T.C., Papathanasiou, M., and Karlos, K. (2008). Textile reinforced mortar (TRM) versus FRP as strengthening material of URM walls: out-of-plane cyclic loading. *Materials and Structures*, 41(1), 143-157.

Penna, A., Lagomarsino, S., and Galasco, A. (2014). A Nonlinear Macroelement Model for the Seismic Analysis of Masonry Buildings. *Earthquake Engineering & Structural Dynamics*, 43(2), 159-179.

Prota, A., Marcari, G., Fabbrocino, G., Manfredi, G., and Aldea, C. (2006). Experimental in-plane behavior of tuff masonry strengthened with cementitious matrix-grid composites. *Journal of Composites for Construction* (ASCE), 10(3), 223-233.

Raka, E., Spacone, E., Sepe, V., and Camata, G. (2015). Advanced Frame Element for Seismic Analysis of Masonry Structures: Model Formulation and Validation. *Earthquake Engineering & Structural Dynamics*, 44(14), 2489-2506.

Turnšek, V. and Sheppard, P. (1980). The Shear and Flexural Resistance of Masonry Walls. *Proceedings of the International Research Conference on Earthquake Engineering*. Skopje, Yugoslavia.

Valluzzi, M.R., Modena, C., and de Felice, G. (2014). Current practice and open issues in strengthening historical buildings with composites. *Materials and structures*, 47(12), 1971-1985.

Vanin, F., Penna, A., and Beyer, K. (2020). A Three-Dimensional Macroelement for Modelling the In-Plane and Out-of-Plane Response of Masonry Walls. *Earthquake Engineering & Structural Dynamics*, 49(14), 1365-1387.

8. CONCLUSIONS AND FUTURE DEVELOPMENTS

8.1 SUMMARY AND CONCLUSIONS

In this thesis, the equivalent frame modeling (EFM) of masonry structures was thoroughly investigated as an approach that ensures a reasonable compromise between accuracy of results and computational effort. The EFM builds upon the identification of piers and spandrels and their idealization through macroelements; consequently, it addresses the smeared response of the masonry panels rather than focusing on the local behavior of the masonry material. This leads to a simplified analysis, with reduced computational effort and easier mechanical property calibration compared to refined approaches such as the finite element method (FEM) or the discrete element method (DEM). As a consequence, this strategy is viable for the static and dynamic analysis of masonry buildings in the ordinary engineering practice.

This dissertation aimed at extending the modeling capabilities of the EFM while maintaining its computational efficiency and ease of use. First, the out-of-plane response of walls was incorporated into the equivalent frame modeling strategy already implemented in the software TREMURI. Then, the possibility of accounting for flexural strengthening of existing masonry structures or longitudinal reinforcement in new construction was also investigated. In both cases, a material with significant tensile strength (and sometimes stiffness) applied to or embedded into the structural members, to overcome one of the main deficiencies of the masonry material, needs to be properly represented in the EFM elements.

The main findings of this work are summarized in the following paragraphs.

- In Chapter 3, the effectiveness of different retrofit solutions for stone masonry buildings with flexible diaphragms was investigated by means of shake-table tests. Nonlinear static analyses were performed on the two retrofitted prototypes by adopting the equivalent frame modeling strategy with nonlinear macroelements implemented in the software TREMURI. Numerical results in terms of capacity curves and damage patterns showed a satisfactory agreement with the experimental outcomes of the two investigated buildings. Additionally, parametric analyses were carried out to investigate the effect of masonry strengthening interventions, simulated by improving the mechanical properties of the masonry material through correction coefficients. Overall, the experimental and numerical study confirmed

the significant benefit achieved by improving the wall-to-diaphragm connections, as out-of-plane overturning mechanisms were prevented. Also, the masonry strengthening interventions induced positive effects, with an increase in the lateral strength associated with a change of failure mechanism from shear- to flexure-dominated.

- In Chapter 4, the experimental response of a stone masonry building aggregate with flexible diaphragms subjected to shake-table tests was investigated. The numerical simulation was carried out through nonlinear static analyses on an equivalent frame model with nonlinear macroelements implemented in the software TREMURI. An unconventional strategy was adopted to account for the out-of-plane behavior of the walls arranged orthogonally to the shaking direction. The work demonstrated the validity of the common modeling assumption for the seismic analysis of masonry structures, as neglecting the out-of-plane wall response did not significantly influence the reliability of the results, as long as local collapse mechanisms were not activated. Additionally, single-wall models showed reasonable results, aligning with those extracted from the conventional three-dimensional model.
- In Chapter 5 the two-dimensional formulation of the macroelement employed in Chapter 3 and Chapter 4 was improved. Additional nonlinear corrections and analytically integrated elasto-fragile tensile response under flexure yielded satisfactory results, aligning with those provided by a fiber discretization of the end-interfaces. Out-of-plane and torsional degrees of freedom were introduced in the macroelement to allow a full three-dimensional formulation. Particular attention was paid to biaxial bending, through a partial discretization of the end-interfaces in longitudinal stripes with integral axial-flexural formulations. Numerical comparisons between analytically integrated and fiber-discretized sectional responses showed negligible differences under bending and axial load. Furthermore, comparisons with an independent software proved the reliability of the results obtained with the three-dimensional macroelement. Finally, an adaptive iterative algorithm, proposed to achieve a high convergence rate and numerical robustness, showed promising results.
- In Chapter 6, the versatility of the proposed end-interface stripe formulation, and the analytical tensile strength introduced, allowed and proved suitable for modeling flexural strengthening or reinforcement solutions. Lumped rebars and surface layers were simulated, ensuring proper collaboration with the end-interfaces by enforcing kinematic constraints in terms of end-interface degrees of freedom. An analytical no-compression, elasto-fragile tensile relationship was assigned to the surface layers, whereas the lumped elements were endowed with an elasto-plastic response, deduced from the J2 plasticity theory. Comparisons with a third-party software and with analytical equations resulted in satisfactory results in terms of

uniaxial flexural strength. Additionally, surface layers were simulated with both analytical and fiber formulations, showing negligible differences in the response.

- In Chapter 7, the macroelement proposed in Chapter 5 and Chapter 6 was employed to simulate an experimental quasi-static cyclic shear-compression test on a masonry pier strengthened on both sides with composite-reinforced mortar (CRM) application. The numerical response showed a good agreement with the experimental hysteresis cycles when the masonry material is assigned an elasto-plastic constitutive law in compression with unloading parallel to the elastic branch, currently requiring a fiber discretization. On the other hand, a recentering unloading branch did not allow for proper damage accumulation, thus overestimating the lateral strength; in this context, stripe and fiber discretization showed equivalent results. Overall, the macroelement was satisfactorily able to capture elastic stiffness, lateral strength, strength decay, and energy dissipation, promoting the proposed formulation as a computationally efficient and effective strategy to numerically model strengthened and reinforced masonry elements.

8.2 FUTURE DEVELOPMENTS

The proposed macroelement opens a wide range of future developments. An elasto-plastic response with unloading parallel to the elastic branch will be added to the end-interface formulation for masonry in compression, again resorting to an analytical integration over the length of each stripe for computational efficiency. This stress-strain relationship has been demonstrated to better account for energy dissipation and residual displacements. Additionally, taking advantage of the versatility of the fiber formulation, more complex constitutive laws could be associated with the end-interfaces, as well as with the additional lumped elements.

The shear behavior of the macroelement will also be addressed. Currently, the central body adopts the nonlinear shear formulation proposed in the original two-dimensional macroelement, without coupling in the two orthogonal directions. However, three-dimensional shear strength domains can be provided. Additionally, the nonlinear shear response of the strengthening and reinforcement solutions can also be accounted for. In particular, the contribution of shear reinforcement could be introduced through an additional cohesion, however preserved in the damage configuration. Therefore, the proposed macroelement may become suitable for accurately modeling other structural typologies, such as reinforced concrete members.

The ability of the three-dimensional macroelement to capture the cyclic biaxial flexural and shear responses will be validated against more refined modeling strategies involving solid finite or discrete elements, previously calibrated against material characterization and component tests. Additionally, the macroelement could be employed to simulate elements

more susceptible to biaxial conditions, such as arches and bridges, and validated against experimental outcomes available in the literature.

Finally, the three-dimensional macroelement will be further validated against the experimental responses of the shake-table tests mentioned in Chapter 3 and Chapter 4, possibly in combination with nonlinear membrane or shell models of the floor diaphragms, zero-length elements simulating wall-to-diaphragm and wall-to-wall intersections, and second-order effects, to capture the out-of-plane response also in terms of local mechanisms. Eventually, the results will be compared to those obtained with the original two-dimensional macroelement and with the more simplified EFM strategies proposed in building codes and guidelines.

Appendix A

ELASTIC STIFFNESS MATRIX OF THE TWO-DIMENSIONAL MACROELEMENT

In this section, the elastic stiffness matrix of the two-dimensional macroelement (Penna *et al.*, 2014) within a new reference system is accurately computed and presented. More specifically, the original left-handed local reference system is turned into a right-handed one to match the global reference system without tedious or error-prone matrix transformations (Figure A.1). Consequently, both the elastic stiffness matrix and the nonlinear corrections need to be properly reviewed. In particular, equation (A.1) reports the matrix form of the linear-elastic governing equations in the new reference system, whereas Figure A.2 visually explains the terms populating the elastic stiffness matrix.

$$\begin{Bmatrix} N_i \\ V_i \\ M_i \\ N_j \\ V_j \\ M_j \\ N_e \\ M_e \end{Bmatrix} = \begin{bmatrix} kA & 0 & 0 & 0 & 0 & 0 & -kA & 0 \\ 0 & \frac{GA}{\chi h} & 0 & 0 & -\frac{GA}{\chi h} & 0 & 0 & \frac{GA}{\chi} \\ 0 & 0 & kI & 0 & 0 & 0 & 0 & -kI \\ 0 & 0 & 0 & kA & 0 & 0 & -kA & 0 \\ 0 & -\frac{GA}{\chi h} & 0 & 0 & \frac{GA}{\chi h} & 0 & 0 & -\frac{GA}{\chi} \\ 0 & 0 & 0 & 0 & 0 & kI & 0 & -kI \\ -kA & 0 & 0 & -kA & 0 & 0 & 2kA & 0 \\ 0 & \frac{GA}{\chi} & -kI & 0 & -\frac{GA}{\chi} & -kI & 0 & \frac{GAh}{\chi} + 2kI \end{bmatrix} \begin{Bmatrix} w_i \\ v_i \\ \varphi_i \\ w_j \\ v_j \\ \varphi_j \\ w_e \\ \varphi_e \end{Bmatrix} \quad \textbf{(A.1)}$$

For completeness, $A = Lt$ represents the cross-section area, being L and t the corresponding length and thickness, $I = tL^3/12$ indicates the in-plane moment of inertia, h is the height of the macroelement, E and G are the Young's and shear modulus of masonry, whereas χ is the appropriate shear factor depending upon the section shape. Furthermore, $k = 2E/h$ indicates the equivalent axial stiffness of the end-interfaces.

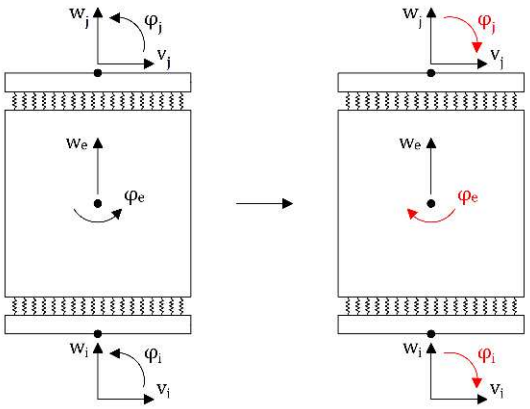

Figure A.1: From left-handed to right-handed local reference system.

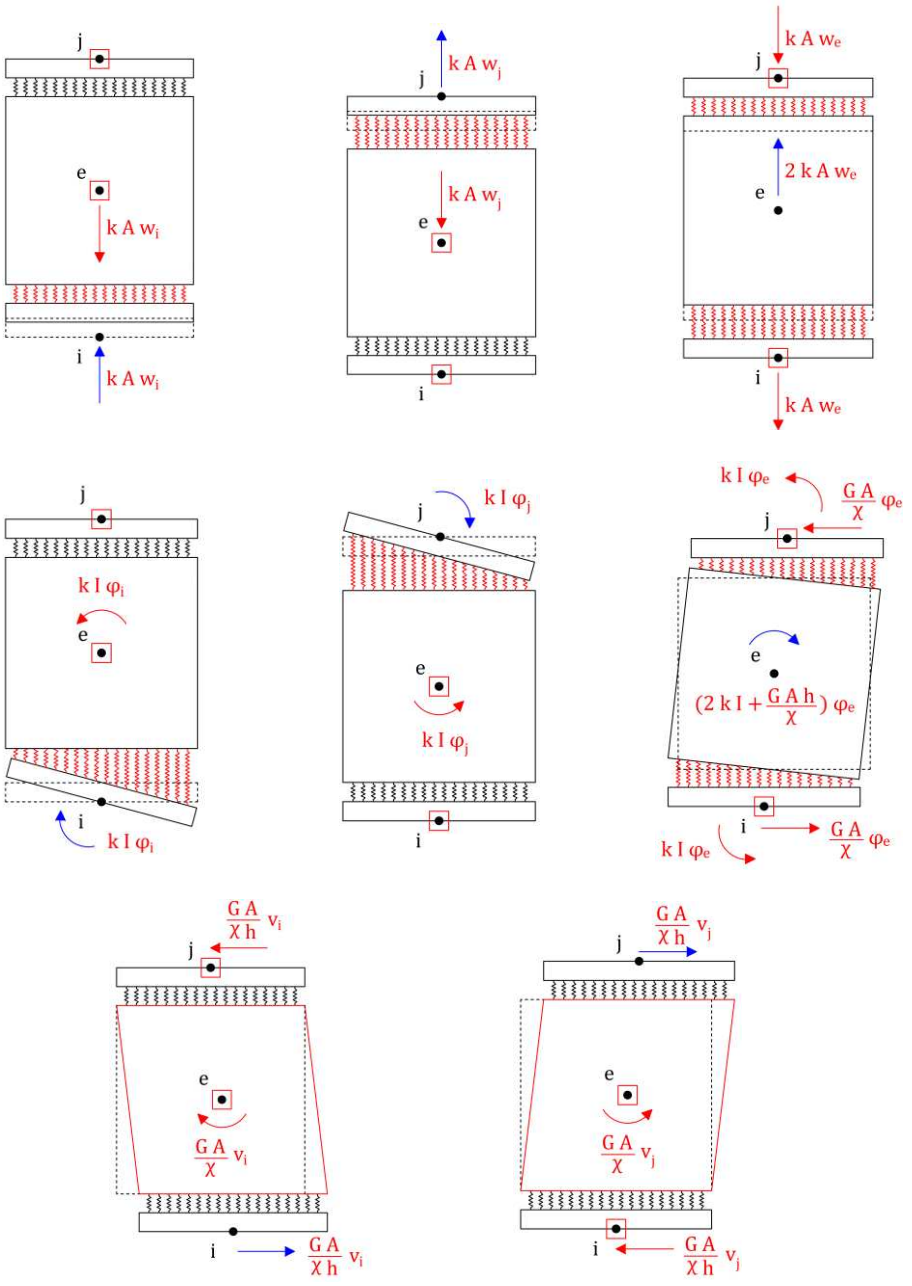

Figure A.2: Two-dimensional elastic stiffness matrix terms: imposed actions in blue and corresponding reactions in red.

Appendix B

ELASTIC STIFFNESS MATRIX OF THE THREE-DIMENSIONAL MACROELEMENT

In this section, the elastic stiffness matrix of the three-dimensional macroelement proposed in this thesis is computed and presented. In particular, the macroelement is endowed with fifteen degrees of freedom, directly oriented along the global reference system when vertically arranged, hence adopting a right-handed rule.

The elastic system of equations is reported in equation (B.2), whereas Figure B.1 and Figure B.2 visually explain the terms populating the elastic stiffness matrix. The following notation is used: $A = Lt$ represents the transversal cross-section area, whereas I_1, I_2, and I_3 indicate the moment of inertia about the local 1- (torsional inertia), 2- (out-of-plane inertia), and 3-axis (in-plane inertia), respectively obtained as follows:

$$I_1 = ab^3\left[\frac{16}{3} - \frac{3.36b}{a}\left(1 - \frac{b^4}{12a^4}\right)\right] \qquad I_2 = \frac{Lt^3}{12} \qquad I_3 = \frac{tL^3}{12} \qquad \textbf{(B.1)}$$

being a and b the long and the short side half-length, respectively. It is worth noticing that the first expression approximates the actual torsional constant of a rectangular cross-section. As a matter of fact, there are no exact analytical equations for non-circular cross-sections, as warping deformations can only be accounted for by resorting to numerical methods. However, the adopted equation proved sufficiently accurate.

For the sake of completeness, $k = 2E/h$ is the stiffness per surface unit, E and G indicate the Young's and shear modulus of masonry, χ is the appropriate shear factor functions of the section shape, whereas h, L, and t represent the height, length, and thickness of the macroelement, respectively.

$$\begin{Bmatrix} N_i \\ V_{2,i} \\ V_{3,i} \\ M_{1,i} \\ M_{2,i} \\ M_{3,i} \\ N_j \\ V_{2,j} \\ V_{3,j} \\ M_{1,j} \\ M_{2,j} \\ M_{3,j} \\ N_e \\ M_{2,e} \\ M_{3,e} \end{Bmatrix} = \begin{bmatrix} kA & 0 & 0 & 0 & 0 & 0 & 0 & 0 & 0 & 0 & 0 & 0 & -kA & 0 & 0 \\ 0 & \frac{GA}{\chi h} & 0 & 0 & 0 & 0 & 0 & -\frac{GA}{\chi h} & 0 & 0 & 0 & 0 & 0 & 0 & \frac{GA}{\chi} \\ 0 & 0 & \frac{GA}{\chi h} & 0 & 0 & 0 & 0 & 0 & -\frac{GA}{\chi h} & 0 & 0 & 0 & 0 & -\frac{GA}{\chi} & 0 \\ 0 & 0 & 0 & \frac{GI_1}{h} & 0 & 0 & 0 & 0 & 0 & -\frac{GI_1}{h} & 0 & 0 & 0 & 0 & 0 \\ 0 & 0 & 0 & 0 & kI_2 & 0 & 0 & 0 & 0 & 0 & 0 & 0 & 0 & -kI_2 & 0 \\ 0 & 0 & 0 & 0 & 0 & kI_3 & 0 & 0 & 0 & 0 & 0 & 0 & 0 & 0 & -kI_3 \\ 0 & 0 & 0 & 0 & 0 & 0 & kA & 0 & 0 & 0 & 0 & 0 & -kA & 0 & 0 \\ 0 & -\frac{GA}{\chi h} & 0 & 0 & 0 & 0 & 0 & \frac{GA}{\chi h} & 0 & 0 & 0 & 0 & 0 & 0 & -\frac{GA}{\chi} \\ 0 & 0 & -\frac{GA}{\chi h} & 0 & 0 & 0 & 0 & 0 & \frac{GA}{\chi h} & 0 & 0 & 0 & 0 & \frac{GA}{\chi} & 0 \\ 0 & 0 & 0 & -\frac{GI_1}{h} & 0 & 0 & 0 & 0 & 0 & \frac{GI_1}{h} & 0 & 0 & 0 & 0 & 0 \\ 0 & 0 & 0 & 0 & 0 & 0 & 0 & 0 & 0 & 0 & kI_2 & 0 & 0 & -kI_2 & 0 \\ 0 & 0 & 0 & 0 & 0 & 0 & 0 & 0 & 0 & 0 & 0 & kI_3 & 0 & 0 & -kI_3 \\ -kA & 0 & 0 & 0 & 0 & 0 & -kA & 0 & 0 & 0 & 0 & 0 & 2kA & 0 & 0 \\ 0 & 0 & -\frac{GA}{\chi} & 0 & -kI_2 & 0 & 0 & 0 & \frac{GA}{\chi} & 0 & -kI_2 & 0 & 0 & \frac{GAh}{\chi} + 2kI_2 & 0 \\ 0 & \frac{GA}{\chi} & 0 & 0 & 0 & -kI_3 & 0 & -\frac{GA}{\chi} & 0 & 0 & 0 & -kI_3 & 0 & 0 & \frac{GAh}{\chi} + 2kI_3 \end{bmatrix} \begin{Bmatrix} w_i \\ v_{2,i} \\ v_{3,i} \\ \varphi_{1,i} \\ \varphi_{2,i} \\ \varphi_{3,i} \\ w_j \\ v_{2,j} \\ v_{3,j} \\ \varphi_{1,j} \\ \varphi_{2,j} \\ \varphi_{3,j} \\ w_e \\ \varphi_{2,e} \\ \varphi_{3,e} \end{Bmatrix} \quad \textbf{(B.2)}$$

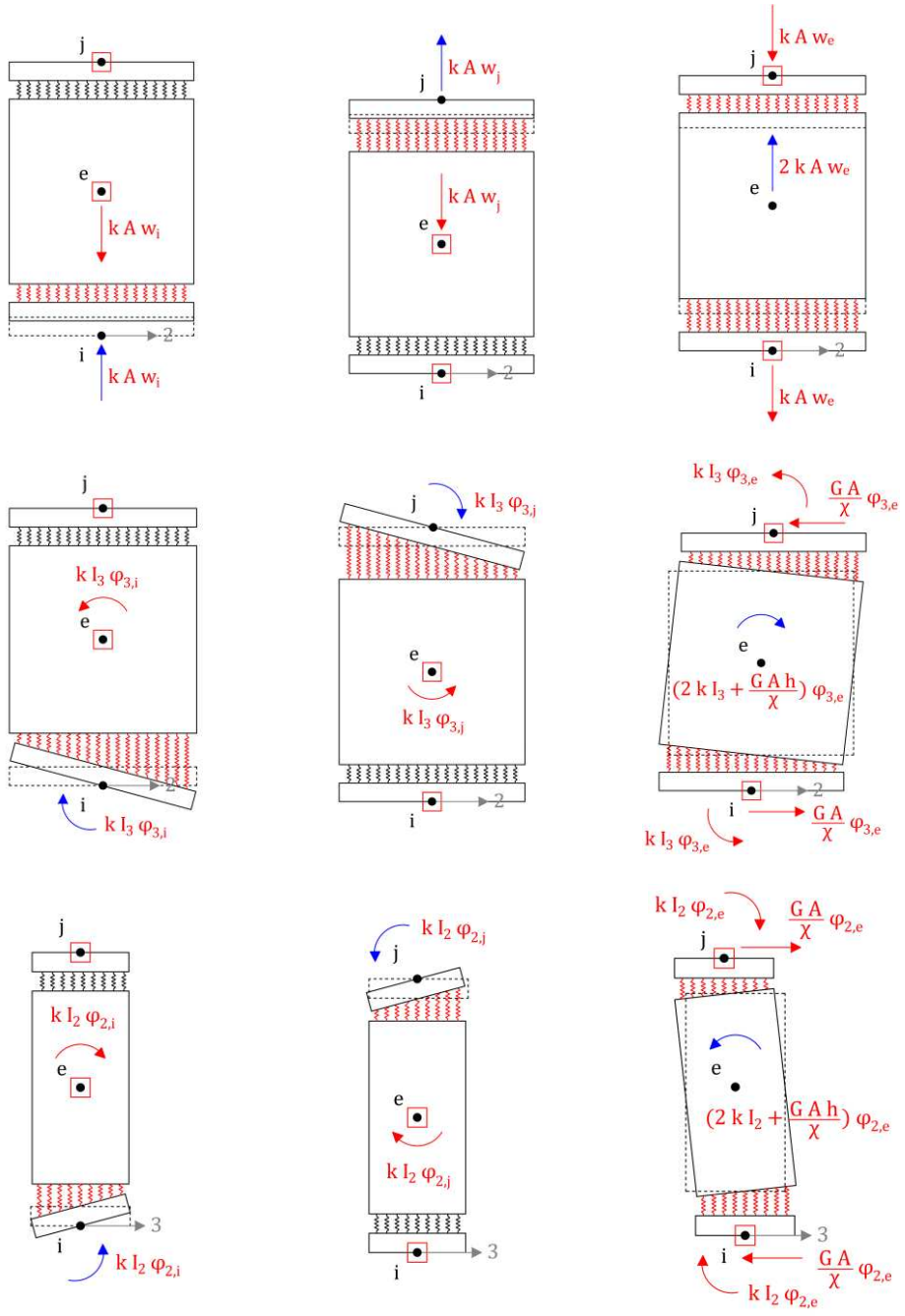

Figure B.1: Three-dimensional elastic stiffness matrix terms: end-interface contributions (imposed actions in blue and corresponding reactions in red).

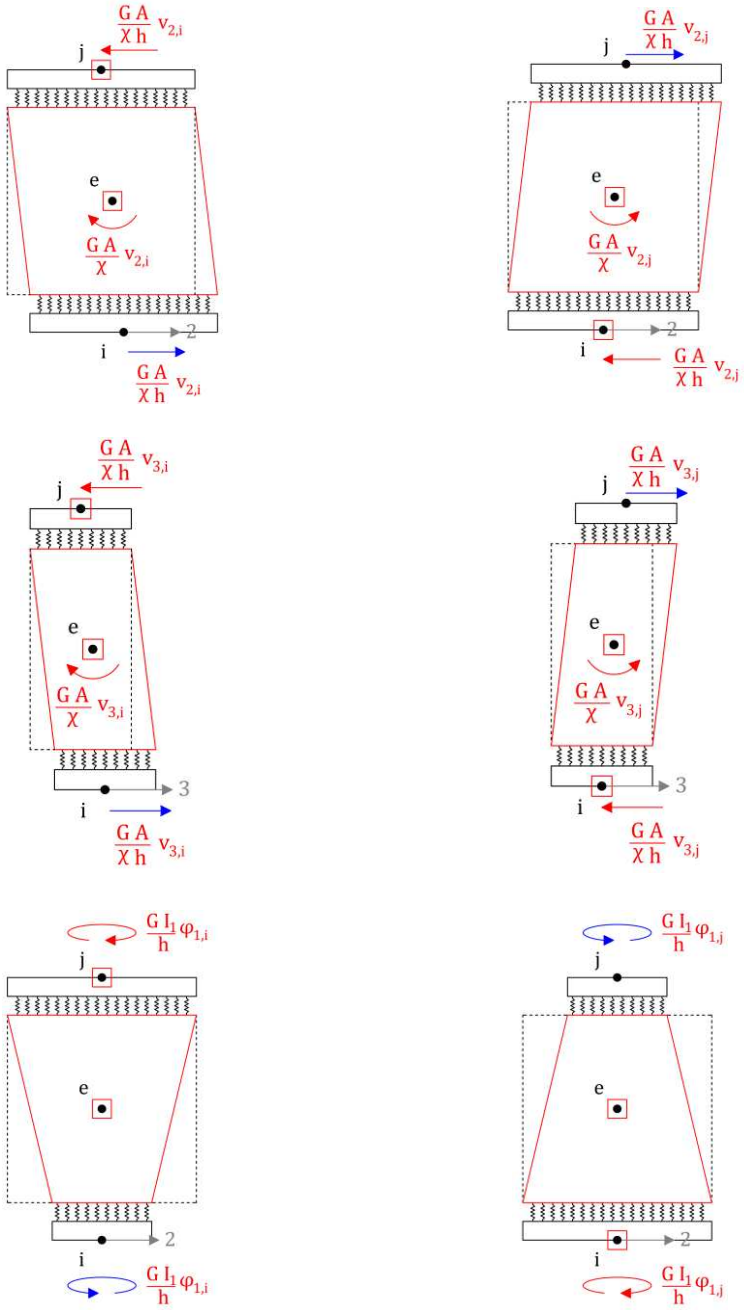

Figure B.2: Three-dimensional elastic stiffness matrix terms: central body contributions (imposed actions in blue and corresponding reactions in red).

Appendix C

ELASTIC STIFFNESS MATRIX OF STRENGTHENING LAYERS

As reported in Chapter 6, one of the main advantages of the stripe formulation is the versatility to introduce additional stripes along the thickness of the end-interfaces, while maintaining the computational effort reasonable. Consequently, surface layers can be explicitly modeled, and a different constitutive law can be assigned to the corresponding stripes.

The elastic stiffness matrix that governs the response of the s^{th} surface layer ($\boldsymbol{K_s^{sl}}$) is obtained as the sum of the flexural and shear contributions, respectively reported in equations (C.4) and (C.5). In fact, the peculiar arrangement of the degrees of freedom of the macroelement allows to easily decouple the kinematics associated with flexural and shear mechanisms. It is worth noticing that, in contrast to the elastic stiffness matrix of the three-dimensional macroelement (reported in Appendix B), the one of the surface layer explicitly incorporates the static moment about the out-of-plane 2-axis, as the layer arrangement may not be symmetric. The last quantity is computed as reported in equation (C.1) together with the moment of inertias about the minor and major sectional axes:

$$I_{2,s} = L_s\, t_s\, e_{3,s}^2 \qquad S_{2,s} = L_s\, t_s\, e_{3,s} \qquad I_{3,s} = \frac{1}{12} t_s\, L_s^3 \tag{C.1}$$

where L_s and t_s represent the length and the thickness of the individual layer, whereas $e_{3,s}$ its out-of-plane coordinate with respect to the centroid of the macroelement section. The latter is reported in (C.2), where the sign is automatically defined once selecting the application side of the layer, being t the thickness of the macroelement section.

$$e_{3,s} = \pm\left(\frac{t}{2} + \frac{t_s}{2}\right) \tag{C.2}$$

It is worth noticing that the moment of inertia about the longitudinal axis ($I_{1,s}$) is not taken into account, as it is considered negligible with respect to the torsional inertia of the section.

The elastic stiffness matrix of the additional layers ($\boldsymbol{K_{sl}}$) is then computed by summing the flexural and shear contribution of the individual elements:

$$\boldsymbol{K_{sl}} = \sum_{S} \left(\boldsymbol{K_s^{sl,F}} + \boldsymbol{K_s^{sl,S}} \right) \tag{C.3}$$

For the sake of completeness, $k_s = 2E_s/h$ is the equivalent axial stiffness per surface unit, E_s and G_s indicate the Young's and shear modulus of the s^{th} surface layer, χ is the appropriate shear factor functions of the section shape, whereas h represents the height of the macroelement.

$$
\boldsymbol{K}_{\boldsymbol{s}}^{\boldsymbol{sl,S}} = \begin{bmatrix}
0 & 0 & 0 & 0 & 0 & 0 & 0 & 0 & 0 & 0 & 0 & 0 \\
0 & \frac{G_s A_s}{\chi h} & 0 & 0 & 0 & 0 & -\frac{G_s A_s}{\chi h} & 0 & 0 & 0 & 0 & \frac{G_s A_s}{\chi} \\
0 & 0 & \frac{G_s A_s}{\chi h} & 0 & 0 & 0 & 0 & -\frac{G_s A_s}{\chi h} & 0 & 0 & -\frac{G_s A_s}{\chi} & 0 \\
0 & 0 & 0 & 0 & 0 & 0 & 0 & 0 & 0 & 0 & 0 & 0 \\
0 & 0 & 0 & 0 & 0 & 0 & 0 & 0 & 0 & 0 & 0 & 0 \\
0 & 0 & 0 & 0 & 0 & 0 & 0 & 0 & 0 & 0 & 0 & 0 \\
0 & 0 & 0 & 0 & 0 & 0 & 0 & 0 & 0 & 0 & 0 & 0 \\
0 & -\frac{G_s A_s}{\chi h} & 0 & 0 & 0 & 0 & \frac{G_s A_s}{\chi h} & 0 & 0 & 0 & 0 & -\frac{G_s A_s}{\chi} \\
0 & 0 & -\frac{G_s A_s}{\chi h} & 0 & 0 & 0 & 0 & \frac{G_s A_s}{\chi h} & 0 & 0 & \frac{G_s A_s}{\chi} & 0 \\
0 & 0 & 0 & 0 & 0 & 0 & 0 & 0 & 0 & 0 & 0 & 0 \\
0 & 0 & 0 & 0 & 0 & 0 & 0 & 0 & 0 & 0 & 0 & 0 \\
0 & 0 & 0 & 0 & 0 & 0 & 0 & 0 & 0 & 0 & 0 & 0 \\
0 & 0 & -\frac{G_s A_s}{\chi} & 0 & 0 & 0 & 0 & \frac{G_s A_s}{\chi} & 0 & 0 & \frac{G_s A_s h}{\chi} & 0 \\
0 & \frac{G_s A_s}{\chi} & 0 & 0 & 0 & 0 & -\frac{G_s A_s}{\chi} & 0 & 0 & 0 & 0 & \frac{G_s A_s h}{\chi}
\end{bmatrix}
$$

(C.4)

$$\boldsymbol{K_s^{sl,F}} = \begin{bmatrix}
k_sA_s & 0 & 0 & 0 & k_sS_{2,s} & 0 & 0 & 0 & 0 & 0 & 0 & 0 & -k_sA_s & -k_sS_{2,s} & 0 \\
0 & 0 & 0 & 0 & 0 & 0 & 0 & 0 & 0 & 0 & 0 & 0 & 0 & 0 & 0 \\
0 & 0 & 0 & 0 & 0 & 0 & 0 & 0 & 0 & 0 & 0 & 0 & 0 & 0 & 0 \\
0 & 0 & 0 & 0 & 0 & 0 & 0 & 0 & 0 & 0 & 0 & 0 & 0 & 0 & 0 \\
k_sS_{2,s} & 0 & 0 & 0 & k_sI_{2,s} & 0 & 0 & 0 & 0 & 0 & 0 & 0 & -k_sS_{2,s} & -k_sI_{2,s} & 0 \\
0 & 0 & 0 & 0 & 0 & kI_3 & 0 & 0 & 0 & 0 & 0 & 0 & 0 & 0 & -k_sI_{3,s} \\
0 & 0 & 0 & 0 & 0 & 0 & k_sA_s & 0 & 0 & 0 & k_sS_{2,s} & 0 & -k_sA_s & -k_sS_{2,s} & 0 \\
0 & 0 & 0 & 0 & 0 & 0 & 0 & 0 & 0 & 0 & 0 & 0 & 0 & 0 & 0 \\
0 & 0 & 0 & 0 & 0 & 0 & 0 & 0 & 0 & 0 & 0 & 0 & 0 & 0 & 0 \\
0 & 0 & 0 & 0 & 0 & 0 & 0 & 0 & 0 & 0 & 0 & 0 & 0 & 0 & 0 \\
0 & 0 & 0 & 0 & 0 & 0 & k_sS_{2,s} & 0 & 0 & 0 & k_sI_{2,s} & 0 & -k_sS_{2,s} & -k_sI_{2,s} & 0 \\
0 & 0 & 0 & 0 & 0 & 0 & 0 & 0 & 0 & 0 & 0 & k_sI_{3,s} & 0 & 0 & -k_sI_{3,s} \\
-k_sA_s & 0 & 0 & 0 & -k_sS_{2,s} & 0 & -k_sA_s & 0 & 0 & 0 & -k_sS_{2,s} & 0 & 2k_sA_s & 2k_sS_{2,s} & 0 \\
-k_sS_{2,s} & 0 & 0 & 0 & -k_sI_{2,s} & 0 & -k_sS_{2,s} & 0 & 0 & 0 & -k_sI_{2,s} & 0 & 2k_sS_{2,s} & 2k_sI_{2,s} & 0 \\
0 & 0 & 0 & 0 & 0 & -k_sI_{3,s} & 0 & 0 & 0 & 0 & 0 & -k_sI_{3,s} & 0 & 0 & 2k_sI_{3,s}
\end{bmatrix} \tag{C.5}$$

Appendix D

IMPLEMENTATION OF A FIBER FORMULATION OF THE END-INTERFACES

Despite the potentialities of the stripe formulation, in case of a particularly demanding load history, a full-fiber discretization might be more suitable, leading to more accurate results. Moreover, because of its straightforward implementation, it can be helpful in validating the correctness of the analytical integration.

A full-fiber formulation consists of discretizing the end-interfaces of the macroelement in both the in-plane and out-of-plane directions. In this context, a uniaxial constitutive law is assigned to each fiber, and the global response is computed by post-integrating the individual fiber contributions. Consequently, a full-fiber discretization is generally computationally demanding, especially compared to the stripe discretization proposed in this thesis. However, as the integration is numerically performed after deriving the uniaxial response of each fiber, complex constitutive laws can be adopted, overcoming the limitation of the stripe formulation.

Kinematic compatibility equations grant proper collaboration of the fibers with the end-interfaces, imposing their axial displacement according to a linear profile of the deformation of the cross-section. Consequently, the axial displacement is a function of the end-interface degrees of freedom (Figure D.1a) and of the fiber in-plane and out-of-plane coordinates with respect to the centroid of the section (Figure D.1b):

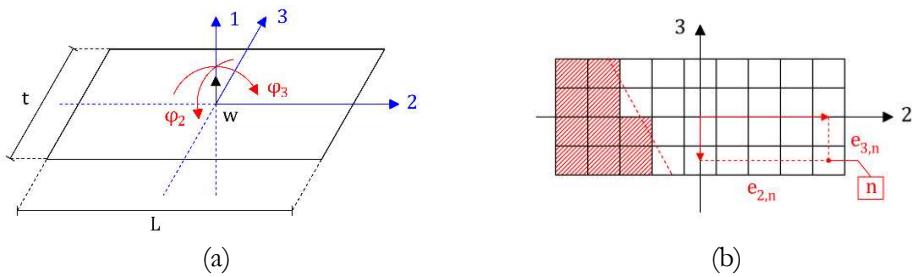

Figure D.1: (a) end-interface degrees of freedom, and (b) fiber discretization of the cross-section.

$$d_n = w + \varphi_2\, e_{3,n} - \varphi_3\, e_{2,n} \tag{D.1}$$

The n^{th} fiber in-plane ($e_{2,n}$) and out-of-plane ($e_{3,n}$) coordinates can be easily derived from equation (D.2), assuming the local reference system as barycentric:

$$e_{2,n} = \Delta L\left(n_2 - \frac{1}{2}\right) - \frac{L}{2} \qquad e_{3,n} = \Delta t\left(n_3 - \frac{1}{2}\right) - \frac{t}{2} \tag{D.2}$$

where ΔL and Δt refer to the length and the thickness of the single fiber, function of the discretization along the local 2- and 3- axes, respectively; L and t indicate the in-plane and out-of-plane cross-section dimensions; whereas n_2 and n_3 represent the fiber counters along the corresponding directions.

Since the fiber discretization involves the behavior of the end-interfaces only, without hence affecting the central body of the macroelement, the shear and the axial-flexural contributions can be computed separately and then summed. This operation is possible because of the kinematics inherent to the macroelement, which allows a complete decoupling between flexural and shear mechanisms.

In particular, the matrix $\boldsymbol{K^S}$ (D.5) is constant as it represents the elastic contribution of the central body, whose terms reflect the equations reported in Appendix B, whereas equation (D.6) shows the assembling algorithm to obtain the flexural contribution $\boldsymbol{K^F}$ starting from the interface-level nonlinear stiffness matrices. More specifically, equations (D.3) and (D.4) depict the interface-level matrices related to the i^{th} and j^{th} interfaces, respectively. In this context, $\mu_{i,n}$ and $\mu_{j,n}$ indicate the ductility demand in the n^{th} fiber of the corresponding interfaces.

$$\boldsymbol{K_i} = \sum_n \left(\frac{k\ \Delta L\ \Delta t}{\mu_{i,n}}\right) \begin{bmatrix} 1 & e_{3,n} & -e_{2,n} \\ e_{3,n} & e_{3,n}^2 & -e_{2,n}\, e_{3,n} \\ -e_{2,n} & -e_{2,n}\, e_{3,n} & e_{2,n}^2 \end{bmatrix} \tag{D.3}$$

$$\boldsymbol{K_j} = \sum_n \left(\frac{k\ \Delta L\ \Delta t}{\mu_{j,n}}\right) \begin{bmatrix} 1 & e_{3,n} & -e_{2,n} \\ e_{3,n} & e_{3,n}^2 & -e_{2,n}\, e_{3,n} \\ -e_{2,n} & -e_{2,n}\, e_{3,n} & e_{2,n}^2 \end{bmatrix} \tag{D.4}$$

It is worth noticing that equations (D.3) and (D.4) refer to the constitutive law reported in Figure D.2. However, equations (D.5) and (D.6) holds for any stress-displacement relationships. This procedure thus applies also in the case of additional lumped elements, as described in Chapter 6.

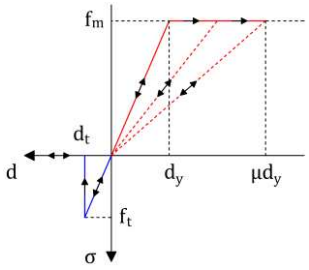

Figure D.2: Nonlinear constitutive law assigned to the individual fibers.

Similarly, the tangent stiffness matrix of the macroelement with a fiber discretization of the end-interfaces is computed as the sum between the central-body (equation (D.5)) and the end-interface contributions. As regards the constitutive law reported in Figure D.2, the end-interface contribution is obtained by simply zeroing the matrices corresponding to the fibers experiencing an increasing value of the ductility damage variable μ or exceeding the elastic tensile threshold. On the contrary, the nonlinear matrices reported in equations (D.3) and (D.4) are directly adopted. Finally, the element-level axial-flexural contribution to the tangent stiffness matrix is obtained by arranging the interface-level matrix terms, as reported in equation (D.6).

$$
\boldsymbol{K}^{s} = \begin{bmatrix}
0 & 0 & 0 & 0 & 0 & 0 & 0 & 0 & 0 & 0 & 0 & 0 & 0 & 0 & 0 & 0 & 0 & 0 \\
0 & \frac{GA}{\chi h} & 0 & 0 & 0 & 0 & 0 & -\frac{GA}{\chi h} & 0 & 0 & 0 & 0 & 0 & 0 & 0 & 0 & 0 & \frac{GA}{\chi} \\
0 & 0 & \frac{GA}{\chi h} & 0 & 0 & 0 & 0 & 0 & -\frac{GA}{\chi h} & 0 & 0 & 0 & 0 & 0 & 0 & 0 & -\frac{GA}{\chi} & 0 \\
0 & 0 & 0 & 0 & \frac{GI_1}{h} & 0 & 0 & 0 & 0 & -\frac{GI_1}{h} & 0 & 0 & 0 & 0 & 0 & 0 & 0 & 0 \\
0 & 0 & 0 & 0 & 0 & 0 & 0 & 0 & 0 & 0 & 0 & 0 & 0 & 0 & 0 & 0 & 0 & 0 \\
0 & 0 & 0 & 0 & 0 & 0 & 0 & 0 & 0 & 0 & 0 & 0 & 0 & 0 & 0 & 0 & 0 & 0 \\
0 & 0 & 0 & 0 & 0 & 0 & 0 & 0 & 0 & 0 & 0 & 0 & 0 & 0 & 0 & 0 & 0 & -\frac{GA}{\chi} \\
0 & -\frac{GA}{\chi h} & 0 & 0 & 0 & 0 & 0 & \frac{GA}{\chi h} & 0 & 0 & 0 & 0 & 0 & 0 & 0 & 0 & 0 & 0 \\
0 & 0 & -\frac{GA}{\chi h} & 0 & 0 & 0 & 0 & 0 & \frac{GA}{\chi h} & 0 & 0 & 0 & 0 & 0 & 0 & 0 & 0 & 0 \\
0 & 0 & 0 & 0 & -\frac{GI_1}{h} & 0 & 0 & 0 & 0 & \frac{GI_1}{h} & 0 & 0 & 0 & 0 & 0 & 0 & 0 & 0 \\
0 & 0 & 0 & 0 & 0 & 0 & 0 & 0 & 0 & 0 & 0 & 0 & 0 & 0 & 0 & 0 & 0 & 0 \\
0 & 0 & 0 & 0 & 0 & 0 & 0 & 0 & 0 & 0 & 0 & 0 & 0 & 0 & 0 & 0 & 0 & 0 \\
0 & 0 & 0 & 0 & 0 & 0 & 0 & 0 & 0 & 0 & 0 & 0 & 0 & 0 & 0 & 0 & 0 & 0 \\
0 & 0 & -\frac{GA}{\chi} & 0 & 0 & 0 & 0 & 0 & \frac{GA}{\chi} & 0 & 0 & 0 & 0 & 0 & 0 & 0 & 0 & 0 \\
0 & \frac{GA}{\chi} & 0 & 0 & 0 & 0 & 0 & -\frac{GA}{\chi} & 0 & 0 & 0 & 0 & 0 & 0 & 0 & 0 & 0 & \frac{GAh}{\chi}
\end{bmatrix}
\tag{D.5}
$$

$$K^F = \begin{bmatrix}
[K_i]_{11} & 0\,0\,0 & [K_i]_{12} & [K_i]_{13} & 0 & 0\,0\,0 & 0 & 0 & -[K_i]_{11} & -[K_i]_{12} & -[K_i]_{13} \\
0 & 0\,0\,0 & 0 & 0 & 0 & 0\,0\,0 & 0 & 0 & 0 & 0 & 0 \\
0 & 0\,0\,0 & 0 & 0 & 0 & 0\,0\,0 & 0 & 0 & 0 & 0 & 0 \\
0 & 0\,0\,0 & 0 & 0 & 0 & 0\,0\,0 & 0 & 0 & 0 & 0 & 0 \\
[K_i]_{21} & 0\,0\,0 & [K_i]_{22} & [K_i]_{23} & 0 & 0\,0\,0 & 0 & 0 & -[K_i]_{21} & -[K_i]_{22} & -[K_i]_{23} \\
[K_i]_{31} & 0\,0\,0 & [K_i]_{32} & [K_i]_{33} & 0 & 0\,0\,0 & 0 & 0 & -[K_i]_{31} & -[K_i]_{32} & -[K_i]_{33} \\
0 & 0\,0\,0 & 0 & 0 & [K_j]_{11} & 0\,0\,0 & [K_j]_{12} & [K_j]_{13} & -[K_j]_{11} & -[K_j]_{12} & -[K_j]_{13} \\
0 & 0\,0\,0 & 0 & 0 & 0 & 0\,0\,0 & 0 & 0 & 0 & 0 & 0 \\
0 & 0\,0\,0 & 0 & 0 & 0 & 0\,0\,0 & 0 & 0 & 0 & 0 & 0 \\
0 & 0\,0\,0 & 0 & 0 & 0 & 0\,0\,0 & 0 & 0 & 0 & 0 & 0 \\
0 & 0\,0\,0 & 0 & 0 & [K_j]_{21} & 0\,0\,0 & [K_j]_{22} & [K_j]_{23} & -[K_j]_{21} & -[K_j]_{22} & -[K_j]_{23} \\
0 & 0\,0\,0 & 0 & 0 & [K_j]_{31} & 0\,0\,0 & [K_j]_{32} & [K_j]_{33} & -[K_j]_{31} & -[K_j]_{32} & -[K_j]_{33} \\
-[K_i]_{11} & 0\,0\,0 & -[K_i]_{12} & -[K_i]_{13} & -[K_j]_{11} & 0\,0\,0 & -[K_j]_{12} & -[K_j]_{13} & [K_i]_{11}+[K_j]_{11} & [K_i]_{12}+[K_j]_{12} & [K_i]_{13}+[K_j]_{13} \\
-[K_i]_{21} & 0\,0\,0 & -[K_i]_{22} & -[K_i]_{23} & -[K_j]_{21} & 0\,0\,0 & -[K_j]_{22} & -[K_j]_{23} & [K_i]_{21}+[K_j]_{21} & [K_i]_{22}+[K_j]_{22} & [K_i]_{23}+[K_j]_{23} \\
-[K_i]_{31} & 0\,0\,0 & -[K_i]_{32} & -[K_i]_{33} & -[K_j]_{31} & 0\,0\,0 & -[K_j]_{32} & -[K_j]_{33} & [K_i]_{31}+[K_j]_{31} & [K_i]_{32}+[K_j]_{32} & [K_i]_{33}+[K_j]_{33}
\end{bmatrix} \tag{D.6}$$

Appendix E

THREE-DIMENSIONAL NONLINEAR CORRECTIONS: TENSION

The stripe formulation of the presented macroelement consists of discretizing the end-interfaces in a series of stripes, whose nonlinear in-plane response is retrieved by applying analytical inelastic corrections to the elastic contributions. In this context, the governing system of equations of the three-dimensional macroelement can be summarized as follows:

$$\boldsymbol{F^{int}(u)} = \boldsymbol{Ku} + \boldsymbol{F^{*}(u)} + \boldsymbol{F^{**}(u)} \tag{E.1}$$

where $\boldsymbol{K}$ is the elastic stiffness matrix, $\boldsymbol{u}$ and $\boldsymbol{F^{int}(u)}$ are the generalized displacement and internal force vectors, whereas $\boldsymbol{F^{*}(u)}$ and $\boldsymbol{F^{**}(u)}$ represent the analytical inelastic correction vectors accounting for the nonlinear response in tension and in compression, respectively.

In this section, the three-dimensional nonlinear corrections accounting for the tensile behavior of the end-interface are presented (E.2). The elasto-fragile response is mostly addressed, as the no-tension behavior consists of a particular case of the latter, where the elastic tensile displacement threshold d_t is set to a zero value.

$$\boldsymbol{F^{*}(u)} = \left\{N_i^* \;\; 0 \;\; 0 \;\; 0 \;\; M_{2,i}^* \;\; M_{3,i}^* \;\; N_j^* \;\; 0 \;\; 0 \;\; 0 \;\; M_{2,j}^* \;\; M_{3,j}^* \;\; N_e^* \;\; M_{2,e}^* \;\; M_{3,e}^*\right\}^T \tag{E.2}$$

The total nodal correction is obtained by summing the contributions of the individual stripes, as reported in the equation (E.3), with $e_{3,n}$ representing the centroid out-of-plane coordinate of the n^{th} stripe with respect to the centroid of the end-interface.

$$N^* = \sum_n N_n^* \qquad M_2^* = \sum_n M_{2,n}^* = \sum_n \left(N_n^* \, e_{3,n}\right) \qquad M_3^* = \sum_n M_{3,n}^* \tag{E.3}$$

Furthermore, the following notation will be used for the i^{th} interface:

$$\begin{cases} w_n = (w_e - w_i) + (\varphi_{2,e} - \varphi_{2,i})\, e_{3,n} \\ \varphi_n = \varphi_{3,e} - \varphi_{3,i} \end{cases} \tag{E.4}$$

and for the j^{th} one:

$$\begin{cases} w_n = (w_j - w_e) + (\varphi_{2,j} - \varphi_{2,e})\, e_{3,n} \\ \varphi_n = \varphi_{3,j} - \varphi_{3,e} \end{cases} \tag{E.5}$$

The corresponding sectional edge displacements of the n^{th} stripe are obtained by assuming small displacements and rotations:

$$\begin{cases} d_{LT,n} = w_n + \varphi_n \dfrac{L}{2} \\ d_{RT,n} = w_n - \varphi_n \dfrac{L}{2} \end{cases} \tag{E.6}$$

It is worth noticing that, for a no-tension behavior, a single correction accounting for the response of both the edges suffices. On the contrary, since a brittle-tensile strength deals with damage variables, each edge needs to be analyzed independently, providing thus corrections separately.

In this context, the quantities and the corresponding expressions governing the constitutive law are reported in equation (E.7), where $L_{T,n}$ and $L_{C,n}$ indicate the length in tension and in compression, whereas $L'_{CR,LT,n}$ and $L'_{CR,RT,n}$ represent the current cracking length at the left and right sides of the considered end-interface. It is worth reminding that, in a no-tension framework, the length in tension coincides with the current cracking length. On the other hand, a net distinction arises for an elasto-fragile constitutive law. Moreover, as already discussed, the maximum-reached values of the cracking length at each edge ($L_{CR,LT,n}$ and $L_{CR,RT,n}$) are stored as state variables to account for damage accumulation.

$$\begin{cases} L'_{CR,LT,n} = \dfrac{w_n}{\varphi_n} + \dfrac{L}{2} - \dfrac{d_t}{\varphi_n} \\ L'_{CR,RT,n} = -\dfrac{w_n}{\varphi_n} + \dfrac{L}{2} + \dfrac{d_t}{\varphi_n} \end{cases} \qquad L_{T,n} = \frac{w_n}{|\varphi_n|} + \frac{L}{2} \qquad L_{C,n} = L - L_{T,n} \tag{E.7}$$

Additionally, the total cracking length $L_{CR,n}$ is also checked step-by-step, computed as the sum of the cracking lengths at the two opposite corners of the n^{th} stripe. In particular, when cracking involves the whole length of a stripe, the formulation on that stripe degenerates to a no-tension behavior.

Since the corrections are individually computed for each edge of the n^{th} stripe, the whole stripe contributions are obtained by summing the left (N^*_{LT}) and (N^*_{RT}) right counterparts, as reported in the following:

i^{th} interface **j^{th} interface**

$$\begin{cases} N^*_{i,n} = N^*_{LT,i,n} + N^*_{RT,i,n} \\ M^*_{2,i,n} = M^*_{2,LT,i,n} + M^*_{2,RT,i,n} \\ M^*_{3,i,n} = M^*_{3,LT,i,n} + M^*_{3,RT,i,n} \end{cases} \qquad \begin{cases} N^*_{j,n} = N^*_{LT,j,n} + N^*_{RT,j,n} \\ M^*_{2,j,n} = M^*_{2,LT,j,n} + M^*_{2,RT,j,n} \\ M^*_{3,j,n} = M^*_{3,LT,j,n} + M^*_{3,RT,j,n} \end{cases} \tag{E.8}$$

As already described, the central body is also responsible for coupling the response of the end-interfaces and ensure equilibrium. For this reason, compatibility relationships are to be extended to the nonlinear corrections:

$$\begin{cases} N^*_{e,n} = -\left(N^*_{i,n} + N^*_{j,n}\right) \\ M^*_{2,e,n} = N^*_{e,n}\, e_{3,n} \\ M^*_{3,e,n} = -\left(M^*_{3,i,n} + M^*_{3,j,n}\right) \end{cases} \tag{E.9}$$

It is worth noticing that the two-dimensional corrections can be easily derived by imposing the out-of-plane rotation terms (φ_2) in equations (E.4) and (E.5) equal to zero, and a number of stripes (n) equal to a unit value.

In the following, the analytical corrections for the nonlinear response in tension of the three-dimensional macroelement are thoroughly presented. In particular, each case is associated to a set of inelastic equations that corresponds to a particular kinematic condition.

Case 1

Figure E.1 depicts a situation in which the current cracking length on the considered edge ($L'_{CR,LT,n}$ or $L'_{CR,RT,n}$) exceeds the stored one ($L_{CR,LT,n}$ or $L_{CR,RT,n}$) and involves a portion of the section, provided that the stripe investigated has not been completely cracked in the previous load steps ($0 > L_{CR,n} > L$). Furthermore, in order for the corrections to be consistent with the stress profile, the current length in tension needs to exceed the stored cracking length ($L_{T,n} \geq L_{CR,LT,n}$ or $L_{T,n} \geq L_{CR,RT,n}$), and the rotation of the section φ_n needs to be clockwise and counterclockwise for the left and right corners, respectively, while keeping the displacement on the considered edge positive ($d_{LT,n} > 0$ and $\varphi_n \geq 0$ or $d_{RT,n} > 0$ and $\varphi_n \leq 0$).

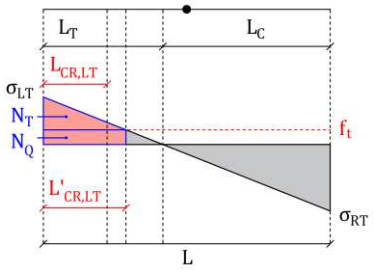

Figure E.1: Conditions addressed within cracking phenomena with limited tensile strength: case 1.

i^{th} interface – Left edge

$$\begin{cases} \left.\begin{aligned} N^*_{Q,LT,i,n} &= k\,\Delta t\,L_{CR,LT,i,n}\left(w_n+\varphi_n\frac{L}{2}-L_{CR,LT,i,n}\,\varphi_n\right)\\ N^*_{T,LT,i,n} &= \frac{k\,\Delta t\,L^2_{CR,LT,i,n}\,\varphi_n}{2}\end{aligned}\right\} \; N^*_{LT,i,n}=N^*_{Q,LT,i,n}+N^*_{T,LT,i,n}\\ M^*_{2,LT,i,n}=N^*_{LT,i,n}\,e_{3,n}\\ \left.\begin{aligned} M^*_{3,Q,LT,i,n} &= N^*_{Q,LT,i,n}\left(\frac{L}{2}-\frac{L_{CR,LT,i,n}}{2}\right)\\ M^*_{3,T,LT,i,n} &= N^*_{T,LT,i,n}\left(\frac{L}{2}-\frac{L_{CR,LT,i,n}}{3}\right)\end{aligned}\right\} \; M^*_{3,LT,i,n}=M^*_{3,Q,LT,i,n}+M^*_{3,T,LT,i,n}\end{cases} \tag{E.10}$$

i^{th} interface – Right edge

$$\begin{cases} \left.\begin{aligned} N^*_{Q,LT,i,n} &= k\,\Delta t\,L_{CR,RT,i,n}\left(w_n-\varphi_n\frac{L}{2}+L_{CR,RT,i,n}\,\varphi_n\right)\\ N^*_{T,RT,i,n} &= -\frac{k\,\Delta t\,L^2_{CR,RT,i,n}\,\varphi_n}{2}\end{aligned}\right\} \; N^*_{RT,i,n}=N^*_{Q,RT,i,n}+N^*_{T,RT,i,n}\\ M^*_{2,RT,i,n}=N^*_{RT,i,n}\,e_{3,n}\\ \left.\begin{aligned} M^*_{3,Q,RT,i,n} &= -N^*_{Q,RT,i,n}\left(\frac{L}{2}-\frac{L_{CR,RT,i,n}}{2}\right)\\ M^*_{3,T,RT,i,n} &= -N^*_{T,RT,i,n}\left(\frac{L}{2}-\frac{L_{CR,RT,i,n}}{3}\right)\end{aligned}\right\} \; M^*_{3,RT,i,n}=M^*_{3,Q,RT,i,n}+M^*_{3,T,RT,i,n}\end{cases} \tag{E.11}$$

j^{th} interface – Left edge

$$\begin{cases} N^*_{Q,LT,j,n} = -k\ \Delta t\ L_{CR,LT,j,n}\left(w_n + \varphi_n \dfrac{L}{2} - L_{CR,LT,j,n}\ \varphi_n\right) \\ N^*_{T,LT,j,n} = -\dfrac{k\ \Delta t\ L^2_{CR,LT,j,n}\ \varphi_n}{2} \end{cases} \Bigg\} \quad N^*_{LT,j,n} = N^*_{Q,LT,j,n} + N^*_{T,LT,j,n}$$

$$\begin{cases} M^*_{2,LT,j,n} = N^*_{LT,j,n}\ e_{3,n} \\ M^*_{3,Q,LT,j,n} = N^*_{Q,LT,j,n}\left(\dfrac{L}{2} - \dfrac{L_{CR,LT,j,n}}{2}\right) \\ M^*_{3,T,LT,j,n} = N^*_{T,LT,j,n}\left(\dfrac{L}{2} - \dfrac{L_{CR,LT,j,n}}{3}\right) \end{cases} \Bigg\} \quad M^*_{3,LT,j,n} = M^*_{3,Q,LT,j,n} + M^*_{3,T,LT,j,n} \qquad \textbf{(E.12)}$$

j^{th} interface – Right edge

$$\begin{cases} N^*_{Q,LT,j,n} = -k\ \Delta t\ L_{CR,RT,j,n}\left(w_n - \varphi_n \dfrac{L}{2} + L_{CR,RT,j,n}\ \varphi_n\right) \\ N^*_{T,RT,j,n} = \dfrac{k\ \Delta t\ L^2_{CR,RT,j,n}\ \varphi_n}{2} \end{cases} \Bigg\} \quad N^*_{RT,j,n} = N^*_{Q,RT,j,n} + N^*_{T,RT,j,n}$$

$$\begin{cases} M^*_{2,RT,j,n} = N^*_{RT,j,n}\ e_{3,n} \\ M^*_{3,Q,RT,j,n} = -N^*_{Q,RT,j,n}\left(\dfrac{L}{2} - \dfrac{L_{CR,RT,j,n}}{2}\right) \\ M^*_{3,T,RT,j,n} = -N^*_{T,RT,j,n}\left(\dfrac{L}{2} - \dfrac{L_{CR,RT,j,n}}{3}\right) \end{cases} \Bigg\} \quad M^*_{3,RT,j,n} = M^*_{3,Q,RT,j,n} + M^*_{3,T,RT,j,n} \qquad \textbf{(E.13)}$$

Case 2

Figure E.2 depicts a situation in which the current cracking length on the considered edge ($L'_{CR,LT,n}$ or $L'_{CR,RT,n}$) involves a portion of the section, provided that the stripe investigated has not been completely cracked in the previous load steps ($0 > L_{CR,n} > L$). Furthermore, in order for the corrections to be consistent with the stress profile, the current length in tension must not exceed the stored cracking length ($L_{T,n} < L_{CR,LT,n}$ or $L_{T,n} < L_{CR,RT,n}$), and the rotation of the section φ_n needs to be clockwise and counterclockwise for the left and right corners, respectively, while keeping the displacement on the considered edge positive ($d_{LT,n} > 0$ and $\varphi_n \geq 0$ or $d_{RT,n} > 0$ and $\varphi_n \leq 0$).

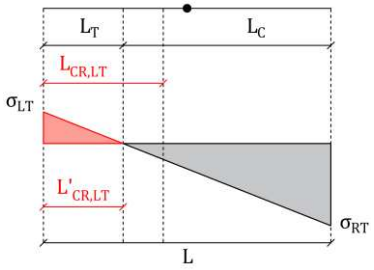

Figure E.2: Conditions addressed within cracking phenomena with limited tensile strength: case 2.

i^{th} interface – Left edge

$$\begin{cases} N^*_{LT,i,n} = \dfrac{L_{T,i,n}\, k\, \Delta t}{2}\left(w_n + \varphi_n \dfrac{L}{2}\right) \\ M^*_{2,LT,i,n} = N^*_{LT,i,n}\, e_{3,n} \\ M^*_{3,LT,i,n} = N^*_{LT,i,n}\left(\dfrac{L}{2} - \dfrac{L_{T,i,n}}{3}\right) \end{cases}$$

i^{th} interface – Right edge

$$\begin{cases} N^*_{RT,i,n} = \dfrac{L_{T,i,n}\, k\, \Delta t}{2}\left(w_n - \varphi_n \dfrac{L}{2}\right) \\ M^*_{2,RT,i,n} = N^*_{RT,i,n}\, e_{3,n} \\ M^*_{3,RT,i,n} = -N^*_{RT,i,n}\left(\dfrac{L}{2} - \dfrac{L_{T,i,n}}{3}\right) \end{cases} \quad \textbf{(E.14)}$$

j^{th} interface – Left edge

$$\begin{cases} N^*_{LT,j,n} = -\dfrac{L_{T,j,n}\, k\, \Delta t}{2}\left(w_n + \varphi_n \dfrac{L}{2}\right) \\ M^*_{2,LT,j,n} = N^*_{LT,j,n}\, e_{3,n} \\ M^*_{3,LT,j,n} = N^*_{LT,j,n}\left(\dfrac{L}{2} - \dfrac{L_{T,j,n}}{3}\right) \end{cases}$$

j^{th} interface – Right edge

$$\begin{cases} N^*_{RT,j,n} = -\dfrac{L_{T,j,n}\, k\, \Delta t}{2}\left(w_n - \varphi_n \dfrac{L}{2}\right) \\ M^*_{2,RT,j,n} = N^*_{RT,j,n}\, e_{3,n} \\ M^*_{3,RT,j,n} = -N^*_{RT,j,n}\left(\dfrac{L}{2} - \dfrac{L_{T,j,n}}{3}\right) \end{cases} \quad \textbf{(E.15)}$$

Case 3

Figure E.3 depicts a situation in which the stored cracking length on the considered edge ($L_{CR,LT,n}$ or $L_{CR,RT,n}$) involves a portion of the section, provided that the stripe investigated has not been completely cracked in the previous load steps ($0 > L_{CR,n} > L$). Furthermore, in order for the corrections to be consistent with the stress profile, the rotation of the section φ_n needs to be counterclockwise and clockwise for the left and right corners, respectively, while keeping the displacement on the considered edge positive ($d_{LT,n} \geq 0$ and $\varphi_n < 0$ or $d_{RT,n} \geq 0$ and $\varphi_n > 0$).

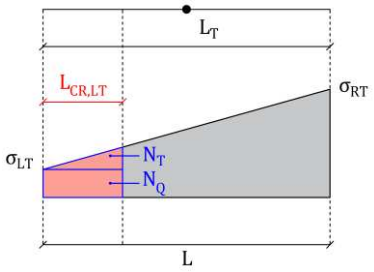

Figure E.3: Conditions addressed within cracking phenomena with limited tensile strength: case 3.

i^{th} interface – Left edge

$$\begin{cases} \left.\begin{aligned} N^*_{Q,LT,i,n} &= k\,\Delta t\,L_{CR,LT,i,n}\left(w_n+\varphi_n\frac{L}{2}\right)\\ N^*_{T,LT,i,n} &= -\frac{k\,\Delta t\,L^2_{CR,LT,i,n}\,\varphi_n}{2}\end{aligned}\right\} \; N^*_{LT,i,n}=N^*_{Q,LT,i,n}+N^*_{T,LT,i,n}\\ M^*_{2,LT,i,n}=N^*_{LT,i,n}\,e_{3,n}\\ \left.\begin{aligned} M^*_{3,Q,LT,i,n} &= N^*_{Q,LT,i,n}\left(\frac{L}{2}-\frac{L_{CR,LT,i,n}}{2}\right)\\ M^*_{3,T,LT,i,n} &= N^*_{T,LT,i,n}\left(\frac{L}{2}-\frac{2L_{CR,LT,i,n}}{3}\right)\end{aligned}\right\} \; M^*_{3,LT,i,n}=M^*_{3,Q,LT,i,n}+M^*_{3,T,LT,i,n}\end{cases} \tag{E.16}$$

i^{th} interface – Right edge

$$\begin{cases} \left.\begin{aligned} N^*_{Q,LT,i,n} &= k\,\Delta t\,L_{CR,RT,i,n}\left(w_n-\varphi_n\frac{L}{2}\right)\\ N^*_{T,RT,i,n} &= \frac{k\,\Delta t\,L^2_{CR,RT,i,n}\,\varphi_n}{2}\end{aligned}\right\} \; N^*_{RT,i,n}=N^*_{Q,RT,i,n}+N^*_{T,RT,i,n}\\ M^*_{2,RT,i,n}=N^*_{RT,i,n}\,e_{3,n}\\ \left.\begin{aligned} M^*_{3,Q,RT,i,n} &= -N^*_{Q,RT,i,n}\left(\frac{L}{2}-\frac{L_{CR,RT,i,n}}{2}\right)\\ M^*_{3,T,RT,i,n} &= -N^*_{T,RT,i,n}\left(\frac{L}{2}-\frac{2L_{CR,RT,i,n}}{3}\right)\end{aligned}\right\} \; M^*_{3,RT,i,n}=M^*_{3,Q,RT,i,n}+M^*_{3,T,RT,i,n}\end{cases} \tag{E.17}$$

j^{th} interface – Left edge

$$\begin{cases} N^*_{Q,LT,j,n} = -k\,\Delta t\,L_{CR,LT,j,n}\left(w_n + \varphi_n\dfrac{L}{2}\right) \\ N^*_{T,LT,j,n} = \dfrac{k\,\Delta t\,L^2_{CR,LT,j,n}\,\varphi_n}{2} \end{cases} \Bigg\} \; N^*_{LT,j,n} = N^*_{Q,LT,j,n} + N^*_{T,LT,j,n}$$

$$\begin{cases} M^*_{2,LT,j,n} = N^*_{LT,j,n}\,e_{3,n} \\ M^*_{3,Q,LT,j,n} = N^*_{Q,LT,j,n}\left(\dfrac{L}{2} - \dfrac{L_{CR,LT,j,n}}{2}\right) \\ M^*_{3,T,LT,j,n} = N^*_{T,LT,j,n}\left(\dfrac{L}{2} - \dfrac{2L_{CR,LT,j,n}}{3}\right) \end{cases} \Bigg\} \; M^*_{3,LT,j,n} = M^*_{3,Q,LT,j,n} + M^*_{3,T,LT,j,n} \qquad \textbf{(E.18)}$$

j^{th} interface – Right edge

$$\begin{cases} N^*_{Q,LT,j,n} = -k\,\Delta t\,L_{CR,RT,j,n}\left(w_n - \varphi_n\dfrac{L}{2}\right) \\ N^*_{T,RT,j,n} = -\dfrac{k\,\Delta t\,L^2_{CR,RT,j,n}\,\varphi_n}{2} \end{cases} \Bigg\} \; N^*_{RT,j,n} = N^*_{Q,RT,j,n} + N^*_{T,RT,j,n}$$

$$\begin{cases} M^*_{2,RT,j,n} = N^*_{RT,j,n}\,e_{3,n} \\ M^*_{3,Q,RT,j,n} = -N^*_{Q,RT,j,n}\left(\dfrac{L}{2} - \dfrac{L_{CR,RT,j,n}}{2}\right) \\ M^*_{3,T,RT,j,n} = -N^*_{T,RT,j,n}\left(\dfrac{L}{2} - \dfrac{2L_{CR,RT,j,n}}{3}\right) \end{cases} \Bigg\} \; M^*_{3,RT,j,n} = M^*_{3,Q,RT,j,n} + M^*_{3,T,RT,j,n} \qquad \textbf{(E.19)}$$

Case 4

Figure E.4 depicts a situation in which the stored cracking length on the considered edge ($L_{CR,LT,n}$ or $L_{CR,RT,n}$) involves a portion of the section, provided that the stripe investigated has not been completely cracked in the previous load steps ($0 > L_{CR,n} > L$). Furthermore, in order for the corrections to be consistent with the stress profile, the rotation of the section φ_n needs to be counterclockwise and clockwise for the left and right corners, respectively, while keeping the displacement on the considered edge negative ($d_{LT,n} < 0$ and $\varphi_n < 0$ or $d_{RT,n} < 0$ and $\varphi_n > 0$). Under the aforementioned conditions, the stored cracking length must exceed the compressive length on the considered edge ($L_{CR,LT,n} > L_{C,n}$ or $L_{CR,RT,n} > L_{C,n}$).

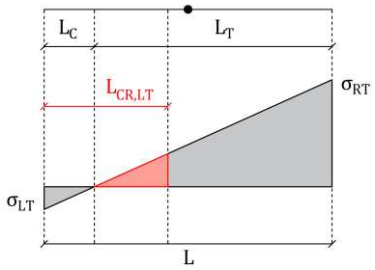

Figure E.4: Conditions addressed within cracking phenomena with limited tensile strength: case 4.

i^{th} interface – Left edge

$$\begin{cases} N^*_{LT,i,n} = -\dfrac{k\,\Delta t\,\varphi_n}{2}\left(L_{CR,LT,i,n} - L_{C,i,n}\right)^2 \\ M^*_{2,LT,i,n} = N^*_{LT,i,n}\,e_{3,n} \\ M^*_{3,LT,i,n} = N^*_{LT,i,n}\left(\dfrac{L}{2} - \dfrac{L_{C,i,n}}{3} - \dfrac{2}{3}L_{CR,LT,i,n}\right) \end{cases}$$

i^{th} interface – Right edge

$$\begin{cases} N^*_{RT,i,n} = \dfrac{k\,\Delta t\,\varphi_n}{2}\left(L_{CR,RT,i,n} - L_{C,i,n}\right)^2 \\ M^*_{2,RT,i,n} = N^*_{RT,i,n}\,e_{3,n} \\ M^*_{3,RT,i,n} = -N^*_{RT,i,n}\left(\dfrac{L}{2} - \dfrac{L_{C,i,n}}{3} - \dfrac{2}{3}L_{CR,RT,i,n}\right) \end{cases} \quad \textbf{(E.20)}$$

j^{th} interface – Left edge

$$\begin{cases} N^*_{LT,j,n} = \dfrac{k\,\Delta t\,\varphi_n}{2}\left(L_{CR,LT,j,n} - L_{C,j,n}\right)^2 \\ M^*_{2,LT,j,n} = N^*_{LT,j,n}\,e_{3,n} \\ M^*_{3,LT,j,n} = N^*_{LT,j,n}\left(\dfrac{L}{2} - \dfrac{L_{C,j,n}}{3} - \dfrac{2}{3}L_{CR,LT,j,n}\right) \end{cases}$$

j^{th} interface – Right edge

$$\begin{cases} N^*_{RT,j,n} = -\dfrac{k\,\Delta t\,\varphi_n}{2}\left(L_{CR,RT,j,n} - L_{C,j,n}\right)^2 \\ M^*_{2,RT,j,n} = N^*_{RT,j,n}\,e_{3,n} \\ M^*_{3,RT,j,n} = N^*_{RT,j,n}\left(\dfrac{L}{2} - \dfrac{L_{C,j,n}}{3} - \dfrac{2}{3}L_{CR,RT,j,n}\right) \end{cases} \quad \textbf{(E.21)}$$

Case 5

Figure E.5 depicts a situation in which the cracking phenomenon involves the whole length of the n^{th} stripe, and the length in tension is equal to the total length ($L_{CR,n} = L_{T,n} = L$). Consequently, the nonlinear corrections consist of removing the entire elastic contributions, as no more load can be withstood. Moreover, since this case represents a degeneration in a no-tension framework, there is no need to express the edge corrections separately.

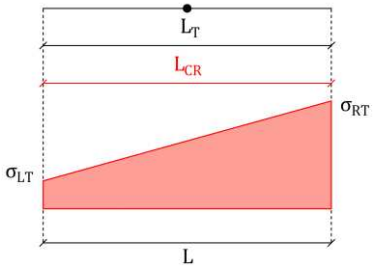

Figure E.5: Conditions addressed within cracking phenomena with limited tensile strength: case 5.

i^{th} interface

$$\begin{cases} N^*_{i,n} = k\,\Delta t\,L\,w_n \\ M^*_{2,i,n} = N^*_{i,n}\,e_{3,n} \\ M^*_{3,i,n} = \left(\dfrac{k\,\Delta t\,L^3}{12}\right)\varphi_n \end{cases} \tag{E.22}$$

j^{th} interface

$$\begin{cases} N^*_{j,n} = -k\,\Delta t\,L\,w_n \\ M^*_{2,j,n} = N^*_{j,n}\,e_{3,n} \\ M^*_{3,j,n} = -\left(\dfrac{k\,\Delta t\,L^3}{12}\right)\varphi_n \end{cases} \tag{E.23}$$

Case 6

Figure E.6 depicts a situation in which the current cracking length involves the whole n^{th} stripe; however, the length in tension does not exceed the total length ($L_{T,n} < L_{CR,n} = L$). Since this case is in common with a no-tension behavior, a unique correction suffices to describe the response of both sides of the section.

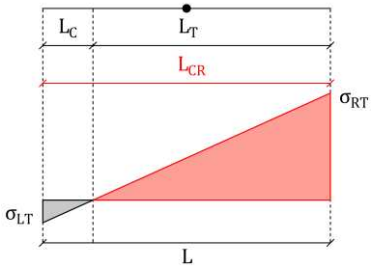

Figure E.6: Conditions addressed within cracking phenomena with limited tensile strength: case 6.

i^{th} interface

$$\begin{cases} N^*_{i,n} = \dfrac{k\,\Delta t}{8|\varphi_n|}(2w_n + L|\varphi_n|)^2 \\ M^*_{2,i,n} = N^*_{i,n}\, e_{3,n} \\ M^*_{3,i,n} = -\dfrac{k\,\Delta t\,(w_n - L|\varphi_n|)(2w_n + L|\varphi_n|)^2}{24|\varphi_n|\varphi_n} \end{cases} \quad \textbf{(E.24)}$$

j^{th} interface

$$\begin{cases} N^*_{i,n} = -\dfrac{k\,\Delta t}{8|\varphi_n|}(2w_n + L|\varphi_n|)^2 \\ M^*_{2,i,n} = N^*_{i,n}\, e_{3,n} \\ M^*_{3,i,n} = \dfrac{k\,\Delta t\,(w_n - L|\varphi_n|)(2w_n + L|\varphi_n|)^2}{24|\varphi_n|\varphi_n} \end{cases} \quad \textbf{(E.25)}$$

NONLINEAR CORRECTION GRADIENT: TENSION

To implement the Newton-Raphson method described in Chapter 5.5, the tangent stiffness matrix needs to be calculated. In this context, this section outlines the tensile response by reporting the terms populating the corresponding gradient $\boldsymbol{\nabla F}^*$ (E.27). Furthermore, unlike for a no-tension behavior, since the elasto-fragile constitutive law deals with damage variables to account for damage accumulation, the corresponding gradient matrix might not be symmetric.

For the sake of simplicity, as the derivatives with respect to the degrees of freedom of the two end-interfaces are mutually identical, the following notation hereafter applies:

$$\frac{\partial F_{i-j}^*}{\partial u_{i-j}} = \frac{\partial F_i^*}{\partial u_i} = \frac{\partial F_j^*}{\partial u_j} \tag{E.26}$$

being F_{i-j}^* and u_{i-j} the generalized internal correction force and displacement quantities, respectively, whereas with the subscript i and j the reference to the i^{th} and j^{th} interfaces is indicated.

It is worth noticing that all the equations reported in this section hold as long as the notations defined in (E.4) and (E.5) are satisfied, depending on the interface considered. If this is not the case, equation (E.26) might not apply.

$$\nabla \boldsymbol{F}^* = \begin{bmatrix}
\frac{\partial N_i^*}{\partial w_i} & 0 & 0 & 0 & \frac{\partial N_i^*}{\partial \varphi_{2,i}} & \frac{\partial N_i^*}{\partial \varphi_{3,i}} & 0 & 0 & 0 & 0 & 0 & 0 & \frac{\partial N_i^*}{\partial w_e} & \frac{\partial N_i^*}{\partial \varphi_{2,e}} & \frac{\partial N_i^*}{\partial \varphi_{3,e}} \\
0 & 0 & 0 & 0 & 0 & 0 & 0 & 0 & 0 & 0 & 0 & 0 & 0 & 0 & 0 \\
0 & 0 & 0 & 0 & 0 & 0 & 0 & 0 & 0 & 0 & 0 & 0 & 0 & 0 & 0 \\
0 & 0 & 0 & 0 & 0 & 0 & 0 & 0 & 0 & 0 & 0 & 0 & 0 & 0 & 0 \\
\frac{\partial M_{2,i}^*}{\partial w_i} & 0 & 0 & 0 & \frac{\partial M_{2,i}^*}{\partial \varphi_{2,i}} & \frac{\partial M_{2,i}^*}{\partial \varphi_{3,i}} & 0 & 0 & 0 & 0 & 0 & 0 & \frac{\partial M_{2,i}^*}{\partial w_e} & \frac{\partial M_{2,i}^*}{\partial \varphi_{2,e}} & \frac{\partial M_{2,i}^*}{\partial \varphi_{3,e}} \\
\frac{\partial M_{3,i}^*}{\partial w_i} & 0 & 0 & 0 & \frac{\partial M_{3,i}^*}{\partial \varphi_{2,i}} & \frac{\partial M_{3,i}^*}{\partial \varphi_{3,i}} & 0 & 0 & 0 & 0 & 0 & 0 & \frac{\partial M_{3,i}^*}{\partial w_e} & \frac{\partial M_{3,i}^*}{\partial \varphi_{2,e}} & \frac{\partial M_{3,i}^*}{\partial \varphi_{3,e}} \\
0 & 0 & 0 & 0 & 0 & 0 & \frac{\partial N_j^*}{\partial w_j} & 0 & 0 & 0 & \frac{\partial N_j^*}{\partial \varphi_{2,j}} & \frac{\partial N_j^*}{\partial \varphi_{3,j}} & \frac{\partial N_j^*}{\partial w_e} & \frac{\partial N_j^*}{\partial \varphi_{2,e}} & \frac{\partial N_j^*}{\partial \varphi_{3,e}} \\
0 & 0 & 0 & 0 & 0 & 0 & 0 & 0 & 0 & 0 & 0 & 0 & 0 & 0 & 0 \\
0 & 0 & 0 & 0 & 0 & 0 & 0 & 0 & 0 & 0 & 0 & 0 & 0 & 0 & 0 \\
0 & 0 & 0 & 0 & 0 & 0 & 0 & 0 & 0 & 0 & 0 & 0 & 0 & 0 & 0 \\
0 & 0 & 0 & 0 & 0 & 0 & \frac{\partial M_{2,j}^*}{\partial w_j} & 0 & 0 & 0 & \frac{\partial M_{2,j}^*}{\partial \varphi_{2,j}} & \frac{\partial M_{2,j}^*}{\partial \varphi_{3,j}} & \frac{\partial M_{2,j}^*}{\partial w_e} & \frac{\partial M_{2,j}^*}{\partial \varphi_{2,e}} & \frac{\partial M_{2,j}^*}{\partial \varphi_{3,e}} \\
0 & 0 & 0 & 0 & 0 & 0 & \frac{\partial M_{3,j}^*}{\partial w_j} & 0 & 0 & 0 & \frac{\partial M_{3,j}^*}{\partial \varphi_{2,j}} & \frac{\partial M_{3,j}^*}{\partial \varphi_{3,j}} & \frac{\partial M_{3,j}^*}{\partial w_e} & \frac{\partial M_{3,j}^*}{\partial \varphi_{2,e}} & \frac{\partial M_{3,j}^*}{\partial \varphi_{3,e}} \\
\frac{\partial N_e^*}{\partial w_i} & 0 & 0 & 0 & \frac{\partial N_e^*}{\partial \varphi_{2,i}} & \frac{\partial N_e^*}{\partial \varphi_{3,i}} & \frac{\partial N_e^*}{\partial w_j} & 0 & 0 & 0 & \frac{\partial N_e^*}{\partial \varphi_{2,j}} & \frac{\partial N_e^*}{\partial \varphi_{3,j}} & \frac{\partial N_e^*}{\partial w_e} & \frac{\partial N_e^*}{\partial \varphi_{2,e}} & \frac{\partial N_e^*}{\partial \varphi_{3,e}} \\
\frac{\partial M_{2,e}^*}{\partial w_i} & 0 & 0 & 0 & \frac{\partial M_{2,e}^*}{\partial \varphi_{2,i}} & \frac{\partial M_{2,e}^*}{\partial \varphi_{3,i}} & \frac{\partial M_{2,e}^*}{\partial w_j} & 0 & 0 & 0 & \frac{\partial M_{2,e}^*}{\partial \varphi_{2,j}} & \frac{\partial M_{2,e}^*}{\partial \varphi_{3,j}} & \frac{\partial M_{2,e}^*}{\partial w_e} & \frac{\partial M_{2,e}^*}{\partial \varphi_{3,i}} & \frac{\partial M_{2,e}^*}{\partial \varphi_{3,i}} \\
\frac{\partial M_{3,e}^*}{\partial w_i} & 0 & 0 & 0 & \frac{\partial M_{3,e}^*}{\partial \varphi_{2,i}} & \frac{\partial M_{3,e}^*}{\partial \varphi_{3,i}} & \frac{\partial M_{3,e}^*}{\partial w_j} & 0 & 0 & 0 & \frac{\partial M_{3,e}^*}{\partial \varphi_{2,j}} & \frac{\partial M_{3,e}^*}{\partial \varphi_{3,j}} & \frac{\partial M_{3,e}^*}{\partial w_e} & \frac{\partial M_{3,e}^*}{\partial \varphi_{3,i}} & \frac{\partial M_{3,e}^*}{\partial \varphi_{3,i}}
\end{bmatrix} \tag{E.27}$$

To properly compute the terms of the correction gradient $\boldsymbol{\nabla F^*}$, the current state of the damage variables must be considered. In particular, the following subcases need to be addressed for each edge of the n^{th} stripe:

i. The damage variable accounting for the cracking length is exceeded at the current load step ($L'_{CR,LT,n} = L_{CR,LT,n}$ or $L'_{CR,RT,n} = L_{CR,RT,n}$)
ii. The damage variable accounting for the cracking length is not exceeded at the current load step ($L'_{CR,LT,n} < L_{CR,LT,n}$ or $L'_{CR,RT,n} < L_{CR,RT,n}$)

To lighten the description, the terms shared among the conditions represented by Figure E.1 through Figure E.6 are hereafter reported. More specifically, equations (E.28) and (E.29) represent the derivatives of the axial force and in-plane bending moment with respect to the out-of-plane rotations:

$$\frac{\partial N^*_{i-j}}{\partial \varphi_{2,i-j}} = \sum_n \frac{\partial N^*_{i-j,n}}{\partial \varphi_{2,i-j}} = \sum_n \left(\frac{\partial N^*_{i-j,n}}{\partial w_{i-j}} \, e_{3,n} \right) \tag{E.28}$$

$$\frac{\partial M^*_{3,i-j}}{\partial \varphi_{2,i-j}} = \sum_n \frac{\partial M^*_{3,i-j,n}}{\partial \varphi_{2,i-j}} = \sum_n \left(\frac{\partial M^*_{3,i-j,n}}{\partial w_{i-j}} \, e_{3,n} \right) \tag{E.29}$$

equations from (E.30) to (E.32) denote the out-of-plane bending terms:

$$\frac{\partial M^*_{2,i-j}}{\partial w_{i-j}} = \frac{\partial N^*_{i-j}}{\partial \varphi_{2,i-j}} \tag{E.30}$$

$$\frac{\partial M^*_{2,i-j}}{\partial \varphi_{2,i-j}} = \sum_n \frac{\partial M^*_{2,i-j,n}}{\partial \varphi_{2,i-j}} = \sum_n \left(\frac{\partial N^*_{i-j,n}}{\partial \varphi_{2,i-j}} \, e_{3,n} \right) \tag{E.31}$$

$$\frac{\partial M^*_{2,i-j}}{\partial \varphi_{3,i-j}} = \sum_n \frac{\partial M^*_{2,i-j,n}}{\partial \varphi_{3,i-j}} = \sum_n \left(\frac{\partial N^*_{i-j,n}}{\partial \varphi_{3,i-j}} \, e_{3,n} \right) \tag{E.32}$$

whereas equations from (E.33) to (E.35) indicate the derivates with respect to the internal degrees of freedom:

$$\frac{\partial N^*_{i-j}}{\partial w_e} = -\frac{\partial N^*_{i-j}}{\partial w_{i-j}} \qquad \frac{\partial N^*_{i-j}}{\partial \varphi_{2,e}} = -\frac{\partial N^*_{i-j}}{\partial \varphi_{2,i-j}} \qquad \frac{\partial N^*_{i-j}}{\partial \varphi_{3,e}} = -\frac{\partial N^*_{i-j}}{\partial \varphi_{3,i-j}} \tag{E.33}$$

$$\frac{\partial M^*_{2,i-j}}{\partial w_e} = -\frac{\partial M^*_{2,i-j}}{\partial w_{i-j}} \qquad \frac{\partial M^*_{2,i-j}}{\partial \varphi_{2,e}} = -\frac{\partial M^*_{2,i-j}}{\partial \varphi_{2,i-j}} \qquad \frac{\partial M^*_{2,i-j}}{\partial \varphi_{3,e}} = -\frac{\partial M^*_{2,i-j}}{\partial \varphi_{3,i-j}} \tag{E.34}$$

$$\frac{\partial M^*_{3,i-j}}{\partial w_e} = -\frac{\partial M^*_{3,i-j}}{\partial w_{i-j}} \qquad \frac{\partial M^*_{3,i-j}}{\partial \varphi_{2,e}} = -\frac{\partial M^*_{3,i-j}}{\partial \varphi_{2,i-j}} \qquad \frac{\partial M^*_{3,i-j}}{\partial \varphi_{3,e}} = -\frac{\partial M^*_{3,i-j}}{\partial \varphi_{3,i-j}} \tag{E.35}$$

Finally, the terms related to the compatibility equations are reported in the following:

$$\frac{\partial N^*_e}{\partial w_{i-j}} = -\frac{\partial N^*_{i-j}}{\partial w_{i-j}} \qquad \frac{\partial N^*_e}{\partial w_e} = -\left(\frac{\partial N^*_i}{\partial w_e} + \frac{\partial N^*_j}{\partial w_e}\right) \tag{E.36}$$

$$\frac{\partial N^*_e}{\partial \varphi_{2,i-j}} = -\frac{\partial N^*_{i-j}}{\partial \varphi_{2,i-j}} \qquad \frac{\partial N^*_e}{\partial \varphi_{2,e}} = -\left(\frac{\partial N^*_i}{\partial \varphi_{2,e}} + \frac{\partial N^*_j}{\partial \varphi_{2,e}}\right) \tag{E.37}$$

$$\frac{\partial N^*_e}{\partial \varphi_{3,i-j}} = -\frac{\partial N^*_{i-j}}{\partial \varphi_{3,i-j}} \qquad \frac{\partial N^*_e}{\partial \varphi_{3,e}} = -\left(\frac{\partial N^*_i}{\partial \varphi_{3,e}} + \frac{\partial N^*_j}{\partial \varphi_{3,e}}\right) \tag{E.38}$$

$$\frac{\partial M^*_{2,e}}{\partial w_{i-j}} = -\frac{\partial M^*_{2,i-j}}{\partial w_{i-j}} \qquad \frac{\partial M^*_{2,e}}{\partial w_e} = -\left(\frac{\partial M^*_{2,i}}{\partial w_e} + \frac{\partial M^*_{2,j}}{\partial w_e}\right) \tag{E.39}$$

$$\frac{\partial M^*_{2,e}}{\partial \varphi_{2,i-j}} = -\frac{\partial M^*_{2,i-j}}{\partial \varphi_{2,i-j}} \qquad \frac{\partial M^*_{2,e}}{\partial \varphi_{2,e}} = -\left(\frac{\partial M^*_{2,i}}{\partial \varphi_{2,e}} + \frac{\partial M^*_{2,j}}{\partial \varphi_{2,e}}\right) \tag{E.40}$$

$$\frac{\partial M^*_{2,e}}{\partial \varphi_{3,i-j}} = -\frac{\partial M^*_{2,i-j}}{\partial \varphi_{3,i-j}} \qquad \frac{\partial M^*_{2,e}}{\partial \varphi_{3,e}} = -\left(\frac{\partial M^*_{2,i}}{\partial \varphi_{3,e}} + \frac{\partial M^*_{2,j}}{\partial \varphi_{3,e}}\right) \tag{E.41}$$

$$\frac{\partial M^*_{3,e}}{\partial w_{i-j}} = -\frac{\partial M^*_{3,i-j}}{\partial w_{i-j}} \qquad \frac{\partial M^*_{3,e}}{\partial w_e} = -\left(\frac{\partial M^*_{3,i}}{\partial w_e} + \frac{\partial M^*_{3,j}}{\partial w_e}\right) \tag{E.42}$$

$$\frac{\partial M^*_{3,e}}{\partial \varphi_{2,i-j}} = -\frac{\partial M^*_{3,i-j}}{\partial \varphi_{2,i-j}} \qquad \frac{\partial M^*_{3,e}}{\partial \varphi_{2,e}} = -\left(\frac{\partial M^*_{3,i}}{\partial \varphi_{2,e}} + \frac{\partial M^*_{3,j}}{\partial \varphi_{2,e}}\right) \tag{E.43}$$

$$\frac{\partial M^*_{3,e}}{\partial \varphi_{3,i-j}} = -\frac{\partial M^*_{3,i-j}}{\partial \varphi_{3,i-j}} \qquad \frac{\partial M^*_{3,e}}{\partial \varphi_{3,e}} = -\left(\frac{\partial M^*_{3,i}}{\partial \varphi_{3,e}} + \frac{\partial M^*_{3,j}}{\partial \varphi_{3,e}}\right) \tag{E.44}$$

Case 1.i

$$\left.\begin{aligned}
\frac{\partial N^*_{Q,LT,i-j}}{\partial w_{i-j}} &= \sum_n \frac{\partial N^*_{Q,LT,i-j,n}}{\partial w_{i-j}} = \sum_n \left(-\frac{k\ \Delta t\ d_t}{\varphi_n}\right) \\
\frac{\partial N^*_{T,LT,i-j}}{\partial w_{i-j}} &= \sum_n \frac{\partial N^*_{T,LT,i-j,n}}{\partial w_{i-j}} = \sum_n \left(-k\ \Delta t\ L_{CR,LT,i-j,n}\right) \\
\frac{\partial N^*_{Q,RT,i-j}}{\partial w_{i-j}} &= \sum_n \frac{\partial N^*_{Q,RT,i-j,n}}{\partial w_{i-j}} = \sum_n \left(\frac{k\ \Delta t\ d_t}{\varphi_n}\right) \\
\frac{\partial N^*_{T,RT,i-j}}{\partial w_{i-j}} &= \sum_n \frac{\partial N^*_{T,RT,i-j,n}}{\partial w_{i-j}} = \sum_n \left(-k\ \Delta t\ L_{CR,RT,i-j,n}\right)
\end{aligned}\right\} \frac{\partial N^*_{i-j}}{\partial w_{i-j}} \qquad \textbf{(E.45)}$$

$$\left.\begin{aligned}
\frac{\partial N^*_{Q,LT,i-j}}{\partial \varphi_{3,i-j}} &= \sum_n \frac{\partial N^*_{Q,LT,i-j,n}}{\partial \varphi_{3,i-j}} = \sum_n \left[\frac{k\ \Delta t\ d_t\ (w_n - d_t)}{\varphi_n^2}\right] \\
\frac{\partial N^*_{T,LT,i-j}}{\partial \varphi_{3,i-j}} &= \sum_n \frac{\partial N^*_{T,LT,i-j,n}}{\partial \varphi_{3,i-j}} = \sum_n \left[-\frac{k\ \Delta t\ L_{CR,LT,i-j,n}\left(L - L_{CR,LT,i-j,n}\right)}{2}\right] \\
\frac{\partial N^*_{Q,RT,i-j}}{\partial \varphi_{3,i-j}} &= \sum_n \frac{\partial N^*_{Q,RT,i-j,n}}{\partial \varphi_{3,i-j}} = \sum_n \left[-\frac{k\ \Delta t\ d_t\ (w_n - d_t)}{\varphi_n^2}\right] \\
\frac{\partial N^*_{T,RT,i-j}}{\partial \varphi_{3,i-j}} &= \sum_n \frac{\partial N^*_{T,RT,i-j,n}}{\partial \varphi_{3,i-j}} = \sum_n \left[\frac{k\ \Delta t\ L_{CR,RT,i-j,n}\left(L - L_{CR,RT,i-j,n}\right)}{2}\right]
\end{aligned}\right\} \frac{\partial N^*_{i-j}}{\partial \varphi_{3,i-j}} \qquad \textbf{(E.46)}$$

$$\frac{\partial M^*_{3,i-j}}{\partial w_{i-j}} = \frac{\partial N^*_{i-j}}{\partial \varphi_{3,i-j}} \qquad \textbf{(E.47)}$$

$$\left.\begin{aligned}
\frac{\partial M^*_{3,Q,LT,i-j}}{\partial \varphi_{3,i-j}} &= \sum_n \frac{\partial M^*_{3,Q,LT,i-j,n}}{\partial \varphi_{3,i-j}} = \sum_n \left[-\frac{k\,\Delta t\; d_t\;(w_n - d_t)^2}{\varphi_n^3} \right] \\
\frac{\partial M^*_{3,T,LT,i-j}}{\partial \varphi_{3,i-j}} &= \sum_n \frac{\partial M^*_{3,T,LT,i-j,n}}{\partial \varphi_{3,i-j}} = \sum_n \left[-\frac{k\,\Delta t}{3\varphi_n^3} \left(w_n^3 + 3 w_n d_t^2 - 3 d_t w_n^2 + \varphi_n^3 \frac{L^3}{8} - d_t^3 \right) \right] \\
\frac{\partial M^*_{3,Q,RT,i-j}}{\partial \varphi_{3,i-j}} &= \sum_n \frac{\partial M^*_{3,Q,RT,i-j,n}}{\partial \varphi_{3,i-j}} = \sum_n \left[\frac{k\,\Delta t\; d_t\;(w_n - d_t)^2}{\varphi_n^3} \right] \\
\frac{\partial M^*_{3,T,RT,i-j}}{\partial \varphi_{3,i-j}} &= \sum_n \frac{\partial M^*_{3,T,RT,i-j,n}}{\partial \varphi_{3,i-j}} = \sum_n \left[\frac{k\,\Delta t}{3\varphi_n^3} \left(w_n^3 + 3 w_n d_t^2 - 3 d_t w_n^2 - \varphi_n^3 \frac{L^3}{8} - d_t^3 \right) \right]
\end{aligned}\right\} \frac{\partial M^*_{3,i-j}}{\partial \varphi_{3,i-j}} \qquad \textbf{(E.48)}$$

Case 1.ii

$$\left.\begin{aligned}
\frac{\partial N^*_{Q,LT,i-j}}{\partial w_{i-j}} &= \sum_n \frac{\partial N^*_{Q,LT,i-j,n}}{\partial w_{i-j}} = \sum_n \left(-k\,\Delta t\, L_{CR,LT,i-j,n}\right) \\
\frac{\partial N^*_{T,LT,i-j}}{\partial w_{i-j}} &= \sum_n \frac{\partial N^*_{T,LT,i-j,n}}{\partial w_{i-j}} = 0 \\
\frac{\partial N^*_{Q,RT,i-j}}{\partial w_{i-j}} &= \sum_n \frac{\partial N^*_{Q,RT,i-j,n}}{\partial w_{i-j}} = \sum_n \left(-k\,\Delta t\, L_{CR,RT,i-j,n}\right) \\
\frac{\partial N^*_{T,RT,i-j}}{\partial w_{i-j}} &= \sum_n \frac{\partial N^*_{T,RT,i-j,n}}{\partial w_{i-j}} = 0
\end{aligned}\right\} \frac{\partial N^*_{i-j}}{\partial w_{i-j}} \qquad \textbf{(E.49)}$$

$$\left.\begin{aligned}
\frac{\partial N^*_{Q,LT,i-j}}{\partial \varphi_{3,i-j}} &= \sum_n \frac{\partial N^*_{Q,LT,i-j,n}}{\partial \varphi_{3,i-j}} = \sum_n \left[-k\,\Delta t\, L_{CR,LT,i-j,n}\left(\frac{L}{2} - L_{CR,LT,i-j,n}\right)\right] \\
\frac{\partial N^*_{T,LT,i-j}}{\partial \varphi_{3,i-j}} &= \sum_n \frac{\partial N^*_{T,LT,i-j,n}}{\partial \varphi_{3,i-j}} = \sum_n \left(-\frac{k\,\Delta t\, L^2_{CR,LT,i-j,n}}{2}\right) \\
\frac{\partial N^*_{Q,RT,i-j}}{\partial \varphi_{3,i-j}} &= \sum_n \frac{\partial N^*_{Q,RT,i-j,n}}{\partial \varphi_{3,i-j}} = \sum_n \left[k\,\Delta t\, L_{CR,RT,i-j,n}\left(\frac{L}{2} - L_{CR,RT,i-j,n}\right)\right] \\
\frac{\partial N^*_{T,RT,i-j}}{\partial \varphi_{3,i-j}} &= \sum_n \frac{\partial N^*_{T,RT,i-j,n}}{\partial \varphi_{3,i-j}} = \sum_n \left(\frac{k\,\Delta t\, L^2_{CR,RT,i-j,n}}{2}\right)
\end{aligned}\right\} \frac{\partial N^*_{i-j}}{\partial \varphi_{3,i-j}} \qquad \textbf{(E.50)}$$

$$\left.\begin{aligned}
\frac{\partial M^{*}_{3,Q,LT,i-j}}{\partial w_{i-j}} &= \sum_{n}\frac{\partial M^{*}_{3,Q,LT,i-j,n}}{\partial w_{i-j}} = \sum_{n}\left[-k\,\Delta t\,L_{CR,LT,i-j,n}\left(\frac{L}{2}-\frac{L_{CR,LT,i-j,n}}{2}\right)\right]\\
\frac{\partial M^{*}_{3,T,LT,i-j}}{\partial w_{i-j}} &= \sum_{n}\frac{\partial M^{*}_{y3T,LT,i-j,n}}{\partial w_{i-j}} = 0\\
\frac{\partial M^{*}_{3,Q,RT,i-j}}{\partial w_{i-j}} &= \sum_{n}\frac{\partial M^{*}_{3,Q,RT,i-j,n}}{\partial w_{i-j}} = \sum_{n}\left[k\,\Delta t\,L_{CR,RT,i-j,n}\left(\frac{L}{2}-\frac{L_{CR,RT,i-j,n}}{2}\right)\right]\\
\frac{\partial M^{*}_{3,T,RT,i-j}}{\partial w_{i-j}} &= \sum_{n}\frac{\partial M^{*}_{3,T,RT,i-j,n}}{\partial w_{i-j}} = 0
\end{aligned}\right\}\ \frac{\partial M^{*}_{3,i-j}}{\partial w_{i-j}} \qquad \textbf{(E.51)}$$

$$\left.\begin{aligned}
\frac{\partial M^{*}_{3,Q,LT,i-j}}{\partial \varphi_{3,i-j}} &= \sum_{n}\frac{\partial M^{*}_{3,Q,LT,i-j,n}}{\partial \varphi_{3,i-j}} = \sum_{n}\left[-k\,\Delta t\,L_{CR,LT,i-j,n}\left(\frac{L}{2}-\frac{L_{CR,LT,i-j,n}}{2}\right)\left(\frac{L}{2}-L_{CR,LT,i-j,n}\right)\right]\\
\frac{\partial M^{*}_{3,T,LT,i-j}}{\partial \varphi_{3,i-j}} &= \sum_{n}\frac{\partial M^{*}_{3,T,LT,i-j,n}}{\partial \varphi_{3,i-j}} = \sum_{n}\left[-\frac{k\,\Delta t\,L^{2}_{CR,LT,i-j,n}}{2}\left(\frac{L}{2}-\frac{L_{CR,LT,i-j,n}}{3}\right)\right]\\
\frac{\partial M^{*}_{3,Q,RT,i-j}}{\partial \varphi_{3,i-j}} &= \sum_{n}\frac{\partial M^{*}_{3,Q,RT,i-j,n}}{\partial \varphi_{3,i-j}} = \sum_{n}\left[-k\,\Delta t\,L_{CR,RT,i-j,n}\left(\frac{L}{2}-\frac{L_{CR,RT,i-j,n}}{2}\right)\left(\frac{L}{2}-L_{CR,RT,i-j,n}\right)\right]\\
\frac{\partial M^{*}_{3,T,RT,i-j}}{\partial \varphi_{3,i-j}} &= \sum_{n}\frac{\partial M^{*}_{3,T,RT,i-j,n}}{\partial \varphi_{3,i-j}} = \sum_{n}\left[-\frac{k\,\Delta t\,L^{2}_{CR,RT,i-j,n}}{2}\left(\frac{L}{2}-\frac{L_{CR,RT,i-j,n}}{3}\right)\right]
\end{aligned}\right\}\ \frac{\partial M^{*}_{3,i-j}}{\partial \varphi_{3,i-j}} \qquad \textbf{(E.52)}$$

Case 2

$$\left.\begin{aligned}\frac{\partial N^*_{LT,i-j}}{\partial w_{i-j}} &= \sum_n \frac{\partial N^*_{LT,i-j,n}}{\partial w_{i-j}} = \sum_n \left[-\frac{k\,\Delta t}{\varphi_n}\left(w_n + \varphi_n \frac{L}{2}\right)\right] \\ \frac{\partial N^*_{RT,i-j}}{\partial w_{i-j}} &= \sum_n \frac{\partial N^*_{RT,i-j,n}}{\partial w_{i-j}} = \sum_n \left[\frac{k\,\Delta t}{\varphi_n}\left(w_n - \varphi_n \frac{L}{2}\right)\right]\end{aligned}\right\} \frac{\partial N^*_{i-j}}{\partial w_{i-j}} \tag{E.53}$$

$$\left.\begin{aligned}\frac{\partial N^*_{LT,i-j}}{\partial \varphi_{3,i-j}} &= \sum_n \frac{\partial N^*_{LT,i-j,n}}{\partial \varphi_{3,i-j}} = \sum_n \left[\frac{k\,\Delta t}{2\varphi_n^2}\left(w_n^2 - \varphi_n^2 \frac{L^2}{4}\right)\right] \\ \frac{\partial N^*_{RT,i-j}}{\partial \varphi_{3,i-j}} &= \sum_n \frac{\partial N^*_{RT,i-j,n}}{\partial \varphi_{3,i-j}} = \sum_n \left[-\frac{k\,\Delta t}{2\varphi_n^2}\left(w_n^2 - \varphi_n^2 \frac{L^2}{4}\right)\right]\end{aligned}\right\} \frac{\partial N^*_{i-j}}{\partial \varphi_{3,i-j}} \tag{E.54}$$

$$\frac{\partial M^*_{y,i-j}}{\partial w_{i-j}} = \frac{\partial N^*_{i-j}}{\partial \varphi_{y,i-j}} \tag{E.55}$$

$$\left.\begin{aligned}\frac{\partial M^*_{3,LT,i-j}}{\partial \varphi_{3,i-j}} &= \sum_n \frac{\partial M^*_{3,LT,i-j,n}}{\partial \varphi_{3,i-j}} = \sum_n \left[-\frac{k\,\Delta t}{6\varphi_n^3}\left(2w_n^3 + \varphi_n^3 \frac{L^3}{4}\right)\right] \\ \frac{\partial M^*_{3,RT,i-j}}{\partial \varphi_{3,i-j}} &= \sum_n \frac{\partial M^*_{3,RT,i-j,n}}{\partial \varphi_{3,i-j}} = \sum_n \left[\frac{k\,\Delta t}{6\varphi_n^3}\left(2w_n^3 - \varphi_n^3 \frac{L^3}{4}\right)\right]\end{aligned}\right\} \frac{\partial M^*_{3,i-j}}{\partial \varphi_{3,i-j}} \tag{E.56}$$

Case 3.i

$$\left.\begin{aligned}
\frac{\partial N^*_{Q,LT,i-j}}{\partial w_{i-j}} &= \sum_n \frac{\partial N^*_{Q,LT,i-j,n}}{\partial w_{i-j}} = \sum_n \left[-\frac{k\,\Delta t}{\varphi_n}(2w_n + \varphi_n L - d_t)\right] \\
\frac{\partial N^*_{T,LT,i-j}}{\partial w_{i-j}} &= \sum_n \frac{\partial N^*_{T,LT,i-j,n}}{\partial w_{i-j}} = \sum_n \left(k\,\Delta t\, L_{CR,LT,i-j,n}\right) \\
\frac{\partial N^*_{Q,RT,i-j}}{\partial w_{i-j}} &= \sum_n \frac{\partial N^*_{Q,RT,i-j,n}}{\partial w_{i-j}} = \sum_n \left[\frac{k\,\Delta t}{\varphi_n}(2w_n - \varphi_n L - d_t)\right] \\
\frac{\partial N^*_{T,RT,i-j}}{\partial w_{i-j}} &= \sum_n \frac{\partial N^*_{T,RT,i-j,n}}{\partial w_{i-j}} = \sum_n \left(k\,\Delta t\, L_{CR,RT,i-j,n}\right)
\end{aligned}\right\} \frac{\partial N^*_{i-j}}{\partial w_{i-j}} \qquad \textbf{(E.57)}$$

$$\left.\begin{aligned}
\frac{\partial N^*_{Q,LT,i-j}}{\partial \varphi_{3,i-j}} &= \sum_n \frac{\partial N^*_{Q,LT,i-j,n}}{\partial \varphi_{3,i-j}} = \sum_n \left[\frac{k\,\Delta t}{\varphi_n^2}\left(w_n^2 - w_n d_t - \varphi_n^2 \frac{L^2}{4}\right)\right] \\
\frac{\partial N^*_{T,LT,i-j}}{\partial \varphi_{3,i-j}} &= \sum_n \frac{\partial N^*_{T,LT,i-j,n}}{\partial \varphi_{3,i-j}} = \sum_n \left[-\frac{k\,\Delta t}{2\varphi_n^2}\left(w_n^2 - 2d_t w_n - \varphi_n^2 \frac{L^2}{4} + d_t^2\right)\right] \\
\frac{\partial N^*_{Q,RT,i-j}}{\partial \varphi_{3,i-j}} &= \sum_n \frac{\partial N^*_{Q,RT,i-j,n}}{\partial \varphi_{3,i-j}} = \sum_n \left[-\frac{k\,\Delta t}{\varphi_n^2}\left(w_n^2 - w_n d_t - \varphi_n^2 \frac{L^2}{4}\right)\right] \\
\frac{\partial N^*_{T,RT,i-j}}{\partial \varphi_{3,i-j}} &= \sum_n \frac{\partial N^*_{T,RT,i-j,n}}{\partial \varphi_{3,i-j}} = \sum_n \left[\frac{k\,\Delta t}{2\varphi_n^2}\left(w_n^2 - 2d_t w_n - \varphi_n^2 \frac{L^2}{4} + d_t^2\right)\right]
\end{aligned}\right\} \frac{\partial N^*_{i-j}}{\partial \varphi_{3,i-j}} \qquad \textbf{(E.58)}$$

$$\left.\begin{aligned}
\frac{\partial M^*_{3,Q,LT,i-j}}{\partial w_{i-j}} &= \sum_n \frac{\partial M^*_{3,Q,LT,i-j,n}}{\partial w_{i-j}} = \sum_n \left[\frac{k\,\Delta t}{2\varphi_n^2}\left(3w_n^2 + w_n\varphi_n L - 4d_t w_n - \varphi^2\frac{L^2}{4} - d_t\varphi_n L + d_t^2\right)\right] \\
\frac{\partial M^*_{3,T,LT,i-j}}{\partial w_{i-j}} &= \sum_n \frac{\partial M^*_{3,T,LT,i-j,n}}{\partial w_{i-j}} = k\,\Delta t\, L_{CR,LT,i-j,n}\left(\frac{L}{2} - L_{CR,LT,i-j,n}\right) \\
\frac{\partial M^*_{3,Q,RT,i-j}}{\partial w_{i-j}} &= \sum_n \frac{\partial M^*_{3,Q,RT,i-j,n}}{\partial w_{i-j}} = \sum_n \left[-\frac{k\,\Delta t}{2\varphi_n^2}\left(3w_n^2 - w_n\varphi_n L - 4d_t w_n - \varphi^2\frac{L^2}{4} + d_t\varphi_n L + d_t^2\right)\right] \\
\frac{\partial M^*_{3,T,RT,i-j}}{\partial w_{i-j}} &= \sum_n \frac{\partial M^*_{3,T,RT,i-j,n}}{\partial w_{i-j}} = k\,\Delta t\, L_{CR,RT,i-j,n}\left(\frac{L}{2} - L_{CR,RT,i-j,n}\right)
\end{aligned}\right\} \frac{\partial M^*_{3,i-j}}{\partial w_{i-j}} \qquad \textbf{(E.59)}$$

$$\left.\begin{aligned}
\frac{\partial M^*_{3,Q,LT,i-j}}{\partial \varphi_{y,i-j}} &= \sum_n \frac{\partial M^*_{3,Q,LT,i-j,n}}{\partial \varphi_{3,i-j}} \\
&= \sum_n \left[-\frac{k\,\Delta t}{4\varphi_n^3}\left(4w_n + w_n^2 L\varphi_n + 4w_n d_t^2 + d_t^2 L\varphi_n - 8w_n^2 d_t - 2w_n d_t L\varphi + \varphi_n^3\frac{L^3}{4}\right)\right] \\
\frac{\partial M^*_{3,T,LT,i-j}}{\partial \varphi_{3,i-j}} &= \sum_n \frac{\partial M^*_{3,T,LT,i-j,n}}{\partial \varphi_{3,i-j}} \\
&= \sum_n \left[\frac{k\,\Delta t}{\varphi_n^3}\left(\frac{2}{3}w_n + 2d_t^2 w_n - 2w_n^2 d_t + w_n^2\varphi_n\frac{L}{4} - d_t\varphi_n w_n\frac{L}{2} + d_t^2\varphi_n\frac{L}{4} + \varphi_n^3\frac{L^3}{48} - \frac{2}{3}d_t^3\right)\right] \\
\frac{\partial M^*_{3,Q,RT,i-j}}{\partial \varphi_{3,i-j}} &= \sum_n \frac{\partial M^*_{3,Q,RT,i-j,n}}{\partial \varphi_{3,i-j}} \\
&= \sum_n \left[\frac{k\,\Delta t}{4\varphi_n^3}\left(4w_n - w_n^2 L\varphi_n + 4w_n d_t^2 - d_t^2 L\varphi_n - 8w_n^2 d_t + 2w_n d_t L\varphi - \varphi_n^3\frac{L^3}{4}\right)\right] \\
\frac{\partial M^*_{3,T,RT,i-j}}{\partial \varphi_{3,i-j}} &= \sum_n \frac{\partial M^*_{3,T,RT,i-j,n}}{\partial \varphi_{3,i-j}} \\
&= \sum_n \left[-\frac{k\,\Delta t}{\varphi_n^3}\left(\frac{2}{3}w_n + 2d_t^2 w_n - 2w_n^2 d_t - w_n^2\varphi_n\frac{L}{4} + d_t\varphi_n w_n\frac{L}{2} - d_t^2\varphi_n\frac{L}{4} - \varphi_n^3\frac{L^3}{48} - \frac{2}{3}d_t^3\right)\right]
\end{aligned}\right\} \frac{\partial M^*_{3,i-j}}{\partial \varphi_{3,i-j}} \qquad \textbf{(E.60)}$$

Case 3.ii

$$\left.\begin{aligned}
\frac{\partial N^*_{Q,LT,i-j}}{\partial w_{i-j}} &= \sum_n \frac{\partial N^*_{Q,LT,i-j,n}}{\partial w_{i-j}} = \sum_n \left(-k\ \Delta t\ L_{CR,LT,i-j,n}\right) \\
\frac{\partial N^*_{T,LT,i-j}}{\partial w_{i-j}} &= \sum_n \frac{\partial N^*_{T,LT,i-j,n}}{\partial w_{i-j}} = 0 \\
\frac{\partial N^*_{Q,RT,i-j}}{\partial w_{i-j}} &= \sum_n \frac{\partial N^*_{Q,RT,i-j,n}}{\partial w_{i-j}} = \sum_n \left(-k\ \Delta t\ L_{CR,RT,i-j,n}\right) \\
\frac{\partial N^*_{T,RT,i-j}}{\partial w_{i-j}} &= \sum_n \frac{\partial N^*_{T,RT,i-j,n}}{\partial w_{i-j}} = 0
\end{aligned}\right\} \frac{\partial N^*_{i-j}}{\partial w_{i-j}} \qquad \textbf{(E.61)}$$

$$\left.\begin{aligned}
\frac{\partial N^*_{Q,LT,i-j}}{\partial \varphi_{3,i-j}} &= \sum_n \frac{\partial N^*_{Q,LT,i-j,n}}{\partial \varphi_{3,i-j}} = \sum_n \left(\frac{-k\ \Delta t\ L_{CR,LT,i-j,n}\ L}{2}\right) \\
\frac{\partial N^*_{T,LT,i-j}}{\partial \varphi_{3,i-j}} &= \sum_n \frac{\partial N^*_{T,LT,i-j,n}}{\partial \varphi_{3,i-j}} = \sum_n \left(\frac{k\ \Delta t\ L^2_{CR,LT,i-j,n}}{2}\right) \\
\frac{\partial N^*_{Q,RT,i-j}}{\partial \varphi_{3,i-j}} &= \sum_n \frac{\partial N^*_{Q,RT,i-j,n}}{\partial \varphi_{3,i-j}} = \sum_n \left(\frac{k\ \Delta t\ L_{CR,RT,i-j,n}\ L}{2}\right) \\
\frac{\partial N^*_{T,RT,i-j}}{\partial \varphi_{3,i-j}} &= \sum_n \frac{\partial N^*_{T,RT,i-j,n}}{\partial \varphi_{3,i-j}} = \sum_n \left(-\frac{k\ \Delta t\ L^2_{CR,RT,i-j,n}}{2}\right)
\end{aligned}\right\} \frac{\partial N^*_{i-j}}{\partial \varphi_{3,i-j}} \qquad \textbf{(E.62)}$$

$$\left.\begin{aligned}
\frac{\partial M^{*}_{3,Q,LT,i-j}}{\partial w_{i-j}} &= \sum_{n}\frac{\partial M^{*}_{3,Q,LT,i-j,n}}{\partial w_{i-j}} = \sum_{n}\left[-k\,\Delta t\,L_{CR,LT,i-j,n}\left(\frac{L}{2}-\frac{L_{CR,LT,i-j,n}}{2}\right)\right]\\
\frac{\partial M^{*}_{3,T,LT,i-j}}{\partial w_{i-j}} &= \sum_{n}\frac{\partial M^{*}_{3,T,LT,i-j,n}}{\partial w_{i-j}} = 0\\
\frac{\partial M^{*}_{3,Q,RT,i-j}}{\partial w_{i-j}} &= \sum_{n}\frac{\partial M^{*}_{3,Q,RT,i-j,n}}{\partial w_{i-j}} = \sum_{n}\left[k\,\Delta t\,L_{CR,RT,i-j,n}\left(\frac{L}{2}-\frac{L_{CR,RT,i-j,n}}{2}\right)\right]\\
\frac{\partial M^{*}_{3,T,RT,i-j}}{\partial w_{i-j}} &= \sum_{n}\frac{\partial M^{*}_{3,T,RT,i-j,n}}{\partial w_{i-j}} = 0
\end{aligned}\right\}\ \frac{\partial M^{*}_{3,i-j}}{\partial w_{i-j}} \qquad \textbf{(E.63)}$$

$$\left.\begin{aligned}
\frac{\partial M^{*}_{3,Q,LT,i-j}}{\partial \varphi_{3,i-j}} &= \sum_{n}\frac{\partial M^{*}_{3,Q,LT,i-j,n}}{\partial \varphi_{3,i-j}} = \sum_{n}\left[-\frac{k\,\Delta t\,L_{CR,LT,i-j,n}\,L}{2}\left(\frac{L}{2}-\frac{L_{CR,LT,i-j,n}}{2}\right)\right]\\
\frac{\partial M^{*}_{3,T,LT,i-j}}{\partial \varphi_{3,i-j}} &= \sum_{n}\frac{\partial M^{*}_{3,T,LT,i-j,n}}{\partial \varphi_{3,i-j}} = \sum_{n}\left[\frac{k\,\Delta t\,L^{2}_{CR,LT,i-j,n}}{2}\left(\frac{L}{2}-\frac{2L_{CR,LT,i-j,n}}{3}\right)\right]\\
\frac{\partial M^{*}_{3,Q,RT,i-j}}{\partial \varphi_{3,i-j}} &= \sum_{n}\frac{\partial M^{*}_{3,Q,RT,i-j,n}}{\partial \varphi_{3,i-j}} = \sum_{n}\left[-\frac{k\,\Delta t\,L_{CR,RT,i-j,n}\,L}{2}\left(\frac{L}{2}-\frac{L_{CR,RT,i-j,n}}{2}\right)\right]\\
\frac{\partial M^{*}_{3,T,RT,i-j}}{\partial \varphi_{3,i-j}} &= \sum_{n}\frac{\partial M^{*}_{3,T,RT,i-j,n}}{\partial \varphi_{3,i-j}} = \sum_{n}\left[\frac{k\,\Delta t\,L^{2}_{CR,RT,i-j,n}}{2}\left(\frac{L}{2}-\frac{2L_{CR,RT,i-j,n}}{3}\right)\right]
\end{aligned}\right\}\ \frac{\partial M^{*}_{3,i-j}}{\partial \varphi_{3,i-j}} \qquad \textbf{(E.64)}$$

Case 4.i

$$\left.\begin{aligned}\frac{\partial N^*_{LT,i-j}}{\partial w_{i-j}} &= \sum_n \frac{\partial N^*_{LT,i-j,n}}{\partial w_{i-j}} = 0\\ \frac{\partial N^*_{RT,i-j}}{\partial w_{i-j}} &= \sum_n \frac{\partial N^*_{RT,i-j,n}}{\partial w_{i-j}} = 0\end{aligned}\right\} \quad \frac{\partial N^*_{i-j}}{\partial w_{i-j}} \tag{E.65}$$

$$\left.\begin{aligned}\frac{\partial N^*_{LT,i-j}}{\partial \varphi_{3,i-j}} &= \sum_n \frac{\partial N^*_{LT,i-j,n}}{\partial \varphi_{3,i-j}} = \sum_n \left(-\frac{k\ \Delta t\ d_t^2}{2\varphi_n^2}\right)\\ \frac{\partial N^*_{RT,i-j}}{\partial \varphi_{3,i-j}} &= \sum_n \frac{\partial N^*_{RT,i-j,n}}{\partial \varphi_{3,i-j}} = \sum_n \left(\frac{k\ \Delta t\ d_t^2}{2\varphi_n^2}\right)\end{aligned}\right\} \quad \frac{\partial N^*_{i-j}}{\partial \varphi_{3,i-j}} \tag{E.66}$$

$$\frac{\partial M^*_{3,i-j}}{\partial w_{i-j}} = \frac{\partial N^*_{i-j}}{\partial \varphi_{3,i-j}} \tag{E.67}$$

$$\left.\begin{aligned}\frac{\partial M^*_{3,LT,i-j}}{\partial \varphi_{3,i-j}} &= \sum_n \frac{\partial M^*_{3,LT,i-j,n}}{\partial \varphi_{3,i-j}} = \sum_n \left[\frac{k\ \Delta t\ d_t^2}{3\varphi_n^3}(3w_n - 2d_t)\right]\\ \frac{\partial M^*_{3,RT,i-j}}{\partial \varphi_{3,i-j}} &= \sum_n \frac{\partial M^*_{3,RT,i-j,n}}{\partial \varphi_{3,i-j}} = \sum_n \left[-\frac{k\ \Delta t\ d_t^2}{3\varphi_n^3}(3w_n - 2d_t)\right]\end{aligned}\right\} \quad \frac{\partial M^*_{3,i-j}}{\partial \varphi_{3,i-j}} \tag{E.68}$$

Case 4.ii

$$\left.\begin{aligned}\frac{\partial N^*_{LT,i-j}}{\partial w_{i-j}} &= \sum_n \frac{\partial N^*_{LT,i-j,n}}{\partial w_{i-j}} = \sum_n \left[-k\,\Delta t\,\left(L_{CR,LT,i-j,n} - L_{C,i-j,n}\right)\right] \\ \frac{\partial N^*_{RT,i-j}}{\partial w_{i-j}} &= \sum_n \frac{\partial N^*_{RT,i-j,n}}{\partial w_{i-j}} = \sum_n \left[-k\,\Delta t\,\left(L_{CR,RT,i-j,n} - L_{C,i-j,n}\right)\right]\end{aligned}\right\} \frac{\partial N^*_{i-j}}{\partial w_{i-j}} \tag{E.69}$$

$$\left.\begin{aligned}\frac{\partial N^*_{LT,i-j}}{\partial \varphi_{3,i-j}} &= \sum_n \frac{\partial N^*_{LT,i-j,n}}{\partial \varphi_{3,i-j}} = \sum_n \left[-\frac{k\,\Delta t}{2}\left(L_{CR,LT,i-j,n} - L_{C,i-j,n}\right)\left(L_{T,i-j,n} - L_{CR,LT,i-j,n}\right)\right] \\ \frac{\partial N^*_{RT,i-j}}{\partial \varphi_{3,i-j}} &= \sum_n \frac{\partial N^*_{RT,i-j,n}}{\partial \varphi_{3,i-j}} = \sum_n \left[\frac{k\,\Delta t}{2}\left(L_{CR,RT,i-j,n} - L_{C,i-j,n}\right)\left(L_{T,i-j,n} - L_{CR,RT,i-j,n}\right)\right]\end{aligned}\right\} \frac{\partial N^*_{i-j}}{\partial \varphi_{3,i-j}} \tag{E.70}$$

$$\frac{\partial M^*_{3,i-j}}{\partial w_{i-j}} = \frac{\partial N^*_{i-j}}{\partial \varphi_{3,i-j}} \tag{E.71}$$

$$\left.\begin{aligned}\frac{\partial M^*_{3,LT,i-j}}{\partial \varphi_{3,i-j}} &= \sum_n \frac{\partial M^*_{3,LT,i-j,n}}{\partial \varphi_{3,i-j}} \\ &= \sum_n \left[k\,\Delta t\,\left(\frac{L^2_{CR,LT,i-j,n}L}{2} - \frac{L^3_{CR,LT,i-j,n}}{3} - \frac{L_{CR,LT,i-j,n}L^2}{4} - \frac{L^2_{C,i-j,n}L}{2} + \frac{L_{C,i-j,n}}{3} + \frac{L_{C,i-j,n}L^2}{4}\right)\right] \\ \frac{\partial M^*_{3,RT,i-j}}{\partial \varphi_{3,i-j}} &= \sum_n \frac{\partial M^*_{3,RT,i-j,n}}{\partial \varphi_{3,i-j}} \\ &= \sum_n \left[k\,\Delta t\,\left(\frac{L^2_{CR,RT,i-j,n}L}{2} - \frac{L^3_{CR,RT,i-j,n}}{3} - \frac{L_{CR,RT,i-j,n}L^2}{4} - \frac{L^2_{C,i-j,n}L}{2} + \frac{L_{C,i-j,n}}{3} + \frac{L_{C,i-j,n}L^2}{4}\right)\right]\end{aligned}\right\} \frac{\partial M^*_{3,i-j}}{\partial \varphi_{3,i-j}} \tag{E.72}$$

Case 5

$$\frac{\partial N^*_{i-j}}{\partial w_{i-j}} = \sum_n \frac{\partial N^*_{i-j,n}}{\partial w_{i-j}} = \sum_n (-k\ \Delta t\ L) \tag{E.73}$$

$$\frac{\partial N^*_{i-j}}{\partial \varphi_{3,i-j}} = \sum_n \frac{\partial N^*_{i-j,n}}{\partial \varphi_{3,i-j}} = 0 \tag{E.74}$$

$$\frac{\partial M^*_{3,i-j}}{\partial w_{i-j}} = \frac{\partial N^*_{i-j}}{\partial \varphi_{3,i-j}} \tag{E.75}$$

$$\frac{\partial M^*_{3,i-j}}{\partial \varphi_{3,i-j}} = \sum_n \frac{\partial M^*_{3,i-j,n}}{\partial \varphi_{3,i-j}} = \sum_n \left(-\frac{k\ \Delta t\ L^3}{12}\right) \tag{E.76}$$

Case 6

$$\frac{\partial N^*_{i-j}}{\partial w_{i-j}} = \sum_n \frac{\partial N^*_{i-j,n}}{\partial w_{i-j}} = \sum_n \left[-\frac{k\ \Delta t}{2|\varphi_n|}(2w_n + |\varphi_n|L)\right] \tag{E.77}$$

$$\frac{\partial N^*_{i-j}}{\partial \varphi_{3,i-j}} = \sum_n \frac{\partial N^*_{i-j,n}}{\partial \varphi_{3,i-j}} = \sum_n \left[\frac{k\ \Delta t}{8|\varphi_n|\varphi_n}(4w_n^2 - \varphi_n^2 L^2)\right] \tag{E.78}$$

$$\frac{\partial M^*_{3,i-j}}{\partial w_{i-j}} = \frac{\partial N^*_{i-j}}{\partial \varphi_{3,i-j}} \tag{E.79}$$

$$\frac{\partial M^*_{3,i-j}}{\partial \varphi_{3,i-j}} = \sum_n \frac{\partial M^*_{3,i-j,n}}{\partial \varphi_{3,i-j}} = \sum_n \left[-\frac{k\ \Delta t}{24|\varphi_n|\varphi_n^2}(8w_n^3 + L^3|\varphi_n|^3)\right] \tag{E.80}$$

Appendix F

THREE-DIMENSIONAL NONLINEAR CORRECTIONS: COMPRESSION

The stripe formulation of the presented macroelement consists of discretizing the end-interfaces in a series of stripes, whose nonlinear in-plane response is retrieved by applying analytical inelastic corrections to the elastic contributions. In this context, the governing system of equations of the three-dimensional macroelement can be summarized as follows:

$$\boldsymbol{F^{int}(u)} = \boldsymbol{Ku} + \boldsymbol{F^{*}(u)} + \boldsymbol{F^{**}(u)} \tag{F.1}$$

where $\boldsymbol{K}$ is the elastic stiffness matrix, $\boldsymbol{u}$ and $\boldsymbol{F^{int}(u)}$ are the generalized displacement and internal force vectors, whereas $\boldsymbol{F^{*}(u)}$ and $\boldsymbol{F^{**}(u)}$ represent the analytical inelastic correction vectors accounting for the nonlinear response in tension and in compression, respectively.

In this section, the three-dimensional nonlinear corrections accounting for the compressive behavior of the end-interface are presented (F.2). More specifically, the first part deals with the toe-crushing phenomenon, which limits the compressive strength of masonry and causes a stiffness degradation (Figure 5.3). On the other hand, the second part focuses on a no-compression behavior, suitable for several strengthening materials composed of meshes embedded in poor-performance binding.

$$\boldsymbol{F^{**}(u)} = \left\{N_i^{**} \;\; 0 \;\; 0 \;\; 0 \;\; M_{2,i}^{**} \;\; M_{3,i}^{**} \;\; N_j^{**} \;\; 0 \;\; 0 \;\; 0 \;\; M_{2,j}^{**} \;\; M_{3,j}^{**} \;\; N_e^{**} \;\; M_{2,e}^{**} \;\; M_{3,e}^{**}\right\}^T \tag{F.2}$$

The total nodal correction is obtained by summing the contributions of the individual stripes, as reported in the equation (F.3), with $e_{3,n}$ representing the centroid out-of-plane coordinate of the n^{th} stripe with respect to the centroid of the end-interface.

$$N^{**} = \sum_n N_n^{**} \qquad M_2^{**} = \sum_n M_{2,n}^{**} = \sum_n \left(N_n^{**}\, e_{3,n}\right) \qquad M_3^{**} = \sum_n M_{3,n}^{**} \tag{F.3}$$

Furthermore, the following notation will be used for the i^{th} interface:

$$\begin{cases} w_n = (w_e - w_i) + (\varphi_{2,e} - \varphi_{2,i})\, e_{3,n} \\ \varphi_n = \varphi_{3,e} - \varphi_{3,i} \end{cases} \quad \textbf{(F.4)}$$

and for the j^{th} one:

$$\begin{cases} w_n = (w_j - w_e) + (\varphi_{2,j} - \varphi_{2,e})\, e_{3,n} \\ \varphi_n = \varphi_{3,j} - \varphi_{3,e} \end{cases} \quad \textbf{(F.5)}$$

The corresponding sectional edge displacements of the n^{th} stripe are obtained by assuming small displacements and rotations:

$$\begin{cases} d_{LT,n} = w_n + \varphi_n \dfrac{L}{2} \\ d_{RT,n} = w_n - \varphi_n \dfrac{L}{2} \end{cases} \quad \textbf{(F.6)}$$

State variables are needed to adequately capture toe-crushing phenomena. In fact, they allow to account for residual displacements and damage accumulation. Consequently, each edge needs to be analyzed independently, providing thus corrections separately. In particular, the current and maximum values of the displacement ductility demand (μ' and μ), as well as of the dimensionless crushing length (ξ' and ξ) are reported for the left edge:

$$\mu'_{LT,n} = \frac{d_{LT,n}}{d_y} \qquad \xi'_{LT,n} = \frac{(\mu'_{LT,n} - 1)\, d_y}{\varphi_n\, L} \quad \textbf{(F.7)}$$

and for the right one:

$$\mu'_{RT,n} = \frac{d_{RT,n}}{d_y} \qquad \xi'_{RT,n} = -\frac{(\mu'_{RT,n} - 1)\, d_y}{\varphi_n\, L} \quad \textbf{(F.8)}$$

of each interface, being $d_y = f_m/k$ the yielding displacement in compression of the end-interfaces.

If the dimensionless crushing length on one side or if the sum of the crushing lengths at the relative section corners is greater than the total length of the macroelement, both the damage variables $\xi_{LT,n}$ and $\xi_{RT,n}$ are set equal to a unit value for consistency reasons, and the same corrections apply. It is worth noticing that this assumption involves a severe

approximation of the stress path along the section, leading to possible unsound results. For this reason, if this situation is experienced, a full-fiber discretization might be more suitable.

Conversely, an analytical no-compression constitutive law does not rely on any state variable. As a consequence, the cyclic response does not involve any energy dissipation. Moreover, a single correction accounting for the behavior of both edges suffices. In this context, the length in compression ($L_{C,n}$), which corresponds to the crushing length, can be expressed as reported in the following:

$$L_{C,n} = \frac{L}{2} - \frac{w_n}{|\varphi_n|} \tag{F.9}$$

When the corrections are individually computed for each edge of the n^{th} stripe, the whole stripe contributions are obtained by summing the left (N_{LT}^{**}) and (N_{RT}^{**}) right counterparts, as reported in the following:

i^{th} **interface**	j^{th} **interface**	
$\begin{cases} N_{i,n}^{**} = N_{LT,i,n}^{**} + N_{RT,i,n}^{**} \\ M_{2,i,n}^{**} = M_{2,LT,i,n}^{**} + M_{2,RT,i,n}^{**} \\ M_{3,i,n}^{**} = M_{3,LT,i,n}^{**} + M_{3,RT,i,n}^{**} \end{cases}$	$\begin{cases} N_{j,n}^{**} = N_{LT,j,n}^{**} + N_{RT,j,n}^{**} \\ M_{2,j,n}^{**} = M_{2,LT,j,n}^{*} + M_{2,RT,j,n}^{**} \\ M_{3,j,n}^{**} = M_{3,LT,j,n}^{**} + M_{3,RT,j,n}^{**} \end{cases}$	**(F.10)**

As already described, the central body is also responsible for coupling the response of the end-interfaces and ensure equilibrium. For this reason, compatibility relationships are to be extended to the nonlinear corrections:

$$\begin{cases} N_{e,n}^{**} = -\left(N_{i,n}^{**} + N_{j,n}^{**}\right) \\ M_{2,e,n}^{**} = N_{e,n}^{**}\, e_{3,n} \\ M_{3,e,n}^{**} = -\left(M_{3,i,n}^{**} + M_{3,j,n}^{**}\right) \end{cases} \tag{F.11}$$

It is worth noticing that the two-dimensional corrections can be easily derived by imposing the out-of-plane rotation terms (φ_2) in equations (F.4) and (F.5) equal to zero, and a number of stipes (n) equal to a unit value.

In the following, the analytical corrections for the nonlinear response in compression of the three-dimensional macroelement are thoroughly presented. In particular, each case is associated to a set of inelastic equations that corresponds to a particular kinematic condition.

Toe-crushing: case 1

As long as there is no overlap between crushing length and length in tension of opposite corners, one condition suffices to describe both the loading and unloading phases (Figure F.1). In particular, the following corrections are to be applied when $\mu_{LT,n} > 1$ (yielding displacement exceeded) and $d_{LT,n} < 0$ (current displacement in compression) for the left edge, or $\mu_{RT,n} > 1$ and $d_{RT,n} < 0$ for the right one.

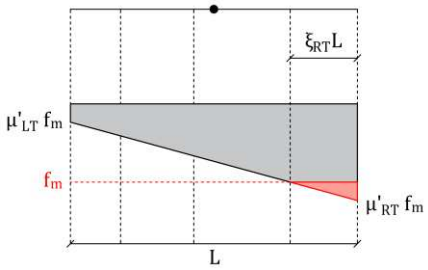

Figure F.1: Conditions addressed within toe-crushing phenomena: case 1.

i^{th} interface – Left edge

$$\begin{cases} N^{**}_{LT,i,n} = \left(\dfrac{\mu_{LT,i,n}-1}{2\mu_{LT,i,n}}\right) \xi_{LT,i,n}\, L\, k\, \Delta t\, d_{LT,i,n} \\ M^{**}_{2,LT,i,n} = N^{**}_{LT,i,n}\, e_{3,n} \\ M^{**}_{3,LT,i,n} = N^{**}_{LT,i,n}\, L \left(\dfrac{1}{2} - \dfrac{\xi_{LT,i,n}}{3}\right) \end{cases}$$

i^{th} interface – Right edge

$$\begin{cases} N^{**}_{RT,i,n} = \left(\dfrac{\mu_{RT,i,n}-1}{2\mu_{RT,i,n}}\right) \xi_{RT,i,n}\, L\, k\, \Delta t\, d_{RT,i,n} \\ M^{**}_{2,RT,i,n} = N^{**}_{RT,i,n}\, e_{3,n} \\ M^{**}_{3,RT,i,n} = -N^{**}_{RT,i,n}\, L \left(\dfrac{1}{2} - \dfrac{\xi_{RT,i,n}}{3}\right) \end{cases} \quad \textbf{(F.12)}$$

j^{th} interface – Left edge

$$\begin{cases} N^{**}_{LT,j,n} = -\left(\dfrac{\mu_{LT,j,n}-1}{2\mu_{LT,j,n}}\right) \xi_{LT,j,n}\, L\, k\, \Delta t\, d_{LT,j,n} \\ M^{**}_{2,LT,j,n} = N^{**}_{LT,j,n}\, e_{3,n} \\ M^{**}_{3,LT,j,n} = N^{**}_{LT,j,n}\, L \left(\dfrac{1}{2} - \dfrac{\xi_{LT,j,n}}{3}\right) \end{cases}$$

j^{th} interface – Right edge

$$\begin{cases} N^{**}_{RT,j,n} = -\left(\dfrac{\mu_{RT,j,n}-1}{2\mu_{RT,j,n}}\right) \xi_{RT,j,n}\, L\, k\, \Delta t\, d_{RT,j,n} \\ M^{**}_{2,RT,j,n} = N^{**}_{RT,j,n}\, e_{3,n} \\ M^{**}_{3,RT,j,n} = -N^{**}_{RT,j,n}\, L \left(\dfrac{1}{2} - \dfrac{\xi_{RT,j,n}}{3}\right) \end{cases} \quad \textbf{(F.13)}$$

Toe-crushing: case 2

Unlike the previous case, Figure F.2 depicts a condition with an overlap between the length in tension and the crushing length of the two opposite edges, i.e., $L_{T,n} + L\xi_{LT,n} > L$ or $L_{T,n} + L\xi_{RT,n} > L$, for the left and right corners, respectively. In this case, cracking and toe-crushing are no longer uncoupled, regardless of the uniaxial recentering behavior of the constitutive law. As a result, the crushing lengths in equations (F.12) and (F.13) are replaced with the compressive counterpart $L_{C,n}$, defined in equation (F.9). Furthermore, as for the previous case, the following corrections are to be applied when $\mu_{LT,n} > 1$ (yielding displacement exceeded) and $d_{LT,n} < 0$ (current displacement in compression) for the left edge, or $\mu_{RT,n} > 1$ and $d_{RT,n} < 0$ for the right one.

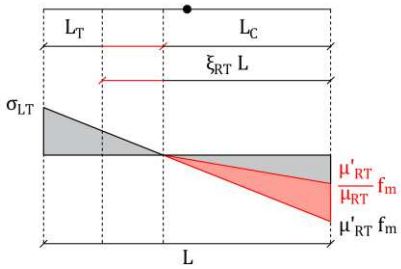

Figure F.2: Conditions addressed within toe-crushing phenomena: case 2.

i^{th} interface – Left edge

$$\begin{cases} N^{**}_{LT,i,n} = \left(\dfrac{\mu_{LT,i,n}-1}{2\mu_{LT,i,n}}\right) L_{C,n}\, k\, \Delta t\, d_{LT,i,n} \\ M^{**}_{2,LT,i,n} = N^{**}_{LT,i,n}\, e_{3,n} \\ M^{**}_{3,LT,i,n} = N^{**}_{LT,i,n} \left(\dfrac{L}{2} - \dfrac{L_{C,n}}{3}\right) \end{cases}$$

i^{th} interface – Right edge

$$\begin{cases} N^{**}_{RT,i,n} = \left(\dfrac{\mu_{RT,i,n}-1}{2\mu_{RT,i,n}}\right) L_{C,n}\, k\, \Delta t\, d_{RT,i,n} \\ M^{**}_{2,RT,i,n} = N^{**}_{RT,i,n}\, e_{3,n} \\ M^{**}_{3,RT,i,n} = -N^{**}_{RT,i,n} \left(\dfrac{L}{2} - \dfrac{L_{C,n}}{3}\right) \end{cases} \quad \textbf{(F.14)}$$

j^{th} interface – Left edge

$$\begin{cases} N^{**}_{LT,j,n} = -\left(\dfrac{\mu_{LT,j,n}-1}{2\mu_{LT,j,n}}\right) L_{C,n}\, k\, \Delta t\, d_{LT,j,n} \\ M^{**}_{2,LT,j,n} = N^{**}_{LT,j,n}\, e_{3,n} \\ M^{**}_{3,LT,j,n} = N^{**}_{LT,j,n} \left(\dfrac{L}{2} - \dfrac{L_{C,n}}{3}\right) \end{cases}$$

j^{th} interface – Right edge

$$\begin{cases} N^{**}_{RT,j,n} = -\left(\dfrac{\mu_{RT,j,n}-1}{2\mu_{RT,j,n}}\right) L_{C,n}\, k\, \Delta t\, d_{RT,j,n} \\ M^{**}_{2,RT,j,n} = N^{**}_{RT,j,n}\, e_{3,n} \\ M^{**}_{3,RT,j,n} = -N^{**}_{RT,j,n} \left(\dfrac{L}{2} - \dfrac{L_{C,n}}{3}\right) \end{cases} \quad \textbf{(F.15)}$$

No-compression: case 1

Figure F.3 depicts a situation in which the portion of the section undergoing compression involves the whole length of the n^{th} stripe ($L_{C,n} = L$). In this case, the nonlinear corrections consist of removing the entire elastic contributions, as no more load can be withstood. Moreover, because of the absence of damage variables, there is no need to express the edge corrections separately.

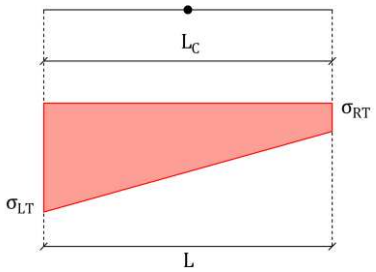

Figure F.3: Conditions addressed within a no-compression behavior: case 1.

i^{th} interface

$$\begin{cases} N^*_{i,n} = k\ \Delta t\ L\ w_n \\ M^*_{2,i,n} = N^*_{i,n}\ e_{3,n} \\ M^*_{3,i,n} = \left(\dfrac{k\ \Delta t\ L^3}{12}\right)\varphi_n \end{cases} \tag{F.16}$$

j^{th} interface

$$\begin{cases} N^*_{j,n} = -k\ \Delta t\ L\ w_n \\ M^*_{2,j,n} = N^*_{j,n}\ e_{3,n} \\ M^*_{3,j,n} = -\left(\dfrac{k\ \Delta t\ L^3}{12}\right)\varphi_n \end{cases} \tag{F.17}$$

No-compression: case 2

Figure F.4 depicts a situation in which the portion of the section undergoing compression involves a part of the n^{th} stripe ($L_{C,n} < L$). As for the previous case, a unique correction suffices to describe the response of both sides of the section.

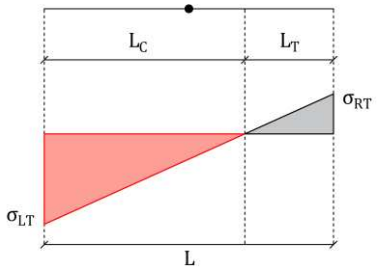

Figure F.4: Conditions addressed within a no-compression behavior: case 2.

i^{th} interface

$$\begin{cases} N^*_{i,n} = -\dfrac{k\,\Delta t}{8|\varphi_n|}(2w_n - L|\varphi_n|)^2 \\ M^*_{2,i,n} = N^*_{i,n}\, e_{3,n} \\ M^*_{3,i,n} = \dfrac{k\,\Delta t\,(w_n + L|\varphi_n|)(2w_n - L|\varphi_n|)^2}{24|\varphi_n|\varphi_n} \end{cases} \quad \textbf{(F.18)}$$

j^{th} interface

$$\begin{cases} N^*_{i,n} = \dfrac{k\,\Delta t}{8|\varphi_n|}(2w_n - L|\varphi_n|)^2 \\ M^*_{2,i,n} = N^*_{i,n}\, e_{3,n} \\ M^*_{3,i,n} = -\dfrac{k\,\Delta t\,(w_n + L|\varphi_n|)(2w_n - L|\varphi_n|)^2}{24|\varphi_n|\varphi_n} \end{cases} \quad \textbf{(F.19)}$$

NONLINEAR CORRECTION GRADIENT: COMPRESSION

To implement the Newton-Raphson method described in Chapter 5.5, the analytical tangent stiffness matrix needs to be calculated. In this context, this section outlines the compressive response by reporting the terms populating the corresponding gradient $\boldsymbol{\nabla F}^{**}$ (F.21). Furthermore, apart from a no-compression behavior, state variables accounting for damage accumulation are required. Consequently, the corresponding gradient matrix might not be symmetric.

For the sake of simplicity, as the derivatives with respect to the degrees of freedom of the two interfaces are mutually identical, the following notation hereafter applies:

$$\frac{\partial F_{i-j}^{**}}{\partial u_{i-j}} = \frac{\partial F_{i}^{**}}{\partial u_{i}} = \frac{\partial F_{j}^{**}}{\partial u_{j}} \tag{F.20}$$

being F_{i-j}^{**} and u_{i-j} the generalized internal correction force and displacement quantities, respectively, whereas with the subscript i and j the reference to the i^{th} and j^{th} interfaces is indicated.

It is worth noticing that all the equations reported in this section hold as long as the notations defined in (F.4) and (F.5) are satisfied, depending on the interface considered. If this is not the case, equation (F.20) might not apply.

$$\nabla \boldsymbol{F}^{**} = \begin{bmatrix}
\frac{\partial N_i^{**}}{\partial w_i} & 0 & 0 & 0 & \frac{\partial N_i^{**}}{\partial \varphi_{2,i}} & \frac{\partial N_i^{**}}{\partial \varphi_{3,i}} & 0 & 0 & 0 & 0 & 0 & 0 & \frac{\partial N_i^{**}}{\partial w_e} & \frac{\partial N_i^{**}}{\partial \varphi_{2,e}} & \frac{\partial N_i^{**}}{\partial \varphi_{3,e}} \\
0 & 0 & 0 & 0 & 0 & 0 & 0 & 0 & 0 & 0 & 0 & 0 & 0 & 0 & 0 \\
0 & 0 & 0 & 0 & 0 & 0 & 0 & 0 & 0 & 0 & 0 & 0 & 0 & 0 & 0 \\
0 & 0 & 0 & 0 & 0 & 0 & 0 & 0 & 0 & 0 & 0 & 0 & 0 & 0 & 0 \\
\frac{\partial M_{2,i}^{**}}{\partial w_i} & 0 & 0 & 0 & \frac{\partial M_{2,i}^{**}}{\partial \varphi_{2,i}} & \frac{\partial M_{2,i}^{**}}{\partial \varphi_{3,i}} & 0 & 0 & 0 & 0 & 0 & 0 & \frac{\partial M_{2,i}^{**}}{\partial w_e} & \frac{\partial M_{2,i}^{**}}{\partial \varphi_{2,e}} & \frac{\partial M_{2,i}^{**}}{\partial \varphi_{3,e}} \\
\frac{\partial M_{3,i}^{**}}{\partial w_i} & 0 & 0 & 0 & \frac{\partial M_{3,i}^{**}}{\partial \varphi_{2,i}} & \frac{\partial M_{3,i}^{**}}{\partial \varphi_{3,i}} & 0 & 0 & 0 & 0 & 0 & 0 & \frac{\partial M_{3,i}^{**}}{\partial w_e} & \frac{\partial M_{3,i}^{**}}{\partial \varphi_{2,e}} & \frac{\partial M_{3,i}^{**}}{\partial \varphi_{3,e}} \\
0 & 0 & 0 & 0 & 0 & 0 & \frac{\partial N_j^{**}}{\partial w_j} & 0 & 0 & 0 & \frac{\partial N_j^{**}}{\partial \varphi_{2,j}} & \frac{\partial N_j^{**}}{\partial \varphi_{3,j}} & \frac{\partial N_j^{**}}{\partial w_e} & \frac{\partial N_j^{**}}{\partial \varphi_{2,e}} & \frac{\partial N_j^{**}}{\partial \varphi_{3,e}} \\
0 & 0 & 0 & 0 & 0 & 0 & 0 & 0 & 0 & 0 & 0 & 0 & 0 & 0 & 0 \\
0 & 0 & 0 & 0 & 0 & 0 & 0 & 0 & 0 & 0 & 0 & 0 & 0 & 0 & 0 \\
0 & 0 & 0 & 0 & 0 & 0 & 0 & 0 & 0 & 0 & 0 & 0 & 0 & 0 & 0 \\
0 & 0 & 0 & 0 & 0 & 0 & \frac{\partial M_{2,j}^{**}}{\partial w_j} & 0 & 0 & 0 & \frac{\partial M_{2,j}^{**}}{\partial \varphi_{2,j}} & \frac{\partial M_{2,j}^{**}}{\partial \varphi_{3,j}} & \frac{\partial M_{2,j}^{**}}{\partial w_e} & \frac{\partial M_{2,j}^{**}}{\partial \varphi_{2,e}} & \frac{\partial M_{2,j}^{**}}{\partial \varphi_{3,e}} \\
0 & 0 & 0 & 0 & 0 & 0 & \frac{\partial M_{3,j}^{**}}{\partial w_j} & 0 & 0 & 0 & \frac{\partial M_{3,j}^{**}}{\partial \varphi_{2,j}} & \frac{\partial M_{3,j}^{**}}{\partial \varphi_{3,j}} & \frac{\partial M_{3,j}^{**}}{\partial w_e} & \frac{\partial M_{3,j}^{**}}{\partial \varphi_{2,e}} & \frac{\partial M_{3,j}^{**}}{\partial \varphi_{3,e}} \\
\frac{\partial N_e^{**}}{\partial w_i} & 0 & 0 & 0 & \frac{\partial N_e^{**}}{\partial \varphi_{2,i}} & \frac{\partial N_e^{**}}{\partial \varphi_{3,i}} & \frac{\partial N_e^{**}}{\partial w_j} & 0 & 0 & 0 & \frac{\partial N_e^{**}}{\partial \varphi_{2,j}} & \frac{\partial N_e^{**}}{\partial \varphi_{3,j}} & \frac{\partial N_e^{**}}{\partial w_e} & \frac{\partial N_e^{**}}{\partial \varphi_{2,e}} & \frac{\partial N_e^{**}}{\partial \varphi_{3,e}} \\
\frac{\partial M_{2,e}^{**}}{\partial w_i} & 0 & 0 & 0 & \frac{\partial M_{2,e}^{**}}{\partial \varphi_{2,i}} & \frac{\partial M_{2,e}^{**}}{\partial \varphi_{3,i}} & \frac{\partial M_{2,e}^{**}}{\partial w_j} & 0 & 0 & 0 & \frac{\partial M_{2,e}^{**}}{\partial \varphi_{2,j}} & \frac{\partial M_{2,e}^{**}}{\partial \varphi_{3,j}} & \frac{\partial M_{2,e}^{**}}{\partial w_e} & \frac{\partial M_{2,e}^{**}}{\partial \varphi_{3,i}} & \frac{\partial M_{2,e}^{**}}{\partial \varphi_{3,i}} \\
\frac{\partial M_{3,e}^{**}}{\partial w_i} & 0 & 0 & 0 & \frac{\partial M_{3,e}^{**}}{\partial \varphi_{2,i}} & \frac{\partial M_{3,e}^{**}}{\partial \varphi_{3,i}} & \frac{\partial M_{3,e}^{**}}{\partial w_j} & 0 & 0 & 0 & \frac{\partial M_{3,e}^{**}}{\partial \varphi_{2,j}} & \frac{\partial M_{3,e}^{**}}{\partial \varphi_{3,j}} & \frac{\partial M_{3,e}^{**}}{\partial w_e} & \frac{\partial M_{3,e}^{**}}{\partial \varphi_{3,i}} & \frac{\partial M_{3,e}^{**}}{\partial \varphi_{3,i}}
\end{bmatrix} \tag{F.21}$$

To properly compute the terms of the correction gradient $\nabla \boldsymbol{F}^{**}$, the current state of the damage variable, when required, must be considered. In particular, for a toe-crushing phenomenon, the following subcases need to be addressed for each edge of the n^{th} stripe:

A. The length of the n^{th} stripe is not totally crushed ($\xi_{LT,n} + \xi_{RT,n} < 1$):
   i. Both the damage variables are exceeded at the current load step ($\mu'_{LT,n} = \mu_{LT,n}$ and $\xi'_{LT,n} = \xi_{LT,n}$ or $\mu'_{RT,n} = \mu_{RT,n}$ and $\xi'_{RT,n} = \xi_{RT,n}$).
   ii. Only the damage variable accounting for the ductility demand is exceeded at the current load step ($\mu'_{LT,n} = \mu_{LT,n}$ and $\xi'_{LT,n} < \xi_{LT,n}$ or $\mu'_{RT,n} = \mu_{RT,n}$ and $\xi'_{RT,n} < \xi_{RT,n}$).
   iii. Only the damage variable accounting for the crushing length is exceeded at the current load step ($\mu'_{LT,n} < \mu_{LT,n}$ and $\xi'_{LT,n} = \xi_{LT,n}$ or $\mu'_{RT,n} < \mu_{RT,n}$ and $\xi'_{RT,n} = \xi_{RT,n}$).
   iv. None of the damage variables are exceeded in the current load step ($\mu'_{LT,n} < \mu_{LT,n}$ and $\xi'_{LT,n} < \xi_{LT,n}$ or $\mu'_{RT,n} < \mu_{RT,n}$ and $\xi'_{RT,n} < \xi_{RT,n}$).

B. The length of the n^{th} stripe is totally crushed ($\xi_{LT,n} + \xi_{RT,n} = 1$):
   i. The damage variable accounting for the ductility demand is exceeded at the current load step ($\mu'_{LT,n} = \mu_{LT,n}$ or $\mu'_{RT,n} = \mu_{RT,n}$).
   ii. The damage variable accounting for the ductility demand is not exceeded at the current load step ($\mu'_{LT,n} < \mu_{LT,n}$ or $\mu'_{RT,n} < \mu_{RT,n}$).

Since the second case of a toe-crushing condition only involves the ductility demand as a damage variable, only the situations listed in group B apply.

To lighten the description, the terms shared among the conditions represented by Figure F.1 through Figure F.4 are hereafter reported. More specifically, equations (F.22) and (F.23) represent the derivatives of the axial force and in-plane bending moment with respect to the out-of-plane rotations:

$$\frac{\partial N^{**}_{i-j}}{\partial \varphi_{2,i-j}} = \sum_n \frac{\partial N^{**}_{i-j,n}}{\partial \varphi_{2,i-j}} = \sum_n \left(\frac{\partial N^{**}_{i-j,n}}{\partial w_{i-j}} \, e_{3,n} \right) \tag{F.22}$$

$$\frac{\partial M^{**}_{3,i-j}}{\partial \varphi_{2,i-j}} = \sum_n \frac{\partial M^{**}_{3,i-j,n}}{\partial \varphi_{2,i-j}} = \sum_n \left(\frac{\partial M^{**}_{3,i-j,n}}{\partial w_{i-j}} \, e_{3,n} \right) \tag{F.23}$$

equations from (F.24) to (F.26) denote the out-of-plane bending terms:

$$\frac{\partial M^{**}_{2,i-j}}{\partial w_{i-j}} = \frac{\partial N^{**}_{i-j}}{\partial \varphi_{2,i-j}} \tag{F.24}$$

$$\frac{\partial M_{2,i-j}^{**}}{\partial \varphi_{2,i-j}} = \sum_n \frac{\partial M_{2,i-j,n}^{**}}{\partial \varphi_{2,i-j}} = \sum_n \left(\frac{\partial N_{i-j,n}^{**}}{\partial \varphi_{2,i-j}} \, e_{3,n} \right) \tag{F.25}$$

$$\frac{\partial M_{2,i-j}^{**}}{\partial \varphi_{3,i-j}} = \sum_n \frac{\partial M_{2,i-j,n}^{**}}{\partial \varphi_{3,i-j}} = \sum_n \left(\frac{\partial N_{i-j,n}^{**}}{\partial \varphi_{3,i-j}} \, e_{3,n} \right) \tag{F.26}$$

whereas equations from (F.27) to (F.29) indicate the derivates with respect to the internal degrees of freedom:

$$\frac{\partial N_{i-j}^{**}}{\partial w_e} = -\frac{\partial N_{i-j}^{**}}{\partial w_{i-j}} \qquad \frac{\partial N_{i-j}^{**}}{\partial \varphi_{2,e}} = -\frac{\partial N_{i-j}^{**}}{\partial \varphi_{2,i-j}} \qquad \frac{\partial N_{i-j}^{**}}{\partial \varphi_{3,e}} = -\frac{\partial N_{i-j}^{**}}{\partial \varphi_{3,i-j}} \tag{F.27}$$

$$\frac{\partial M_{2,i-j}^{**}}{\partial w_e} = -\frac{\partial M_{2,i-j}^{**}}{\partial w_{i-j}} \qquad \frac{\partial M_{2,i-j}^{**}}{\partial \varphi_{2,e}} = -\frac{\partial M_{2,i-j}^{**}}{\partial \varphi_{2,i-j}} \qquad \frac{\partial M_{2,i-j}^{**}}{\partial \varphi_{3,e}} = -\frac{\partial M_{2,i-j}^{**}}{\partial \varphi_{3,i-j}} \tag{F.28}$$

$$\frac{\partial M_{3,i-j}^{**}}{\partial w_e} = -\frac{\partial M_{3,i-j}^{**}}{\partial w_{i-j}} \qquad \frac{\partial M_{3,i-j}^{**}}{\partial \varphi_{2,e}} = -\frac{\partial M_{3,i-j}^{**}}{\partial \varphi_{2,i-j}} \qquad \frac{\partial M_{3,i-j}^{**}}{\partial \varphi_{3,e}} = -\frac{\partial M_{3,i-j}^{**}}{\partial \varphi_{3,i-j}} \tag{F.29}$$

Finally, the terms related to the compatibility equations are reported in the following:

$$\frac{\partial N_e^{**}}{\partial w_{i-j}} = -\frac{\partial N_{i-j}^{**}}{\partial w_{i-j}} \qquad \frac{\partial N_e^{**}}{\partial w_e} = -\left(\frac{\partial N_i^{**}}{\partial w_e} + \frac{\partial N_j^{**}}{\partial w_e} \right) \tag{F.30}$$

$$\frac{\partial N_e^{**}}{\partial \varphi_{2,i-j}} = -\frac{\partial N_{i-j}^{**}}{\partial \varphi_{2,i-j}} \qquad \frac{\partial N_e^{**}}{\partial \varphi_{2,e}} = -\left(\frac{\partial N_i^{**}}{\partial \varphi_{2,e}} + \frac{\partial N_j^{**}}{\partial \varphi_{2,e}} \right) \tag{F.31}$$

$$\frac{\partial N_e^{**}}{\partial \varphi_{3,i-j}} = -\frac{\partial N_{i-j}^{**}}{\partial \varphi_{3,i-j}} \qquad \frac{\partial N_e^{**}}{\partial \varphi_{3,e}} = -\left(\frac{\partial N_i^{**}}{\partial \varphi_{3,e}} + \frac{\partial N_j^{**}}{\partial \varphi_{3,e}} \right) \tag{F.32}$$

$$\frac{\partial M_{2,e}^{**}}{\partial w_{i-j}} = -\frac{\partial M_{2,i-j}^{**}}{\partial w_{i-j}} \qquad \frac{\partial M_{2,e}^{**}}{\partial w_e} = -\left(\frac{\partial M_{2,i}^{**}}{\partial w_e} + \frac{\partial M_{2,j}^{**}}{\partial w_e} \right) \tag{F.33}$$

$$\frac{\partial M_{2,e}^{**}}{\partial \varphi_{2,i-j}} = -\frac{\partial M_{2,i-j}^{**}}{\partial \varphi_{2,i-j}} \qquad \frac{\partial M_{2,e}^{**}}{\partial \varphi_{2,e}} = -\left(\frac{\partial M_{2,i}^{**}}{\partial \varphi_{2,e}} + \frac{\partial M_{2,j}^{**}}{\partial \varphi_{2,e}} \right) \tag{F.34}$$

$$\frac{\partial M_{2,e}^{**}}{\partial \varphi_{3,i-j}} = -\frac{\partial M_{2,i-j}^{**}}{\partial \varphi_{3,i-j}} \qquad \frac{\partial M_{2,e}^{**}}{\partial \varphi_{3,e}} = -\left(\frac{\partial M_{2,i}^{**}}{\partial \varphi_{3,e}} + \frac{\partial M_{2,j}^{**}}{\partial \varphi_{3,e}} \right) \tag{F.35}$$

$$\frac{\partial M_{3,e}^{**}}{\partial w_{i-j}} = -\frac{\partial M_{3,i-j}^{**}}{\partial w_{i-j}} \qquad \frac{\partial M_{3,e}^{**}}{\partial w_e} = -\left(\frac{\partial M_{3,i}^{**}}{\partial w_e} + \frac{\partial M_{3,j}^{**}}{\partial w_e} \right) \tag{F.36}$$

$$\frac{\partial M_{3,e}^{**}}{\partial \varphi_{2,i-j}} = -\frac{\partial M_{3,i-j}^{**}}{\partial \varphi_{2,i-j}} \qquad \frac{\partial M_{3,e}^{**}}{\partial \varphi_{2,e}} = -\left(\frac{\partial M_{3,i}^{**}}{\partial \varphi_{2,e}} + \frac{\partial M_{3,j}^{**}}{\partial \varphi_{2,e}}\right) \tag{F.37}$$

$$\frac{\partial M_{3,e}^{**}}{\partial \varphi_{3,i-j}} = -\frac{\partial M_{3,i-j}^{**}}{\partial \varphi_{3,i-j}} \qquad \frac{\partial M_{3,e}^{**}}{\partial \varphi_{3,e}} = -\left(\frac{\partial M_{3,i}^{**}}{\partial \varphi_{3,e}} + \frac{\partial M_{3,j}^{**}}{\partial \varphi_{3,e}}\right) \tag{F.38}$$

Toe-crushing: case 1.A.i

$$\left.\begin{aligned}\frac{\partial N^{**}_{LT,i-j}}{\partial w_{i-j}} &= \sum_n \frac{\partial N^{**}_{LT,i-j,n}}{\partial w_{i-j}} = \sum_n \left[-\frac{k\,\Delta t}{\varphi_n}\left(w_n + \varphi_n \frac{L}{2} - d_y\right)\right] \\ \frac{\partial N^{**}_{RT,i-j}}{\partial w_{i-j}} &= \sum_n \frac{\partial N^{**}_{RT,i-j,n}}{\partial w_{i-j}} = \sum_n \left[\frac{k\,\Delta t}{\varphi_n}\left(w_n - \varphi_n \frac{L}{2} - d_y\right)\right]\end{aligned}\right\} \frac{\partial N^{**}_{i-j}}{\partial w_{i-j}} \quad \textbf{(F.39)}$$

$$\left.\begin{aligned}\frac{\partial N^{**}_{LT,i-j}}{\partial \varphi_{3,i-j}} &= \sum_n \frac{\partial N^{**}_{LT,i-j,n}}{\partial \varphi_{3,i-j}} = \sum_n \left[-\frac{k\,\Delta t}{2\varphi_n^2}\left(\varphi_n^2 \frac{L^2}{4} - d_y^2 + 2d_y w_n - w_n^2\right)\right] \\ \frac{\partial N^{**}_{RT,i-j}}{\partial \varphi_{3,i-j}} &= \sum_n \frac{\partial N^{**}_{RT,i-j,n}}{\partial \varphi_{3,i-j}} = \sum_n \left[\frac{k\,\Delta t}{2\varphi_n^2}\left(\varphi_n^2 \frac{L^2}{4} - d_y^2 + 2d_y w_n - w_n^2\right)\right]\end{aligned}\right\} \frac{\partial N^{**}_{i-j}}{\partial \varphi_{3,i-j}} \quad \textbf{(F.40)}$$

$$\frac{\partial M^{**}_{3,i-j}}{\partial w_{i-j}} = \frac{\partial N^{**}_{i-j}}{\partial \varphi_{3,i-j}} \quad \textbf{(F.41)}$$

$$\left.\begin{aligned}\frac{\partial M^{**}_{3,LT,i-j}}{\partial \varphi_{3,i-j}} &= \sum_n \frac{\partial M^{**}_{3,LT,i-j,n}}{\partial \varphi_{3,i-j}} = \sum_n \left[\frac{k\,\Delta t}{24\varphi_n^3}\left(8d_y^3 - \varphi_n^3 L^3 - 24w_n d_y^2 - 8w_n^3 + 24w_n^2 d_y\right)\right] \\ \frac{\partial M^{**}_{3,RT,i-j}}{\partial \varphi_{3,i-j}} &= \sum_n \frac{\partial M^{**}_{3,RT,i-j,n}}{\partial \varphi_{3,i-j}} = \sum_n \left[\frac{k\,\Delta t}{24\varphi_n^3}\left(8w_n^3 - \varphi_n^3 L^3 + 24w_n d_y^2 - 8d_y^3 - 24w_n^2 d_y\right)\right]\end{aligned}\right\} \frac{\partial M^{**}_{3,i-j}}{\partial \varphi_{3,i-j}} \quad \textbf{(F.42)}$$

Toe-crushing: case 1.A.ii and case 1.B.i

$$\left.\begin{aligned}\frac{\partial N^{**}_{LT,i-j}}{\partial w_{i-j}} &= \sum_n \frac{\partial N^{**}_{LT,i-j,n}}{\partial w_{i-j}} = \sum_n \left(-\frac{k\,\Delta t\,L\,\xi_{LT,i-j,n}}{2}\right)\\ \frac{\partial N^{**}_{RT,i-j}}{\partial w_{i-j}} &= \sum_n \frac{\partial N^{**}_{RT,i-j,n}}{\partial w_{i-j}} = \sum_n \left(-\frac{k\,\Delta t\,L\,\xi_{RT,i-j,n}}{2}\right)\end{aligned}\right\} \frac{\partial N^{**}_{i-j}}{\partial w_{i-j}} \tag{F.43}$$

$$\left.\begin{aligned}\frac{\partial N^{**}_{LT,i-j}}{\partial \varphi_{3,i-j}} &= \sum_n \frac{\partial N^{**}_{LT,i-j,n}}{\partial \varphi_{3,i-j}} = \sum_n \left(-\frac{k\,\Delta t\,L^2\,\xi_{LT,i-j,n}}{4}\right)\\ \frac{\partial N^{**}_{RT,i-j}}{\partial \varphi_{3,i-j}} &= \sum_n \frac{\partial N^{**}_{RT,i-j,n}}{\partial \varphi_{3,i-j}} = \sum_n \left(-\frac{k\,\Delta t\,L^2\,\xi_{RT,i-j,n}}{4}\right)\end{aligned}\right\} \frac{\partial N^{**}_{i-j}}{\partial \varphi_{3,i-j}} \tag{F.44}$$

$$\left.\begin{aligned}\frac{\partial M^{**}_{3,LT,i-j}}{\partial w_{i-j}} &= \sum_n \frac{\partial M^{**}_{3,LT,i-j,n}}{\partial w_{i-j}} = \sum_n \left[\left(\frac{\partial N^{**}_{LT,i-j,n}}{\partial w_{i-j}}\right)\left(\frac{L}{2}-\frac{\xi_{LT,i-j,n}L}{3}\right)\right]\\ \frac{\partial M^{**}_{3,RT,i-j}}{\partial w_{i-j}} &= \sum_n \frac{\partial M^{**}_{3,RT,i-j,n}}{\partial w_{i-j}} = \sum_n \left[-\left(\frac{\partial N^{**}_{RT,i-j,n}}{\partial w_{i-j}}\right)\left(\frac{L}{2}-\frac{\xi_{RT,i-j,n}L}{3}\right)\right]\end{aligned}\right\} \frac{\partial M^{**}_{3,i-j}}{\partial w_{i-j}} \tag{F.45}$$

$$\left.\begin{aligned}\frac{\partial M^{**}_{3,LT,i-j}}{\partial \varphi_{3,i-j}} &= \sum_n \frac{\partial M^{**}_{3,LT,i-j,n}}{\partial \varphi_{3,i-j}} = \sum_n \left[\left(\frac{\partial N^{**}_{LT,i-j,n}}{\partial \varphi_{3,i-j}}\right)\left(\frac{L}{2}-\frac{\xi_{LT,i-j,n}L}{3}\right)\right]\\ \frac{\partial M^{**}_{3,RT,i-j}}{\partial \varphi_{3,i-j}} &= \sum_n \frac{\partial M^{**}_{3,RT,i-j,n}}{\partial \varphi_{3,i-j}} = \sum_n \left[-\left(\frac{\partial N^{**}_{LT,i-j,n}}{\partial \varphi_{3,i-j}}\right)\left(\frac{L}{2}-\frac{\xi_{LT,i-j,n}L}{3}\right)\right]\end{aligned}\right\} \frac{\partial M^{**}_{3,i-j}}{\partial \varphi_{3,i-j}} \tag{F.46}$$

Toe-crushing: case 1.A.iii

$$\left.\begin{aligned}\frac{\partial N^{**}_{LT,i-j}}{\partial w_{i-j}} &= \sum_n \frac{\partial N^{**}_{LT,i-j,n}}{\partial w_{i-j}} = \sum_n \left[-\frac{k\,\Delta t\,(\mu_{LT,i-j,n}-1)}{2\mu_{LT,i-j,n}\,\varphi_n}\left(2w_n+\varphi_n L-d_y\right)\right]\\ \frac{\partial N^{**}_{RT,i-j}}{\partial w_{i-j}} &= \sum_n \frac{\partial N^{**}_{RT,i-j,n}}{\partial w_{i-j}} = \sum_n \left[-\frac{k\,\Delta t\,(\mu_{RT,i-j,n}-1)}{2\mu_{RT,i-j,n}\,\varphi_n}\left(2w_n+\varphi_n L-d_y\right)\right]\end{aligned}\right\}\ \frac{\partial N^{**}_{i-j}}{\partial w_{i-j}} \tag{F.47}$$

$$\left.\begin{aligned}\frac{\partial N^{**}_{LT,i-j}}{\partial \varphi_{3,i-j}} &= \sum_n \frac{\partial N^{**}_{LT,i-j,n}}{\partial \varphi_{3,i-j}} = \sum_n \left[\frac{k\,\Delta t\,(\mu_{LT,i-j,n}-1)}{8\mu^2_{LT,i-j,n}\,\varphi_n^2}\left(4w_n^2-4w_n d_y-\varphi_n^2L^2\right)\right]\\ \frac{\partial N^{**}_{RT,i-j}}{\partial \varphi_{3,i-j}} &= \sum_n \frac{\partial N^{**}_{RT,i-j,n}}{\partial \varphi_{3,i-j}} = \sum_n \left[-\frac{k\,\Delta t\,(\mu_{LT,i-j,n}-1)}{8\mu^2_{LT,i-j,n}\,\varphi_n^2}\left(4w_n^2-4w_n d_y-\varphi_n^2L^2\right)\right]\end{aligned}\right\}\ \frac{\partial N^{**}_{i-j}}{\partial \varphi_{3,i-j}} \tag{F.48}$$

$$\left.\begin{aligned}\frac{\partial M^{**}_{3,LT,i-j}}{\partial w_{i-j}} &= \sum_n \frac{\partial M^{**}_{3,LT,i-j,n}}{\partial w_{i-j}} = \sum_n \left[\left(\frac{\partial N^{**}_{LT,i-j,n}}{\partial w_{i-j}}\right)\left(\frac{L}{2}-\frac{\xi_{LT,i-j,n}L}{3}\right)+\frac{N^{**}_{LT,i-j,n}}{3\varphi_n}\right]\\ \frac{\partial M^{**}_{3,RT,i-j}}{\partial w_{i-j}} &= \sum_n \frac{\partial M^{**}_{3,RT,i-j,n}}{\partial w_{i-j}} = \sum_n \left[-\left(\frac{\partial N^{**}_{RT,i-j,n}}{\partial w_{i-j}}\right)\left(\frac{L}{2}-\frac{\xi_{RT,i-j,n}L}{3}\right)+\frac{N^{**}_{RT,i-j,n}}{3\varphi_n}\right]\end{aligned}\right\}\ \frac{\partial M^{**}_{3,i-j}}{\partial w_{i-j}} \tag{F.49}$$

$$\left.\begin{aligned}\frac{\partial M^{**}_{3,LT,i-j}}{\partial \varphi_{3,i-j}} &= \sum_n \frac{\partial M^{**}_{3,LT,i-j,n}}{\partial \varphi_{3,i-j}} = \sum_n \left[\left(\frac{\partial N^{**}_{LT,i-j,n}}{\partial \varphi_{3,i-j}}\right)\left(\frac{L}{2}-\frac{\xi_{LT,i-j,n}L}{3}\right)-\frac{N^{**}_{LT,i-j,n}(w_n-d_y)}{3\varphi_n^2}\right]\\ \frac{\partial M^{**}_{3,RT,i-j}}{\partial \varphi_{3,i-j}} &= \sum_n \frac{\partial M^{**}_{3,RT,i-j,n}}{\partial \varphi_{3,i-j}} = \sum_n \left[-\left(\frac{\partial N^{**}_{RT,i-j,n}}{\partial \varphi_{3,i-j}}\right)\left(\frac{L}{2}-\frac{\xi_{RT,i-j,n}L}{3}\right)-\frac{N^{**}_{RT,i-j,n}(w_n-d_y)}{3\varphi_n^2}\right]\end{aligned}\right\}\ \frac{\partial M^{**}_{3,i-j}}{\partial \varphi_{3,i-j}} \tag{F.50}$$

Toe-crushing: case 1.A.iv and case 1.B.ii

$$\left.\begin{aligned}\frac{\partial N^{**}_{LT,i-j}}{\partial w_{i-j}} &= \sum_n \frac{\partial N^{**}_{LT,i-j,n}}{\partial w_{i-j}} = \sum_n \left[-\frac{k\,\Delta t\,\xi_{LT,i-j,n} L\left(\mu_{LT,i-j,n}-1\right)}{2\mu_{LT,i-j,n}}\right] \\ \frac{\partial N^{**}_{RT,i-j}}{\partial w_{i-j}} &= \sum_n \frac{\partial N^{**}_{RT,i-j,n}}{\partial w_{i-j}} = \sum_n \left[-\frac{k\,\Delta t\,\xi_{RT,i-j,n} L\left(\mu_{RT,i-j,n}-1\right)}{2\mu_{RT,i-j,n}}\right]\end{aligned}\right\} \frac{\partial N^{**}_{i-j}}{\partial w_{i-j}} \tag{F.51}$$

$$\left.\begin{aligned}\frac{\partial N^{**}_{LT,i-j}}{\partial \varphi_{3,i-j}} &= \sum_n \frac{\partial N^{**}_{LT,i-j,n}}{\partial \varphi_{3,i-j}} = \sum_n \left[-\frac{k\,\Delta t\,\xi_{LT,i-j,n} L^2\left(\mu_{LT,i-j.n}-1\right)}{4\mu_{LT,i-j,n}}\right] \\ \frac{\partial N^{**}_{RT,i-j}}{\partial \varphi_{3,i-j}} &= \sum_n \frac{\partial N^{**}_{RT,i-j,n}}{\partial \varphi_{3,i-j}} = \sum_n \left[\frac{k\,\Delta t\,\xi_{RT,i-j,n} L^2\left(\mu_{RT,i-j.n}-1\right)}{4\mu_{RT,i-j,n}}\right]\end{aligned}\right\} \frac{\partial N^{**}_{i-j}}{\partial \varphi_{3,i-j}} \tag{F.52}$$

$$\left.\begin{aligned}\frac{\partial M^{**}_{3,LT,i-j}}{\partial w_{i-j}} &= \sum_n \frac{\partial M^{**}_{3,LT,i-j,n}}{\partial w_{i-j}} = \sum_n \left[\left(\frac{\partial N^{**}_{LT,i-j,n}}{\partial w_{i-j}}\right)\left(\frac{L}{2}-\frac{\xi_{LT,i-j,n}L}{3}\right)\right] \\ \frac{\partial M^{**}_{3,RT,i-j}}{\partial w_{i-j}} &= \sum_n \frac{\partial M^{**}_{3,RT,i-j,n}}{\partial w_{i-j}} = \sum_n \left[-\left(\frac{\partial N^{**}_{RT,i-j,n}}{\partial w_{i-j}}\right)\left(\frac{L}{2}-\frac{\xi_{RT,i-j,n}L}{3}\right)\right]\end{aligned}\right\} \frac{\partial M^{**}_{3,i-j}}{\partial w_{i-j}} \tag{F.53}$$

$$\left.\begin{aligned}\frac{\partial M^{**}_{3,LT,i-j}}{\partial \varphi_{3,i-j}} &= \sum_n \frac{\partial M^{**}_{3,LT,i-j,n}}{\partial \varphi_{3,i-j}} = \sum_n \left[\left(\frac{\partial N^{**}_{LT,i-j,n}}{\partial \varphi_{3,i-j}}\right)\left(\frac{L}{2}-\frac{\xi_{LT,i-j,n}L}{3}\right)\right] \\ \frac{\partial M^{**}_{3,RT,i-j}}{\partial \varphi_{3,i-j}} &= \sum_n \frac{\partial M^{**}_{3,RT,i-j,n}}{\partial \varphi_{3,i-j}} = \sum_n \left[-\left(\frac{\partial N^{**}_{RT,i-j,n}}{\partial \varphi_{3,i-j}}\right)\left(\frac{L}{2}-\frac{\xi_{RT,i-j,n}L}{3}\right)\right]\end{aligned}\right\} \frac{\partial M^{**}_{3,i-j}}{\partial \varphi_{3,i-j}} \tag{F.54}$$

Toe-crushing: case 2.B.i

$$\left.\begin{aligned}\frac{\partial N^{**}_{LT,i-j}}{\partial w_{i-j}} &= \sum_n \frac{\partial N^{**}_{LT,i-j,n}}{\partial w_{i-j}} = \sum_n \left[-\frac{k\,\Delta t}{2\varphi_n}\left(2w_n + \varphi_n L - d_y\right)\right] \\ \frac{\partial N^{**}_{RT,i-j}}{\partial w_{i-j}} &= \sum_n \frac{\partial N^{**}_{RT,i-j,n}}{\partial w_{i-j}} = \sum_n \left[\frac{k\,\Delta t}{2\varphi_n}\left(2w_n - \varphi_n L - d_y\right)\right]\end{aligned}\right\} \frac{\partial N^{**}_{i-j}}{\partial w_{i-j}} \tag{F.55}$$

$$\left.\begin{aligned}\frac{\partial N^{**}_{LT,i-j}}{\partial \varphi_{3,i-j}} &= \sum_n \frac{\partial N^{**}_{LT,i-j,n}}{\partial \varphi_{3,i-j}} = \sum_n \left[\frac{k\,\Delta t}{2\varphi_n^2}\left(w_n - w_n d_y - \varphi_n^2 \frac{L}{4}\right)\right] \\ \frac{\partial N^{**}_{RT,i-j}}{\partial \varphi_{3,i-j}} &= \sum_n \frac{\partial N^{**}_{RT,i-j,n}}{\partial \varphi_{3,i-j}} = \sum_n \left[-\frac{k\,\Delta t}{2\varphi_n^2}\left(w_n - w_n d_y - \varphi_n^2 \frac{L}{4}\right)\right]\end{aligned}\right\} \frac{\partial N^{**}_{i-j}}{\partial \varphi_{3,i-j}} \tag{F.56}$$

$$\left.\begin{aligned}\frac{\partial M^{**}_{3,LT,i-j}}{\partial w_{i-j}} &= \sum_n \frac{\partial M^{**}_{3,LT,i-j,n}}{\partial w_{i-j}} = \sum_n \left[\left(\frac{\partial N^{**}_{LT,i-j,n}}{\partial w_{i-j}}\right)\left(\frac{L}{3} - \frac{w_n}{3\varphi_n}\right) + \frac{N^{**}_{LT,i-j,n}}{3\varphi_n}\right] \\ \frac{\partial M^{**}_{3,RT,i-j}}{\partial w_{i-j}} &= \sum_n \frac{\partial M^{**}_{3,RT,i-j,n}}{\partial w_{i-j}} = \sum_n \left[-\left(\frac{\partial N^{**}_{RT,i-j,n}}{\partial w_{i-j}}\right)\left(\frac{L}{3} + \frac{w_n}{3\varphi_n}\right) + \frac{N^{**}_{RT,i-j,n}}{3\varphi_n}\right]\end{aligned}\right\} \frac{\partial M^{**}_{3,i-j}}{\partial w_{i-j}} \tag{F.57}$$

$$\left.\begin{aligned}\frac{\partial M^{**}_{3,LT,i-j}}{\partial \varphi_{3,i-j}} &= \sum_n \frac{\partial M^{**}_{3,LT,i-j,n}}{\partial \varphi_{3,i-j}} = \sum_n \left[\left(\frac{\partial N^{**}_{LT,i-j,n}}{\partial \varphi_{3,i-j}}\right)\left(\frac{L}{3} - \frac{w_n}{3\varphi_n}\right) - \frac{N^{**}_{LT,i-j,n}\,w_n}{3\varphi_n^2}\right] \\ \frac{\partial M^{**}_{3,RT,i-j}}{\partial \varphi_{3,i-j}} &= \sum_n \frac{\partial M^{**}_{3,RT,i-j,n}}{\partial \varphi_{3,i-j}} = \sum_n \left[-\left(\frac{\partial N^{**}_{RT,i-j,n}}{\partial \varphi_{3,i-j}}\right)\left(\frac{L}{3} + \frac{w_n}{3\varphi_n}\right) - \frac{N^{**}_{RT,i-j,n}\,w_n}{3\varphi_n^2}\right]\end{aligned}\right\} \frac{\partial M^{**}_{3,i-j}}{\partial \varphi_{3,i-j}} \tag{F.58}$$

Toe-crushing: case 2.B.ii

$$\left.\begin{aligned}\frac{\partial N^{**}_{LT,i-j}}{\partial w_{i-j}} &= \sum_n \frac{\partial N^{**}_{LT,i-j,n}}{\partial w_{i-j}} = \sum_n \left[-\frac{k\,\Delta t\left(\mu_{LT,i-j,n}-1\right)}{\mu_{LT,i-j,n}}\left(\frac{w_n}{\varphi_n}+\frac{L}{2}\right)\right] \\ \frac{\partial N^{**}_{RT,i-j}}{\partial w_{i-j}} &= \sum_n \frac{\partial N^{**}_{RT,i-j,n}}{\partial w_{i-j}} = \sum_n \left[\frac{k\,\Delta t\left(\mu_{RT,i-j,n}-1\right)}{\mu_{RT,i-j,n}}\left(\frac{w_n}{\varphi_n}-\frac{L}{2}\right)\right]\end{aligned}\right\} \frac{\partial N^{**}_{i-j}}{\partial w_{i-j}} \tag{F.59}$$

$$\left.\begin{aligned}\frac{\partial N^{**}_{LT,i-j}}{\partial \varphi_{3,i-j}} &= \sum_n \frac{\partial N^{**}_{LT,i-j,n}}{\partial \varphi_{3,i-j}} = \sum_n \left[\frac{k\,\Delta t\left(\mu_{LT,i-j,n}-1\right)}{2\mu_{LT,i-j,n}}\left(\frac{w_n^2}{\varphi_n^2}-\frac{L^2}{4}\right)\right] \\ \frac{\partial N^{**}_{RT,i-j}}{\partial \varphi_{3,i-j}} &= \sum_n \frac{\partial N^{**}_{RT,i-j,n}}{\partial \varphi_{3,i-j}} = \sum_n \left[-\frac{k\,\Delta t\left(\mu_{RT,i-j,n}-1\right)}{2\mu_{RT,i-j,n}}\left(\frac{w_n^2}{\varphi_n^2}-\frac{L^2}{4}\right)\right]\end{aligned}\right\} \frac{\partial N^{**}_{i-j}}{\partial \varphi_{3,i-j}} \tag{F.60}$$

$$\frac{\partial M^{**}_{3,i-j}}{\partial w_{i-j}} = \frac{\partial N^{**}_{i-j}}{\partial \varphi_{3,i-j}} \tag{F.61}$$

$$\left.\begin{aligned}\frac{\partial M^{**}_{3,LT,i-j}}{\partial \varphi_{3,i-j}} &= \sum_n \frac{\partial M^{**}_{3,LT,i-j,n}}{\partial \varphi_{3,i-j}} = \sum_n \left[\left(\frac{\partial N^{**}_{LT,i-j,n}}{\partial \varphi_{3,i-j}}\right)\left(\frac{L}{3}-\frac{w_n}{3\varphi_n}\right)-\frac{N^{**}_{LT,i-j,n}\,w_n}{3\varphi_n^2}\right] \\ \frac{\partial M^{**}_{3,RT,i-j}}{\partial \varphi_{3,i-j}} &= \sum_n \frac{\partial M^{**}_{3,RT,i-j,n}}{\partial \varphi_{3,i-j}} = \sum_n \left[-\left(\frac{\partial N^{**}_{RT,i-j,n}}{\partial \varphi_{3,i-j}}\right)\left(\frac{L}{3}+\frac{w_n}{3\varphi_n}\right)-\frac{N^{**}_{RT,i-j,n}\,w_n}{3\varphi_n^2}\right]\end{aligned}\right\} \frac{\partial M^{**}_{3,i-j}}{\partial \varphi_{3,i-j}} \tag{F.62}$$

No-compression: case 1

$$\frac{\partial N_{i-j}^{**}}{\partial w_{i-j}} = \sum_n \frac{\partial N_{i-j,n}^{**}}{\partial w_{i-j}} = \sum_n (-k\ \Delta t\ L) \tag{F.63}$$

$$\frac{\partial N_{i-j}^{**}}{\partial \varphi_{3,i-j}} = \sum_n \frac{\partial N_{i-j,n}^{**}}{\partial \varphi_{3,i-j}} = 0 \tag{F.64}$$

$$\frac{\partial M_{3,i-j}^{**}}{\partial w_{i-j}} = \frac{\partial N_{i-j}^{**}}{\partial \varphi_{3,i-j}} \tag{F.65}$$

$$\frac{\partial M_{3,i-j}^{**}}{\partial \varphi_{3,i-j}} = \sum_n \frac{\partial M_{3,i-j,n}^{**}}{\partial \varphi_{3,i-j}} = \sum_n \left(-\frac{k\ \Delta t\ L^3}{12}\right) \tag{F.66}$$

No-compression: case 2

$$\frac{\partial N_{i-j}^{**}}{\partial w_{i-j}} = \sum_n \frac{\partial N_{i-j,n}^{**}}{\partial w_{i-j}} = \sum_n \left[\frac{k\ \Delta t}{2|\varphi_n|}(2w_n - |\varphi_n|L)\right] \tag{F.67}$$

$$\frac{\partial N_{i-j}^{**}}{\partial \varphi_{3,i-j}} = \sum_n \frac{\partial N_{i-j,n}^{**}}{\partial \varphi_{3,i-j}} = \sum_n \left[-\frac{k\ \Delta t}{8|\varphi_n|\varphi_n}(4w_n^2 - \varphi_n^2 L^2)\right] \tag{F.68}$$

$$\frac{\partial M_{3,i-j}^{**}}{\partial w_{i-j}} = \frac{\partial N_{i-j}^{**}}{\partial \varphi_{3,i-j}} \tag{F.69}$$

$$\frac{\partial M_{3,i-j}^{**}}{\partial \varphi_{3,i-j}} = \sum_n \frac{\partial M_{3,i-j,n}^{**}}{\partial \varphi_{3,i-j}} = \sum_n \left[\frac{k\ \Delta t}{24|\varphi_n|\varphi_n^2}(8w_n^3 - L^3|\varphi_n|^3)\right] \tag{F.70}$$